Electronic structure and Fermi surface topology of binary and ternary compounds

P. V. SREENIVASA REDDY

A Thesis Submitted to

Indian Institute of Technology Hyderabad

In Partial Fulfillment of the Requirements for

The Degree of Doctor of Philosophy

भारतीय प्रौद्योगिकी संस्थान हैदराबाद

Indian Institute of Technology Hyderabad

Department of Physics

April 2018

Declaration

I declare that this written submission represents my ideas in my own words, and where ideas or words of others have been included, I have adequately cited and referenced the original sources. I also declare that I have adhered to all principles of academic honesty and integrity and have not misrepresented or fabricated or falsified any idea/data/fact/source in my submission. I understand that any violation of the above will be a cause for disciplinary action by the Institute and can also evoke penal action from the sources that have thus not been properly cited, or from whom proper permission has not been taken when needed.

Sreenivasa Reddy.

(P. V. SREENIVASA REDDY)

PH13P0001

Approval Sheet

This thesis entitled "Electronic structure and Fermi surface topology of binary and ternary compounds" by P. V. SREENIVASA REDDY is approved for the degree of Doctor of Philosophy from IIT Hyderabad

Zakir Hossain

Prof. ZAKIR HOSSAIN
Dept. of Physics
IIT Kanpur
External Examiner

Dr. V. KANCHANA
Associate Professor
Dept. of Physics
IIT Hyderabad
Adviser

Vandana Sharma
Dr. VANDANA SHARMA

IIT Hyderabad
Examiner

Dr. BHABANI S. MALLIK

IIT Hyderabad
Chairman

Acknowledgements

I can not imagine the work whatever I have carried out until the final stage of my Ph. D. and writing of this Ph. D. thesis without the help of several people. This is the stage where I have the opportunity to show my gratitude towards them by conveying my acknowledgement heart-fully. For some people these words are not sufficient.

First and foremost I would like to thank my thesis adviser **Dr. V. Kanchana**, for her valuable guidance, patience, caring and unconditional availability and consistent encouragement which I received throughout the research work. This thesis would not have been possible without her support and encouragement. I cannot thank her enough. I am forever grateful to her. In one sentence to say 'all her inputs made me a self-consistent person in my research life'.

Besides my supervisor, I would like to extend my sincere thanks to **Dr. G. Vaitheeswaran**, ACRHEM, University of Hyderabad, for his valuable advises and constructive criticism. He is always available with hundreds of literatures which I need for my research work, without which I would not have gone ahead a single step in my research work. I am forever grateful to him.

I extend my sincere thanks to all my adviser's collaborators **Prof. David J. Singh**, University of Missouri, Columbia, USA, **Prof. N. E. Christensen** and late **Prof. A. Svane**, Aarhus University, Denmark, **Prof. Andrei V Ruban**, Royal Institute of Technology (KTH), Stockholm, Sweden, **Dr. P. Modak** and **Dr. Ashok K. Verma**, Bhabha Atomic Research Centre, India, **Prof. S. B. Dugdale** and **T. E. Millichamp**, University of Bristol, UK, for their fruitful suggestions and discussions as a part of my work.

My sincere thanks must also go to my doctoral committee members: **Dr. Jyoti Ranjan Mohanty**, Department of Physics, IIT Hyderabad and **Dr. Bharat Bhooshan Panigrahi**, HOD, Department of Materials Science and Metallurgical Engineering, IIT Hyderabad, for their encouragement, insightful comments.

I would like to acknowledge **Dr. Saket Asthana**, HOD, Department of Physics, and **Prof. A. K. Giri**, Department of Physics and IITH for providing necessary infrastructure and resources to accomplish my research work. I gratefully acknowledge all the faculty members of the Department of Physics, IITH. My sincere thanks goes to **Prof. U. B. Desai**, Director of Indian Institute of Technology Hyderabad for providing challenging environment for doing research. I am also thankful to **Prof. F. A. Khan** and **Prof. Ch. Subrahmanyam** for providing all academic needs.

I wish to thank the Department of Science and Technology (DST), Government of India, New Delhi, through Indian institute of Technology Hyderabad for providing financial assistance in the form of Research Fellowship which supported me to perform my work comfortably.

I would also like to extend my thanks to my past group members **Dr. Swetarekha Ram, Dr. Vijay Kumar Gudelli** and **Dr. Shwetha Gummula** and present group members **Mrs. Sreeparvathy PC, Mr. P. Rambabu** and **Mr. Vineet** for their continuous support. I would also like to thank my friends and research scholars of the Department of Physics and other departments for their continuous encouragement. I would also thank my friends **Dr. N. V. Subba Reddy, Dr. Janardhan Reddy, Mr. Balaji Jampala, Mr. Jagan Mohan Reddy and others** who helped me a lot to come to the present stage. Saying a word 'thank you' is not sufficient to them. I would also like to thank my present and old room mates.

I would like to extend my sincere acknowledgements to Physics lab staff, stores, academic, administration, High Performance Computational staff members, library staff and Security staff for

their constant support in my academic and non-academic works.

I would like to thank my family, especially my father **P. Venkata Rami Reddy**, mother **P. Tiripalamma** and to my sister **Venkata Lakshmi** and their family members, for their continuous love and support.

Dedication

To my **Parents** and
all my **Friends** who brought me to this stage

Abstract

To explore the material properties, electronic structure calculations are very much useful and can be obtained from the well known density functional theory(DFT) calculations. In the present thesis, we have focussed on the Fermi surface calculations and try to link the same with other physical properties. In addition, we have also explored the pressure effect on properties of the system. For the present study, we have selected different types of compounds which are Ni-based Heusler compounds, Nb-based A-15 compounds, Sn-based binary compounds and few magnetic compounds(one Zr-based Heusler compound and other Mn-based compounds).

Electronic structure, mechanical, vibrational properties of Ni-based Heusler compounds, Ni_2XAl (X=Ti, Zr, Hf, V, Nb, and Ta), Ni_2NbGa and Ni_2NbSn, are presented both at ambient and under compression. Among the mentioned compounds, Ni_2NbAl, Ni_2NbGa and Ni_2NbSn are experimentally reported as superconductors at ambient and our calculated superconducting transition temperature (T_c) and electron-phonon coupling constant (λ_{ep}) values are in good agreement with the experiments. In addition, we have predicted superconducting nature in Ni_2VAl with electron-phonon coupling constant (λ_{ep}) around 0.68, which leads to superconducting transition temperature (T_c) around $\sim$4 K (by using coulomb pseudopotential $\mu^* = 0.13$), which is a relatively high transition temperature for Ni based Heusler alloys and are compared with other Ni_2NbY (Y = Al, Ga and Sn) compounds. From the calculated Fermi surfaces, flat Fermi sheets are observed along X-Γ direction in all the compounds. These flat Fermi sheets exhibit nesting feature, thereby leading to a Kohn anomaly in the phonon dispersion relation for the transverse acoustic mode TA2 along the (1,1,0) direction. As pressure increases, change in the number of Fermi surfaces is observed in Ni_2NbAl and a corresponding non-linear decrease in the total density of states is observed under compression in this compound. Hardening of the phonon modes is observed in all the compounds with increase in pressure. But in the superconducting Ni_2VAl and Ni_2NbY (Y = Al, Ga and Sn) compounds, acoustic TA2 mode with observed Kohn anomaly, is found to soften with pressure. As a consequence, T_c and λ_{ep} vary non-monotonically under pressure in superconducting compounds.

In addition to Heusler compounds, electronic structure calculations of A-15 type Nb_3Y (Y = Al, Ga, In, Ge, Sn, Os, Ir and Pt) compounds are performed at ambient and high pressures. Mechanical stability is confirmed in all the compounds both at ambient as well as under compression from the calculated elastic constants. We have observed four holes and two electron Fermi surfaces (FS) for the compounds Nb_3Y (Y = Al, Ga, In, Ge, Sn), two hole and two electron FS for Nb_3Y (Y = Os, Ir) and one hole and three electron FS for Nb_3Pt and FS nesting feature is observed at M high symmetry point and along X-Γ in all the compounds. A continuous change in the FS topology is observed under pressure in all the compounds which is also reflected in the calculated elastic constants and density of states under pressure indicating the electronic topological transitions (ETT). The ETT observed around 21.5 GPa, 17.5 GPa in Nb_3Al and Nb_3Ga respectively are in good agreement with the anomalies observed by the experiments. In the case of Nb_3Sn, observed ETT is in agreement with recent experimental anomalies at the pressure around 6 GPa.

Electronic structure and vibrational properties of SnAs and SnSb are presented and analysed in detail. Total energy calculations show first order phase transition from NaCl structure to CsCl one at around 37 GPa and 13 GPa for SnAs and SnSb respectively, which is also confirmed from enthalpy calculations and agree well with experimental work. Phonon dispersion and hence the electron-phonon coupling, λ_{ep}, and superconducting transition temperature, T_c, across the phase

transition are computed for both the compounds. These calculations give an ambient pressure T_c, in the NaCl structure, of 3.08 K for both SnAs and SnSb in good agreement with experiment whilst at the transition pressure, in the CsCl structure, a drastically increased value of T_c=12.2 K, 9.18 K is found for SnAs and SnSb respectively. Calculations also show a dramatic increase in the electronic density of states at this pressure. The lowest energy acoustic phonon branch in each structure also demonstrate some softening effects. Electronic structure calculations of the Fermi surface in both the phases are presented for the first time, together with further calculations of the generalised susceptibility.

In addition to non-magnetic compounds, we have performed electronic structure calculations for magnetic compounds Zr_2TiAl and Cu_2Sb type Mn-based compounds. In Zr_2TiAl, total energy calculations shows antiferromagnetic $L1_1$-like (AFM) phase with alternating (111) spin-up and spin-down layers to be a stable phase among some other types of magnetic configurations with magnetic moment on Ti being $1.22\mu_B$. The phonon dispersion relations further confirm the stability of the magnetic phase in Zr_2TiAl, while the non-magnetic phase is found to have imaginary phonon modes and the same is also found from the calculated elastic constants. In Zr_2TiAl, the magnetic moment of Ti is found to decrease under pressure eventually driving the system to the non-magnetic phase at around 46 GPa, where the phonon modes are found to be positive indicating the stability of the non-magnetic phase. A continuous change in the band structure under compression leads to the corresponding change of the Fermi surface topology and Electronic Topological Transitions (ETT) in both majority and minority spin cases of Zr_2TiAl, which are also evident from the calculated elastic constants and density of states calculations for the material under compression. In the case of Mn-based compounds MnAlGe, MnGaGe and MnZnSb, quasi two dimensional nature is observed from the Fermi surface calculations. Under compression decrease in the magnetic moment of Mn atom and change in the band and FS topology is observed in all the Mn-based compounds. Non-linear nature in the elastic constants is observed under compression in all the compounds. Particularly in MnZnSb, a sudden drop in magnetic moment is observed at around $V/V_0 = 0.94$ and also a spin flipping in the total density of states at the same compression is observed. Negative values in the elastic constants are observed in MnZnSb at the same compression around $V/V_0 = 0.94$ where we find a change in the band and FS topology correspondingly. For MnZnSb, pressure values corresponding to the compression around $V/V_0 = 0.94$ are in good agreement with experimentally observed anomalies in the calculations of lattice parameters under pressure, which might imply a possible structural phase transition or an ETT (which we have discussed in the present work) in MnZnSb around this compression. Finally we have given the concluding remarks for the complete thesis work and also presented a discussion regarding the future work.

Contents

Nomenclature

List of symbols

k_B	Boltzman's constant
h	Planck's constant
$\hbar$	Reduced Planck's constant (J. s)
V_{eff}	Interaction between the electrons mediated by the electron-phonon coupling
M	Atomic mass
$N(E_F)$	Density of states at Fermi level
E_F	Fermi level
V_{ext}	External nuclear potential
$\widehat{H}$	Hamiltonian
m_i	Electronic mass
Z_I	Nuclear charges
M_I	Nuclear mass
$\widehat{T}_e$	Kinetic energy of the electron
$\widehat{V}_{ee}$	Potential energy of the electron
$\widehat{T}_n$	Kinetic energy of the nucleus
$\widehat{V}_{en}$	Potential energy of the electron and nucleus
$\widehat{V}_{nn}$	Potential energy of the nucleus
E_0	Ground state energy
E_{xc}	Exchange-correlation energy
V_{KS}	Kohn-Sham potential
j_l	Spherical Bessel functions
$n(r)$	Electronic density as a function of position
R_{MT}	Muffin-tin radius
K_{Max}	Plane wave cut-off
G_{max}	Charge-density Fourier expansion (a.u.$^{-1}$)
C_{ij}	Elastic constants (GPa)
G_H	Hill's shear modulus (GPa)
G_R	Reuss shear modulus (GPa)
G_v	Voigt shear modulus (GPa)
E	Young's modulus (GPa)
B	Bulk modulus (GPa)
A	Anisotropy factor
v_l	Longitudinal sound velocity (km/s)
v_t	Transverse sound velocity (km/s)
v_m	Mean sound velocity (km/s)
Θ_D	Debye temperature (K)
T_c	Superconducting transition temperature (K)

Greek Letters

Subscripts

i, j	Number of electron index
I, J	Number of nucleus index
e	Electron
n	Nucleus

Abbreviations

DFT	Density-functional theory
LDA	Local density approximation
GGA	Genelarized gradient approximation
LAPW	Linearized augmented planewave
FP-LAPW	Full-potential linearized augmented planewave
SOC	Spin-orbit coupling
BZ	Brillouin zone
DOS	Density of states
HF	Hartree-Fock
AE	All electron
ps	Pseudo function

Chapter 1

Introduction

One of the most important characteristics of a metal is its Fermi surface (FS), the surface of constant energy in k-space. The Fermi surface can also be known as the equal-energy surface separating occupied states in quasi-momentum space from empty states (at absolute zero). According to Mackintosh [1], 'a solid with a Fermi surface' can be called as metal. The importance of the Fermi surface can also be known by a statement given by Kaganov and Lifshitz [2], the Fermi surface is "the stage on which the 'drama of the life of the electron' is played out", indicating the key concept that 'Fermi surface' is responsible or will illustrate the properties of the materials which are mainly due to the electrons at the Fermi level. Onsager [3] first described the connection between the magnetic oscillation and the Fermi surface on the basis of the electron dynamics and the quantum mechanical concepts. Later the same idea is developed by Lifshitz together with Kosevich [4]. The knowledge about the FS of a metal is an important tool to understand various properties of a metallic system such as structural transition, elastic, magnetic properties etc. First principles band structure calculations serve as a good source to analyse these above properties which are related to the FS topology. The geometrical characteristics of Fermi surface, such as the shape, curvature, and cross-sectional area, are related to the physical properties of metals. For example, the velocity of electron on the Fermi surface can be estimated from the knowledge of the effective mass, which is calculated from the cyclotron resonance frequency. Dynamical properties of an electron on the Fermi surface depends on the shape of the Fermi surface which can guide the electrical properties of a metal with respect to the Brillouin zone [5]. The discussion regarding the importance of the Fermi surface with some examples is given in the following section.

1.1 Importance of Fermi surface

Fermi surface topology is very much helpful in explaining the electronic topological transitions(ETT). According to Lifshitz, the connectivity of the Fermi surface will change at some points, due to various reasons such as van Hove singularity [6], because of the variation of thermal, static or chemical pressure [7]. The transition can be brought about either by alloying the material which is changing the electron per atom ratio or by applying pressure or due to the uniaxial stress. The changes in the connectivity will be of four types. First, opening up of a electron or hole pocket. Second, closing of a electron or hole pocket. Third, formation of a neck. Fourth, the pinching off of a neck [8]. A

change in the Fermi surface topology and its effect on the properties of the electrons motivated both experimentalists and theoreticians and I. M. Lifshitz [7] named this type of transitions as $2\frac{1}{2}$ order phase transition. It became complicated to prove this through experiments and experimental data interpretations. This resulted in the deceleration on the studies of electronic topological transitions (ETT) until the discovery of giant anomaly in the thermopower at the vicinity of ETT [9].

Anomaly in the thermopower measurements as a function of concentration is observed in Li-Mg alloys by Egorov and Fedorov [9]. The reason may be due to the presence of ETT and later it was confirmed by Bruno et al [10] with the observation of a neck arising in the Fermi surface at N-point which is at the concentration of Li around 0.80%. In some of the Cd-Mg alloys, anomalies are observed [11, 12, 13, 14] in the conductivity, thermopower and low temperature heat capacity values at two different Mg concentration levels of $c \sim 0.11$ and $c \sim 0.06$. The first one is due to the appearance of new electron band at L-point and the second is due to the change in the band topology at K-point.

In some of the heavy fermion systems, the Fermi surface is found to evolve under an applied magnetic field (see, e.g. [15, 16]) which can be called as ETTs driven by Zeeman effect. In some compounds, such as URhGe, both ferromagnetism and superconductivity are found to coexist [17] because of triplet equal-spin Cooper pairs. In this compound, application of magnetic field initially kills the superconductivity and it reappears at high magnetic field [18]. The Fermi surface in URhGe was measured by Yelland et al [19] and they reported ETT in this compound by observing the evolution of Fermi surface as a function of applied magnetic field and also observed the disappearance of a minority spin Fermi surface pocket with a Fermi velocity (v_F) falling to zero at the ETT. The change in the Hall coefficient at particular magnetic field agree with the disappearance of a heavy (small v_F) sheet [20].

In the case of $Sr_3Ru_2O_7$, metamagnetic behaviour [21] is observed and also the connection between field induced changes in the Fermi surface across the metamagnetic transition (most likely due to a van Hove singularity close to the Fermi energy) and the presence of a spin density wave (SDW) [22] is observed. It is likely that the presence of a SDW could be associated with appearance of a nested Fermi surface.

In Fe-based High T_c superconductors like Fe-pnictide superconductors, the Fermi surface is playing an important role in relating magnetism and superconductivity [23]. For example in $CaFe_2As_2$, the tetragonal structure gives way to apparently concomitant SDW and orthorhombic transitions [24, 25] at 170 K. With the application of small pressure the transition is suppressed and superconductivity appears at low temperature [26] but with the application of high pressures a 'collapsed tetragonal' (cT) phase emerges which is non-magnetic [27]. In the recent studies (e.g. [28, 29]), the connection between the disappearance of the Γ centred hole pockets at the cT transition with the disappearance of magnetism and bulk superconductivity is established. To know more about ETT, a review by Blanter et al [8] can provide more theoretical insight and another review by Bruno et al [30] can provide several examples.

The Fermi surface topology is also useful to explain anomalies in the phonon dispersion. One can imagine that a phonon with a wavevector 'q' establishes a potential which the electrons will then try to screen so that the ions are effectively interacting with each other through this screened potential. Due to this the forces between the ions will change and hence the vibrational frequency also can change. Kohn pointed that these singularities in the electron response can be reflected

in the phonon spectra [31]. Later Taylor [32] started to examine the effect of the curvature of the Fermi surface on Kohn anomalies. After that Afanas'ev and Kagan [33] examined the flat nature of the Fermi surface and reported that they will have more effect on the Kohn anomalies and called them as 'nested Fermi surfaces'. In general, Fermi surface nesting describes the situation in which different sheets of Fermi surface or different parts of the same sheet can be made to coincide through a translation of some particular 'q' vector. It is also observed that the logarithmic divergence in the bare susceptibility (which is coming from the perfectly nested planar Fermi surface) will have a smooth peak for finite curvature.

An electronic instability which is known as Peierls transition at zero temperature in one dimensional crystal occurs because of the perfect nesting in a one-dimensional Fermi surface. For a long time the CDWs in the metal are commonly interpreted within the Peierls picture, associating the appearance of CDWs in metals with the presence of nesting in the Fermi surface. After a while Mazin and Johannes [34] cast a doubt whether the Fermi surface nesting could be responsible for the formation of CDWs only in one-dimension (which was where Peierls first made his observation) or higher dimensions also, and they pointed out that the Peierls mechanism is very weak in one dimension. In recent work done by Zhu et al [35], the classification of CDWs changed based on the mechanism behind their formation. Here they proposed two types of CDWs. Type I is due to Fermi surface nesting and type II is due to 'q' dependent electron phonon coupling.

Some alloys will remember their previous forms when subjected to some external pressure or temperature [36] and the materials are called as shape memory alloys. Some of these materials may transform to martensite phase at low temperatures. These transitions are preceded by 'premartensitic' phenomena like strong phonon softening, diffuse scattering in electron diffraction well above the actual martensitic transformation, and are believed to have a common origin associated with Fermi surface nesting [37]. In the case of β-phase NiAl shape-memory alloy, calculations of the electronic structure and the phonon dispersions indicated that the softening was linked with a nesting feature in the Fermi surface [38], subsequently identified experimentally by Dugdale et al [39]. Similar conclusions were drawn for Ni-Ti [40] and AuZn [41]. There also exist some ferromagnetic shape memory alloys, like the Heusler alloy Ni_2MnGa, which is the most well-known example [42]. For these alloys, an external magnetic field can provide the stimulus required for the alloy to change its shape. With a Curie temperature of about $\sim$380 K , the premartensitic and martensitic transformations occur within the ferromagnetic state ($\sim$250 K and $\sim$220 K , respectively). The exchange splitting, and therefore the Fermi surface topology will be evolving as a function of temperature, something not taken into account in earlier investigations of Fermi surface nesting [43]. Calculations of bare susceptibility is one of the way to know the nesting feature at particular 'q' vector. Lee et al calculated the bare susceptibility as a function of the saturation magnetisation [44] and proved that one particular nested sheet of Fermi surface is promoting the premartensitic phonon softening [45], and caused the system to undergo martensitic transformation. Experimentally, the Fermi surface of Ni_2MnGa was reported by the positron annihilation experiments of Haynes et al [46], revealing the nesting vectors that could be compatible with the premartensitic ordering.

As mentioned above, Fermi surface plays an important role in explaining the different physical properties of the metallic systems. These physical properties vary under the application of external stimuli like pressure, temperature, etc. In the present thesis we have applied uniform pressure on the studied compounds and observed its importance in the physical properties of metallic systems.

In the following section we have discussed how the application of pressure will effect the physical properties of the systems.

1.2 Application of pressure and it's importance on the physical properties of solids

Pressure is a thermodynamic variable which plays an important role in solid state physics. Applying high pressure is a powerful tool to understand the properties of materials. Pressure can affect the interatomic distances while leaving the thermal energy of the system invariant. The basic effect of pressure is compression of the material which leads to the overlapping of adjacent atomic orbitals. This will affect the electronic properties by means of broadening of the bands, delocalization of electrons, decrease in the magnitude of the forbidden gap between the bands. These changes will be reflected in the variation of electrical resistivity of semiconductors, insulators, semi metals and metals. The synthesis of materials like diamond and Boron nitride under high pressure is one of the important industrial applications of high pressure. In the field of superconductivity, pressure induced superconductivity is an important phenomenon in the field of high pressure research. Some of the pressure induced effects are given in the following.

One of the interesting area in high pressure research is pressure induced metallisation. Metallisation pressure of Iodine is around 20 GPa, Xenon is around 130 GPa, Hydrogen is above 300 GPa and Cesium iodide (CsI) is predicted to be metallize around 80 GPa [47]. Recently, pressure induced metallization at around 60 GPa with absence of structural transition is observed in layered molybdenum diselenide($MoSe_2$) [48]. Very recently, Zhou et al [49] observed pressure induced metallization and superconducting phase in ReS_2 at around 90 GPa with super conducting transition temperature around 2K.

Another interesting phenomenon in the high pressure research is structural phase transitions in solids. A phase transition from NaCl phase to CsCl phase is observed [50] in some of the rare earth tellurides CrTe(4.8), PrTe(9.5), NdTe(22.9), PmTe(8.1), SmTe(9.6), EuTe(13.0), GdTe(25.2), TbTe(9.5), DyTe(3.1), HoTe(46.6), ErTe(12.7), TmTe(14.9) and YbTe(17.7) compounds with corresponding pressure values given in brackets in the units of GPa.

Pressure induced valence transition which occurs due to the delocalisation of electrons is another active area of research in the high pressure field. For example, in some rare earth chalcogenide compounds like SmS(0.65), SmSe(1.5-4), SmTe(2-5), TmTe(1.5-3), YbTe(15-20) the valence of the rare earth ion changes from divalent(2+) to trivalent(3+) state under pressure [51]. In the case of EuO [52] a divalent to an intermediate valence state, with the resulting effective valency of 2.35 is observed above 48 GPa pressure. In the case of AgO, Chunju Hou et al [53] observed a pressure induced semiconductor to metal transition at around 75 GPa and at around 77 GPa structural transition from monoclinic ($P2_1/c$) to trigonal ($R\bar{3}m$) is observed along with a valence state transition from the mixed-valence state to a single-valence state.

Another important observation is electron transfer form '*s*' to '*d*' states with the application of pressure. In alkali and alkaline earth metals, pressure induced '*s*-*d*' electron transfer is observed. The pressure dependence of T_c from high pressure electrical resistivity study and the band structure calculations have revealed the '*s*-*d*' transfer of electrons in the elements like Ba, Ca and Sr[54]. In general, it was shown that the pressure induced superconductivity among the transition metals

is related to a change in the electronic band structure namely '*s*-*d*' transfer which results in the enhancement of T_c. In many of band structure calculations '*s*-*d*' transfer is a common feature under pressure. As pressure increases '*s*' bands will tend to move towards the '*d*' bands. Because of this the spacing between '*s*' and '*d*' will reduce and the probability of electron transfer form '*s*' to '*d*' will increase which causes increase in '*d*' band occupancy. This process is known as '*s*-*d*' transfer of electrons. In metals, valence '*d*' electrons are relatively localized compared to '*s*' and '*p*' electrons. If we give a small energy to '*s*' electrons in the form of pressure, these '*s*' electrons will transfer to '*d*' states which will affect the other properties of the systems under pressure.

Pressure has long been known to have a profound effect on the superconducting properties of elements and compounds [55, 56]. After the discovery of superconductivity in Hg, several thousand materials have been found to be superconductors which includes pure elements as well as their alloys. Many of them become superconductors under certain conditions like high pressure, thin films and amorphous state. The importance of high pressure in the field of superconductivity was realized after the discovery of superconductivity to be around 30 K in La-Ba-Cu-O system by Bednorz and Müller [57] in the year of 1986. For the same system, Chu et al[58] in 1987 showed that the critical temperature T_c increases from 30 K to above 40 K by applying a pressure of around 1.5 GPa. In the same year, another discovery of 90 K superconductivity was reported in Y-Ba-Cu-O system by Wu et al [59]. There is no categorical rule guiding the dependence of T_c on pressure. There are several elements that become superconducting under pressure. These include semiconductors like Si, Ge and Sb which exhibit metallic character under pressure and metals like Sc, Y, Ce and U which belong to transition and lanthanide-actinide series in the periodic table. Among non-transition metals, except thallium, all others show a decrease in T_c under pressure. In thallium, T_c increases upto 20 kbar and then decreases with increase of pressure. Sn undergoes a structural phase transition under pressure and in both of its phases, T_c decreases as pressure increases. In SnO, Forthaus et al [60] observed the appearance of a superconducting phase under pressure which is having dome like phase diagram with a maximum T_c value of 1.43 K at around 9.3 GPa and also found the disappearance of superconductivity above the pressure of 16 GPa. In metals, at the beginning of the transition series like Ti and Zr, positive values of dT_c/dp are observed. The pressure dependence of $N(E_F)$ in transition metals can be determined by the dependence of $N(E_F)$ on the number of valence electrons N_e [61]. T_c will rise when $(dN(E_F)/dN_e)>0$ and T_c decreases if $(dN(E_F)/dN_e)<0$. According to this, dT_c/dp in Ti and Zr should be positive and in Ta and Nb, it should be negative. This exactly agrees with the experimental results. However, this simple argument does not account for the experimental observations on the pressure dependence of T_c in V and Mo. Thus, there is no universal behaviour in the variation of T_c under pressure. Recent studies achieved a world record in high superconducting transition temperature with a value of 203 K at the pressure of 200 GPa by Drozdov et al [62] in H_2S highlighting the importance of pressure in the investigation of superconductors.

In the present thesis we have discussed the importance of the Fermi surface to understand the physical properties of the studied systems and how these properties will change with the application of pressure. In the next section we have given the overview of the studied compounds.

1.3 Overview of the compounds of present study

1.3.1 Heusler compounds

The Heusler class of materials are well known for their plenty of applications ranging from spintronic to thermoelectric and superconductors to topological insulators due to their wide range of material properties that can be engineered. Because of this researchers are showing a lot of interest on these type of compounds. Upto now more than 1000 Heusler compounds were prepared which are having a multitude of different properties. These Heusler compounds seem to be the material of choice for many applications because of their tunable electronic structure properties. This helps in the design of materials with desirable properties from half-metallic ferromagnet [63, 64] over completely ferrimagnet [65] to non-magnetic semiconductors [66, 67]. In the present days, the search of new materials for spintronics applications was growing within the Heusler class of compounds which was started before 30 years [63]. These materials have passionate applications in spintronics [68, 69, 70], optoelectronics [71], as shape memory [72] alloys and as superconductors [73, 74]. Over the past few decades, new areas of applications emerged comprising the environmental technologies such as thermoelectric [75, 76] and solar cell applications [77]. Recently, a new trend in the material properties which belong to new quantum state of matter is observed [78, 79]. These materials are named as topological insulators and are having technological importance due to the conduction of electrons being extremely high because of its surface states and might attract application in high performance electronic systems. This could be one of the future research perspective on Heusler compounds enabling them to be more productive.

Ternary intermetallic Heusler compounds can be represented with general formula XYZ (known as Half-Heusler) or X_2YZ, where X and Y elements generally belong to transition metals (having 'd' states) and Z belongs to main group element. In 1903 Fritz Heusler [80, 81] discovered these class of materials. Important feature of these compounds is, the properties of the total system is completely different from the properties of the individual elements contained in this type of compounds. For example, if we consider the compound Cu_2MnAl, which is reported as magnetic none of its constitutional elements possess magnetic order independently. Similarly, in another compound TiNiSn, which is reported to have semiconducting nature all it's constitutional elements posses metallic character [82]. The count on the number of these type of compounds is endless and can be prepared by mixing all the elements in the periodic table and leading to several applications and need to be explored.

Early reports on Heusler phases appear in the context of X_2MnZ alloys, where X = Ni, Pd, Au and Z = Al, Si, Ga, Ge, In, Sn, Sb, with a particular focus on their chemical and magnetic order, and on an ordering transition that can be induced by composition, temperature, or pressure. Remarkably, a ferromagnetic to antiferromagnetic transition was observed in $Pd_2MnIn_{1-x}Sn_x$. Webster and coworkers [83]were the first to explore the magnetic properties of Co_2MnZ compounds, which they stated were quite different from previously studied Heuslers, as the former compounds incorporate elements other than Mn that carry a substantial local magnetic moment. After this Ishida et al [84] first began exploring half metallic ferrimagnets in Co_2-based Heusler compounds, such as Co_2MnSn, Co_2TiAl, and Co_2TiSn. In addition, NiMnSb, Co_2MnSi, Mn_2VAl attracted a lot of attention, as it was identified early as a half metallic ferrimagnets by numerical methods. Nevertheless, experimental and theoretical studies have focused largely on the Co-based compounds. Renewed interest

in the Mn-based compounds was triggered by the discovery of structurally distorted cubic systems: namely the tetragonally distorted Heusler compounds. The most renowned member, Mn_3Ga, which is known as tetragonal Heusler material, was already explored in the 1970s itself, yet the potential for spintronic applications was not recognized until the late 2000s. Among the Mn-based Heusler compounds, a particularly interesting material is Mn_2CoAl, which is the first example of a spin-gapless semiconductor in the Heusler family of compounds. After this CoFeCrAl, CoMnCrSi, CoFeVSi, FeMnCrSb and FeTiVSi are predicted to be spin-gapless semiconductors. Among the Heusler family, shape memory materials Ni_2MnGa and Mn_2NiGa have particular interest for their reversible structural phase transitions from cubic to tetragonal lattices.

Among the Heusler alloys, Ni based compounds Ni_2XAl (X=Ti, Zr, Hf, V, Nb, and Ta), Ni_2NbGa and Ni_2NbSn attracted much because of there paramagnetic nature. Though the Heusler compounds are well known for their ferromagnetic properties, it is interesting to note the existence of paramagnetic compounds, one among them is the above mentioned series Ni_2XAl [85]. Ni_2TiAl and many other Ni-based compounds have been explored from various perspective, eversince it was found that the high temperature creep resistance of NiAl could be improved by Ti addition [86], which stabilized the compounds in the Heusler type structure. The structural properties of Ni_2TiAl was further studied experimentally by Taylor and Floyd [87], using X-rays and electron spectroscopy and Umakoshi et al [88] further confirmed Ni_2TiAl to have small lattice mismatch with B2 phase and found the same to possess good stability. This series attracted further interest and a complete phase diagram of Ni_2TAl (T = Zr, Nb and Ta) was obtained by Raman and Schubert [89]. Theoretical insight on the above mentioned series was also provided by Lin and Freeman [85] further substantiating the stability of $L2_1$ structure of Ni_2XAl (X = Zr, Nb and Ta). Further, Da Rocha et al. [90] have reported the specific heat and electronic structure of the above mentioned series. Among those compounds, Ni_2NbAl, Ni_2NbGa and Ni_2NbSn are experimentally found to be superconductors with superconducting transition temperature(T_c) 2.15 K [91], 1.54 K [91] and 2.9 K [91] respectively. All the above literature explain the importance of Heusler alloys and a chapter of this thesis deals with the same as discussed in the subsequent section. In our work the key point is the prediction of superconducting nature in Ni_2VAl compound and it is compared with other superconducting Heusler compounds Ni_2NbAl, Ni_2NbGa and Ni_2NbSn.

1.3.2 A-15 compounds

A-15 compounds are having Cr_3Si type crystal structure and can be indicated with formula A_3B, where A belongs to transition metal and B can be any element in the periodic table. The A_3B type intermetallic compound Cr_3Si is discoverd by Boren et al in 1933 [92]. Even though several other compounds with same A-15 structure were discovered in later years, no research interest was found among the researchers until the discovery of superconducting vanadium silicide V_3Si with superconducting transition temperature around 17 K in 1953 [93]. Later several superconductors were found and among them Nb-Ge have the highest T_c of 23.2 K [93] and was highest until the discovery of cuprate superconductors. The discovery of superconductivity in Nb_3Sn by Matthias et al [94] attracted further importance. Nb_3Sn is used to produce high magnetic field applications, for example, NMR spectrometers and high end MRI scanners. To get the magnetic fields above 10 Tesla doped Nb_3Sn are pretty much useful. The interest in these A-15 compounds are not only due to the rather high T_c but also their high critical current density and critical magnetic field, along

with acceptable mechanical properties make them viable for applications. Some of these compounds undergo cubic to tetragonal martensitic transformation near to their superconducting transition temperatures T_c [95]. For example, the martensitic transition temperatures of V_3Si (21 K) and Nb_3Sn (45 K) are close to their respective superconducting transition temperatures of 17 K and 18 K. Acoustic phonon instabilities were found to be responsible for martensitic transition in previous studies [96]. A similar behaviour was also seen in $Nb_3Al_xGe_{1-x}$ [97], V_3Ga [98, 99], V_3Ge [99] and Nb_3Al [100] compounds. Experiments [101] also indicated a dimerization of the transition-metal chains accompanied by a tetragonal distortion of the lattice during the transformation. It has been proposed that the tetragonal transformation is driven by band Jahn-Teller like mechanism. These A-15 compounds exhibits different behaviour in electronically derived properties at low temperatures such as knight shifts, electrical resistivity etc [102]. This unusual behaviour of various properties of A-15 family compounds has been related to the sharp peak in electronic density of states near to the Fermi level arising from the '*d*' states of the transition metal atoms [102]. To know more about the A-15 compounds a review on 'superconducting A-15 compounds' by Dew-Hughes [103] is very much helpful. Hence it is clear that the properties of these compounds are mainly related to their electron behaviour and can be understood from the electronic structure details.

For the present study we are considering Nb_3Y (Y = Al, Ga, In, Ge, Sn, Os, Ir and Pt) compounds. First principle electronic structure calculations are performed to visualise the Fermi surface for the above mentioned compounds and to evaluate how the FS topology changes with applied pressure leading to ETTs in the present compounds at different compressions and the pressure values are comparable with available experimental reports.

1.3.3 Binary Sn-based compounds

Binary compounds with AB type have particular interest because of their structural phase transition with the application of pressure. In the case of lanthanide monophosphides LnP (Ln = La, Ce, Pr, Nd, Sm, Gd, Tb, Tm and Yb), the phase change occurs at pressures around 25-50 GPa [104]. In the case of the calcium chalcogenides like CaS, CaSe and CaTe, it is observed at 40 GPa, 38 GPa and 33 GPa, respectively[105]. A similar transition is also observed in IIIB-nitrides (ScN, YN) and IIIA-nitrides (GaN, InN) [106]. In the case of AgBr, an intermediate KOH-type structure is also observed from 8 to 35 GPa [107] between the NaCl-type and CsCl-type structures. The semiconducting family of tin based monochalcogenides, SnCh (Ch = O, S, Se, Te), have band gaps ranging between 1.1 and 2.9 eV and lone pair effects in these compounds have been studied by Lefebvre et al [108].

In these compounds, if A is from IIIrd group elements and B is from Vth group elements, then the properties of the compounds is closely related to group IV elements. These individual type elements (III group, V group) have purely covalent nature of bonding, but the compounds formed from these elements are having some additional ionic bonding nature. In the case of BN, the structure is analogous to that of graphite. There are some similarities between the phase transformations of BN and of carbon. At high-pressures zincblende BN (borazon), which is analogous to diamond, will become wurtzite form analogous to lonsdaleite(called as hexagonal diamond). In the compounds III-V (AlSb, GaP, GaAs, GaSb, InP, InAs, InSb) and II-VI (ZnS, ZnSe, ZnTe, CdTe) a phase transition is observed from diamond or zincblende type to β-Sn or NaCl type structure under pressure [109].

In present work we have chosen SnAs and SnSb which are non-transition metal binary compounds and are found to have superconducting nature at ambient condition. These compounds are found to

be stable in NaCl type at ambient and undergo a phase transition from NaCl to CsCl type with the application of pressure. In 1984, Losev et al [110, 111] used x-ray diffraction to observe the NaCl to CsCl structure transformation in SnAs at a pressure of around 32 GPa with an associated volume discontinuity of around 5%. Recently, superconductivity was reported in NaCl-type SnAs by Wang et al [112] with a superconducting critical temperature, T_c, of 3.58 K and electron-phonon coupling constant, λ_{ep}, to be around 0.62. Calculations, using density functional theory (DFT) and density functional perturbation theory (DFPT), have also been performed by Tütüncü et al [113] on NaCl-type SnAs to investigate the electronic structure and hence the electron-phonon coupling, finding good agreement with experimental work. Further DFT calculations by Shrivastava et al [114] showed the effect of pressure on the electronic structure of SnAs, further demonstrating the structural change that occur. Recently Hase et al [115] reported that the moderate charge fluctuation and electron phonon interaction is the cause for superconductivity at ambient pressure. SnSb is useful in energy storage applications [116] and also posses NaCl type structure as ground state and it is observed to undergo a phase change at high pressures from NaCl to CsCl type structure. DFT calculations by Shrivastava et al [117] has shed light on the effect of pressure on the electronic structure of SnSb, further demonstrating the structural change that occurs. In this work we have predicted the superconducting nature in the high pressure phase of both SnAs and SnSb compounds and the values are found to be higher compared to ambient NaCl phase in both the compounds. We have also observed the change in the FS topology at the phase transition in both the compounds which is discussed elaborately in this work

1.3.4 Mn-based Cu_2Sb type magnetic compounds

Cu_2Sb compounds crystallizes in a tetragonal structure with space group $P4/nmm$ (with multiplicity Z = 2). In this Cu atom possess two non equivalent sites, Cu(I) and Cu(II). Literature regarding the crystal chemistry is well established and can be found in ref. [118]. Antiferromagnetic nature is observed in Cu_2Sb compound with a Néel temperature around ∼373 K [119]. Later it was shown to be nonmagnetic [120] by using solid state NMR experiments. For the same compound, superconductivity is also reported with a value of around ∼0.085 K [121]. Among these Cu_2Sb type, M_2Pn (M = transition element and Pn = Pnictogen) compound is found to possess remarkable magnetic properties. Similar type compound, Mn_2Sb is found to be ferrimagnetic with Néel temperature around ∼550 K [122] and M_2As (M = Mn, Cr and Fe) compounds are found to be antiferromagnetic with Néel temperature 573, 393 and 353 K respectively [123].

Among the various kinds of Cu_2Sb type compounds Mn_2Sb becomes ferrimagnetic below T_N=550 K. The spin ordering of the ferrimagnetic state is an antiparallel arrangement of unequal magnetic moments associated with two kinds of manganese atoms (Mn(I), Mn(II)) present in the unitcell. The magnetic moment of Mn(II) is antiparallel to that of Mn(I) and the value of the former is much larger than that of the latter.

In the present work, we have taken MnAlGe, MnGaGe and MnZnSb compounds which are having the same tetragonal Cu_2Sb-type. These compounds are derived from Mn_2Sb which is ferrimagnet with a Néel temperature of 550 K, where Mn atoms have inequivalent sites, MnI and MnII. By doping MnII atoms with non-magnetic elements like Al, Ga and Zn, we can get the ternary MnAlGe, MnGaGe and MnZnSb compounds. These compounds are reported to be ferromagnet with Curie temperature 503, 453 and 320 K respectively for MnAlGe, MnGaGe and MnZnSb. From the crystal

structure point of view, the magnetic Mn layers are separated by two non-magnetic layers containing elements Al-Ge or Ga-Ge or Zn-Sb which projects these layered compounds to possess nearly two dimensional magnetic nature. The distance between Mn-Mn along a or b-axis(inplane) is equivalent with lattice parameter 'a or b' and along 'c' axis(out of plane) is equivalent to lattice parameter 'c'. In these compounds, as length of 'c' axis increases Curie temperature is also found to increase [124] indicating the importance of interlayer distance along 'c' axis, in raising the Curie temperature.

These Mn-based magnetic materials of present study are ferromagnetic with a large uniaxial magneto crystalline anisotropy with the easy axis along tetragonal 'c' axis. These type of materials have useful applications in spintronic devices [125]. To study the application of MnAlGe in magneto-optics field, Sherwood et al [126] prepared the polycrystalline thin films and found to have promising application in magneto-optical devices. These systems can be used in magneto-optical devices for the storage of large amount of information. Particularly present compounds are suitable for storage applications [127] with a capacity of 10^7 bits/cm^2. Apart from the above mentioned studies, self-consistent band structure calculations were performed by Motizuki et al [128] and confirmed that the magnetic moments arise from the itinerant electrons. Later quasi two dimensional magnetism in MnGaGe is observed by Mohn and Schwarz [129]. In 2006, kimura et al [130] confirmed a strong two dimensional nature in these compounds from the calculated Fermi surfaces particularly for spin down case.

In 1963, Velge and De Vos [131] observed the influence of milling on the magnetic properties of MnAlGe, where the saturation magnetisation and the coercivity decrease appreciably after the mechanical loading which does not involve a reduction in particle size and concluded that structural imperfections may lead to the decrease in the coercivity. After that, a linear decrease in the 'a' and 'c' lattice parameters is observed with increasing pressure upto 4 GPa in both MnAlGe and MnGaGe by Kanomata et al [132]. In the case of MnZnSb Mastuzaki et al [133] studied the effect of pressure on Curie temperature and lattice parameters up to 8 GPa and observed anomalies in the pressure ranges between 4.2 to 6 GPa. In the present compounds increase in the Curie temperature is observed with pressure. The values of dT_c/dP is found to be 32 K/GPa, 30 K/GPa and 28 K/GPa for MnAlGe [134], MnGaGe [135] and MnZnSb [133] respectively and superexchange between Mn-Mn atoms is the reason for the positive pressure effect on Curie temperature in these compounds. In our work we have focussed on the electronic structure and FS topology of these compounds both at ambient and under compression and found the enhancement of the quasi two dimensionality from the FS calculation under compression.

1.4 Overview of the thesis

In the present thesis we have studied the importance of Fermi surface in explaining the physical properties for different types of compounds at ambient conditions and how the application of pressure will effect the Fermi surface and other physical properties of the studied compounds. We have paid attention to different types of compounds which possess varied applications. We have initiated the present work through the state-of-art Density Functional Theory (DFT), and the present thesis work is organised as follows. The first chapter includes importance of Fermi surface and pressure effect on the Fermi surface and other physical properties of the systems. The remaining part of the thesis is divided into three parts, the first part describes the methodology used for the calculations

which forms the chapter 2. The second part contains the results and discussions of the investigated compounds which are presented in chapters 3 - 6. Final part includes the conclusions and future plans and are presented in chapter 7. A precise note on all the chapters of the present thesis is given below.

In chapter 2, a light description of several approximations is presented for finding the solution of interacting many-particle systems which is too complicated. Solving the Schrodinger equation is very important to understand the behaviour of the system which is having wave functions, $\psi(r_1, r_2, r_3, ...r_N)$, with 3N variables(where N is the number of particles). But it is difficult to solve the quantum mechanical problem with too many degrees of freedom. Thereafter several approximate methods evolved to model the interacting many-particle systems such as Hatree-Fock method, augmented plane wave method, orthogonalized plane wave method etc. In 1960s accurate and improved calculations are done on electronic structure after the density functional theory (DFT) based on the Hohenberg-Kohn theorem came to existence. Since 1990, the electronic structure calculation based on the density functional theory has a great success in determining the ground state properties and became more popular in condensed mater physics, chemistry and material science. DFT now serves as an excellent tool to have a basic and quantitative understanding of solids in condensed matter at microscopic level since it is based on quantum theory. In this chapter we have described the details of DFT and the full-potential linearised augmented plane wave method and pseudopotential method as implemented in WIEN2k and PWSCF code and an overview of the exchange-correlation functional such as local-density approximation (LDA) and generalized gradient approximation (GGA) is also presented.

We have presented the results of investigated compounds in four chapters. Among them, chapter 3 deals with Ni-based Heusler compounds, chapter 4 deals with Nb-based A-15 type compounds, chapter 5 deals with binary Sn based compounds and chapter 6 deals with magnetic compounds.

In chapter 3, we have discussed the electronic structure, elastic, Fermi surface, vibrational properties of Ni_2XAl (X=Ti, Zr, Hf, V, Nb, and Ta), Ni_2NbGa and Ni_2NbSn compounds at ambient conditions and under compression. Along with this, we have predicted superconducting nature in Ni_2VAl and compared with Ni_2NbAl, Ni_2NbGa and Ni_2NbSn compounds which are experimentally reported as superconductors at ambient. Pressure effect on the superconducting nature is also studied.

In chapter 4, we have elaborated the discussion regarding electronic structure and Fermi surface topology in Nb_3Y (Y = Al, Ga, In, Ge, Sn, Os, Ir and Pt) compounds at ambient conditions. Under compression electronic topological transitions are observed in all the compounds and are analysed with help of change in the Fermi surface topology.

In chapter 5, we have presented the electronic, Fermi surface, elastic and superconducting properties of binary SnAs and SnSb compounds both at ambient and with applied pressure. A phase transition form NaCl to CsCl type is observed in both the compounds at different pressures and also enhanced superconductivity in the CsCl phase is observed compared to ambient NaCl phase in both the compounds.

In chapter 6, we have discussed the electronic structure, magnetic, elastic properties of Zr_2TiAl and Mn-based MnAlGe, MnGaGe and MnZnSb compounds both at ambient and under compression. First time in the literature, we are reporting the magnetic ground state in Zr_2TiAl compound at ambient which is also confirmed from the phonon calculations. Under compression a magnetic to

non-magnetic phase transitions is observed in Zr_2TiAl (at V/V_0=0.75). This magnetic to non-magnetic phase transition is confirmed from the calculated magnetic moment, Fermi surface and phonon dispersion curves under compression. In the case of Mn-based compounds a quasi two dimensional nature is observed from the Fermi surface calculations. Under compression decrease in the magnetic moment of Mn atom and change in the band and FS topology is observed in all the Mn-based compounds. In MnZnSb, negative values in the elastic constants are observed under compression which may be related to phase transition or can demonstrate an ETT . At the corresponding compression we have observed a change in the band structure and Fermi surface topology and the pressure values corresponding to these anomalies are in good agreement with the available experiment values.

Chapter 2

Methodology

This chapter deals with the methodology that is used for the electronic structure calculations of the present investigated compounds. The discussion starts with the many-body problem of solids and proceed further to get the solution by using quantum mechanical approach by solving the Schrödinger equation. A brief discussion about Density Functional Theory (DFT) is added which is a practical tool used in solving the many-body equation. Finally, we have given different exchange correlational functionals which are used to calculate the electronic structure properties.

2.1 Quantum Many body problem

One of the main goals of physics is to find the physical properties of interacting many body systems by using electronic structure, which is a spacial density of electron distribution in the solid and quasi particle spectrum. Researchers try to derive the properties using the laws of quantum mechanics. Computing the exact ground state and exited states is the precise solution of the many particle system.

The solids are considered to be tightly packed regular and periodic arrangement of atoms (usually $\sim 10^{23}$) with strong interaction among them. These interactions lead to various physical properties of solid such as electrical, mechanical, magnetic, thermal, optical properties etc. To understand these properties more precisely, we need to understand the possible interactions that exist within a solid. The interactions within the solids are, nucleus-nucleus, nucleus-electron and electron-electron, which are the major interactions one need to count in the solids. All these interactions will lead to give the total energy called as "Hamiltonian" of the solid, which is given as follows:

$$H = T_N + T_e + V_{N-e} + V_{N-N} + V_{e-e} \tag{2.1}$$

Here H is the Hamiltonian of the system, T and V stands for the kinetic and potential energies respectively. 'N' indicates nucleus and 'e' stands for electrons. V_{N-N} and V_{e-e} are the Coulombic repulsive potential energy between nucleus-nucleus ($N-N$) and electron-electron ($e-e$), respectively. V_{N-e} is the nucleus and electron Coulombic attractive potential energy. The Hamiltonian equation 2.1, is only for a single atom which gives the possible information about the interactions among them. In general, a solid will have almost $\sim 10^{23}$ atoms. In order to get the information about a solid one need to solve 10^{23} number of equations, which requires a huge effort. Solving these many equations within the limits of classical approximations is a challenging problem which is framed as "Many-body problem". To solve this problem, various approximations and mechanisms are derived. Here we have discussed one of the possible ways to get the solution through quantum mechanical method using the density functional theory (DFT).

Quantum mechanical approach to many-body problem

The properties exhibited by solids are basically from electrons, nucleus. To understand the microscopic interaction in the solids, quantum mechanical approach is essential. Considering the solids with 'M' number of nuclei with I^{th}, J^{th} nucleus positioned at R_I, R_J, respectively and 'N' number of electrons with i^{th}, j^{th} electrons positioned at r_i, r_j, respectively, the Hamiltonian for this system as given by

$$\widehat{H} = -\frac{1}{2}\sum_{I=1}^{M}\frac{\bigtriangledown_I^2}{M_I} - \frac{1}{2}\sum_{i=1}^{N}\frac{\bigtriangledown_i^2}{m_i} - \sum_{I=1}^{M}\sum_{i=1}^{N}\frac{Z_I}{|R_I - r_i|} + \sum_{\substack{i,j=1 \\ i\neq j}}^{N}\frac{1}{|r_i - r_j|} + \sum_{\substack{I,J=1 \\ I\neq J}}^{M}\frac{1}{|R_I - R_J|} \tag{2.2}$$

where Z_I is the atomic number and M_I, m_i are the atomic mass of the nuclei and electrons respectively. The first two terms represent the kinetic energies of the nuclei ($\widehat{T}_N$) and the electrons ($\widehat{T}_e$) respectively. The third term is the attractive Coulombic interaction between the electrons and the nuclei ($\widehat{V}_{N-e}$) and finally the last two are the repulsive Coulombic terms for the nuclei ($\widehat{V}_{N-N}$) and

electrons ($\widehat{V}_{e-e}$). In-short, the above equation can be written as

$$\widehat{H} = \widehat{T}_N + \widehat{T}_e + \widehat{V}_{N-e} + \widehat{V}_{N-N} + \widehat{V}_{e-e} \tag{2.3}$$

The solution for this Hamiltonian can be obtained by solving the time-independent Schrödinger equation (SE) given as

$$\widehat{H}\psi(r, R) = E\psi(r, R) \tag{2.4}$$

where $\psi(r, R)$ is the many-body wave function which depends on the positions of the particles in the system, E is the energy of the many-body system. However the equation represented here look very simple but it involves $3M$ and $3N$ number of nuclei and electrons. To get an reasonable solution to this many-body equation, one need to look for the approximations. In the next section we have presented the possible approximations that are considered to reduce the complexity of this many-body problem.

2.1.1 Born-Oppenheimer approximation

The first approximation to the many-body problem was given by Born-Oppenheimer. According to this approximation, the nuclei and electrons are differentiated by considering the mass difference among them. This approximation states that the nuclei with heavier mass can be considered to be fixed in space from the perspective of electrons [136]. The nuclei at rest induce a constant Coulombic potential on the electrons. This inherently decouple the nuclei kinetic energy as zero and potential energy term ($\widehat{V}_N + \widehat{V}_{N-e} \approx V_{ext}$) as constant from the many-body equation. The Hamiltonian after the Born-Oppenheimer approximation is given by,

$$\widehat{H} = \widehat{T}_e + \widehat{V}_{e-e} + V_{ext} \tag{2.5}$$

With this approximation the complexity of the many body problem reduces, but solving this also need more efforts. Further approximations are made on this in order to reduce the complexity of the problem.

2.1.2 Hartree approximation

In the Born-Oppenheimer approximation the complex term included in equation 2.5 is the electron-electron interaction term i.e. the potential energy of the electrons. According to Hartree approximation, the non-interacting nature of the electrons reduce the complexity of the Hamiltonian of Born-Oppenheimer approximation. According to this approximation, the total electron-electron potential can be written as the sum of individual particle potential,

$$V_H = \sum_{i=1}^{N} V_{r_i} \tag{2.6}$$

This approximation is also known as the individual particle approximation. With this approximation the many-body wave function $\psi(r_1, r_2, r_3, ...r_N)$ will become $\psi(r_1, r_2, r_3, ...r_N) = \phi_1(r_1) \times \phi_2(r_2) \times \phi_3(r_3) \times ..... \times \phi_N(r_N)$ ($\phi(r)$ represents the electron wave function), *i.e* total wave function can be

represent as multiplication of individual electron wave functions. With Hartree approximation, the Hamiltonian can be written as,

$$\widehat{H} = \widehat{T}_e + V_{ext} + \widehat{V}_H \tag{2.7}$$

where V_H is the Hartree potential as mentioned by equation 2.6, which will reduce the complexity of many-body '3N' equation into a 'N'-one electron equation. Though this makes the many-body problem simple, it failed to include the anti-symmetric nature of electron (Fermionic) and also the electron-electron interaction. We need further approximations to consider the fermionic nature in the electron wave function.

2.1.3 Hartree-Fock approximation

To overcome the above mentioned drawbacks further development on the N-one electronic Schrödinger equation has been initiated with the consideration of Coulombic and anti-symmetric nature of electrons. The Hartree-Fock (HF) approximation assumes that the interacting anti-symmetric electrons wave function can be treated with the single Slater determinant. The wave function with Slater determinant can be written as,

$$\psi(r_1, r_2, r_3, ...r_N) = \frac{1}{\sqrt{N!}} \begin{vmatrix} \phi_1(r_1) & \phi_2(r_1) & \phi_3(r_1) & ... & \phi_N(r_1) \\ \phi_1(r_2) & \phi_2(r_2) & \phi_3(r_2) & ... & \phi_N(r_2) \\ . & . & . & ... & . \\ . & . & . & ... & . \\ \phi_1(r_N) & \phi_2(r_N) & \phi_3(r_N) & ... & \phi_N(r_N) \end{vmatrix} \tag{2.8}$$

From the above equation, it is understood that the wave function is anti-symmetric in nature with respect to the interchange of the any two particles, which explains the exchange interaction of the electrons. According to the HF approximation the wave function can be expressed as the linear combination of anti-symmetrised products of one electron states. The HF approximation for the two electrons system can be written as

$$\psi_{HF}(r_1, r_2) = \frac{1}{\sqrt{2}} \left[\phi_1(r_1)\phi_2(r_2) - \phi_1(r_2)\phi_2(r_1)\right]. \tag{2.9}$$

With this approximation the Hamiltonian of the many-electron system will be

$$\widehat{H} = \widehat{T}_e + V_{ext} + \widehat{V}_{HF} \tag{2.10}$$

where the $\widehat{V}_{HF}$ is the corrected version of the HF approximation potential over the Hartree approximation. $\widehat{V}_{HF}$ is given by

$$\widehat{V}_{HF} = \int v_x(r, r')\phi_i(r'_i)dr' = -\sum_j^N \int \frac{\phi_j(r)\phi_j^*(r')}{|r_i - r_j|}\phi_i(r'_i)dr' \tag{2.11}$$

The equation 2.10 gives the total energy of the N-one electron system which have interactions between the electrons including the exchange energy. This approximation was successful in describing various

systems, but failed in achieving the predictive power of the systems because of the poor exchange and correlation limits of the electrons. To minimise the problem, further approximations are needed. In this regard, density functional theory has given an optimum solution to the many-body problem which is explained in detail in the next section.

2.2 Introduction to density functional theory

To minimise the complex nature in the HF approximation of one electron wave function alternative theories are proposed. In 1964, Hohenberg and Kohn [137] proposed a theory which is based on the electron's ground state density and is capable of describing all the properties of the system. It is named as Density Functional Theory (DFT), which originates from the Hohenberg-Kohn theory [137] and the Kohn-Sham [138] equations. The introduction of the electron density in the picture of wave function, leads to a situation where the complexity of $3N$ number of electron system has reduced to 3. This provides more feasible solution to solid state problem of the condensed matter physics. More details about the DFT formulation and its implementation can be found in many books, thesis and review papers [139, 140, 141, 142, 143, 144, 145, 146], here we have addressed an outline of the same. Before looking into its details, we first discuss how the density of the electrons are related to the wave function. The density of the electrons $n(r)$ can be expressed as,

$$n(r) = N \int d^3r_2 d^3r_3 ....d^3r_N \psi(r, r_2, ...r_N)\psi^*(r, r_2, ...r_N). \tag{2.12}$$

Further we will look at how this electron density has been taken as a tool to estimate the materials properties using DFT.

2.2.1 Thomas-Fermi theory

Replacing the wave function with electron density was first proposed by Thomas-Fermi from their independent work [147, 148]. In their model, they expressed the kinetic energy of the system in terms of electron density $n(r)$ which can be expresses as follows,

$$T[n(r)] = C_F \int n^{5/3}(r)dr \tag{2.13}$$

where $C_F = \frac{3}{10}(3\pi^2)^{2/3}$=2.871, $n(r)$ define the electron density and yields the total number of electrons N by integration

$$\int n(r)dr = N. \tag{2.14}$$

The Thomas-Fermi model has given only the relation for the kinetic energy in terms of electron density explicitly for an homogeneous system. The total energy of the system after including the electron density will be

$$E_{TF}[n(r)] = C_F \int n^{5/3}(r)dr - Z \int \frac{n(r)}{r}dr + \frac{1}{2}\int\int \frac{n(r)n(r')}{|r-r'|}drdr' \tag{2.15}$$

Thomas-Fermi has laid the first step to replace the density of electrons in the place of wave function, which is a crude way of an approximation for the kinetic energy term alone. Further developments are carried out for the practical implementation of this using the Hohenberg and Kohn theorems.

2.2.2 Hohenberg-Kohn theorems

Based on the idea given by the Thomas and Fermi, the modern DFT has taken its initiation with work of Hohenberg and Kohn (HK) [137]. According to this, the Hamiltonian of the interacting particles of the system is given by,

$$\begin{aligned} \widehat{H} = -\frac{1}{2}\sum_i {\nabla_i}^2 - \sum_i v_{ext}(r_i) + \sum_{i\neq j}\frac{1}{|r_i - r_j|} \\ where \quad v_{ext}(r_i) = -\sum_I \frac{Z_I}{|r_i - R_I|} \end{aligned} \tag{2.16}$$

Here $v_{ext}(r_i)$ is the external potential which includes the interaction among electrons and nuclei. The theory of HK is based on two theorems:

Theorem-I states that, for any system with interacting particles in an external potential $v_{ext}(r)$, the total energy of the system is determined uniquely by the ground state density $n_0(r)$. From this one can find all the properties of the system with the help of the ground state density $n_0(r)$.

Theorem-II states that, for any external potential $v_{ext}(r)$, a universal functional for the energy in terms of the density $n(r)$ can be defined and also the global minimum of this functional gives the exact ground-state energy of the system. The density $n(r)$ that minimizes this functional is known as the exact ground-state density $n_0(r)$, i.e.

$$E_0 = \psi_{min} \rightarrow n_0\langle \widehat{T}_e + V_{ext} + \widehat{V}_{HF}\rangle \tag{2.17}$$

The above said two theorems of HK explains that there is a one-to-one relation among the external potential $v_{ext}(r)$ and the ground state density $n_0(r)$. By minimising the universal energy functional, one can reach the exact ground state energy of a system. This gives an optimum possible solution for the many-electron problem. The original proofs for the above mentioned two theorems can be found in Ref. [137, 149]. Even with the HK approximation, one would require to solve the many-electron Schrödinger equation, but provides good approximation to the ground-state density as well as the energy. Further improvements were carried out by Kohn-Sham (KS) leading to DFT which we will discuss in the next section.

2.2.3 Kohn-Sham method

Based on Hohenberg-Kohn theorems, Kohn and Sham (KS) [138] developed a method which allow to minimise the functional by varying $n(r)$ over all densities of N electrons. According to KS, the ground state density of the system consist of independent electrons and each one experiencing the same external potential, whose ground state density of non-interacting system $n_{KS}(r)$ is equal to the ground state density $n(r)$ of interacting system, i. e. $n_{KS}(r) = n(r)$. KS have given the complete formalism to the many-body equation which is known as Kohn-Sham equation. The following section

will briefly explain how this has been achieved.

Kohn-Sham Equation:

The KS approach has given the energy equation as,

$$E_{KS} = T[n] + V_{ext}[n] + V_H[n] + E_{xc}[n] \tag{2.18}$$

Now we will see the individual terms in the above equation. $T[n]$ represents the independent particle kinetic energy which is given by,

$$T[n] = -\frac{1}{2}\sum_{i=1}^{N}\langle\psi_i|\delta|\psi_i\rangle. \tag{2.19}$$

$V_{ext}[n]$ is the external potential energy which acts on the electrons and is given by,

$$v_{ext}[n] = \int v_{ext}(r)n(r)dr. \tag{2.20}$$

V_H is the Hartree potential due to the electron-electron Coulomb interaction which is given by,

$$v_H = \int \frac{n(r')}{|r-r'|}dr' \tag{2.21}$$

The final term E_{xc} is the exchange-correlation energy which goes beyond the Hartree approximation for better description of the system. In general the Schrödinger form of the Kohn-Sham equation is given as follows:

$$H_{KS}\psi_i = E_{KS}\psi_i \tag{2.22}$$

where H_{KS} and v_{eff} are the Kohn-Sham Hamiltonian and effective potential which are defined by

$$\begin{aligned} H_{KS} &= [-\frac{1}{2}\nabla^2 + v_{eff}(r)] \\ v_{eff} &= v_{ext} + v_H + v_{xc}. \end{aligned} \tag{2.23}$$

The Khon-Sham equation of 2.22 is used in the DFT based algorithms to find the minimum of this function iteratively by solving the v_{eff} for electron density. The final minimum value gives the ground state-energy and the density of the system. Thereby we can extract all the physical quantities which are required for a solid system. Eventhough KS-equations gives the exact solution, it contains an undefined exchange-correlation functional v_{xc}, which need to be evaluated through the necessary approximations, which will be discussed in successive section.

2.3 Exchange-correlation functionals

The Kohn-Sham equation of 2.22 gives the exact solution for many-electron system. But the quality of the calculated results of a real system will depend on the exchange correlation term E_{xc}, which need to be approximated properly to get the correct information about the system. The challenging task in DFT will be the approximation of E_{xc}. In principle the term E_{xc} contain both exchange and

correlation parts which is explained as below.

The Exchange Energy (E_x)

The difference in the electrostatic energy due to the anti-symmetric nature of the particles gives the exchange energy, which was given by Pauli's exclusion principle. The exchange energy of the two particles in the form of the wave function can be written as:

$$E_x = -\frac{1}{2}\sum_{ij}\int\int \frac{\psi_i^*(r)\psi_i(r')\psi_j^*(r')\psi_j(r)}{|r-r'|}drdr' \tag{2.24}$$

Calculations including this term for solids are very expensive and one need to reduce its complexity through proper approximations for practical applications.

The Correlation Energy (E_c)

The electrons in the system are correlated to each other which gives the correlation energy. From the definition of the correlation energy, it is formally defined as the difference between the exact non-relativistic energy and the energy in the Hartree-Fock limit. But there is no analytical expression as mentioned for the exchange energy, it can only be calculated by the exact solution of the many-electron Schrödinger equation by the proper approximation for practical applications.

The combination of both exchange and correlation energy together will contribute for the exchange correlation term, i.e.

$$E_{xc} = E_x + E_c \tag{2.25}$$

For practical applications to describe the real systems, one need to approximate the exchange correlation energy functional based on the electron density. Based on this, many approximations have evolved according to the specific interest of the properties which includes: the local (spin) density approximation (LDA), generalized gradient approximation (GGA), meta-generalized gradient approximation, hybrid functionals *etc.* Below we have explained the traditional functional like LDA and GGA.

2.3.1 The local-density approximation (LDA)

The first approximation which describes the exchange correlational functional is the local density approximation given by Kohn and Sham [138]. This is simplest approximation for the exchange correlational functional. According to this, the electron density of the system is considered locally as an uniform electron gas. The exchange correlation functional defined by the LDA is given by

$$E_{xc}^{LDA}[n(r)] = \int n(r)\epsilon_{xc}^{hom}(n(r))dr. \tag{2.26}$$

Here ϵ_{xc}^{hom} is exchange-correlation energy per particle of the interacting homogeneous electron gas of density $n(r)$. The LDA functional is described for systems with slow varying densities like weakly perturbed electron gas. LDA was very successful for evaluating the properties like bond lengths and lattice parameters. But it failed in many system in describing the cohesive energies, bulk modulus

and under/over estimation of strength of bonds or lattice constants in molecules and metals.

2.3.2 The generalised gradient approximation (GGA)

The homogeneous system described by the LDA is not a reasonable approximation for all the systems, which is not really possible in many of the systems. This makes LDA to be less efficient in dealing with many of the real systems. To improve this, a gradient term which deals with the inhomogeneous system was introduced with in the Generalised Gradient Approximation (GGA). Under this approximation the exchange correlation functional becomes as follows:

$$E_{xc}^{GGA}[n(r)] = \int n(r)\epsilon^{xc}[n(r), \delta n(r)]dr. \tag{2.27}$$

The functional defined by the GGA is refered as the semi-local functional, where the density gradient represents the non-local nature of the real system. GGA has shown better performance than the LDA for various systems in describing the molecules and metal ground state properties, but it failed to capture proper bulk moduli [150, 151, 152] similar to LDA. In general it is well known that LDA overestimate the binding energy and GGA underestimate the same. The basic similarity among the two functionals is that they fail to describe the exact band gaps of insulators and semiconductors. The underestimation of the band gap of semiconductors or insulators is about 30-50 % with both the functionals. But in the present thesis we deal with metallic systems, so the given functional are enough to get the properties for metallic systems. In the present thesis, we have used the LDA/GGA functional to calculate the electronic structure properties of some superconducting and magnetic compounds by using WIEN2k code based on full-potential linearized augmented plane wave method (FP-LAPW) which is discussed in the next section. Apart from the FP-LAPW we have used pseudo-potential method for dynamical properties for some of the compounds. It is very important to understand how these methods are implemented using density functional theory and the same is discussed in the next section.

2.4 Methods

In this section we will briefly discuss the two most popular methods that are used to calculate the electronic band structure, mechanical properties and dynamical properties of the investigated compounds in the present thesis work. These are (i) the linearized augmented plane wave (LAPW) method and (ii) pseudo-potentials in combination with the plane wave basis set.

2.4.1 Linearized Augmented Plane Wave (LAPW) Method

Before discussing the LAPW method we will first explain the Augmented plane wave method.

Augmented plane wave method (APW)

According to the APW method the unit cell is divided into two regions: atomic sphere (non-overlapping) also known as Muffin-Tin (MT) spheres and interstitial (I) [153]. The potential in

these regions are expressed as follows:

$$V(r) = \begin{cases} \sum_{lm} V_{lm}(r) Y_{lm}(r) & (r \in MT) \\ \\ \sum_{G} V_G e^{iG.r} & (r \in I) \end{cases} \tag{2.28}$$

Based on the above mentioned two regions, different basis sets are used. In the atomic regions the wave functions will vary rapidly, whereas in the interstitial region the wave functions are smoothly varying which are shown as followingly:

$$\phi_{k_n}^{APW}(r, \epsilon_l) = \begin{cases} \sum_{lm} A_{lm,k_n} u_l(r,\epsilon_l) Y_{lm}(r) & (r \in MT) \\ \\ \frac{1}{\sqrt{V}} e^{ik_n.r} & (r \in I) \end{cases} \tag{2.29}$$

where $k_n = k + G_n$, G_n are the reciprocal lattice vectors, k is the wave vector inside the first Brillouin zone and V is the volume of unit cell. From this equation, it is evident that the wave function with in the atomic spheres (MT) were described by radial functions using spherical harmonics, whereas in the interstitial it is formulated using the plane waves. The coefficients A_{lm} are calculated by matching the wave functions of the atomic sphere and the interstitial regions. Further the augmented plane wave function will be used to expand the Kohn-Sham wave function (ψ) as followingly:

$$\psi_k(r) = \sum_n c_n \phi_{k_n(r)} \tag{2.30}$$

The disadvantage of the APW method is the unknown parameter 'ϵ_l' in 2.29, which will not give the eigen values from a single diagonalization. For this we use the function $u_l(r, \epsilon_l)$, which results in an eigenvalue problem which is non-linear in energy and are needed to be solved self-consistently which makes the APW method computationally inefficient.

Linearized Augmented Plane Wave (LAPW) method

LAPW method was introduced to solve the problems that occured in APW method due to the non-linearity of $u_l(r, \epsilon_l)$. Taylor series is used to expand ϵ_l in LAPW method as shown below:

$$u_l(r, \epsilon_l) = u_l(r, \epsilon_l^1) + (\epsilon_l - \epsilon_l^1)\dot{u}_l(r, \epsilon_l^1) + O((\epsilon_l - \epsilon_l^1)^2) \tag{2.31}$$

where $\dot{u}_l = \partial u_l / \partial \epsilon_l$. The ϵ_l^1 is a fixed point energy around which the Taylor expansion is carried out. The basis set for the LAPW method defined as:

$$\phi_{k_n}^{LAPW}(r) = \begin{cases} \sum_{lm} [A_{lm,k_n} u_l(r,\epsilon_l) + B_{lm,k_n} \dot{u}_l(r,\epsilon_l)] Y_{lm}(r) & (r \in MT) \\ \\ \frac{1}{\sqrt{V}} e^{ik_n.r} & (r \in I) \end{cases} \tag{2.32}$$

From the above equation it is understood that there is no difference in the interstitial basis set of APW and LAPW methods, and the main difference is only in Muffin-Tin spheres, in which the basis set will depend both on energy u_l and its energy derivative, $\dot{u}_l$. The inclusion of energy and its derivative in LAPW method will increase the accuracy compared to the APW method. In the case of LAPW, we also employ the matching wave functions in the MT and the interstitial regions to determine coefficients of A_{lm} and B_{lm}.

APW+lo method

Further improvement on the linearization of APW method is achieved with the inclusion of local orbitals (lo). The defined basis set for the APW+lo method is as follows:

$$\phi_{lm}^{APW+lo}(r) = \begin{cases} [A_{lm}u_l(r,\epsilon_l)+B_{lm}\dot{u}_l(r,\epsilon_l)]Y_{lm}(r) & (r\in MT) \\ 0 \quad (r\in I) \end{cases} \tag{2.33}$$

The APW+lo method gives a small basis set like the APW method but with the same accuracy as that of the LAPW method. Normalisation is used to evaluate the coefficients of A_{lm} and B_{lm} using the condition that the local orbital is zero at the Muffin-Tin boundary. In the present thesis we have used full-potential LAPW (FP-LAPW) and APW+lo methods as implemented in WIEN2k code [153] to evaluate the electronic structure properties.

2.4.2 Pseudopotential method

In order to reduce the complexity and computational time involved with the all-electron methods, we have used the pseudopotential method to evaluate the dynamical properties. A system contains both core and valence electrons, which describe the materials properties in all-electron methods. The core electrons can be treated as inactive and can be assumed that they do not participate in evaluating the materials properties, and only valence electrons are used to describe the material properties based on the pseudopotential method. The wave functions in the pseudopotential method must not have any radial nodes within the core region and at a certain distance r_c (radius of cut-off) the pseudo wave function becomes equal to the real wave function. The condition that need to be satisfied in pseudopotential method is that pseudo wave function and pseudopotential should be identical to the all electron wave function and potential outside a radius of cut-off r_c. The other condition is that pseudo wave functions and its first and second derivatives must be continuous at r_c. The Schrödinger equation in pseudopotential method will be,

$$(\frac{1}{2}\nabla^2 + V)\psi = \varepsilon\psi \tag{2.34}$$

Here ψ is the wave function for the all electron (AE) atomic system with angular momentum component l. The pseudo wave function is of the form

$$\psi_l^{ps} = \sum_{i=1}^{n} \alpha_i j_l \tag{2.35}$$

Here α_i is the fitting parameter and j_l are the spherical Bessel functions. In the present thesis, we have used the pseudopotential method to evaluate the structural optimization and phonon dispersion calculations as implemented in PWSCF [154] code.

Chapter 3

Pressure effect on electronic structure and vibrational properties of Ni_2XAl (X=Ti, Zr, Hf, V, Nb, and Ta), Ni_2NbGa and Ni_2NbSn compounds

In this chapter we have studied the electronic structure, mechanical, vibrational properties of Ni-based Heusler compounds, Ni_2XAl (X=Ti, Zr, Hf, V, Nb, and Ta), Ni_2NbGa and Ni_2NbSn, both at ambient conditions and under compression. Calculated ground state properties agree well with other available data. All the studied compounds are found to be mechanically and dynamically stable at ambient conditions. Among the mentioned compounds, Ni_2NbAl, Ni_2NbGa and Ni_2NbSn are experimentally reported as superconductors at ambient conditions and our calculated superconducting transition temperature (T_c) and electron-phonon coupling constant (λ_{ep}) values are in good agreement with the experiments. We have also predicted superconducting nature in Ni_2VAl with $\lambda_{ep} = 0.68$, which leads to $T_c = \sim 4$ K (assuming a Coulomb pseudopotential $\mu^* = 0.13$), which is a relatively high transition temperature for Ni based Heusler alloys and also higher when compared with other Ni_2NbY (Y = Al, Ga and Sn) compounds. From the Fermi surface calculations, flat Fermi sheets are observed along X-Γ direction in all the compounds. In the superconducting Ni_2VAl and Ni_2NbY (Y = Al, Ga and Sn) compounds these Fermi surface exhibit nesting and leads to Kohn anomaly in the phonon dispersion relation for the transverse acoustic mode TA2 along the (1,1,0) direction. Under compression change in the number of Fermi surfaces is observed in Ni_2NbAl and a corresponding non-linear decrease in the total density of states is observed under compression in this compound. Under compression hardening in the phonon modes is observed in all the compounds. But in the superconducting Ni_2VAl and Ni_2NbY (Y = Al, Ga and Sn) compounds, Kohn anomaly observed in acoustic TA2 mode, is found to soften with pressure. As a consequence, T_c and λ_{ep} vary non-monotonically under pressure in superconducting compounds.

3.1 Introduction

Heusler alloys are ternary intermetallic compounds of the form X_2YZ, where X is generally a transition metal, Y is yet another transition metal from group VIIIB-IB and Z is a '*sp*' metal or a metalloid. These compounds display a wide range of physical properties including halfmetallicity [68, 155, 156, 157], magnetic ordering [158, 159], heavy fermion behaviour [160, 161, 162], shape memory effect [163, 164] and thermoelectricity [165, 166].

Ternary intermetallic Heusler alloys like Ni_2XAl (X=Ti, Zr, Hf, V, Nb, and Ta), Ni_2NbGa and Ni_2NbSn are having chemical formula A_2YZ and crystallize in cubic $L2_1$- structure, where A and Y are the transition metals and Z is a non-magnetic element [167]. Though the Heusler compounds are well known for their ferromagnetic properties, it is interesting to note the existence of paramagnetic compounds, one among them is the above mentioned series Ni_2XAl [85]. Ni_2TiAl and many other Ni-based compounds have been explored from various perspective, ever since it was found that the high temperature creep resistance of NiAl could be improved by Ti addition [86], which stabilized the compounds in the Heusler type structure. The structural properties of Ni_2TiAl was further studied experimentally by Taylor and Floyd [87], using X-rays and electron spectroscopy and Umakoshi et al. [88] further confirmed Ni_2TiAl to have small lattice mismatch with B2 phase and found the same to possess good stability. This series attracted further interest and a complete phase diagram of Ni_2TAl (T = Zr, Nb and Ta) was obtained by Raman and Schubert [89]. Theoretical insight on the above mentioned series was also provided by Lin and Freeman [85] further substantiating the stability of $L2_1$ structure of Ni_2XAl (X = Zr, Nb and Ta). Further, Da Rocha et al. [90] have reported the specific heat and electronic structure of the above mentioned series. Heusler alloys ever remain a perennial resource of compounds with plethora of studies available explaining the transport, electrical conductivity, magnetic and many other properties owned by them [168, 169, 170].

Among the Heusler compounds, some are having superconducting nature with maximum superconducting transition temperature (T_c) around 4.7 K (YPd_2Sn). Superconductivity was first reported for the Heusler alloys by Ishikawa et al. [171], where they focused mainly on the systems RPd_2Sn and RPd_2Pb with R being a rare-earth metal. Among the known Heusler superconductors, Ni-based alloys Ni_2NbX (X = Al, Ga and Sn) have attracted much attention due to their intermediate electron phonon coupling constant [91, 172, 73]. Interestingly, Ni_2NbX (X = Al, Ga and Sn) compounds are paramagnets and are found to be superconductors although Ni is a ferromagnet and Ni compounds are often magnetic. Here we predict Ni_2VAl to be a superconductor. Importantly, this provides an experimentally testable prediction that if confirmed and taken in conjunction with the correct predictions for the related compounds, would strongly restrict the possible role of spin-fluctuations associated with Ni magnetism in the superconducting properties of these phases. In Ni_2NbX (X = Al, Ga and Sn) compounds, the presence of Nb works against magnetism associated with Ni leading to the paramagnetic ground states of these compounds [91, 73]. The same paramagnetic nature is recently observed in ScT_2Al (T= Ni, Pd, Pt, Cu, Ag, Au) [173]. The Ni_2NbX superconductors have T_c of 2.15 K (Ni_2NbAl) [91], 1.54 K (Ni_2NbGa) [91] and 2.9 K (ref. [91]) (3.4 K (ref. [172, 73])) (Ni_2NbSn) with calculated electron phonon coupling constants [91] (λ_{ep}) of 0.52, 0.50 and 0.61 respectively. Electronic structures and cohesive properties of Ni_2NbAl and Ni_2VAl were studied by Lin et al [85] and a large value of cohesive energy is observed with a pronounced hybridization between Ni-Nb/V-Al atoms. The interaction between these atoms creates deep valleys in density of states which separate bonding and anti-bonding region. It is this type of covalency

that works against magnetism.

Superconductivity in conventional intermetallics has been traditionally discussed in terms of the density of states at the Fermi level and the number of valence electrons per atom. From the Matthias rule [174, 175], the number of valence electrons per atom should be close to 5 or 7. Even though the Heusler superconducting compounds follow the above prescription, the superconducting transition temperatures of these compounds are relatively low. Among the compositional elements of Ni_2VAl, vanadium is reported to be a superconductor with superconducting transition temperature (T_c) of 5.3 K [176] and 3.6 K [177]. From previous literatures [177], the total density of states (DOS) value of bcc Vanadium is 1.46 (states/eV/f.u.). Pressure effect on the T_c has been studied experimentally and theoretically for bcc Vanadium [176, 177, 178, 179] upto 120 GPa in which the T_c is found to increase linearly with pressure. However, high density of states also favours spin-fluctuations, which work against electron-phonon superconductivity [180]. In this work the total DOS of Ni_2VAl is observed to be more than the value of vanadium and the number of electrons/atom is observed to be 7 in the present compound obeying the Matthias rule.

We also studied the pressure dependence, as pressure provides a tuning parameter that is very useful in understanding trends and mechanisms. Previous studies on 'Hf' based Heusler alloys have shown an increase in the superconducting transition temperature with decreasing lattice parameter [181], while certain other cases show an increase in T_c with increase in lattice constant [181]. We note that the behaviour can also be more complex under pressure [182]. Fundamentally, superconductivity is an instability of the Fermi surface [183], and so pressure induced changes in Fermi surface can lead to non-trivial changes in superconducting properties.

Another interesting feature that connects with superconductivity is the presence of van Hove singularities [6], in the electronic structure, leading to peaks in the density of states as found in some of the Pd based Huesler compounds [74, 184, 185]. Interesting behaviour might be anticipated if the Fermi level can be brought to this peak by means of alloying. Another noteworthy point present in these compounds is the softening of the TA2 acoustic phonon modes, which can be well correlated with the FS nesting and the corresponding nesting vector decides the position of the Kohn anomaly present in these compounds. Further to these, we also find a softening in the acoustic phonons under pressure leading to the variation in the T_c, which is discussed in detail in the present chapter.

The organization of the chapter is as follows. Computational details are presented in the section 3.2. Results and discussions of ground state, electronic structure, mechanical, vibrational, superconducting properties and pressure effect on these properties are presented in the section 3.3. The conclusions are given in section 3.5.

3.2 Method of calculations

The Full Potential Linearized Augmented Plane Wave (FP-LAPW) method as implemented in Wien2k code [153] is used to calculate the ground state and electronic structure of the present compounds. We adopt Generalized Gradient Approximation (GGA) of Perdew-Burke-Ernzerhof (PBE) [186]. Throughout the calculations, the R_{MT} (radius of muffin tin spheres) value for each atom was fixed as 1.78 a.u for Ni atom, 1.78 a.u for X (X=Ti, V, Zr, Nb, Hf and Ta) atom, 1.67 a.u for Al atom, 2.0 a.u for Ga and 2.3 a.u for Sn atoms. For the energy convergence, the criterion R_{MT}*K_{max}=9 was used, where K_{max} is the plane wave cut-off. The potential and charge density

were Fourier expanded up to G_{max}=12 a.u^{-1}. The valence states included in the calculations are Ni ($3d^8, 4s^2$), Al ($3s^2, 3p^1$), Ti ($3d^2$,$4s^2$), V ($3d^3$,$4s^2$), Zr ($4d^2$,$5s^2$), Nb ($4d^4$,$5s^1$), Hf ($4f^{14}$,$5d^2$,$6s^2$), Ta ($4f^{14}$,$5d^3$,$6s^2$), Ga ($3d^{10}, 4s^2, 4p^1$), Sn ($4d^{10}, 5s^2, 5p^2$) and the remaining orbitals are treated as core states. All the electronic structure calculations are performed with $44 \times 44 \times 44$ k-mesh in the Monkhorst-Pack [187] scheme which gives 2168 k-points in the irreducible part of the Brillouin Zone (BZ). Tetrahedron method [188] was used to integrate the Brillouin zone. Energy convergence up to 10^{-5} Ry is used to get the proper convergence of the self consistent calculation. Birch-Murnaghan [189] equation of state is used to find the equilibrium lattice parameter and bulk modulus by fitting the total energies as a function of primitive cell volume. We have not found any significant change in the electronic structure at the Fermi level with the inclusion of spin-orbit coupling (SOC). So, the reported calculations are performed without SOC.

Phonon dispersions and electron-phonon interactions were computed using the plane wave pseudopotential method (PWSCF) which is implemented in QUANTUM ESPRESSO [154]code. The GGA-PBE exchange correlation functional is used in the present calculations for all the compounds. The electron ion interaction is described by using ultrasoft pseudopotential for Ni_2XAl (X= Ti, Zr, Hf, Ta) compounds with kinetic energy cutoff of 42 Ry (ecutwfc) and for the remaining compounds norm-conserving pseudopotentials are used with maximum plane wave cut-off energy (ecutwfc) of 90 Ry and the electronic charge density was expanded up to 360 Ry (In case of Ni_2VAl it is 140 and 560 Ry). A $16 \times 16 \times 16$ k-points grid within the BZ is used for the phonon calculations. Gaussian broadening of 0.02 Ry and a $4 \times 4 \times 4$ uniform grid of 'q'-points are used for phonon calculations.

3.3 Results and discussion

3.3.1 Ground state, electronic structure properties

The basic ground state properties are calculated using the Birch-Murnaghan equation of state and the results are reported in Table 3.1, along with the available experimental results. The ground state properties of Ni_2XAl (X=Ti, Zr, Hf, V, Nb, and Ta), Ni_2NbGa and Ni_2NbSn are evaluated using the experimental lattice parameter and atomic positions [85, 90, 91, 172, 73, 190]. The calculated equilibrium lattice constant and bulk modulus values are presented in Table 3.1 along with the available experimental and other theoretical work and a good agreement is seen between the present values and earlier reports. The calculated bulk moduli is higher for Ni_2TaAl and lower for Ni_2ZrAl.

We have calculated the band structure along the high symmetry directions in the irreducible Brillouin zone with and without inclusion of SOC. From Fig. 3.1 (given for only Ni_2NbSn) it is seen that the SOC effect is very small around the Fermi level and we have proceeded with the further calculations excluding SOC. We have also checked the effect of Hubbard 'U' and found no appreciable changes in the band structure as these are metallic systems and are not correlated. This is consistent with the recent studies on Heusler based compounds where the authors also concluded the same [191].

The band structures for all the compounds are given in Fig. 3.2. The overall profile of all these Ni_2XAl compounds are the same, whereas the number of bands crossing the E_F is not the same for all the compounds. For Ni_2TiAl, Ni_2ZrAl and Ni_2HfAl three bands cross the E_F, two of them crossing at the L-point from valence band to conduction band (Here the conduction bands refer to

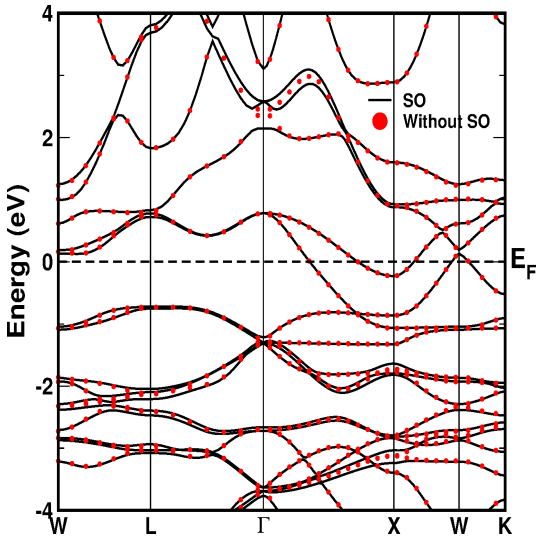

Figure 3.1: Band structure of Ni_2NbSn with and without inclusion of spin-orbit coupling(SOC) at the theoretical equilibrium volume.

the bands above the Fermi level and they are primarily X-derived states) and the third band crosses the E_F from conduction band to valence band at X-point (band structure of Ni_2TiAl is shown in Fig. 3.2). For Ni_2VAl, we observe two bands to cross the Fermi level at X-point from conduction band to valence band. For Ni_2NbAl, Ni_2TaAl and Ni_2NbGa compounds, we find only one band to cross the E_F from conduction band to valence band at X-point at ambient conditions. In addition to that, we have an extra band at the X point in Ni_2NbSn.

The electronic density of states (DOS) is shown in Fig. 3.3 along with the atom projected DOS. Even though these compounds are composed of different elements from different rows in the periodic table, the total DOS for all the compounds looks similar reflecting the similar band profiles. For all the compounds we observe valleys at energies around -6 eV, -1 eV, 0.5 eV. In the case of Ni_2NbSn there is another valley at around -3 eV. This feature indicates that the interaction between the constituent atoms is strong [85]. From the Fig. 3.3, it is evident that the contribution at E_F is mainly dominated by Ni-'d_{e_g}' states with an admixture of X-'$d_{t_{2g}}$' and Al/Ga/Sn-'p' states. The states at nearly -6 eV is mainly derived from the Al/Ga/Sn-'s' states. For all the compounds, the bonding and the anti-bonding regions are well separated from the non-bonding region and our calculations agree well with the earlier studies [85]. As we move to compounds containing X from V-B elements, we could observe the states to shift below E_F due to band filling and is clearly evident from Fig. 3.2. Apart from this, our calculated density of states at the Fermi level show a decreasing trend as we move from top to bottom of the periodic table. Among all the compounds Ni_2VAl has the highest value of DOS at E_F with 3.51 states/eV/f.u. and Ni_2TaAl has lowest value with 2.13 states/eV/f.u. From the atom projected DOS we have observed that the primary contribution to the total DOS at E_F is due to Ni atom ('d_{eg}' states), the secondary contribution is due to X atom ('$d_{t_{2g}}$' states) and the least contribution arises from Al/Ga/Sn atom ('p' states). The calculated Sommerfield coefficient γ is also given in the Table 3.1, which is proportional to the density of states at the Fermi level. In the case of conventional superconductors, T_c value is propotional to γ. Increase in the γ leads to increase in the T_c of that material. In this chapter, the order of T_c values

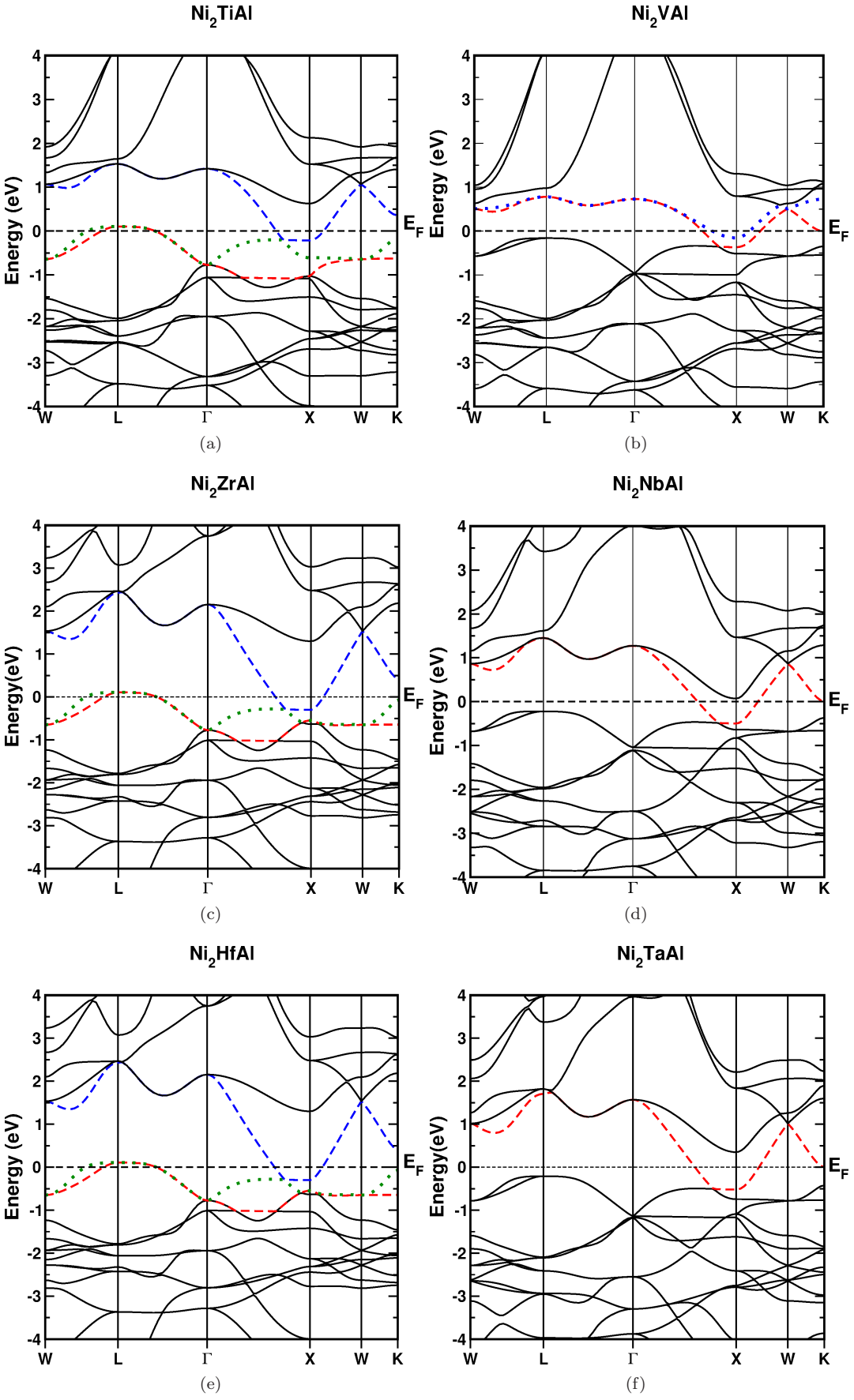
Ni2TiAl
Ni2VAl
Ni2ZrAl
Ni2NbAl
Ni2HfAl
Ni2TaAl
Energy (eV)
Energy(eV)
E_F
W
L
Γ
X
W
K
(a)
(b)
(c)
(d)
(e)
(f)

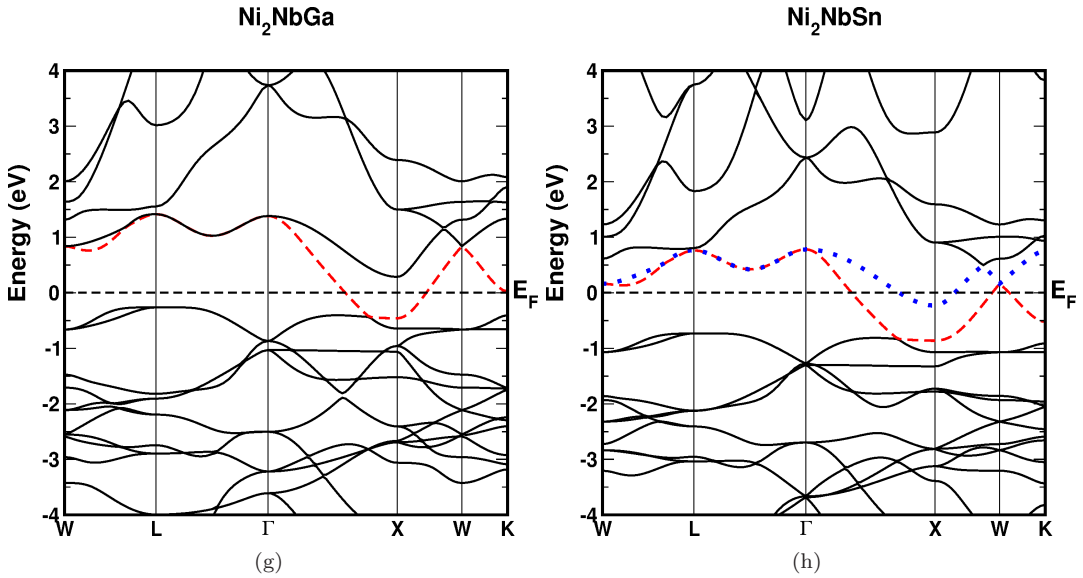

Figure 3.2: Band structure at ambient conditions for (a) Ni_2TiAl (b) Ni_2VAl (c) Ni_2ZrAl, (d) Ni_2NbAl, (e) Ni_2HfAl, (f) Ni_2TaAl, (g) Ni_2NbGa and (h) Ni_2NbSn respectively.

follows as $Ni_2VAl > Ni_2NbSn > Ni_2NbAl > Ni_2NbGa$ (3.84 > 3.21 > 1.92 > 1.18). The same order also followed by γ values as 8.27 > 5.52 > 5.36 > 5.19.

Experimental specific heat can be calculated using the expression, $(1 + \lambda) \times \gamma_{th}$. The λ in the enhancement factor is related to but not identical to the superconducting 'λ' and includes in addition contributions from spin fluctuations and other interactions if present. The inferred values are in the range ∼0.5-1 for Ni_2NbAl and Ni_2VAl, in reasonable accord with the calculated superconducting 'λ' which is explained in the subsequent section. The values for Ni_2NbGa and especially Ni_2NbSn are anomalously low. The origin of this is not clear, and warrants further investigation. Site disorder in samples is one possibility. In any case, we also note that the $N(E_F)$ are not high enough to place any of the compounds near Stoner criterion for ferromagnetism.

The van Hove singularity is observed in both valence and conduction bands at the L-point close to E_F around 1 eV and -1 eV energy range. From the earlier available reports [74, 184, 185], one saddle point is observed in Pd based compounds, at L point. But in the case of present compounds, we have two saddle points in both valence and conduction regions near the E_F. The flat bands associated with the van Hove singularity at the L-point result in a maximum density of states.

In addition, the Fermi surfaces (FS) of all the investigated compounds at ambient conditions are shown in Fig. 3.4, for the corresponding band which crosses the E_F as shown in Fig. 3.2. We observe the Fermi surface topology to be quite similar for Ni_2TiAl, Ni_2ZrAl and Ni_2HfAl indicating the dominating nature of the Ni-'*d*' states with small contribution from X-'*d*' states at E_F. For Ni_2TiAl, Ni_2ZrAl and Ni_2HfAl compounds which contain IV-B elements, we find the Fermi surface to be of electron character at X-point and hole character at L-point respectively and is also evident from the band structure plot from Fig. 3.2, whereas in Ni_2VAl, Ni_2NbAl and Ni_2TaAl compounds which contain V-B elements, we find the band to cross only at X-point resulting in the electron pocket at the same point. From Fig. 3.4(j,k) it is evident that Ni_2VAl has two FS as a result of two

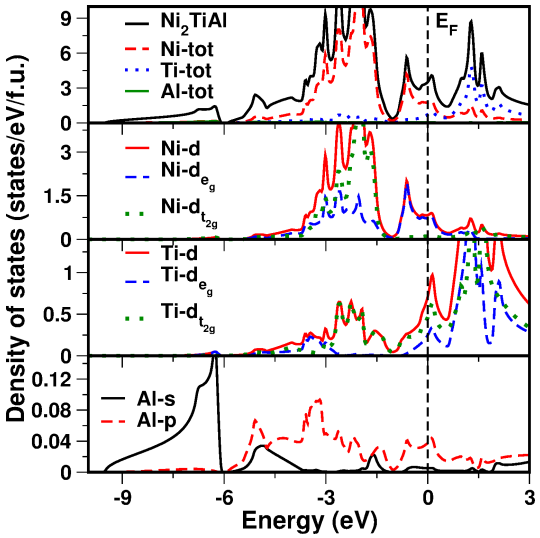
Ni2TiAl
Ni-tot
Ti-tot
Al-tot
EF
Ni-d
Ni-deg
Ni-dt2g
Ti-d
Ti-deg
Ti-dt2g
Al-s
Al-p
Density of states (states/eV/f.u.)
Energy (eV)

(a)

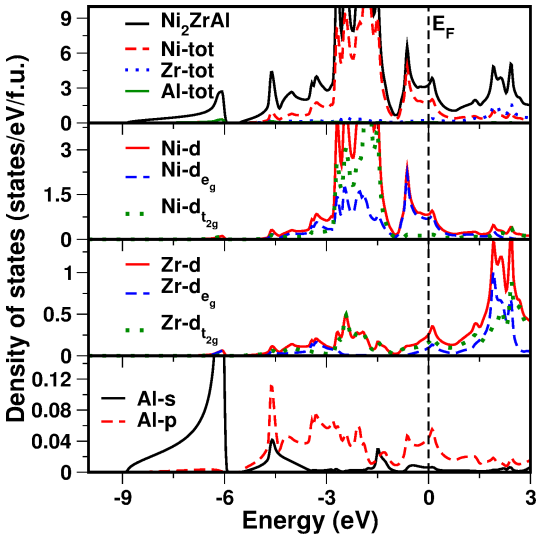
Ni2ZrAl
Ni-tot
Zr-tot
Al-tot
EF
Ni-d
Ni-deg
Ni-dt2g
Zr-d
Zr-deg
Zr-dt2g
Al-s
Al-p
Density of states (states/eV/f.u.)
Energy (eV)

(b)

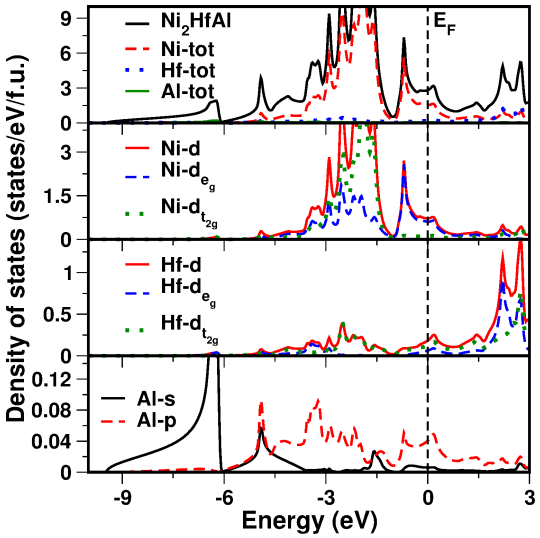
Ni2HfAl
Ni-tot
Hf-tot
Al-tot
EF
Ni-d
Ni-deg
Ni-dt2g
Hf-d
Hf-deg
Hf-dt2g
Al-s
Al-p
Density of states (states/eV/f.u.)
Energy (eV)

(c)

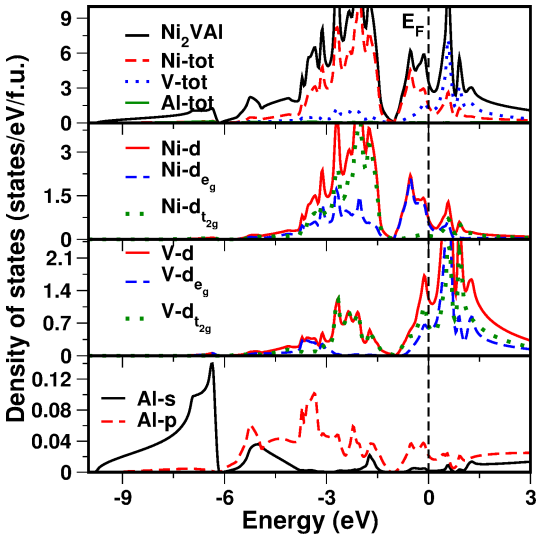
Ni2VAl
Ni-tot
V-tot
Al-tot
EF
Ni-d
Ni-deg
Ni-dt2g
V-d
V-deg
V-dt2g
Al-s
Al-p
Density of states (states/eV/f.u.)
Energy (eV)

(d)

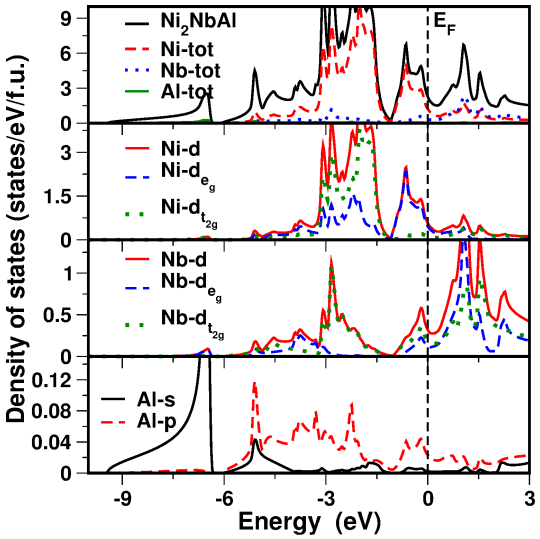
Ni2NbAl
Ni-tot
Nb-tot
Al-tot
EF
Ni-d
Ni-deg
Ni-dt2g
Nb-d
Nb-deg
Nb-dt2g
Al-s
Al-p
Density of states (states/eV/f.u.)
Energy (eV)

(e)

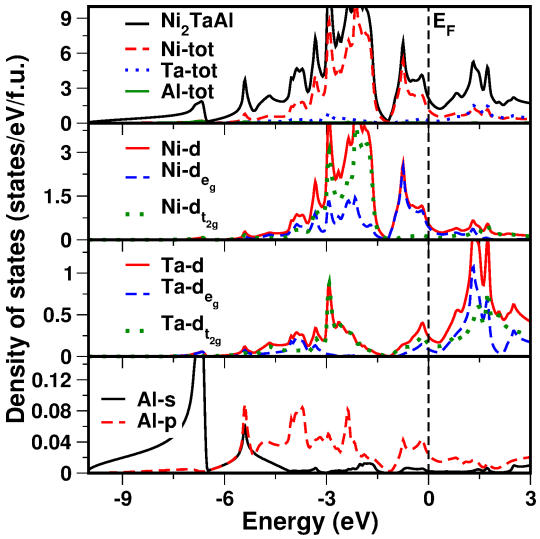
Ni2TaAl
Ni-tot
Ta-tot
Al-tot
EF
Ni-d
Ni-deg
Ni-dt2g
Ta-d
Ta-deg
Ta-dt2g
Al-s
Al-p
Density of states (states/eV/f.u.)
Energy (eV)

(f)

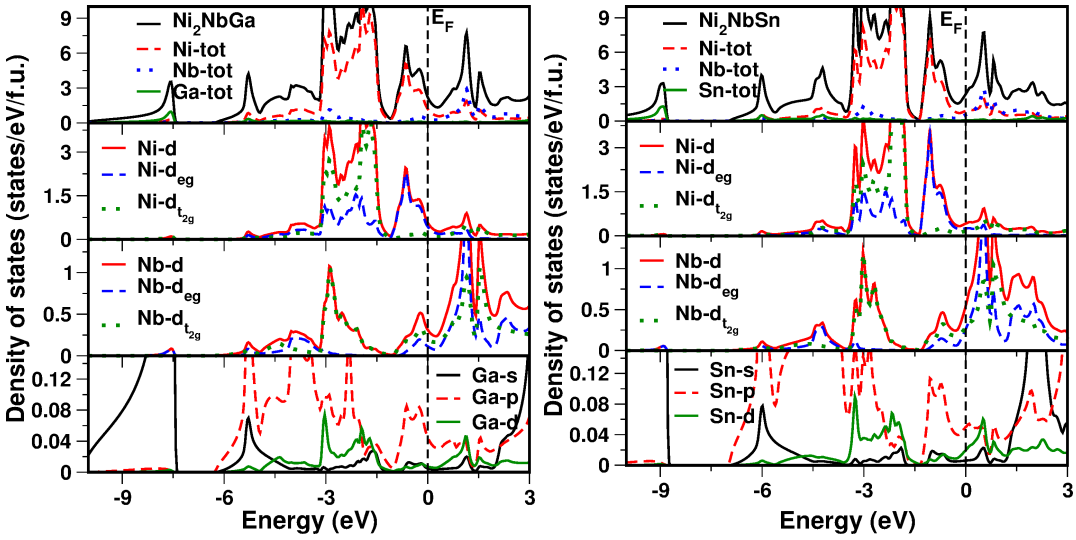

Figure 3.3: Density of states at ambient conditions for (a) Ni_2TiAl (b) Ni_2ZrAl (c) Ni_2HfAl (d) Ni_2VAl (e) Ni_2NbAl (f) Ni_2TaAl (g) Ni_2NbGa, (h) Ni_2NbSn compounds respectively.

bands crossing the E_F (see Fig. 3.2(b)) and the remaining two compounds Ni_2NbAl, Ni_2TaAl have only one FS, due to a single band crossing the E_F (see Fig. 3.2(d,f)). Ni_2NbGa and Ni_2NbSn have one and two FS correspondingly equivalent to the bands that cross the E_F. In Ni_2TiAl, first two FS have hole nature and the last one has electronic nature. Overall, in Ni_2TiAl, Ni_2ZrAl and Ni_2HfAl compounds first two FS have hole nature and last FS has electronic nature and in the remaining Ni_2VAl, Ni_2NbAl, Ni_2TaAl, Ni_2NbGa and Ni_2NbSn compounds, we have only electron FS. In all the compounds we have observed parallel sheets in FS which indicate a nesting feature.

3.3.2 Elastic constants

To account for the mechanical stability of all the investigated compounds we have calculated the elastic constants. All the above mentioned compounds crystallize in the cubic structure and have three non-zero elastic constants C_{11}, C_{12}, C_{44}. The calculated single crystal elastic constants at equilibrium volume are given in Table 3.2 for all the compounds. The calculated elastic constants of all the compounds satisfy the Born mechanical stability criteria [192] i.e. $C_{11} > 0$, $C_{44} > 0$, $C_{11} > C_{12}$, and $C_{11} + 2C_{12} > 0$, which indicate these compounds to be mechanically stable at ambient conditions. From the single crystal elastic constants, we have calculated the Young's modulus E, Voigt-Reuss-Hill modulus G_H [193], Poisson's ratio σ, Anisotropy factor A and are reported in Table 3.2. The relations between C_{11}, C_{12}, C_{44} and the above mentioned parameters can be found elsewhere [194, 195, 196, 197].

To determine the thermal characteristics of a material, Debye temperature (Θ_D) is one of the important parameter. This can be obtained directly from the given relation.

$$\Theta_D = \frac{h}{k}\left[\frac{3n}{4\pi}\left(\frac{\rho N_A}{M}\right)\right]^{1/3} v_m \tag{3.1}$$

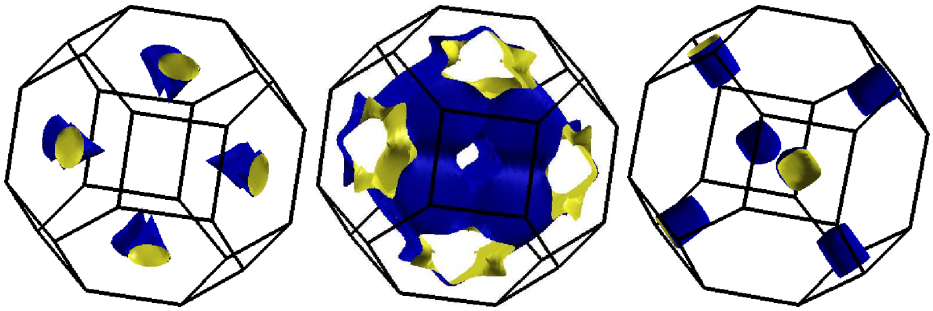

(a) (b) (c)

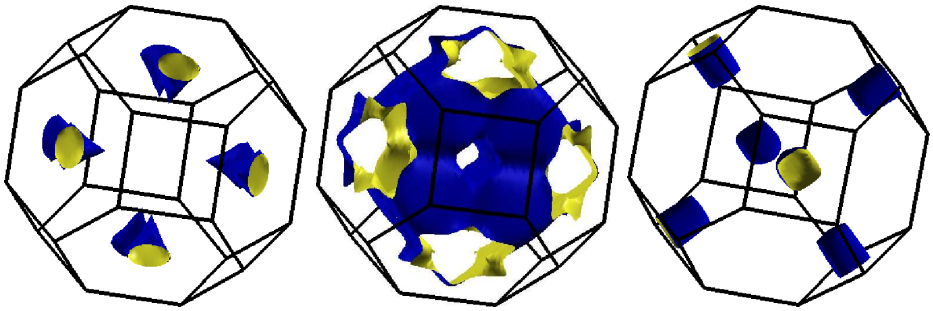

(d) (e) (f)

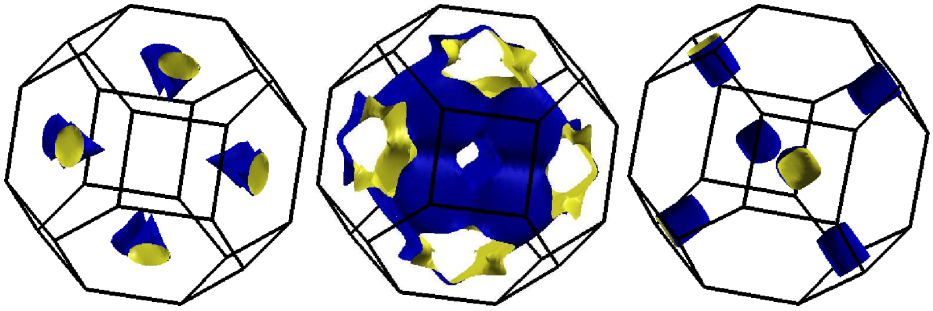

(g) (h) (i)

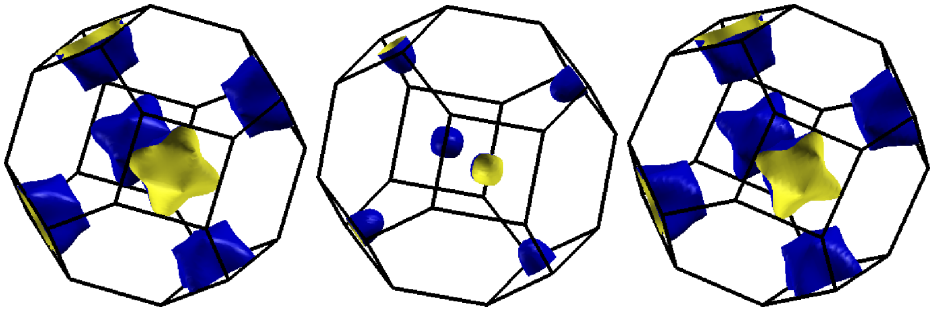

(j) (k) (l)

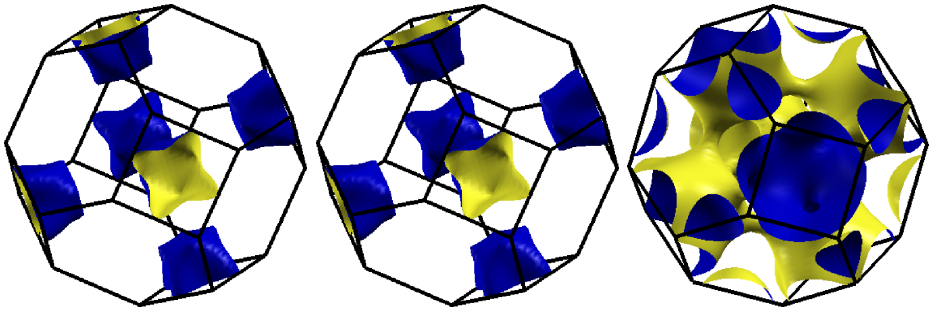

(m) (n) (o)

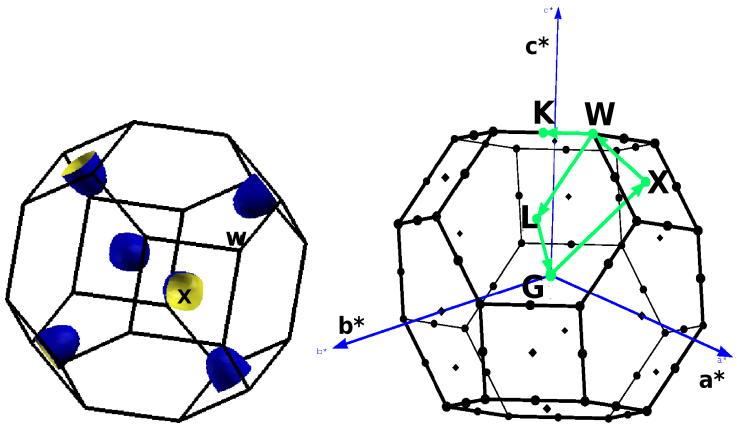

(p) (q)

Figure 3.4: Fermi surfaces (a, b, c) of Ni_2TiAl (d, e, f) of Ni_2ZrAl (g, h, i) of Ni_2HfAl, (j,k) of Ni_2VAl, (l) of Ni_2NbAl, (m) of Ni_2TaAl, (n) of Ni_2NbGa, (o, p) of Ni_2NbSn and (q) Brillouin zone high symmetry points.

where 'h' is the Planck's constant, 'N_A' is the Avogadro's number, 'k' is the Boltzmann's constant, 'ρ' is the density, 'n' is the number of atoms in the unit cell, 'M' is the molecular weight and 'v_m' is the mean sound velocity, which can be calculated by using the following relation.

$$v_m = \left[\frac{1}{3}\left(\frac{2}{v_t^3} + \frac{1}{v_l^3}\right)\right]^{-1/3} \tag{3.2}$$

where 'v_t' and 'v_l' are the transverse and longitudinal sound velocities obtained using both the shear modulus (G_H) and the bulk modulus (B).

$$v_l = \sqrt{\frac{(B + \frac{4}{3}G_H)}{\rho}} \tag{3.3}$$

$$v_t = \sqrt{\frac{G_H}{\rho}} \tag{3.4}$$

The calculated values for all the above defined parameters are given in Table 3.2. From Table 3.2, it is seen that Ni_2TiAl has higher Young's modulus in comparison with other compounds which might imply Ni_2TiAl to be stiffer among the other compounds studied. The elastic anisotropy gives the possibility of inducing micro cracks in the materials [194] and the calculated value of the elastic anisotropy of all the studied compounds are given in the Table 3.2.

The Cauchy's pressure (C_{12} - C_{44}) can be used to comment on the ductile or brittle nature of the compounds. Here Cauchy's pressure for all the compounds is positive indicating the ductile nature. Pugh's ratio ($\frac{G_H}{B}$) [198] is another index for explaining the ductile and brittle nature of the compounds. Larger and smaller values of Pugh's ratio indicate the brittle and ductile nature of the material respectively. The critical number which separates the ductile and brittle nature was reported to be 0.57. This series of compounds have the Pugh's ratio values lesser than this critical number indicating the ductile nature. The Poisson's [199] ratio indicate the stability of the crystal

against shear and takes the values inbetween -1 to 0.5, where -1 and 0.5 serve as lower and upper bounds respectively. The lower bound is the one where the material does not change its shape and the upper bound is where the volume remains unchanged. These compounds have the Poisson's ratio values closer to the upper limit indicating the stiffness of these compounds. From the reported values as shown in Table 3.2, we could see the Poisson's ratio to be higher for the compounds having IV-B group elements and lower for compounds which have V-B group elements. The Debye temperature which is used to estimate the thermal properties of material is also calculated with the help of mean sound velocity. From Table 3.2, we find Debye temperature and mean sound velocities to decrease as we move from top to bottom in the periodic table and higher θ_D values indicate higher thermal conductivity associated with these compounds.

From the same table the calculated Debye temperature (θ_D) values agree well with experiments. For superconducting compounds, BCS theory predicts that T_c should increase with increasing frequency of the lattice vibrations. For some Heusler compounds [181] T_c decreases with the increasing θ_D. In the case of Ni_2NbX where X= Al, Ga, both T_c and θ_D show the BCS theory behaviour. In the case of Ni_2NbSn it is showing opposite manner. In Pd based Huesler compounds Klimzuk et al [181] found a decrease in T_c with increasing θ_D. In their study, T_c of (Sc, Y, Lu)Pd_2Sn compounds increases with $N(E_F)$ and found the opposite trend in case of APd_2M (A = Zr, Hf; M = Al, In) compounds. Finally they conclude that the change in T_c is dependent on the system.

3.3.3 Vibrational properties

The calculated phonon dispersion curves are shown in Fig. 3.5 along with the total and partial phonon density of states. The primitive unit cells of the present compounds have one formula unit with four atoms which gives 12 phonon branches including three acoustic and nine optical branches. The absence of imaginary phonon frequencies indicates the dynamical stability at the ambient condition. The higher frequency optical phonon modes are separated form others in all the compounds except Ni_2NbSn. This separation is due to the mass difference between different kind of atoms in the unit cell. In all the compounds except Ni_2NbGa and Ni_2NbSn these higher frequency optical modes are due to the lighter Al atom. In the remaining compounds, it is due to Nb atom. At the zone centre, we have three optical phonon modes and in that one T_{2g} mode is Raman active and two T_{1u} modes are infrared active. From the phonon dispersion curves, we have observed doubly degenerate acoustic and optical modes along Γ-X and triple degeneracy of same modes along X-Γ direction in all the compounds. This degeneracy is due to the symmetry of the crystal in cubic phase. Longitudinal acoustic mode (LA) is interacting with T_{2g} optical modes except in Ni_2HfAl. We have observed degenerate transverse acoustic (TA) modes along Γ-X and Γ-L directions in all the compounds. In other directions these TA modes become non degenerate and split into TA1 (high frequency) and TA2 (low frequency) modes. There is an anomaly (dip) in TA2 mode from X-Γ direction in Ni_2NbAl, Ni_2NbGa, Ni_2VAl compounds. In the case of Ni_2NbSn, it is observed at X high symmetry point. As discussed below these dips are related to the Fermi surface and reflected in the phonon dispersion.

In metals such dips can arise from Fermi surface nesting, i.e. Kohn anomalies in the phonon spectrum. This anomaly is observed in Ni_2MnGa [200, 201, 202], Ni_2MnIn [203] and Ni_2MnX (X= Sn, Sb) [204]. From the phonon dispersion of the present compounds we observed dip (softening) in the lower frequency acoustic mode (TA2) along X-Γ direction in both Ni_2NbAl, Ni_2NbGa and

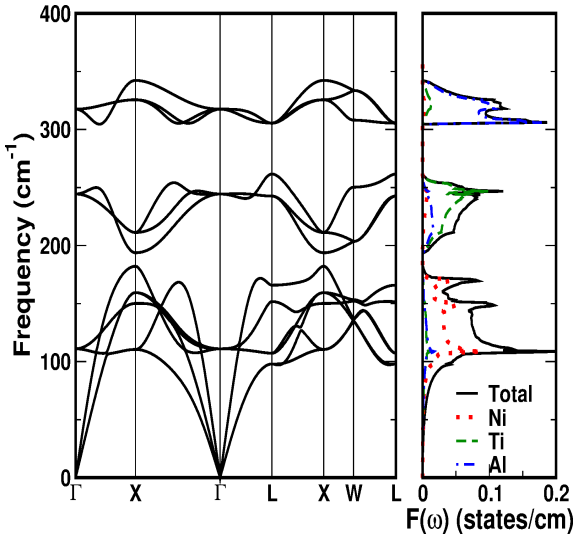
Frequency (cm^{-1})
Γ X Γ L X W L
F(ω) (states/cm)
Total
Ni
Ti
Al

(a)

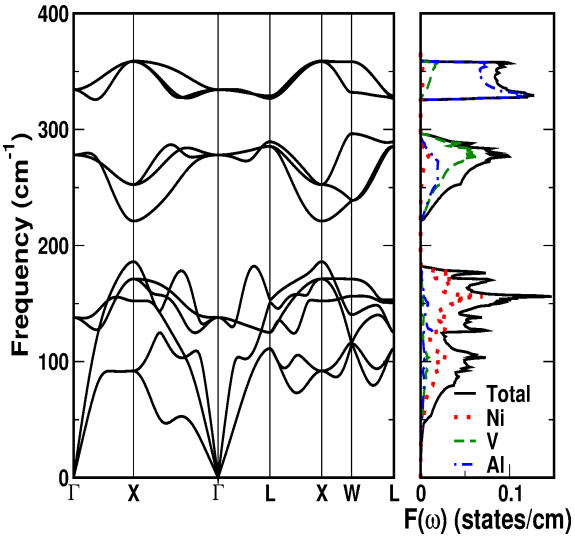
Frequency (cm^{-1})
Γ X Γ L X W L
F(ω) (states/cm)
Total
Ni
V
Al

(b)

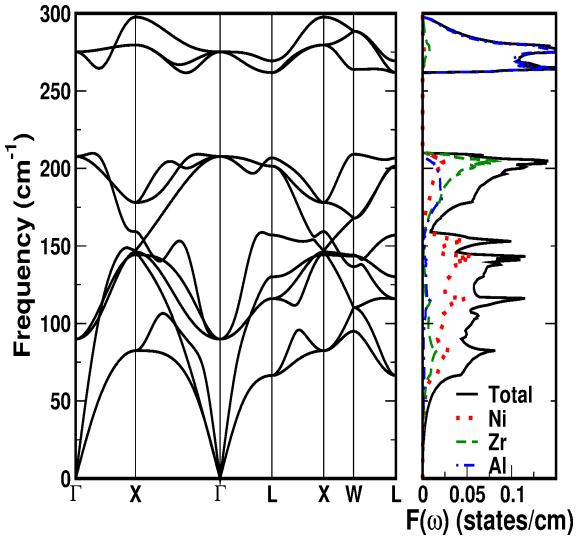
Frequency (cm^{-1})
Γ X Γ L X W L
F(ω) (states/cm)
Total
Ni
Zr
Al

(c)

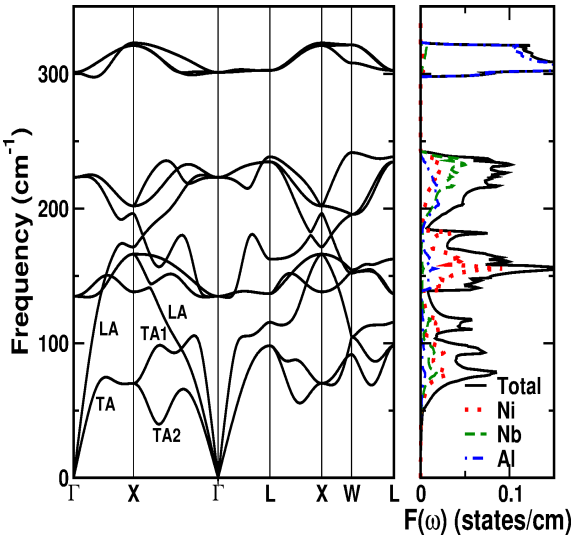
Frequency (cm^{-1})
LA
TA
TA1
LA
TA2
Γ X Γ L X W L
F(ω) (states/cm)
Total
Ni
Nb
Al

(d)

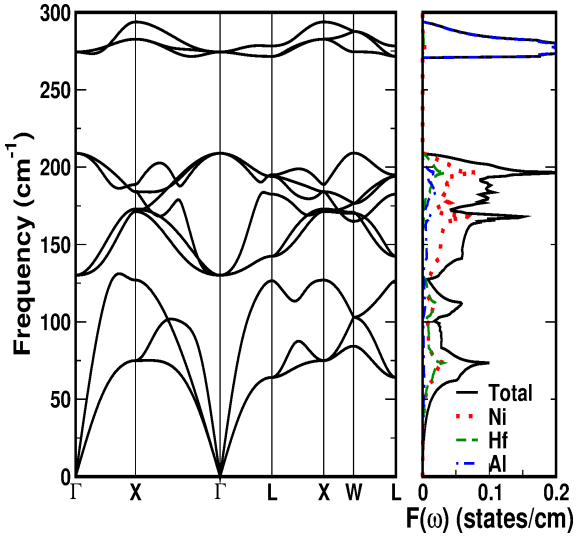
Frequency (cm^{-1})
Γ X Γ L X W L
F(ω) (states/cm)
Total
Ni
Hf
Al

(e)

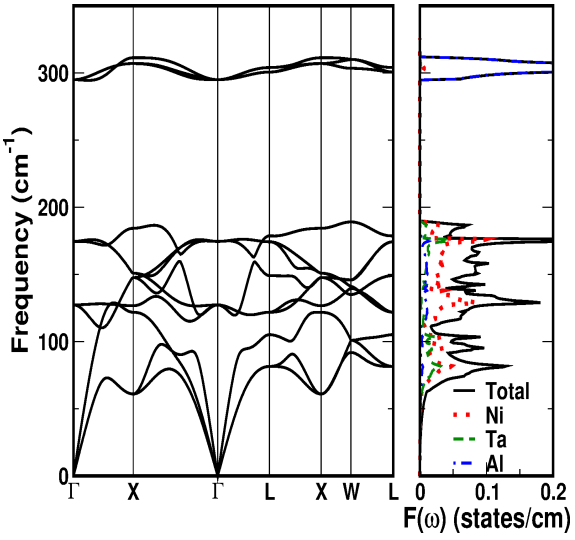
Frequency (cm^{-1})
Γ X Γ L X W L
F(ω) (states/cm)
Total
Ni
Ta
Al

(f)

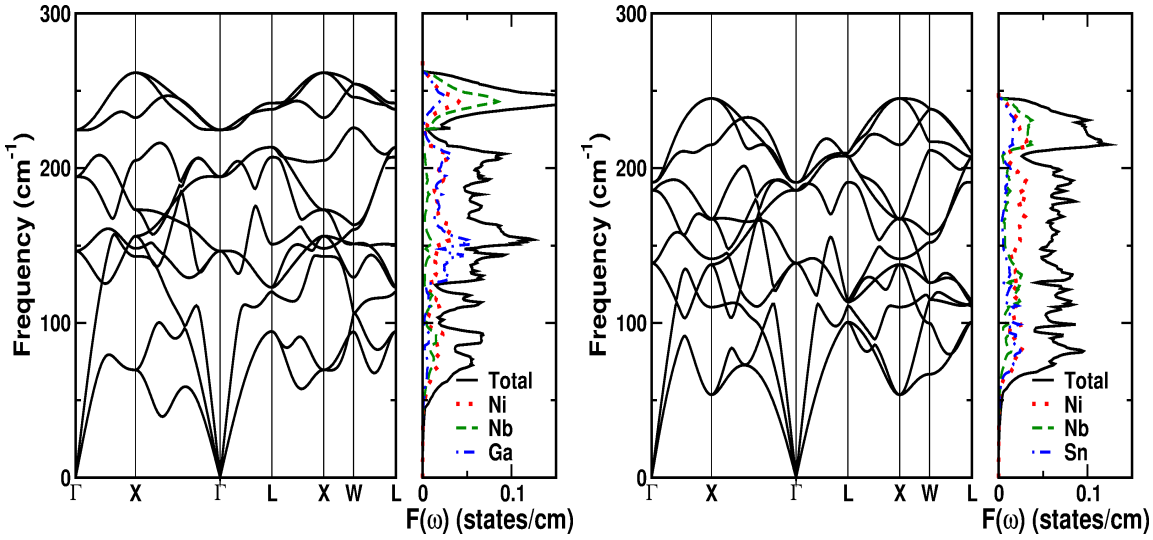

(g) (h)

Figure 3.5: Phonon dispersion along with partial phonon density of states for (a) Ni_2TiAl, (b) Ni_2VAl (c) Ni_2ZrAl, (d) Ni_2NbAl, (e) Ni_2HfAl, (f) Ni_2TaAl, (g) Ni_2NbGa and (h) Ni_2NbSn respectively.

Ni_2VAl compounds and near the X-point in Ni_2NbSn. From the FS, we observed flat portions of X- point Fermi surfaces in all the investigated compounds to be nested with the similar portion on the other side. FS with nesting vector direction is given in Fig. 3.6(a). From this we observed that the nesting vector is of length ∼0.61 of X-X distance connecting the flat surfaces of FS. In the case of Ni_2NbGa and Ni_2VAl it is at ∼0.64 and ∼0.67 of X-X distance. The nesting vector is around $0.7\times2\pi/a$ along the Γ-X direction in Ni_2NbAl. In case of Ni_2NbGa and Ni_2VAl it is observed at $0.68\times2\pi/a$, $0.62\times2\pi/a$ respectively in the same direction as Ni_2NbAl. The same nature is observed in Ni_2NbSn at X high symmetry point. To know the exact 'q' vector where the anomaly is observed, we have plotted the acoustic phonon modes along Γ-X direction for Ni_2NbAl, Ni_2NbGa and Ni_2VAl compounds as shown in Fig. 3.6(b,c,d,e), where we observed a strong Kohn anomaly at 'q' point $q = (\xi, \xi, 0)2\pi/a$ with $\xi = 0.7$, 0.68 and 0.62 in Ni_2NbAl, Ni_2NbGa and Ni_2VAl respectively. The associated phonon branches have mainly Ni character. In the case of Ni_2MnGa, Ni_2MnSn and Ni_2MnSb compounds also the same type of atoms are involved in the branches showing Kohn anomalies.

3.3.4 Superconductivity of Ni_2NbAl, Ni_2NbGa, Ni_2NbSn and Ni_2VAl

The electron phonon coupling constants (λ_{ep}) were extracted from the Eliashberg function ($\alpha^2F(\omega)$) which can be used to determine the T_c of a conventional phonon mediated superconductor. The calculated $\alpha^2F(\omega)$ are plotted in Fig. 3.7 for all the investigated compounds. From this figure the lower energy phonon modes, which are mainly due to Ni atom at that particular frequency are more involved in the process of scattering the electrons in all the compounds. The T_c of the present compounds is calculated by using Allen-Dynes [205] formula which is given in the equation below,

$$T_c = \frac{\omega_{ln}}{1.2} exp(-\frac{1.04(1+\lambda_{ep})}{\lambda_{ep} - \mu^*(1+0.62\lambda_{ep})}) \tag{3.5}$$

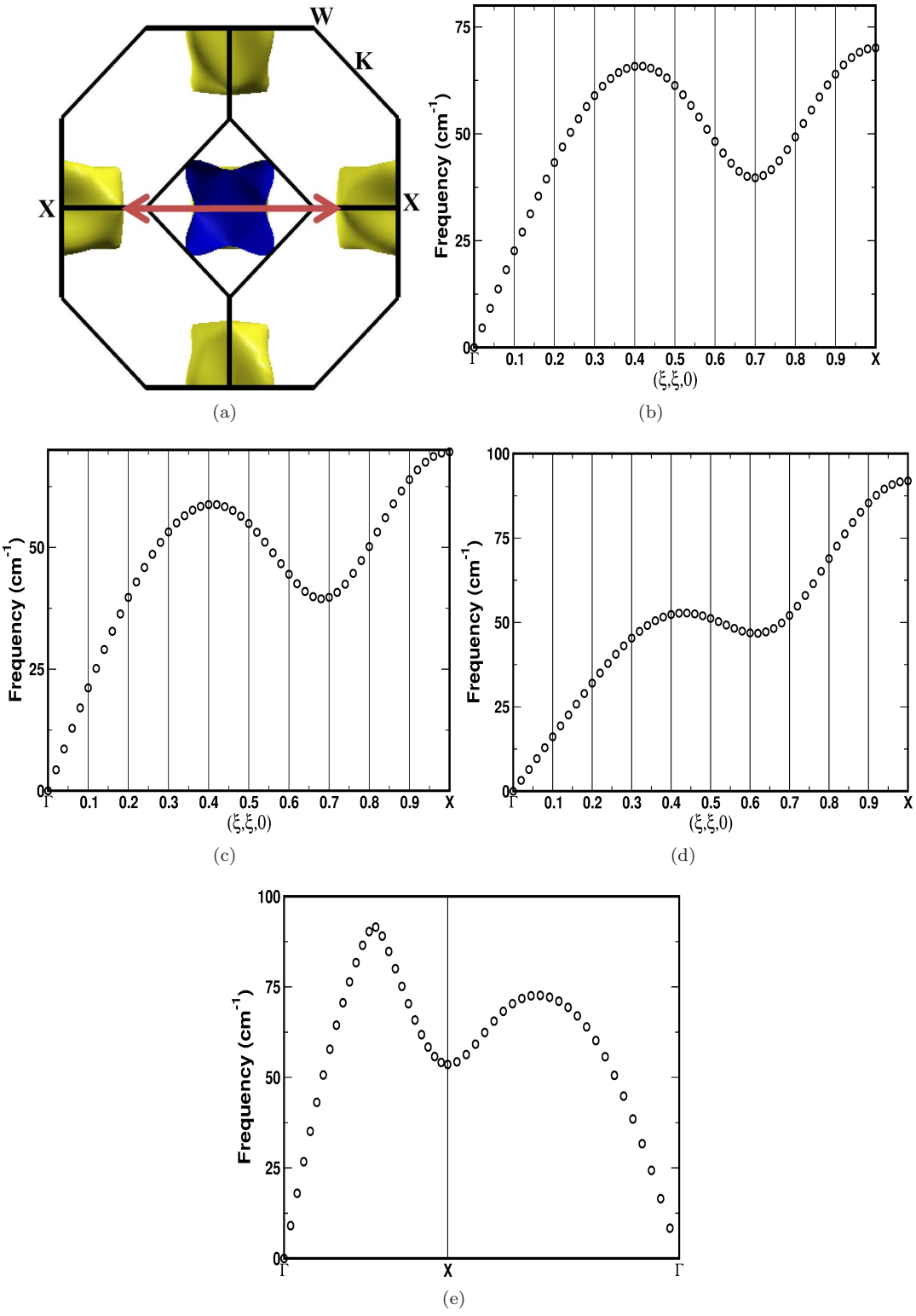

Figure 3.6: (a) Direction of nesting vector and TA2 acoustic phonon mode along Γ-X direction in (b) Ni_2NbAl (c) Ni_2NbGa, (d) Ni_2VAl and (e) Ni_2NbSn.

where ω_{ln} is logarithmically averaged phonon frequency, λ_{ep} is electron phonon coupling constant and μ^* is Coulomb pseudopotential which is a parameter that normally takes a value of 0.1-0.15.

The electron phonon coupling constant (λ_{ep}) is usually extracted from the Eliashberg function ($\alpha^2F(\omega)$) which can be used to determine the T_c of a conventional phonon mediated superconductor. $\alpha^2F(\omega)$ is written as

$$\alpha^2F(\omega) = \frac{1}{2\pi N(\epsilon_f)} \sum_{qj} \frac{\nu_{qj}}{\hbar\omega_{qj}} \delta(\omega - \omega_{qj}) \tag{3.6}$$

This function is related to the phonon DOS ($F(\omega) = \sum_{qj} \delta(\omega - \omega_{qj})$) and differs from the phonon DOS by having a weight factor $1/2\pi N(\epsilon_f)$ inside the summation. In the above formula $N(\epsilon_f)$ is the electronic density of states at the E_F and ν_{qj} is the phonon line width which can be represented as below.

$$\nu_{qj} = 2\pi\omega_{qj} \sum_{knm} |g^{qj}_{(k+q)m,kn}|^2 \delta(\varepsilon_{kn} - \varepsilon_F)\delta(\varepsilon_{(k+q)m} - \varepsilon_F) \tag{3.7}$$

where Dirac delta function express the energy conservation conditions and 'g' is the electron phonon matrix element. The electron phonon coupling constant (λ_{ep}) can be expressed in terms of $\alpha^2F(\omega)$ as shown below.

$$\lambda_{ep} = 2\int \frac{d\omega}{\omega} \alpha^2F(\omega) = \int \lambda(\omega) d\omega \tag{3.8}$$

where $\lambda(\omega) = \frac{2\alpha^2F(\omega)}{\omega}$

The calculated T_c values for Ni_2NbAl, Ni_2NbGa, Ni_2NbSn and Ni_2VAl compounds are given in Table 3.3 for μ^* values of 0.13 and 0.15. The calculated values agree well with the experiments with $\mu^* = 0.13$ for Ni_2NbX (X= Al, Ga, Sn) compounds. Among the investigated compounds, Ni_2VAl is found to have relatively high T_c of 3.84 K with high λ_{ep} value 0.68 with $\mu^* = 0.13$. As we discussed Ni_2VAl has high electronic DOS and high Sommerfield coefficient γ at E_F compared to other compounds indicating the compound to be a superconductor with high T_c value than the other compounds. From the calculated T_c and λ_{ep} values, the superconducting nature of the Ni_2VAl compound is evident. These calculated values are in the range of the present Ni_2NbX (X= Al, Ga, Sn) and other Ni based superconducting Heusler compound $ZrNi_2Ga$ [185].

3.4 Pressure effect on electronic structure, elastic constants, vibrational and superconducting properties

As mentioned, pressure is a effective tuning parameter for exploring the relationships between Fermi surface and other physical properties. This motivated us to proceed further to see the effect of pressure on the above mentioned properties for the compounds studied. For all the compounds we compressed the volume up to -15% of the initial volume. We have studied the electronic structure properties under compression for all the mentioned compounds. Except Ni_2NbAl, we did not find any drastic changes in the band structure and FS topology for the investigated compounds. In the case of Ni_2NbAl we find an extra band to cross E_F at the compression of V/V_0=0.93 (pressure of 17 GPa) at X point and correspondingly addition of a Fermi surface, which is having electron nature, is observed at the same compression and the corresponding band and Fermi surfaces are given in

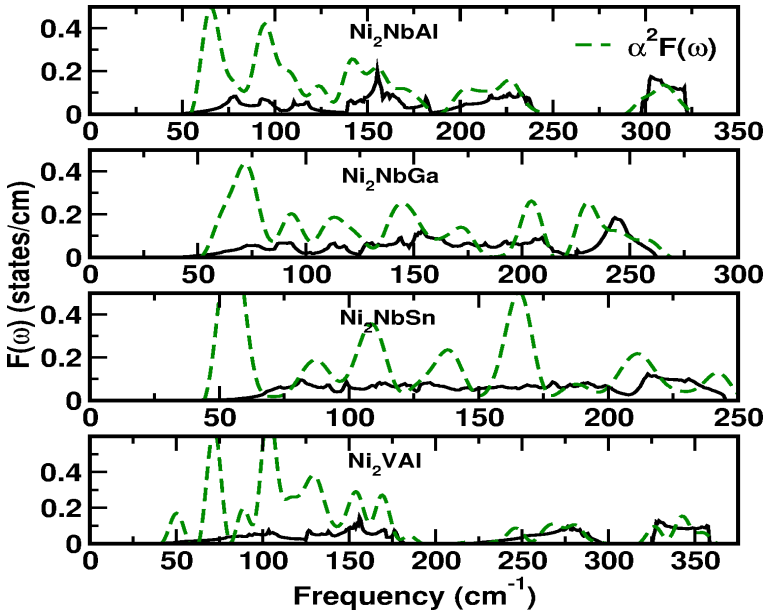

Figure 3.7: Eliashberg function $\alpha^2F(\omega)$ and phonon-density of states for superconducting Ni_2NbAl, Ni_2NbGa, Ni_2NbSn and Ni_2VAl compounds from top to bottom.

Fig. 3.8.

The electronic DOS under compression is shown in Fig. 3.9 for all the compounds. From the plot, the total electronic DOS linearly decreases with pressure in all the compounds but in the case of Ni_2NbAl it is non-linear at $V/V_0 = 0.93$ and is clearly represented in the inset.

We have also calculated the single crystalline elastic constants for all the compounds under compression to check the effect of pressure on the mechanical stability in the present compounds and are plotted in Fig 3.10(a,b). From this we can observe that all the compounds are satisfying the Born's [192] stability criteria under compression indicating the mechanically stable nature of the present compounds under the compression range we have studied. We also observed that the values of three independent elastic constants increases under compression in all the compounds as usual. It is also observed that C_{11}, C_{12} are more sensitive to pressure while C_{44} is quite insensitive to pressure for the same compounds, where C_{44} is related to transverse distortion which is almost flat indicating the effect of pressure on this to be weaker.

We have calculated the phonon dispersion under compression. We find hardening of frequencies for all the compounds with pressure as shown in Fig. 3.11. In the case of superconducting Ni_2NbAl, Ni_2NbGa, Ni_2NbSn and Ni_2VAl, we find hardening of frequencies for all the modes except in the lowest frequency acoustic mode which softens under compression. In Fig. 3.12, we have given only the lower frequency acoustic mode under compression for Ni_2NbAl, Ni_2NbGa, Ni_2NbSn and Ni_2VAl compounds to show the softening nature in that particular mode. From this figure, we have observed that the softening becomes more pronounced under compression at the same 'q' vector where the Kohn anomaly is found in all compounds. The softening in phonon frequency, corresponding to the Kohn anomaly, under pressure in the Nb compounds implies a pressure dependent structural phase transition. Near the transition pressure this is presumably of charge density wave character. In Ni_2NbAl it is observed to be imaginary at compressions around V/V_0= 0.92 and 0.85. In this

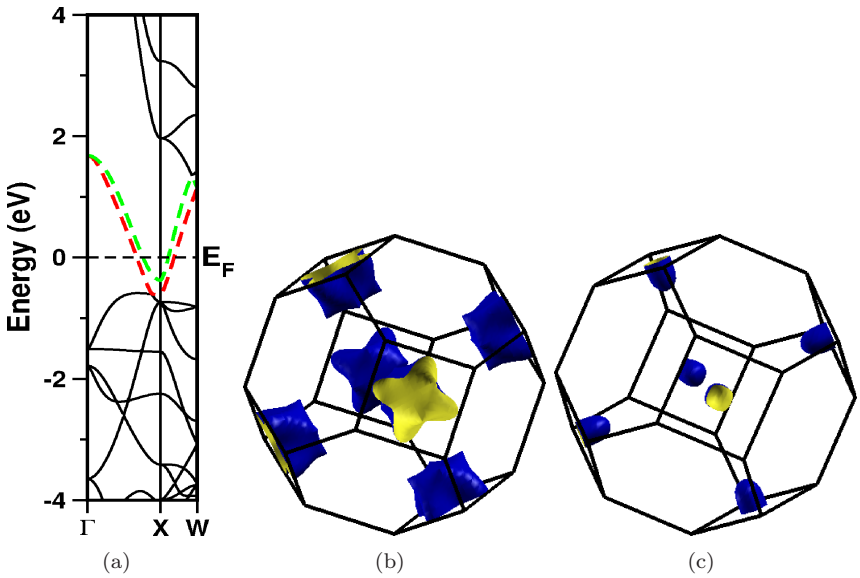

Figure 3.8: (a) Band structure under compression (at $V/V_0 = 0.93$) for Ni_2NbAl and the corresponding FS (b, c) at the same compression.

compound, we find an extra Fermi surface at $V/V_0 = 0.93$. The change in the FS topology could be a reason for the imaginary mode at $V/V_0 = 0.92$ and the nesting feature under compression also becomes more prominent due to increase in the size of the FS under compression. In the remaining compounds, no extra FS is observed but the size of the FS increases under compression which might lead to an increase in the effect of nesting under compression. In Ni_2MnSb [204] authors observed the imaginary frequency in TA2 mode at ambient conditions which is due to the presence of Khon anomaly in this system. The appearance of imaginary frequencies under compression in TA2 mode in Ni_2NbAl, Ni_2NbGa, Ni_2NbSn and Ni_2VAl compounds may be due to the presence of same Kohn anomaly under compression. This acoustic mode softening is also observed in other Heusler compounds. In $HfPd_2Al$ [206] it is observed at the pressure of 7.5 GPa, Pd_2ZrAl [74] at ambient conditions. In the case of YPd_2Sn [207], authors found anomaly in the transverse acoustic mode and reported that to be the reason for the increase in electron-phonon coupling parameter of that phonon branch. The anomaly in the transverse acoustic mode is also observed in non Heusler compounds [208, 209, 210, 211, 212], where the authors reported that these phonon anomalies play an important role in understanding superconductivity in those compounds. As discussed previously, we have observed the anomalies in the phonon frequencies along X-Γ direction in Ni_2NbAl, Ni_2NbGa and Ni_2VAl compounds and at X point in Ni_2NbSn. We already know that the lower frequency phonon modes would contribute more to the electron phonon coupling, which further has an impact on the T_c of that material. This indicate that the softening may lead to change in the λ_{ep} and T_c in these compounds.

We have calculated the electron-phonon coupling constant and superconducting transition temperature for superconducting Ni_2NbAl, Ni_2NbGa, Ni_2NbSn and Ni_2VAl compounds under compression and are shown in Fig 3.13. From these plots, all the compounds show a non-monotonic variation in T_c and the electron-phonon coupling constant under compression are behaving in the opposite

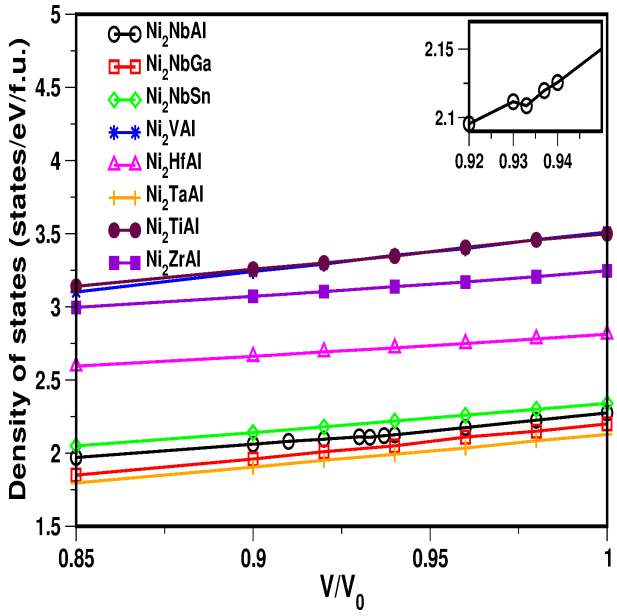

Figure 3.9: Electronic density of states under compression.

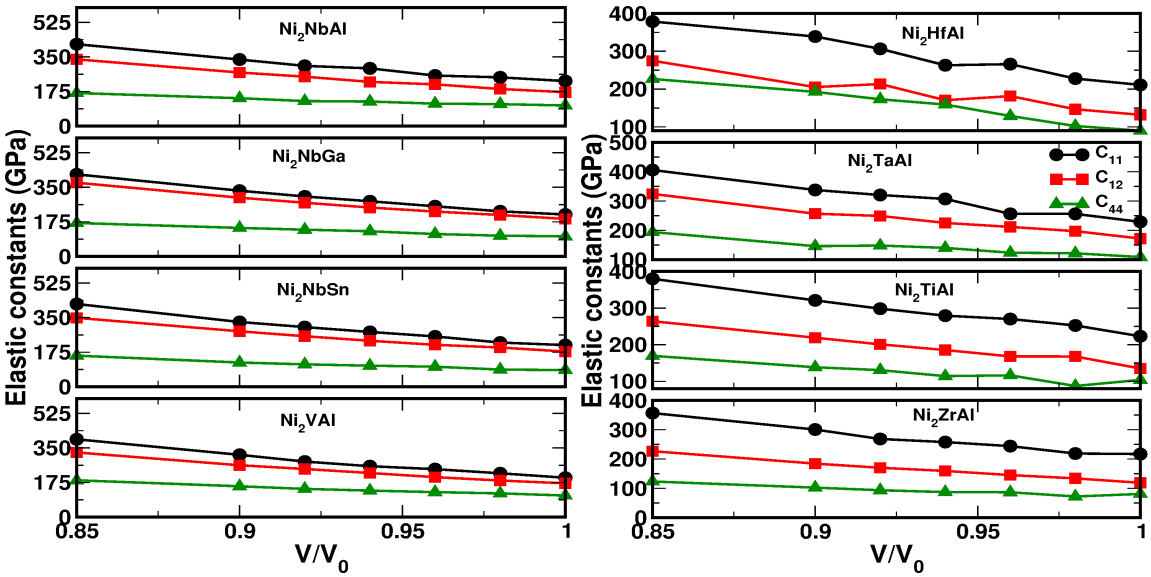

(a) (b)

Figure 3.10: (a, b) Elastic constants under compression.

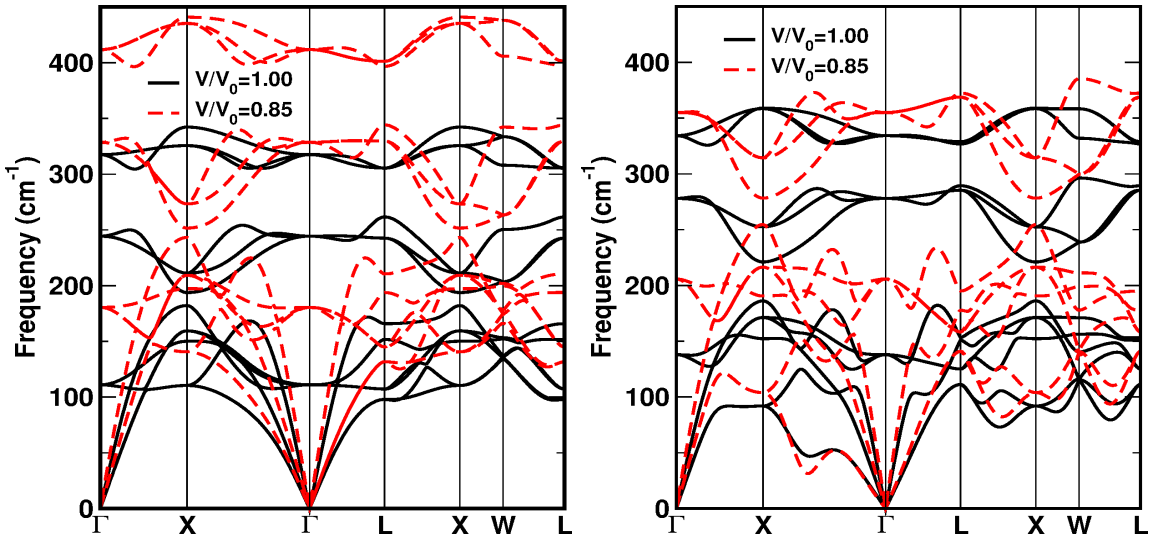
Frequency (cm^{-1})
V/V$_0$=1.00
V/V$_0$=0.85
Γ X Γ L X W L

(a) (b)

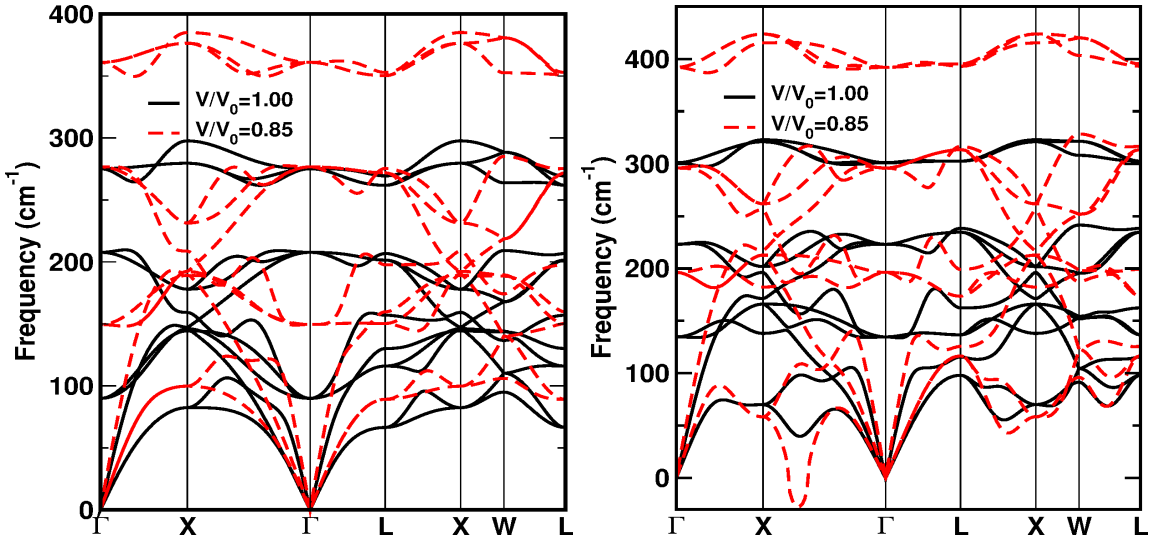
Frequency (cm^{-1})
V/V$_0$=1.00
V/V$_0$=0.85
Γ X Γ L X W L

(c) (d)

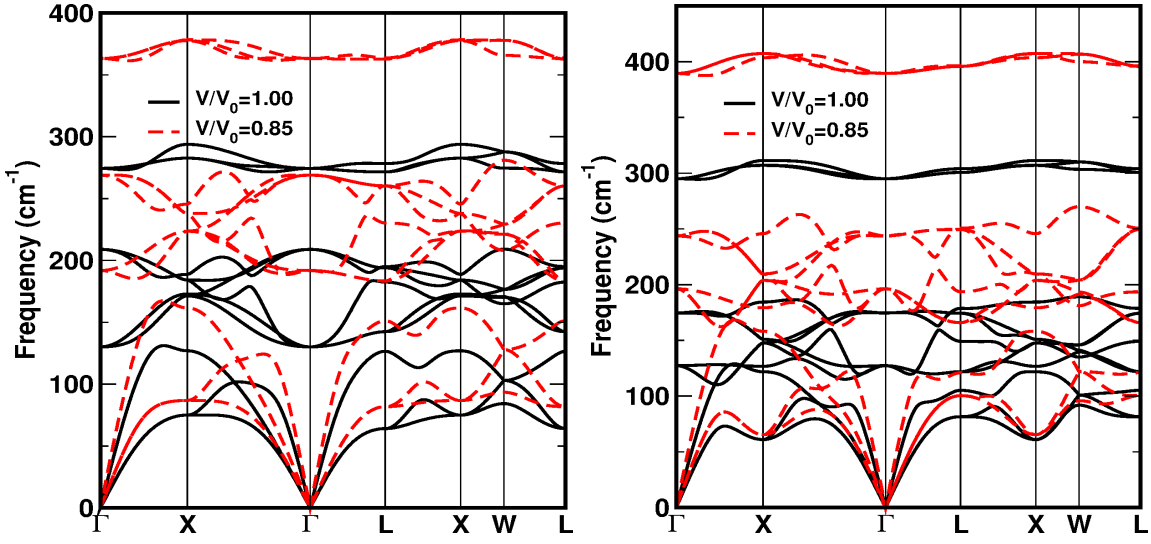
Frequency (cm^{-1})
V/V$_0$=1.00
V/V$_0$=0.85
Γ X Γ L X W L

(e) (f)

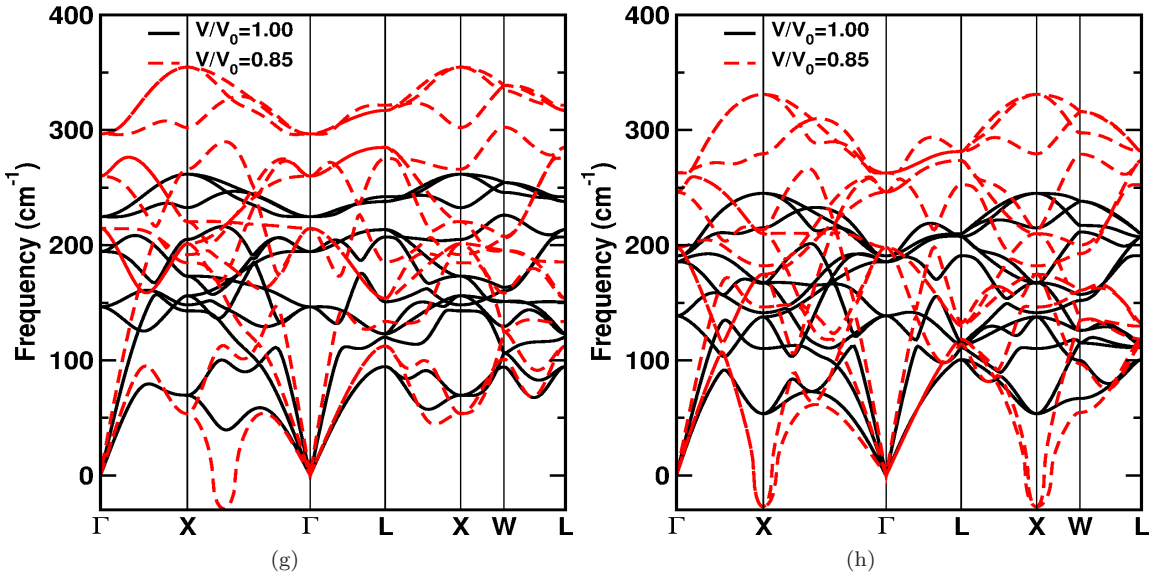

Figure 3.11: Phonon dispersion at ambient conditions and at the compression V/V_0=0.85 for (a) Ni_2TiAl, (b) Ni_2VAl (c) Ni_2ZrAl, (d) Ni_2NbAl, (e) Ni_2HfAl, (f) Ni_2TaAl, (g) Ni_2NbGa and (h) Ni_2NbSn respectively.

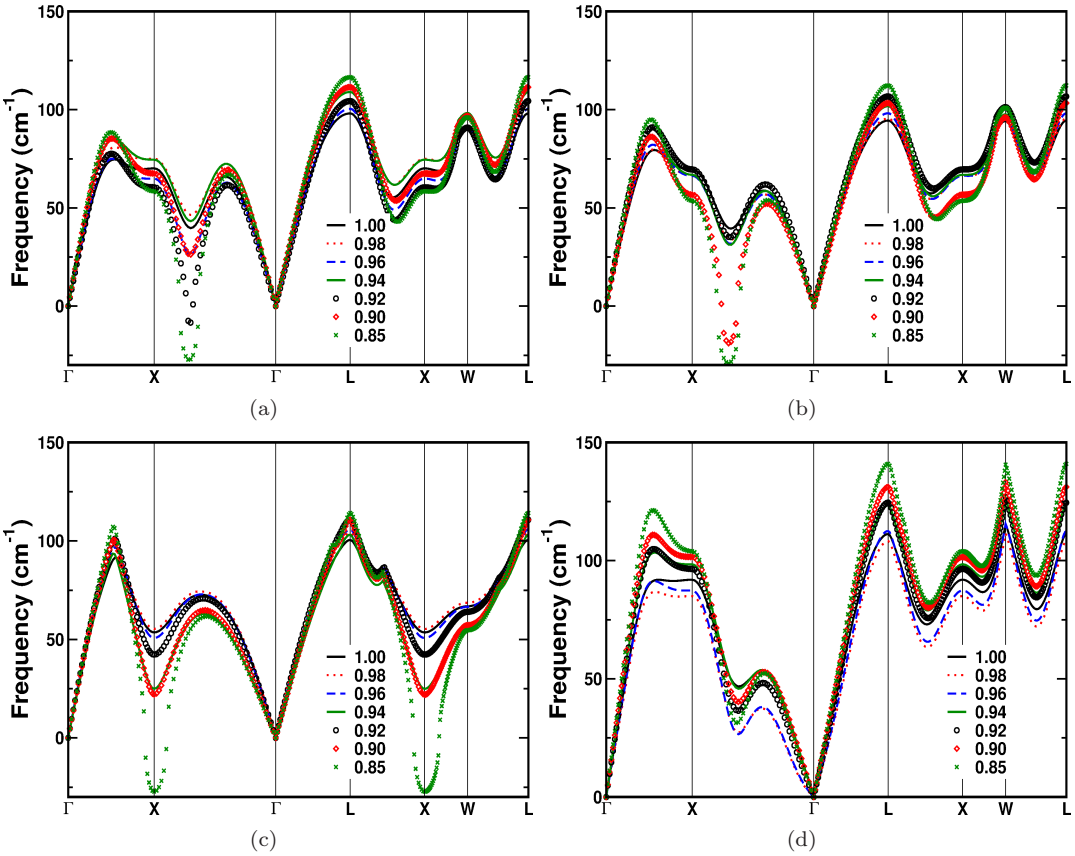

Figure 3.12: Softening of lower frequency acoustic mode under compression in (a) Ni_2NbAl, (b) Ni_2NbGa, (c) Ni_2NbSn and (d) Ni_2VAl.

manner to ω_{ln}. In the previous work [213, 214] it was reported that the softening of the phonon DOS leads to the increase in the T_c of that material. In Ni_2NbAl, the T_c plot under compression in our previous work [215] is different from this work. In our previous work we used ultrasoft pseudopotentials and also we did not find any softening nature in the phonon dispersion curve as well as phonon density of states. In the present work we have used norm-conserving pseudopotentials. These are more difficult to converge and require more computational resources but are more reliable.

3.5 Conclusions

We have studied the ground state, electronic structure, mechanical, vibrational properties of all compounds using the density functional theory within generalised gradient approximation at ambient conditions and under compression. Our calculated ground state properties agree well with experimental and other theoretical results. In all the compounds, the DOS at E_F is arrived mainly from Ni d_{eg} states with an admixture of X $d_{t_{2g}}$ states. Nesting features in FS are evident in all the compounds. The calculated single crystalline elastic constants satisfy the Born stability criteria indicating the mechanical stability of the investigated compounds both at ambient conditions and under compression. The absence of the imaginary frequencies in phonon dispersion indicate the dynamical stability of the present compounds. Kohn anomaly is observed in TA2 mode in Ni_2NbX (X = Al, Ga and Sn) and Ni_2VAl compounds which might be due to the nesting in the FS. The computed T_c using Allen-Dynes formula agree well with the experimental results for Ni_2NbX (X = Al, Ga and Sn). Importantly, Ni_2VAl is predicted to be a superconductor which has a T_c value in the range of Heusler compounds. From the calculated Eliashberg function ($\alpha^2F(\omega)$), we have observed that Ni atom contribution is more towards T_c in all the compounds. Under compression we have observed the change in the band structure of Ni_2NbAl, where we find an extra band to cross the E_F. In addition we also observed a pronounced softening of the Kohn anomalies existing in acoustic TA2 mode under compression. This phonon softening again lead to softening in the phonon density of states. A non-monotonic variation in the T_c under compression is noticed which is due to softening in the lower frequency acoustic mode and phonon DOS. Among the compounds studied, we observe that the variation in T_c under pressure is minimal in Ni_2VAl. It will be of interest to experimentally search for superconductivity in Ni_2VAl and study its pressure dependence.

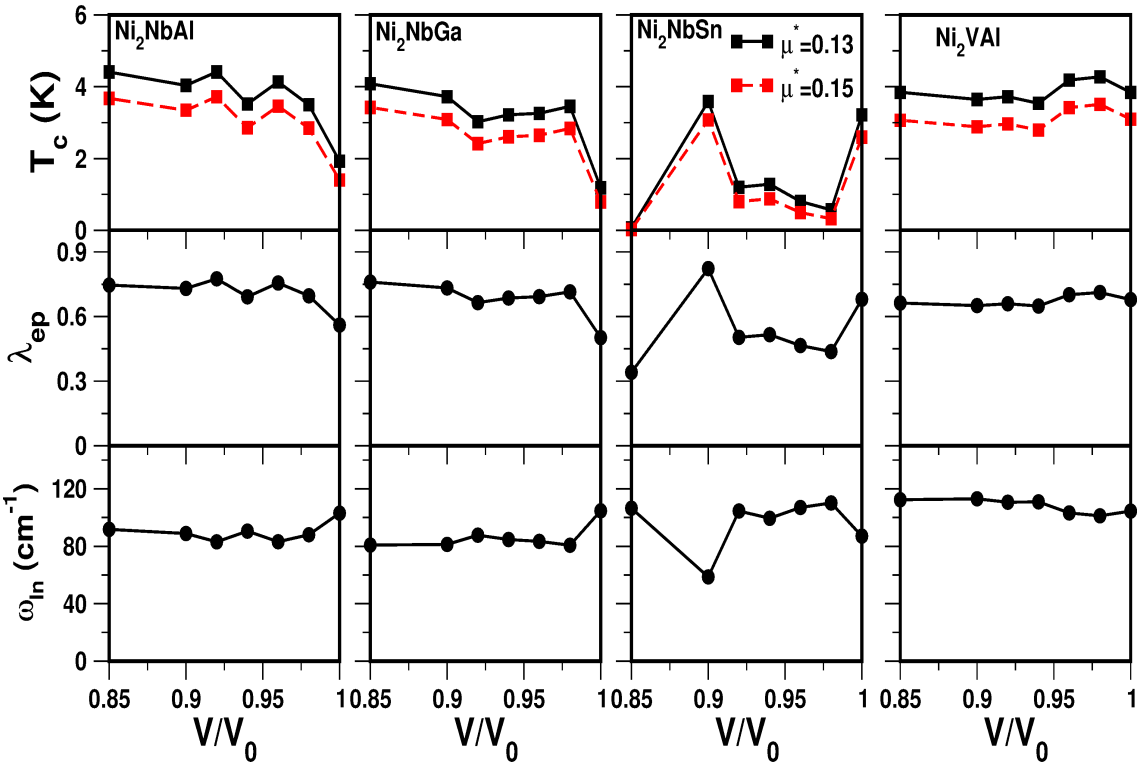

Figure 3.13: Logarithmic frequency, electron-phonon coupling and superconducting transition temperature under compression for Ni_2NbX (X = Al, Ga and Sn) and Ni_2VAl compounds.

Table 3.1: Calculated theoretical equilibrium lattice parameter (a_{the}) compared with the experimental lattice parameter (a_{exp}) (in the units of Å), bulk modulus (B) (in the units of GPa), density of states at the Fermi level (N(E_F)) (states/eV/f.u.) and Somerfield coefficient (γ) (mJ/mol K^2) of Ni_2XAl (X=Ti, Zr, Hf, V, Nb, Ta), Ni_2NbGa and Ni_2NbSn.

Parameters	a_{the}	a_{exp}	B	N(E_F)	γ
Ni_2TiAl	5.90	5.87[a]	164	3.50	8.25
Ni_2ZrAl	6.13	6.12[a]	151	3.25	7.65
Ni_2HfAl	6.10	6.08[a]	158	2.81	6.63
Ni_2VAl	5.80	5.80[b]	181	3.51	8.27
Ni_2NbAl	5.99	5.97[a]	181	2.27	5.36
Ni_2TaAl	5.98	5.96[b]	191	2.13	5.02
Ni_2NbGa	5.991	5.956[c]	182	2.20	5.19
Ni_2NbSn	6.202	6.157[c], 6.160[d]	170	2.34	5.52

a : Ref. [85]; *b* : Ref. [90]; *c* : Ref. [91]; *d* : Ref. [172]

Table 3.2: Calculated elastic constants (in the units of GPa) and derived quantities for Ni_2XAl (X=Ti, Zr, Hf, V, Nb, Ta), Ni_2NbGa and Ni_2NbSn at the theoretical lattice constant. Where E is Young's modulus(in GPa), v_l, v_t, v_m are the longitudinal, transverse and mean sound velocities in the units of km/s. CP = Cauchy's pressure. PR = Pugh's ratio. Θ_D = Debye temperature in the units of Kelvin.

Parameters	Ti	Zr	Hf	V	Nb	Ta	Ni_2NbGa	Ni_2NbSn
C_{11}	223	217	211	200	212	229	194	188
C_{12}	135	119	132	171	167	172	176	162
C_{44}	104	81	90	109	98	109	95	72
E	193	174	171	138	150	172	111	104
A	2.36	1.65	2.27	7.69	4.37	3.89	10.99	5.57
CP	30.18	37.41	41.64	62.33	68.26	63.01	81.17	89.14
PR	0.45	0.44	0.41	0.28	0.30	0.33	0.22	0.22
σ	0.30	0.31	0.32	0.37	0.36	0.35	0.40	0.40
G_H	74.00	66.37	64.85	50.43	54.99	63.79	39.88	37.19
v_l	13.00	11.88	10.17	12.22	11.81	10.48	10.43	9.80
v_t	6.89	6.25	5.24	5.51	5.48	5.04	4.29	4.03
v_m	7.71	6.99	5.86	6.21	6.17	5.66	4.86	4.56
Θ_D	617.89	539.17	454.73	506.42	487.11	446.99	241	219
Θ_D(exp)				358^b	280^a, 300^b		240^a	206^a

a : Ref. [91]; b : Ref. [90]

Table 3.3: Calculated T_c (in the units of K) and λ_{ep} values with experimental reports for Ni_2NbX (X = Al, Ga, Sn) and Ni_2VAl.

Parameters	Ni_2NbAl	Ni_2NbGa	Ni_2NbSn	Ni_2VAl
T_c (experimental)	2.15^a	1.54^a	2.90^a, 3.4^b, 3.4^c	–
T_c (this work with $\mu^* = 0.13$)	1.92	1.18	3.21	3.84
T_c (this work with $\mu^* = 0.15$)	1.40	0.79	2.60	3.09
λ (experiment)	0.52^a, 0.514^d	0.50^a	0.61^a	–
λ (this work)	0.56	0.50	0.68	0.68

a : Ref. [91]; b : Ref. [172]; c : Ref. [73]; d : Ref. [90]

Chapter 4

Electronic topological transitions in Nb_3Y (Y = Al, Ga, In, Ge, Sn, Os, Ir and Pt) compounds

In the present chapter, first principles electronic structure calculations of A-15 type Nb_3Y (Y = Al, Ga, In, Ge, Sn, Os, Ir and Pt) compounds are performed at ambient conditions and high pressures. Mechanical stability is confirmed in all the compounds both at ambient conditios as well as under compression from the calculated elastic constants. We have observed four holes and two electron Fermi surfaces (FS) for the compounds Nb_3Y (Y = Al, Ga, In, Ge, Sn), two hole and two electron FS for Nb_3Y (Y = Os, Ir) and one hole and three electron FS for Nb_3Pt together with FS nesting feature observed at M and along X - Γ in all the compounds. A continuous change in the FS topology is observed under pressure in all the compounds which is also reflected in the calculated elastic constants and density of states under pressure indicating the electronic topological transitions (ETT). The ETT observed at around 21.5 GPa, 17.5 GPa in Nb_3Al and Nb_3Ga are in good agreement with the anomalies observed by the experiments around the same compression.

4.1 Introduction

Eversince the discovery of superconductivity in V_3Si with T_c ~17 K in the year 1953 by Hardy and Hulm [93], the family of compounds with composition X_3Y (X= V, Nb, Cr, Ti, Mo, Zr, Ta, W to Hf and Y= Al, Ga, Ge, In, Sn, Os, Ir, Pt etc) had attracted considerable attention of researchers as some of them possess quite high superconducting transition temperature (T_c). The interest in these compounds are not only due to the rather high T_c but also their high critical current density and critical magnetic field, along with acceptable mechanical properties make them viable for applications. These compounds crystallize in the A15 type crystal structure (see Fig. 4.1), where X atoms form three mutually orthogonal chain like structure parallel to the edges of the unit cell.

Some of these compounds undergo cubic to tetragonal martensitic transformation near to their superconducting transition temperatures T_c [95]. For example, the martensitic transition temperatures of V_3Si (21 K) and Nb_3Sn (45 K) are close to their respective superconducting transition temperatures 17 and 18 K. Acoustic phonon instabilities were found to be responsible for martensitic transition in previous studies [96]. A similar behaviour was also seen in the $Nb_3Al_xGe_{1-x}$ [97], V_3Ga [98, 99], V_3Ge [99] and Nb_3Al [100] compounds. Experiments [101] also indicated a dimerization of the transition-metal chains accompanied by a tetragonal distortion of the lattice during the transformation. It has been proposed that the tetragonal transformation is driven by band Jahn-Teller like mechanism. These A15 compounds exhibit different behaviour in electronically derived properties at low temperatures such as knight shifts, electrical resistivity etc [102]. This unusual behaviour of various properties of A15 family compounds has been related to the sharp peak in electronic density of states near to the Fermi level arising from the '*d*' states of the transition metal atoms [102]. Hence it is clear that many properties of these compounds are related to their electronic structures.

In these X_3Y compounds, X atoms have low site symmetry and are responsible for the high T_c values in this class of materials. X-'*d*' electrons are found to play dominant role in the electronic structure properties around the Fermi level (E_F). In these compounds if Y is a transition metal, the T_c of these materials will be low because of the Y-'*d*' electrons which will be competing with the X-'*d*' bands. In some compounds, for a given X element T_c is found to be increase as decrease in the mass and size of Y element. In the compounds Nb_3X(X= Os, Ir, Pt), the studies of X-ray photoemission spectra informed that the '4d' and the '5d' energy bands of these Nb_3X compounds seems to be more and more separated with increasing atomic number of the X element [216].

Recent experiments [217] have explored the possible relationship between superconductivity and martensitic transition in V_3Si and Nb_3Sn compounds by measuring electrical resistance and specific heat under high pressure. They have observed that initially T_c increases with pressure and merges with martensitic transition temperature at high pressure, where further T_c increase is ceased and concluded that the martensitic transition play an important role in superconductivity of these compounds. So to understand this, a thorough understanding of electronic structures is necessary. So far only a few electronic structure studies are available [218, 219, 220, 221] but a systematic study especially under high pressure is still lacking. Some elements like Cd [222] and Co [223] show a continuous change in FS topology under pressure which highlights the ETT in these elements. In this work, we have carried out a systematic study of electronic properties under pressure for Nb based A15 compounds namely Nb_3Y (Y = Al, Ga, In, Ge, Sn, Os, Ir and Pt).

Since any property that involves the conduction electrons in a metal must depend on the shape of the Fermi surface and on the wave functions of the electrons at or near the Fermi surface of that

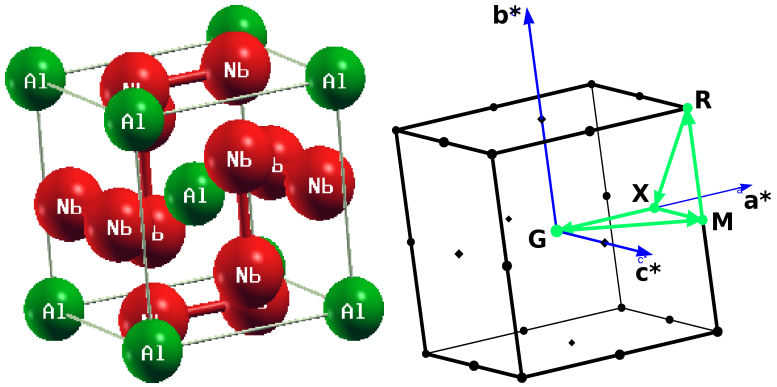

(a) (b)

Figure 4.1: (a) Crystal structure of Nb_3X (X= Al, Ga, In, Ge and Sn) and (b) Brillouin zone high symmetry points.

metal [224] it will be interesting to study the Fermi surface topology and their pressure variations for these compounds. Further, Bilbro and McMillan [225] have studied the interaction of charge density wave (CDW) and superconductivity (SC) in A15 materials within mean field approximation and predicted that both states compete with each other for developing their respective gaps in the same Fermi surface. In Nb_3Sn, opening of a charge-density wave gap is observed and expected that it would be due to the dimerization of Nb atoms and nesting at the Fermi surface [226], and this further indicate the possibility of nesting feature in these type of compounds. Charge density wave, Fermi surface nesting and Peierls instability may be inter-related in these compounds. Calculation of the susceptibility [227] $\chi(\vec{q},\omega)$ for a given system is one of the way to understand the possibility of Fermi surface nesting and formation of CDW. Zero energy value of the Lindhard response function $\chi_0(\vec{q}) \equiv \chi_0(\vec{q},\omega=0)$ can be used to determine the presence of Fermi surface nesting. There should be a peak in the imaginary part of the response function $\mathrm{Im}\big[\chi_0(\vec{q})\big]$ at the Fermi surface nesting vector. The formation of charge density wave requires a large real part of the susceptibility, $\mathrm{Re}\big[\chi_0(\vec{q})\big]$. Hence in this work we have also calculated the Lindhard response functions $\chi_0(\vec{q}) \equiv \chi_0(\vec{q},\omega=0)$ for these compounds to study the possible Fermi surface nesting in these systems.

We have predicted Fermi surface nesting for all the compounds at ambient conditions as well as under pressure. The Fermi surface nesting is found to be enhanced under pressure for all the compounds except for Nb_3Sn, Nb_3Os, Nb_3Ir and Nb_3Pt. We have also predicted an electronic topological transition (ETT) at different compressions for all the compounds.

4.2 Method of calculations

Density functional calculations have been performed in the present work to calculate the electronic structure and elastic constants. The Full-Potential Linearized Augmented Plane Wave (FP-LAPW) method as implemented in WIEN2k [153] code is used. We have used PBE-GGA [186] (Perdew-Burke-Ernzerhof parametrization of the Generalized Gradient Approximation) approximation for the exchange correlation potential. Throughout the calculations, the R_{MT} (radius of muffin tin spheres) value for each atom was fixed as 1.90 a.u for Nb, 1.80 a.u for Al and 2.10 a.u for both

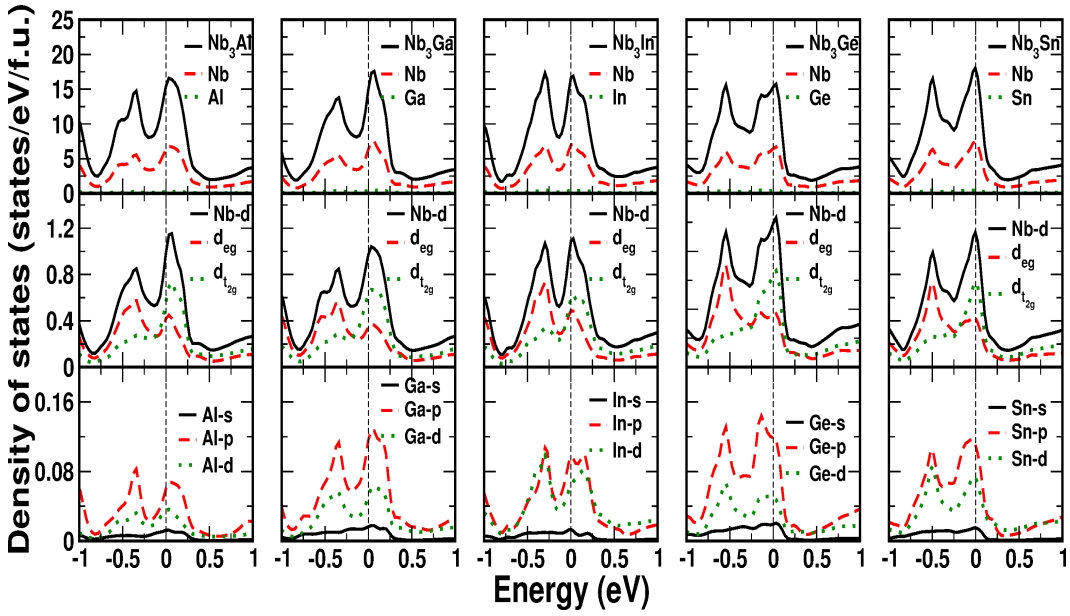

(a)

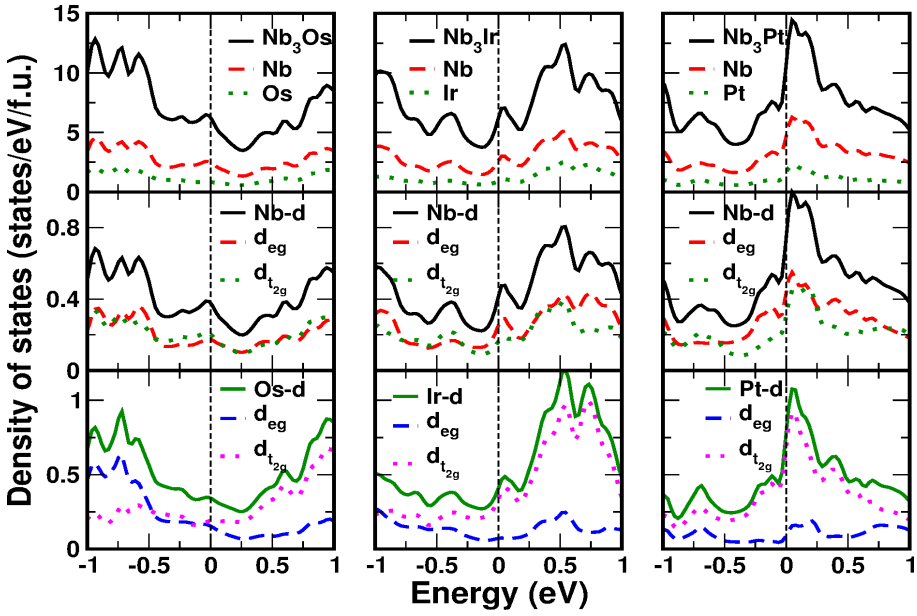

(b)

Figure 4.2: Density of states at ambient conditions for (a) Nb_3Y (Y= Al, Ga, In, Ge, Sn) and (b) Nb_3Y (Y= Os, Ir, Pt).

Ga and Ge, 2.20 a.u for In, 2.25 a.u for Sn and 2.30 a.u for Os, Ir and Pt atoms. For the energy convergence, the criterion R_{MT}*K_{max}=9 was used, where K_{max} is the plane wave cut-off. The potential and charge density were Fourier expanded up to G_{max}=12 a.u^{-1}. For band structure and density of states calculations we have taken total 20000 k points in the Monkhorst-Pack [187] scheme which gives 560 k-points in the irreducible part of the Brillouin Zone (BZ). Tetrahedron method [188] was used to integrate the Brillouin zone. Energy convergence up to 10^{-5} Ry is used to get the proper convergence of the self consistent calculation. All Fermi surface and Lindhard functions are calculated with $44 \times 44 \times 44$ k-mesh to get smoother Fermi surfaces and accurate Lindhard function. Birch-Murnaghan [189] equation of state was used to fit the total energies as a function of primitive cell volume to obtain the bulk modulus and the equilibrium lattice parameter for the investigated compounds. We have checked the effect of spin-orbit coupling (SOC) and have not found any significant changes at the Fermi level with the inclusion of SOC in Nb_3Y (Y = Al, Ga, In, Ge, Sn) compounds and further calculations are performed for these compounds without including SOC. For the remaining Nb_3Y (Y= Os, Ir and Pt), compounds we have included SOC. Real and imaginary part of the Lindhard response function $Re[\chi(q)]$ for $\omega = 0$ is calculated directly from the energy eigenvalues using,

$$Re[\chi(q)] = \sum_{kjj'} \frac{f_{kj} - f_{k+qj'}}{\in_{kj} - \in_{qj'}} \tag{4.1}$$

and

$$Im[\chi(q)] = \sum_{kjj'} \delta(\in_F - \in_{kj})\delta(\in_F - \in_{k+qj'}) \tag{4.2}$$

Where f is Fermi-Dirac distribution function, $\in_{kj}$ and $\in_{qj'}$ are the energy eigenvalues for band indices j and j', and $\in_F$ is the Fermi energy. We have evaluated these functions within constant matrix element approximation and considered only those bands which cross the Fermi level.

4.3 Results and discussions

4.3.1 Ground state properties and elastic constants

Calculated ground state properties of Nb_3Y (Y = Al, Ga, In, Ge, Sn, Os, Ir and Pt) are listed in Table 4.1 together with available experimental and theoretical results. Calculated values are in good agreement with the experiments [228, 229, 230, 231, 232] as well as with earlier theoretical results [220, 102, 231, 233, 234]. Our calculated bulk moduli are in good agreement with earlier theoretical results [220, 221, 219, 233, 234] and the values are higher for compounds with Y= Os, Ir and Pt (transition elements) compared to other compounds containing IIIA and IVA ('p'-state elements). Among the compounds containing IIIA and IVA group element, bulk modulus increases as we move from compounds containing IIIA group elements (X = Al, Ga, In) to IVA group (X = Ge, Sn). Single crystal elastic constants were calculated to establish the mechanical stability of these compounds and the calculated values are given in the Table 4.2 together with available data [219, 221, 233]. Calculated values satisfy the Born mechanical stability criteria [192] i.e. $C_{11}>0$, $C_{44}>0$, $C_{11} > C_{12}$, and $C_{11} + 2C_{12}>0$. polycrystalline elastic constants were also calculated from the single crystals elastic constants[194, 195, 196, 197] and these values are listed in the same table. Calculated Young's modulus values are higher for compounds containing transition element 'Y' indicating the stiffness

of these compounds among other compounds. The presence of elastic anisotropy [194] in the present compounds is also confirmed by calculating the anisotropy factor(A). Calculated positive values of Cauchy's pressure(C_{12}-C_{44}) indicate the ductile nature of the present compounds and it is also confirmed from the calculated Pugh's ratio ($\frac{G_H}{B}$) [198] value. These Pugh's ratio is less than 0.57 which is known as critical number to separate brittle and ductile nature. The Poisson's [199] ratio indicate the stability of the crystal against shear and takes the values in between -1 to 0.5, where -1 and 0.5 serve as lower and upper limits respectively. From the calculated Poisson's ratio values, we observed that all the compounds have the value closer to the upper limit indicating the stiffness of the present compounds.

4.3.2 Density of states

The calculated density of states (DOS) are plotted in Fig. 4.2 along with partial density of states for all the compounds. We have also tabulated the total DOS at E_F ($N(E_F)$) for each compound in Table 4.1 and compared with earlier calculations. The calculated $N(E_F)$ and overall DOS features agree well with available data [220, 102, 235, 102, 235, 234]. In the Nb_3Y (Y=Al, Ga, In, Ge, Sn) compounds there is a pseudo gap on both the sides of the Fermi level which originates mainly due to crystal field splitting of Nb-'*d*' states but in the case of Nb_3Y (Y=Os, Ir and Pt) compounds the pseudo gap is observed only one side. We have found that the $N(E_F)$ is more for Nb_3Y (Y=Al, Ga, In, Ge, Sn) compounds compared to Nb_3Y (Y=Os, Ir and Pt). The Fermi level shifts towards right (i.e from shoulder to peak) in total DOS for compounds containing group IVA elements compared to those containing group IIIA elements and is consistent with the fact that group IVA elements have one extra electron. The total DOS at Fermi level is found to increase in both IIIA and IVA group as we move from top to bottom of the periodic table and is evident from Fig. 4.2 as the Fermi level shifts towards the peak in total DOS. From partial DOS it is clearly seen that there is strong hybridisation between Nb-'*d*' and Y-'*p*/*d*' states in Nb_3Y close to Fermi level. In addition the covalent nature between Nb and Y atom is also observed from the DOS plots. We have also calculated Sommerfeld coefficient γ and given in Table 4.1 along with available data. The calculated γ values are in good agreement with available data [219] for Nb_3Al and are proportional to $N(E_F)$. From the same table the calculated γ values are found to be lesser in Nb_3Y (Y=Os, Ir and Pt) compounds compared to other compounds. The calculated γ values are proportional to the $N(E_F)$ in the present compounds.

4.3.3 Band structure and Fermi surface topology

Band structure calculations are performed for all the compounds along different high symmetry directions in the Brillouin zone (high symmetry directions are given in Fig. 4.1(b)). Effect of SOC on compounds containing Y= IIIA and IVA group elements is very less [236] and the calculations are done without including SOC for these compounds. For the compounds containing transition elements (Y= Os, Ir and Pt) we have included SOC. The electronic band structure for all the compounds are shown in Fig. 4.3. Overall band profile is similar within Nb_3(Y = Al, Ga, In, Ge, Sn) compounds and Nb_3(Y = Os, Ir, Pt) compounds. In all the compounds we have observed multiple degenerate bands at R point. Close to E_F, the bands originate from the hybridization of Nb-'*d*' and Y-'*p*/*d*' states and is consistent with our findings from partial DOS. From the keen

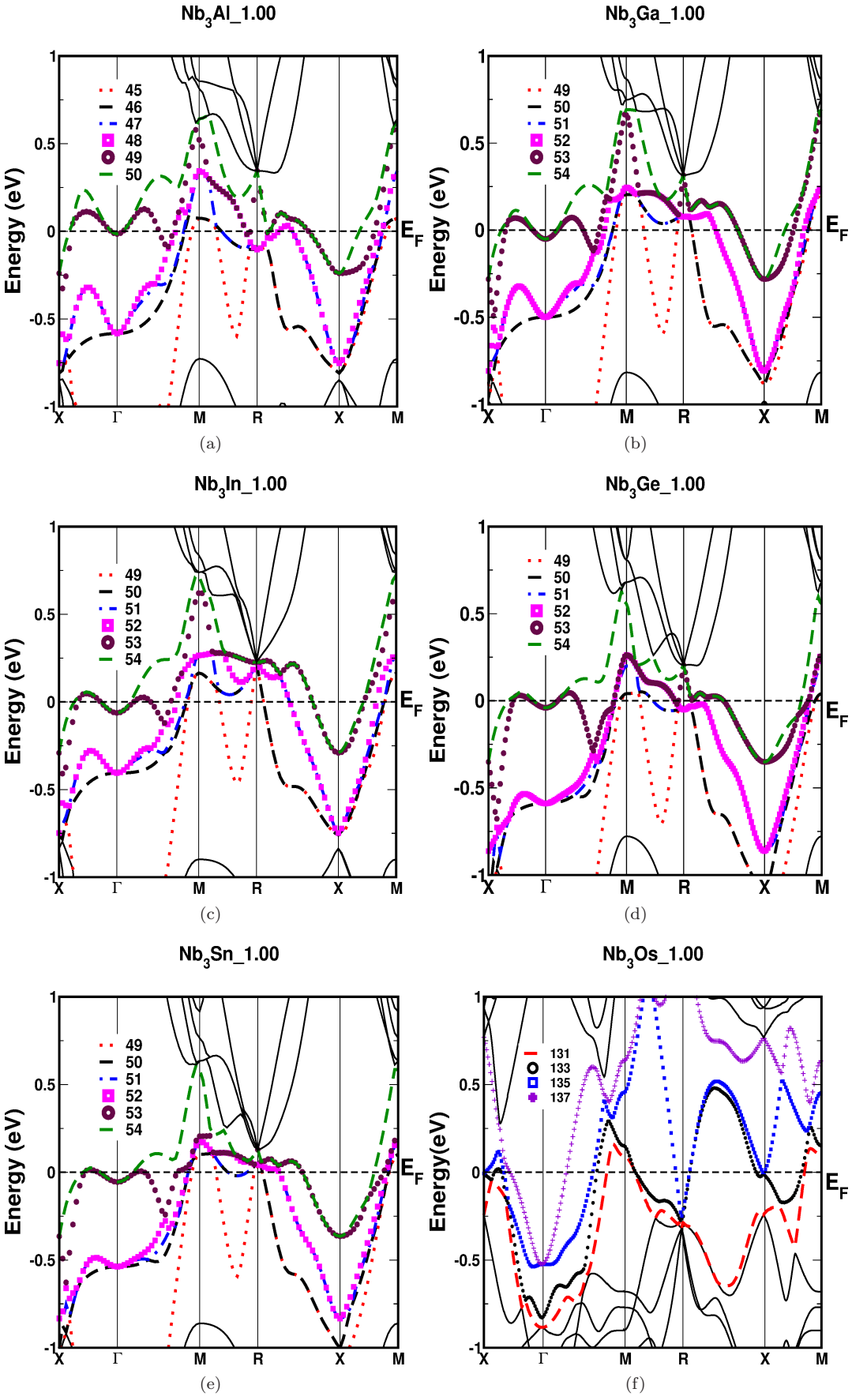
Nb3Al_1.00
45
46
47
48
49
50
Energy (eV)
EF
X
Γ
M
R
X
M
(a)
Nb3Ga_1.00
49
50
51
52
53
54
Energy (eV)
EF
X
Γ
M
R
X
M
(b)
Nb3In_1.00
49
50
51
52
53
54
Energy (eV)
EF
X
Γ
M
R
X
M
(c)
Nb3Ge_1.00
49
50
51
52
53
54
Energy (eV)
EF
X
Γ
M
R
X
M
(d)
Nb3Sn_1.00
49
50
51
52
53
54
Energy (eV)
EF
X
Γ
M
R
X
M
(e)
Nb3Os_1.00
131
133
135
137
Energy(eV)
EF
X
Γ
M
R
X
M
(f)

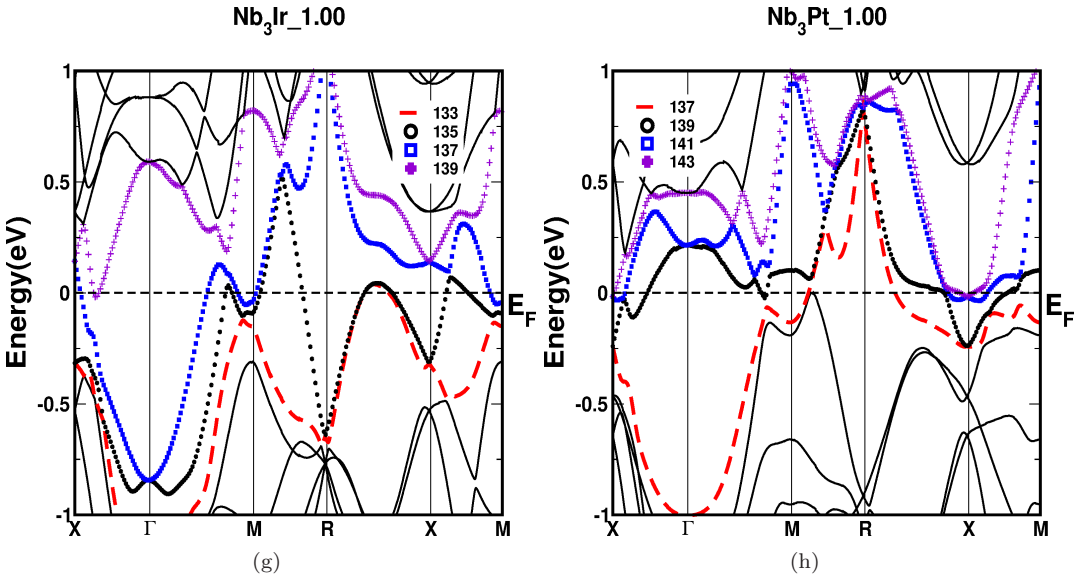

Figure 4.3: Band structure without spin-orbit coupling for (a) Nb_3Al, (b) Nb_3Ga, (c) Nb_3In, (d) Nb_3Ge, (e) Nb_3Sn and with spin-orbit coupling for (f) Nb_3Os, (g) Nb_3Ir, (h) Nb_3Pt at ambient conditions (V/V_0=1.00). The ligands in each figure indicate the bands which are crossing E_F and are shown with different colours and numbers.

observation of band structure, shifting of bands above the E_F around R point is observed when we move from compounds possessing IIIA group elements (Y = Al, Ga, In) to IVA group (Y = Ge, Sn) but in other compounds the scenario is completely different. Number of bands to cross E_F is found to be six and four in Nb_3(Y = Al, Ga, In, Ge, Sn) and Nb_3(Y = Os, Ir, Pt) compounds respectively and are indicated in different colour with their numbers. In Nb_3(Y = Al, Ga, In, Ge, Sn) compounds first four bands are of hole nature as the bands are crossing from valence to conduction band and the remaining two bands are having electron nature. In the case of Nb_3Al, first four bands which are of hole nature and indicated with numbers 45 to 48 and are crossing E_F at M point and in addition to this, the bands 47 and 48 are crossing E_F along R-X as shown in Fig. 4.3(a). In the case of Nb_3Ga and Nb_3In these bands are indicated with numbers from 49 to 52, as in Fig. 4.3(b, c) and the scenario at M point is the same as Nb_3Al but at R point these bands are shifted above the E_F. This shifting is more in Nb_3In when compared with Nb_3Ga which is evident from band structure in Fig. 4.3(c). The last two bands, which are having electronic nature indicated with numbers 49 and 50 in Nb_3Al are crossing E_F at Γ, along R-X and at X point. In addition to this, band number 49 is crossing E_F along Γ-M. In the case of Nb_3Ga and Nb_3In these two bands are indicated with numbers 53 and 54. For these two bands the scenario is same as in Nb_3Al except along R-X, where the band crossing is absent due to shifting of bands above the E_F.

The band structure for the compounds Nb_3Ge and Nb_3Sn is given in Fig. 4.3(d, e) where Y is replaced with IVA group elements. These compounds are having one extra electron per formula unit compared to the compounds which are having Y = Al, Ga and In. If we move from compounds containing IIIA to IVA elements, i.e from Nb_3Ga to Nb_3Ge and Nb_3In to Nb_3Sn, we can observe the shifting of bands below E_F due to one extra electron in latter compounds. In the case of Nb_3Ge, first four hole natured bands are crossing the E_F only at M point. In Nb_3Sn, behaviour of these bands

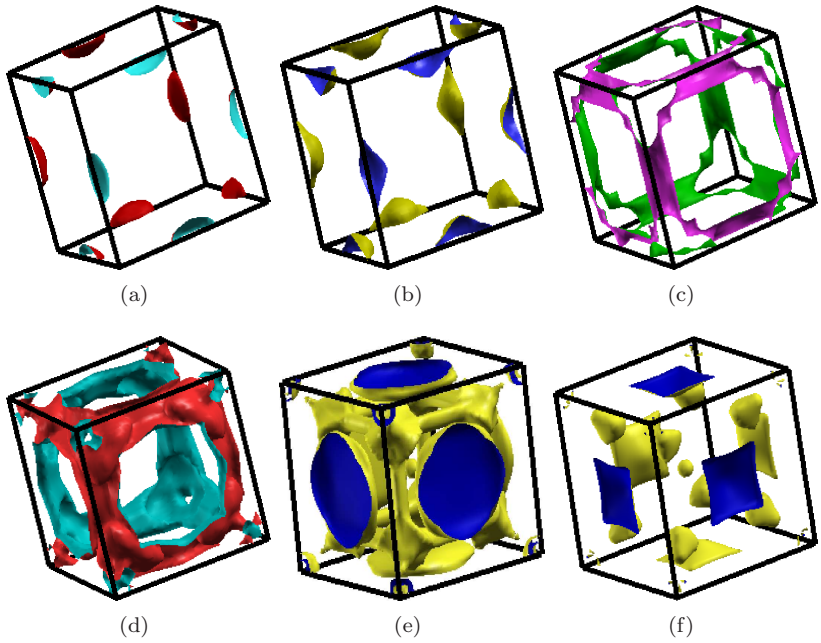

Figure 4.4: Fermi surface for Nb_3Al at ambient conditions (a) band no. 45, (b) band no. 46, (c) band no. 47, (d) band no. 48, (e) band no. 49 and (f) band no. 50. The first four FS are having hole nature and remaining two are having electron nature. The first two FS are having pockets at M points. The next two FS are having ribbon like sheets along BZ edges. The last two FS are having sheets in middle of the BZ faces with a pocket at Γ point.

at M is similar as Nb_3Ge and are also crossing the E_F at R point due to shifting of bands above E_F when compared to Nb_3Ge. The next two electronic natured bands in Nb_3Ge are crossing E_F at Γ, along R-X and at X. In addition to this, band 53 is crossing E_F along Γ-M and near R. In Nb_3Sn, these bands have similar behaviour as Nb_3Ge except near R point due to shifting of bands above the E_F at that point. In Nb_3Al, the calculated band structure properties agree well with reports by Rajagopalan [219], and for the remaining compounds our study is in good agreement with that of Paduani [235].

In Nb_3Os (Fig. 4.3(f)), we have observed four bands to cross E_F. First band (red coloured) cross E_F at M point from valence to conduction band with back bending camel back shape indicating hole nature. Second band (green coloured one) also has similar nature at M point with additional band crossings along R-X, Γ-X and X-M directions leading to complex hole nature with multiple band crossings. The remaining two bands have electron nature due to the bands crossing E_F from conduction to valence band. Third band (blue coloured) cross E_F both at Γ and R points and the last band cross only at Γ point. As we move from Nb_3Os to Nb_3Ir, one more '*d*' electron is added resulting in increased number of conduction electrons. Due this, E_F will shift towards the conduction region compared to Nb_3Os. In Nb_3Ir(Fig. 4.3(g)), we have four bands to cross the E_F where first two have hole nature and remaining two are of electron nature. First band (red coloured) cross E_F only along R-X and the second band cross E_F along R-X, X-M, M-Γ and M-R indicating a complex hole nature. Third band cross E_F at Γ and M points and the remaining one is crossing the E_F only along Γ-X direction. In the case of Nb_3Pt (Fig. 4.3(h)) we have two more free electrons

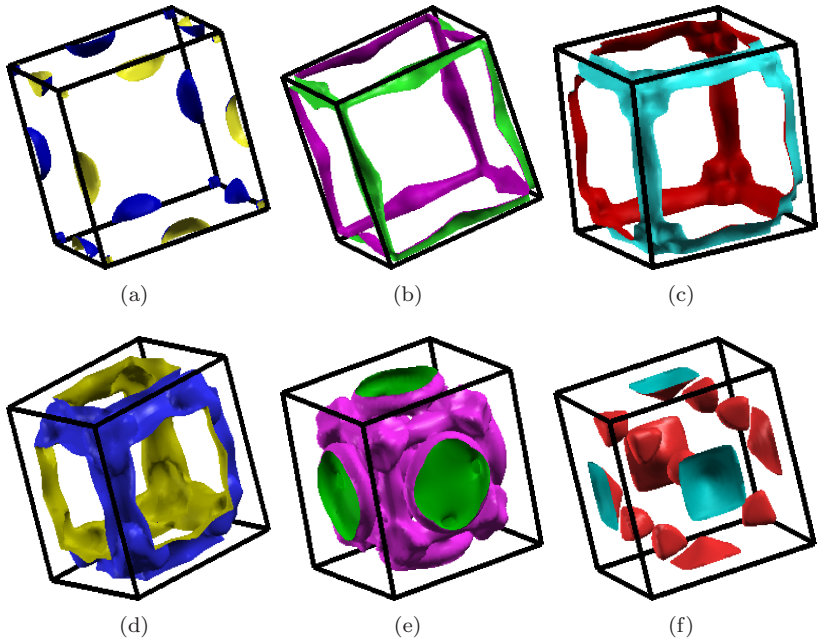

Figure 4.5: Fermi surface for Nb_3Ga at ambient conditions (a) band no. 49, (b) band no. 50, (c) band no. 51, (d) band no. 52, (e) band no. 53 and (f) band no. 54. The first four FS are having hole nature and remaining two are having electron nature. The first FS is having pockets at M points and BZ corners. The next three FS are having ribbon like sheets along BZ edges. The last two FS are having sheets in middle of the BZ faces with a pocket at Γ point.

compared to Nb_3Os which are due to Pt which have two more 'd' electrons compared to Os. The number of bands to cross E_F in Nb_3Pt is the same as in remaining Nb_3Os and Nb_3Pt compounds except for the increase in the electronic nature of bands. In Nb_3Pt, we have observed one hole and three electron nature bands across the E_F. First band (red coloured) cross the E_F around R point which is having hole nature and the remaining three bands cross E_F at X point and are having electronic nature. In this compound, at E_F, we have also observed camel's back shape at X point due to the bands which are indicated with blue and violet colours. In the band structure topology, this feature leads to high density of states at that point which have strong effect on the ground state properties [237, 238]. In Nb_3Pt, this feature may lead to high density of states compared to Nb_3Os and Nb_3Ir compounds. For Nb_3Os, Nb_3Ir and Nb_3Pt compounds available superconducting transition temperature(T_c) values are around 0.94, 1.76, 10 K respectively [103] and the calculated $N(E_F)$ values are 6.35, 6.07, 11.04 states/eV/f.u. respectively, indicating T_c to almost follow the $N(E_F)$ trend in these compounds, while for the remaining compounds this nature is not observed.

The behaviour of the metal at the Fermi level can be known by visualising the Fermi surface and its shape. To understand more about the present compounds near Fermi level we have calculated the FS for all the compounds and the FS topology is given from Fig. 4.4 to Fig. 4.11. The number of Fermi surfaces are equal to the number of bands crossing the E_F for a particular compound. In the case of Nb_3Al first four FS are having hole nature and among them first two FS have pockets at M point (Fig. 4.4(a,b)) due to bands crossing the E_F only at this point. The next two FS (Fig. 4.4(c,d)) are due to the bands (47, 48) crossing E_F both at M and along R-X. Due to this

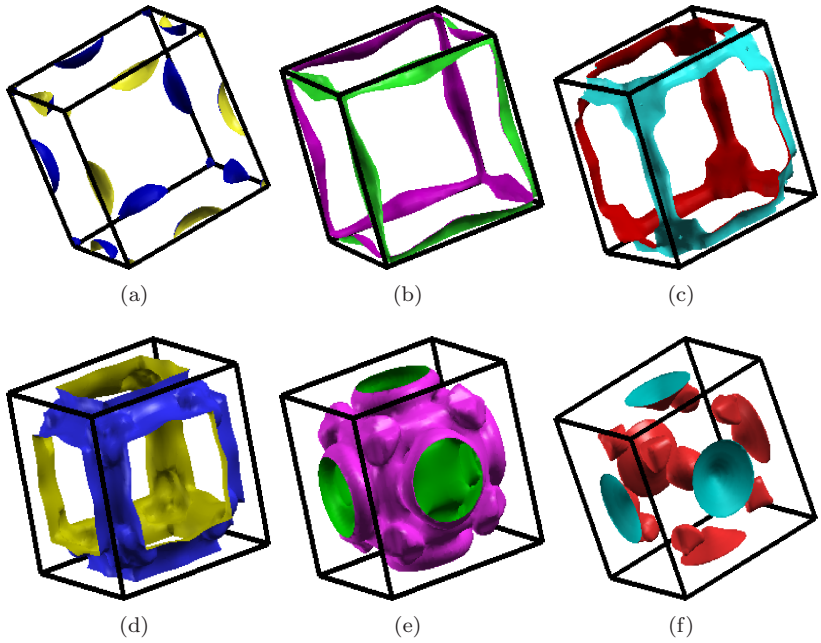

Figure 4.6: Fermi surface for Nb_3In at ambient conditions (a) band no. 49, (b) band no. 50, (c) band no. 51, (d) band no. 52, (e) band no. 53 and (f) band no. 54. The first four FS are having hole nature and remaining two are having electron nature. The first FS has pockets at M points and BZ corners. The next three FS are having ribbon like sheets along BZ edges. The last two FS are having sheets in middle of the BZ faces with a pocket at Γ point.

we have sheet like FS along M-R and the last two FS are having electron nature. In these last two FS, we have pockets at Γ, R, X and along R-X due to the crossing of the two bands (49, 50) at these high symmetry points as discussed in band structure. In the case of Nb_3Ga and Nb_3In, we have observed the presence of pocket/sheet at/near R point in the first three FS and absence of pockets at same R point in the remaining three FS as compared to Nb_3Al which might be due to the shifting of bands above the E_F as discussed before and the corresponding FS are shown in Fig. 4.5 and 4.6. In these two compounds the first FS is similar to Nb_3Al except having an extra pocket at R point. The next two FS are having ribbon like sheet along R-M which is due to the bands (50, 51) continuously residing in the conduction band. Remaining three FS in these two compounds are similar to Nb_3Al except for the absence of pockets at R points (Fig. 4.5(d, e, f) and Fig. 4.6(d, e, f)). When we move from IIIA to IVA group elements (Nb_3Ga to Nb_3Ge and Nb_3In to Nb_3Sn), decrease in the width and length of sheet near M point in hole natured FS (first four FS) is observed which is due to the shifting of bands below E_F which will cause the reduction in the area of bands in the conduction region. In the case of electron natured FS, an opposite trend is observed due to increase in the area of bands in valence region. A drastic change in FS topology is revealed in these two FS, resulting from an extra electron of IVA elements in these compounds. In the case of Nb_3Ge (FS in Fig. 4.7), hole natured FS have pockets only at M point due to the bands (49 to 52) as discussed in band structure. In the case of Nb_3Sn(FS in Fig. 4.8), these FS have extra pockets at R due to the shifting of bands above E_F. Last two FS in both of the superconducting compounds have electronic nature due to bands (53, 54) crossing E_F from conduction to valence band as discussed in the band

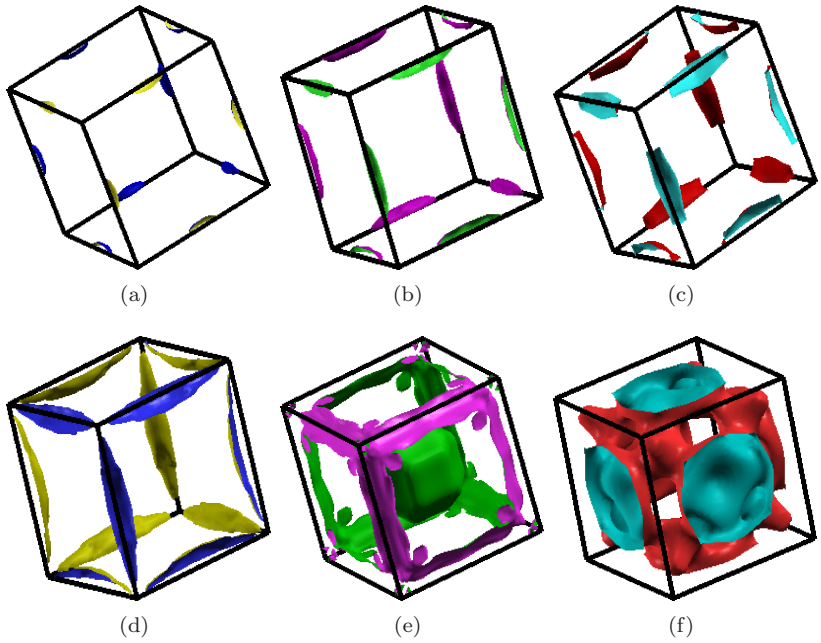

Figure 4.7: Fermi surface for Nb_3Ge at ambient conditions (a) band no. 49, (b) band no. 50, (c) band no. 51, (d) band no. 52, (e) band no. 53 and (f) band no. 54. The first four FS are having hole nature and remaining two are having electron nature. First four FS are having pockets at M points. Next FS has ribbon like sheets along BZ edges with a pocket at Γ point. The last FS has sheets in middle of the BZ faces with a pocket at Γ point.

structure. From Fig. 4.9, where the FS are given for Nb_3Os, the first FS have simple hole pockets at M point and the second one have complex hole FS. The remaining two FS have electron nature with large pockets around the Γ point (in both FS) and at R (only in third FS). As we move from Nb_3Os to Nb_3Ir, the E_F is found to shift towards the conduction region. Due to this the FS as shown in Fig. 4.9(a) is found to be absent in Nb_3Ir and the complex FS as shown in Fig. 4.9(b) transform to be a simple one as shown in Fig. 4.10(a) with some small hole pockets along R-X. The FS as shown in Fig. 4.9(c) is elongated in all directions with openings at X and R points as shown in Fig. 4.10(b). The FS as shown in Fig. 4.9(d) will remain almost similar with increase in the size with additional electron pockets at M point as shown in Fig. 4.10(c). In comparison with Nb_3Os, we have additional FS as shown in Fig. 4.10(d) with small electron pockets along Γ-X point. As we move from Nb_3Ir to Nb_3Pt the FS topology is completely changing except for the number of FS. The First FS (Fig. 4.11(a)) have hole pockets at R point and the remaining FS have pockets at X point. From Fig. 4.11(c) and 4.11(d), it is observed that the FS have plate like parallel shapes with wider and small areas respectively. The calculated FS are in good agreement with the Paduani's [235] study but in the case of Nb_3Ge, the author's found only five Fermi surfaces, but in our calculations we have six FS corresponding to six bands crossing the E_F [235]. From the FS of the investigated compounds, we observed hole pockets at M point in the first three FS of Nb_3Al, Nb_3Ge and Nb_3Sn and in the remaining compounds it is observed only in the first FS. In addition to this, we have also observed parallel sheet like structures in the last two FS of all the compounds. This might indicate the probability of nesting at M and along X-Γ in all the compounds. Particularly in Nb_3Al (FS for

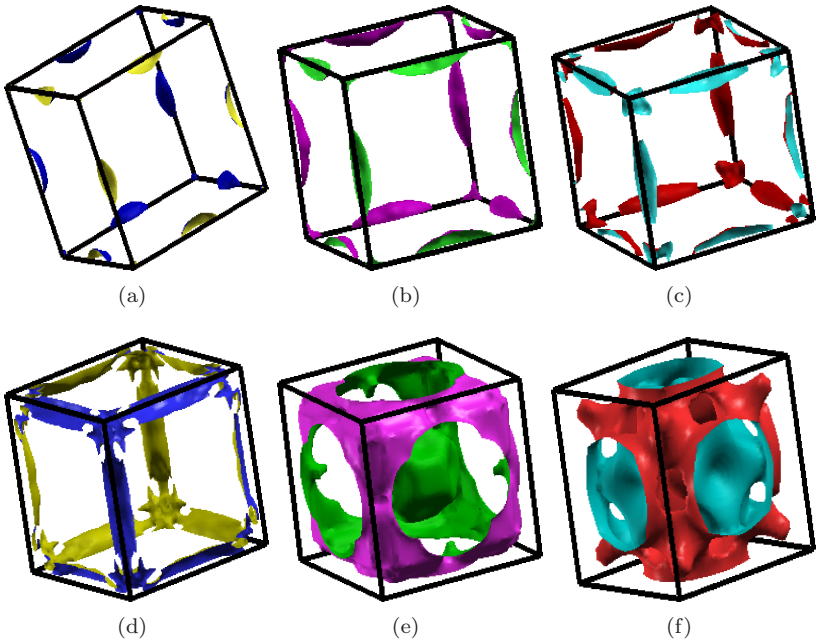

Figure 4.8: Fermi surface for Nb_3Sn at ambient conditions (a) band no. 49, (b) band no. 50, (c) band no. 51, (d) band no. 52, (e) band no. 53 and (f) band no. 54. The first four FS are having hole nature and remaining two are having electron nature. First three FS are having pockets at M points and corners of the BZ. Fourth FS has ribbon like sheets along BZ edges. Fifth FS is having sheets along BZ edges with a pocket at Γ point. The last FS is having sheets in middle of the BZ faces with a pocket at Γ point.

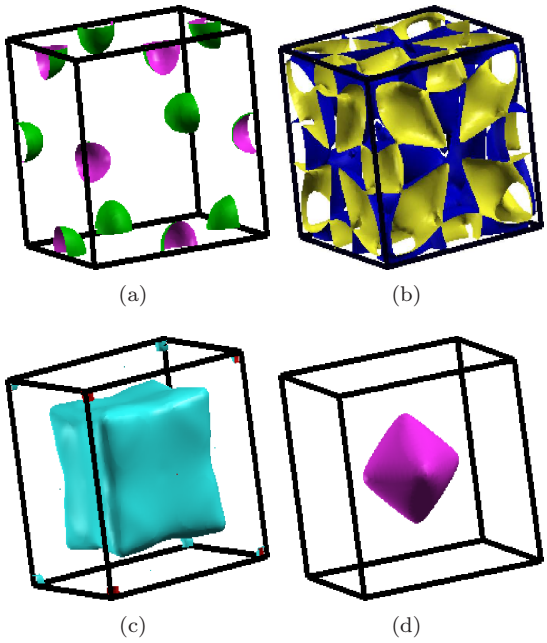

Figure 4.9: Fermi surface for Nb_3Os at ambient conditions (a) band no. 131, (b) band no. 133, (c) band no. 135, (d) band no. 137. The first two FS are having hole nature and remaining two are having electron nature. The first FS has simple pockets at M points. The second FS has complex hole sheets. The third FS has pockets at R and Γ points and the last FS has electron pocket only at Γ point.

band no. 49 (Fig. 4.4(e))), Nb_3Ga (FS for band no. 53 (Fig. 4.5(e))), Nb_3In (FS for band no. 53 (Fig. 4.6(e))) and Nb_3Pt (FS for band no. 141 (Fig. 4.11(c))) we observed the nesting feature along X-Γ.

To confirm this nesting feature, we have calculated the Lindhard susceptibility for all the investigated compounds and are given in Fig. 4.12. In the case of Nb_3Y(Y= Al, Ga, In, Ge, Sn), from the imaginary part of susceptibility plots, we have observed peaks at M point and along X-Γ in all the compounds indicating the nesting feature at these points. In all the compounds, the peak at M point in $\mathrm{Im}(\chi_0)$ is due to the hole pockets at M point in the FS. The remaining peaks along X-Γ are due to the last two FS which are having electronic nature in all the compounds. From the calculated real part of susceptibility plots, we have not observed any peaks except for Nb_3Sn where one sharp peak is observed at R point. One can speculate this as the probability for the CDW formation in Nb_3Sn as reported experimentally by Escudero et al [226]. In the case of Nb_3Os, Nb_3Ir and Nb_3Pt compounds Lindhard susceptibilities are calculated along Γ-X. In the case of Nb_3Os (Fig. 4.12(f)), a peak in the real and imaginary parts is observed at 'q' vector around $(0.25, 0, 0)2\pi/a$ indicating the nesting feature in this compound. Similarly, we have observed peaks in the imaginary part of susceptibility in Nb_3Pt (Fig. 4.12(h)) at 'q' vectors $(0.28, 0, 0)2\pi/a$ and $(0.44, 0, 0)2\pi/a$ respectively.

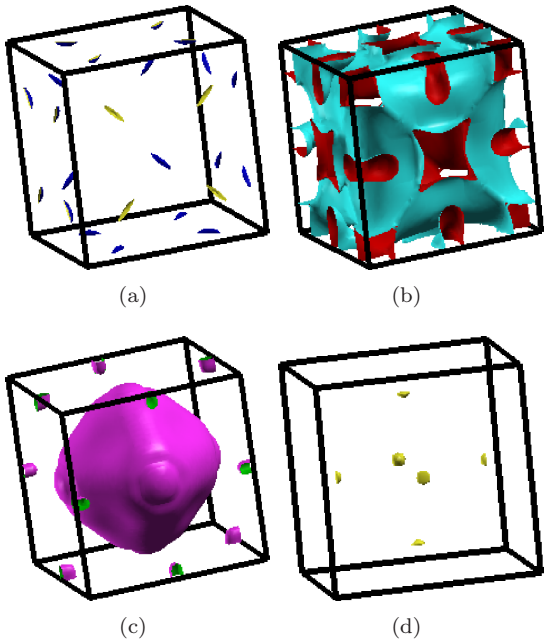

Figure 4.10: Fermi surface for Nb_3Ir at ambient conditions (a) band no. 133, (b) band no. 135, (c) band no. 137, (d) band no. 139. The first FS has hole nature with small pockets along R-X and the remaining three FS are having electron nature. Second FS has complex nature. Third FS has big electron pocket around Γ with additional pockets at M points. Last FS has small pockets at X point.

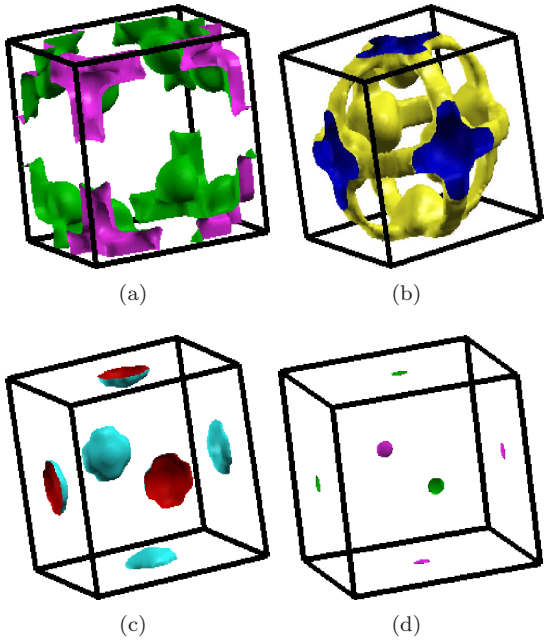

Figure 4.11: Fermi surface for Nb_3Pt at ambient conditions(a) band no. 137, (b) band no. 139, (c) band no. 141, (d) band no. 143. The first FS has hole nature and remaining three are having electron nature. The first FS has pockets at R points. The second FS is having pockets around X points connecting each other. Last two FS are having electron pockets only at X points.

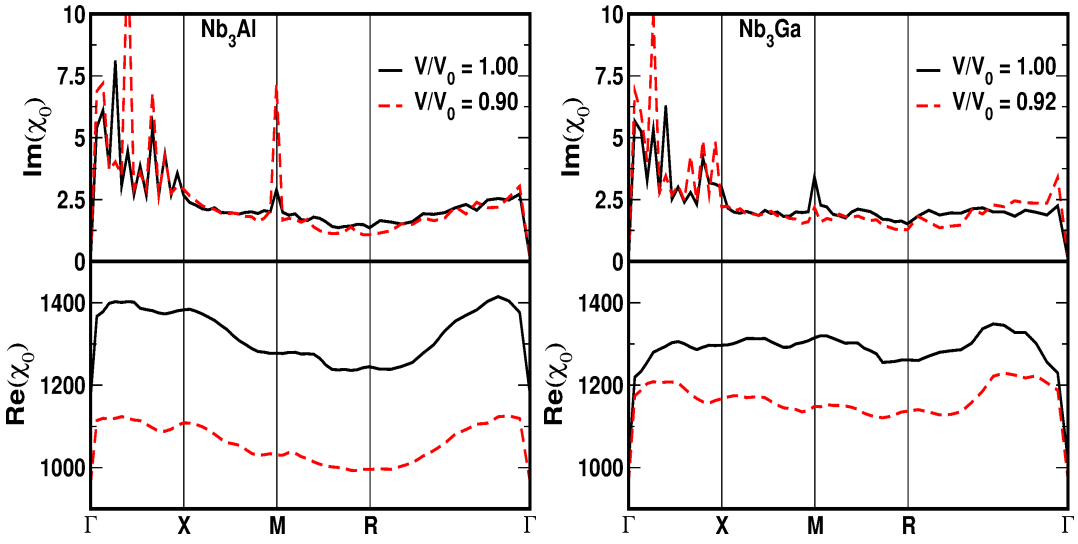
Nb3Al
V/V0 = 1.00
V/V0 = 0.90
Im(χ0)
Re(χ0)
Γ X M R Γ

(a)

Nb3Ga
V/V0 = 1.00
V/V0 = 0.92
Im(χ0)
Re(χ0)
Γ X M R Γ

(b)

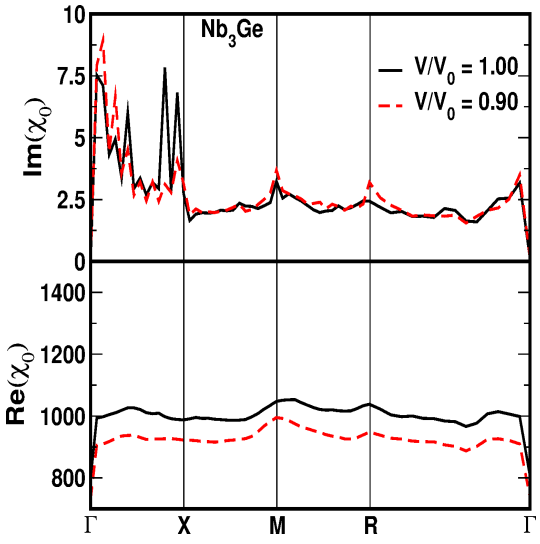
Nb3Ge
V/V0 = 1.00
V/V0 = 0.90
Im(χ0)
Re(χ0)
Γ X M R Γ

(c)

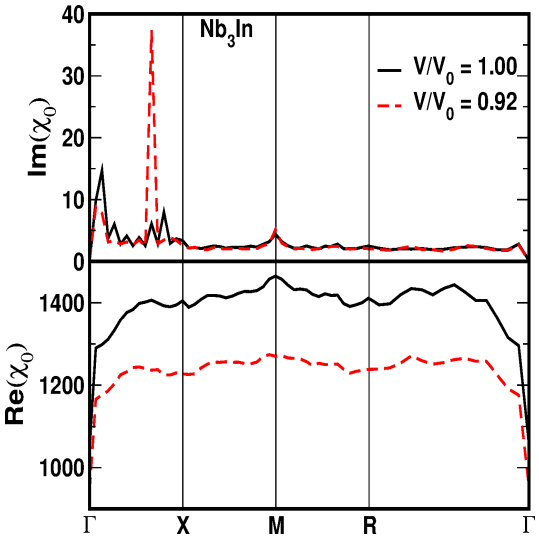
Nb3In
V/V0 = 1.00
V/V0 = 0.92
Im(χ0)
Re(χ0)
Γ X M R Γ

(d)

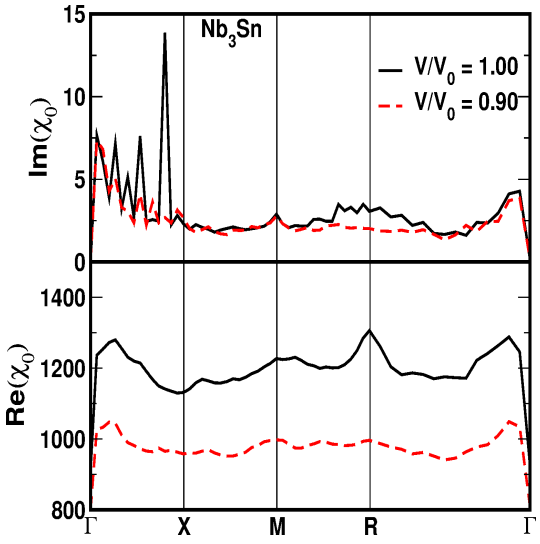
Nb3Sn
V/V0 = 1.00
V/V0 = 0.90
Im(χ0)
Re(χ0)
Γ X M R Γ

(e)

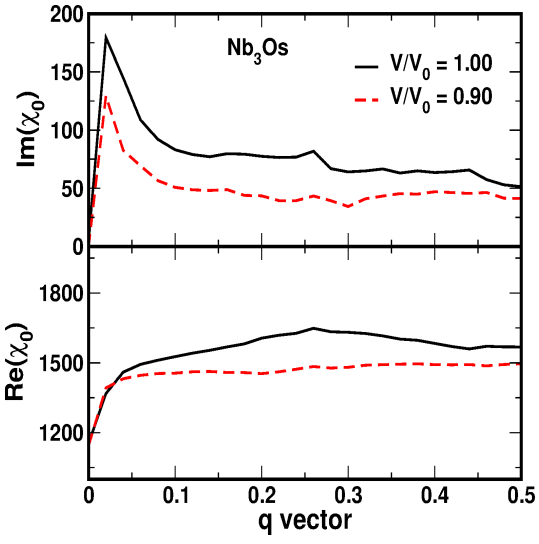
Nb3Os
V/V0 = 1.00
V/V0 = 0.90
Im(χ0)
Re(χ0)
q vector

(f)

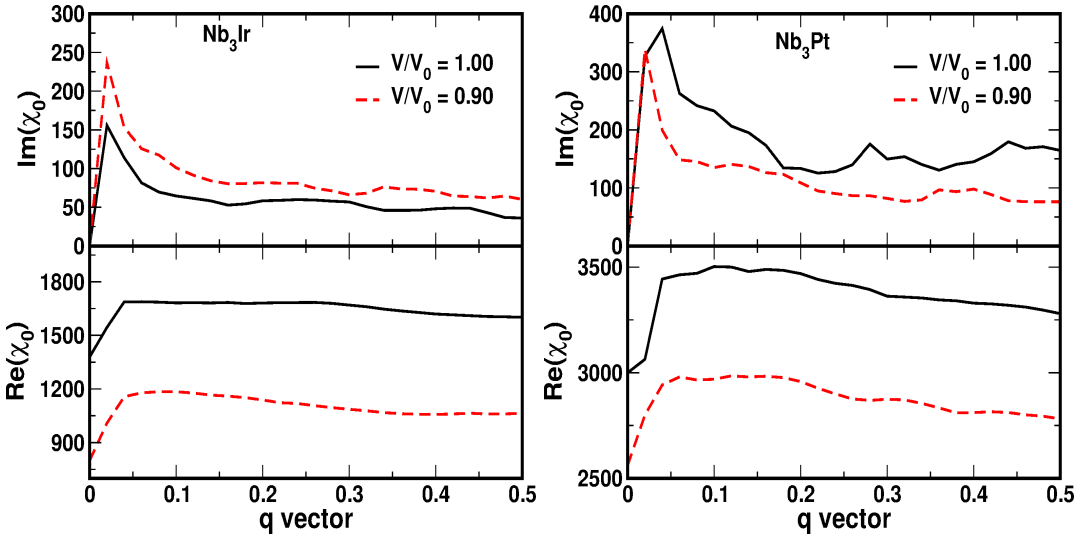

(g) (h)

Figure 4.12: Real and imaginary parts of Lindhard susceptibility plots for (a) Nb_3Al, (b) Nb_3Ga, (c) Nb_3Ge, (d) Nb_3In and (e) Nb_3Sn (f) Nb_3Os, (g) Nb_3Ir and (h) Nb_3Pt respectively.

4.4 Pressure effect on the electronic structure and elastic constants

Pressure effect on the band structure and the FS topology is studied in this section. We have observed a continuous FS topology change in all the investigated compounds under compression. In the case of Nb_3Al, major change in the band structure is found along R-X direction which is due to continuous shifting of bands below the E_F with applied pressure. Due to this, a continuous change in the FS topology is found in Nb_3Al up to the applied pressure. The changes are also reflecting in the calculated elastic constants and density of states under compression. We have given the band structure and maximum topology changed FS of Nb_3Al at $V/V_0 = 0.90$ in Fig. 4.13. The bands related to these changes are 47, 48 and 49. The major changes occurred along the X-R direction of the BZ where band no 47 and 48 descend through Fermi level under pressure causing destruction of Fermi sheets along this direction. Above this compression, FS at X point is completely vanishing in this compound. From the calculated imaginary part of the susceptibility at this compression, we observe huge peaks at M point and at q=(0,0.2,0)$2\pi/a$ indicating the pronounced nesting feature at this compression compared to ambient where the height of these peaks is very less. At M point it is due to the FS change observed in band 47 at this compression, where we find flat sheet at M point in the FS, but this flatness of this sheet is absent at ambient.

In the case of Nb_3Ga, maximum change in the band structure is observed along M-R and R-X continuously with applied pressure due to the bands 50, 51 and 53 shifting below E_F with applied pressure upto V/V_0=0.90 which results in maximum change in the FS topology. Above this pressure band 52 is also found to contribute more for the FS topology change. For Nb_3Ga, complete band structure at V/V_0=0.92 is given in Fig. 4.14. From these figure, we observed that the bands 50 and 51 descend through Fermi level along M-R direction of the BZ under compression causing an ETT.

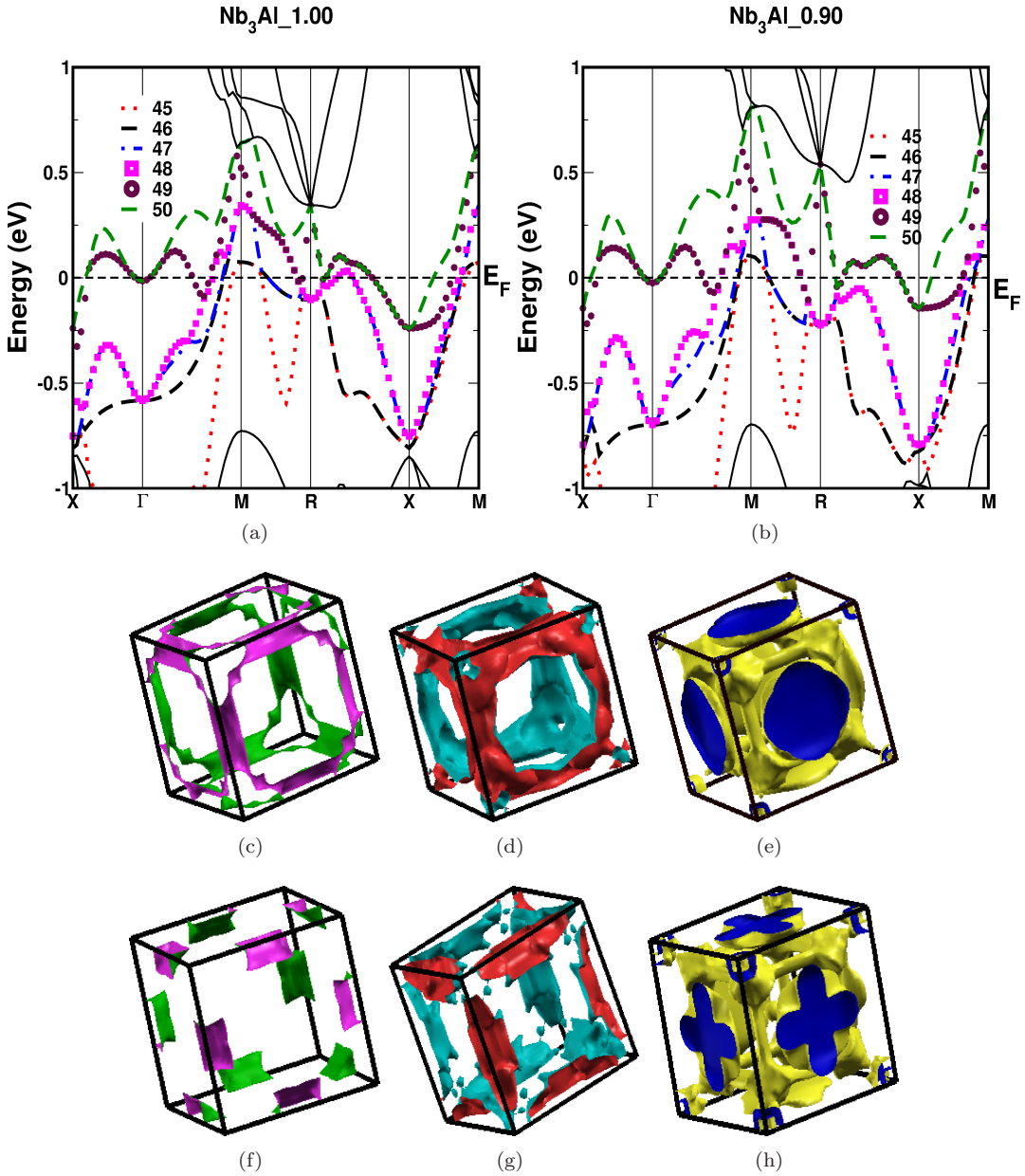

Figure 4.13: Band structure of Nb_3Al at (a) $V/V_0 = 1.00$, (b) $V/V_0 = 0.90$ (pressure around 21.5 GPa). (c), (d), (e) FS for band no. 47, 48 and 49 at $V/V_0 = 1.00$ and (f), (g), (h) FS for same bands at $V/V_0 = 0.90$ where change in FS topology is observed.

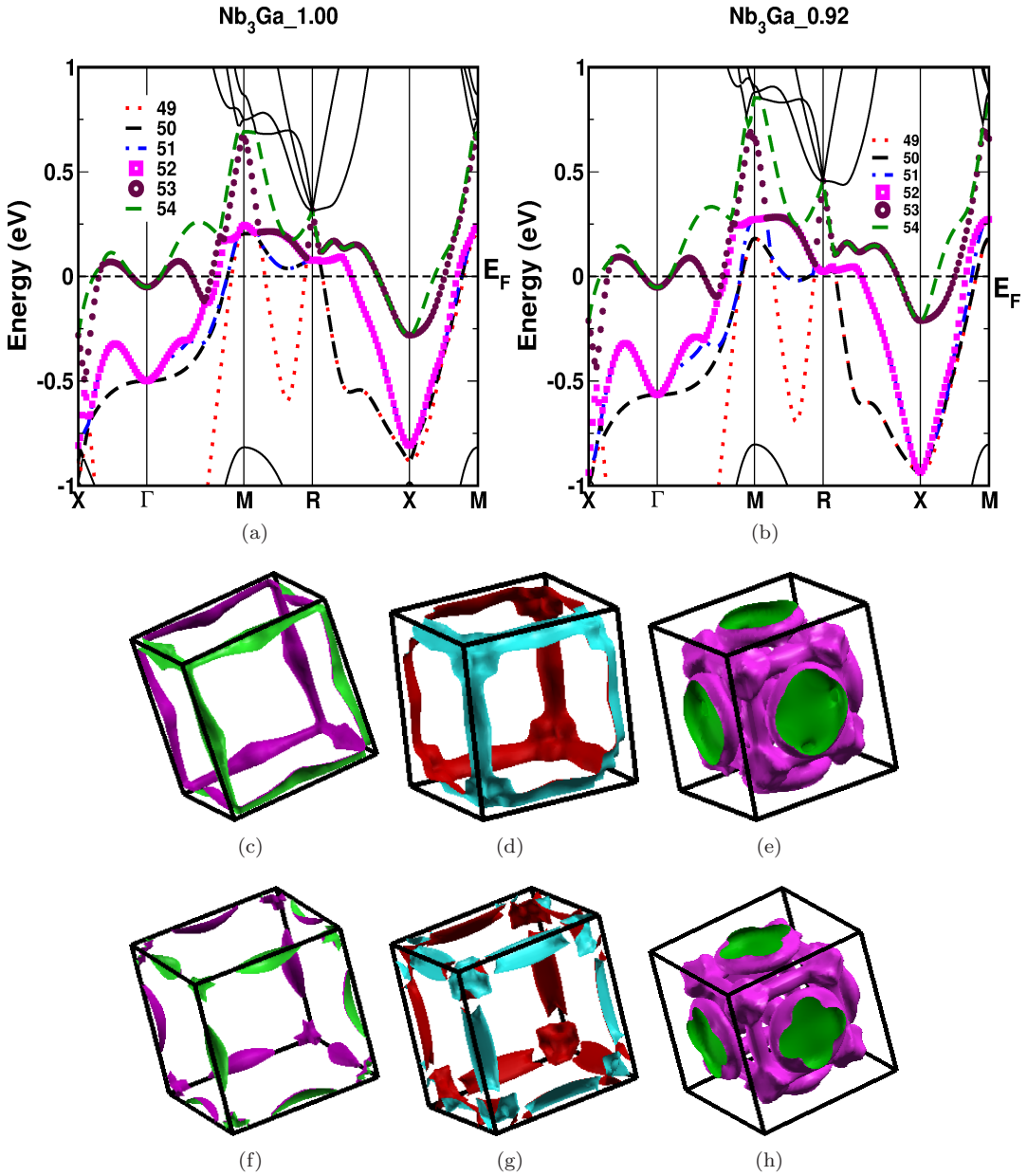

Figure 4.14: Band structure of Nb_3Ga at (a) $V/V_0 = 1.00$, (b) $V/V_0 = 0.92$ (pressure around 17.5 GPa). (c), (d), (e) FS for band no. 50, 51 and 53 at $V/V_0 = 1.00$ and (f), (g), (h) FS for same bands at $V/V_0 = 0.92$ where change in FS topology is observed.

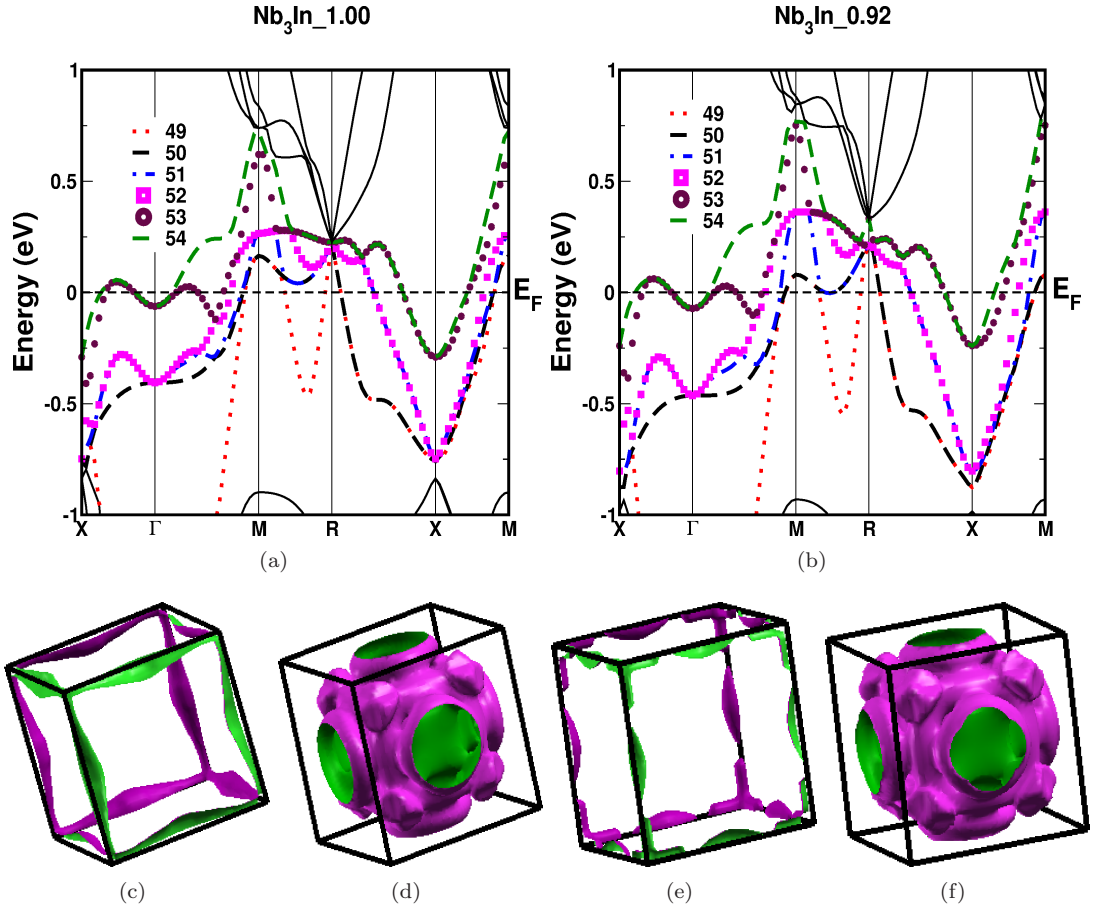

Figure 4.15: Band structure of Nb_3In at (a) $V/V_0 = 1.00$, (b) $V/V_0 = 0.92$ (pressure of 21 GPa). (c), (d) FS for band no. 50 and 53 at $V/V_0 = 1.00$ and (e), (f) FS for same bands at $V/V_0 = 0.92$ where change in FS topology is observed.

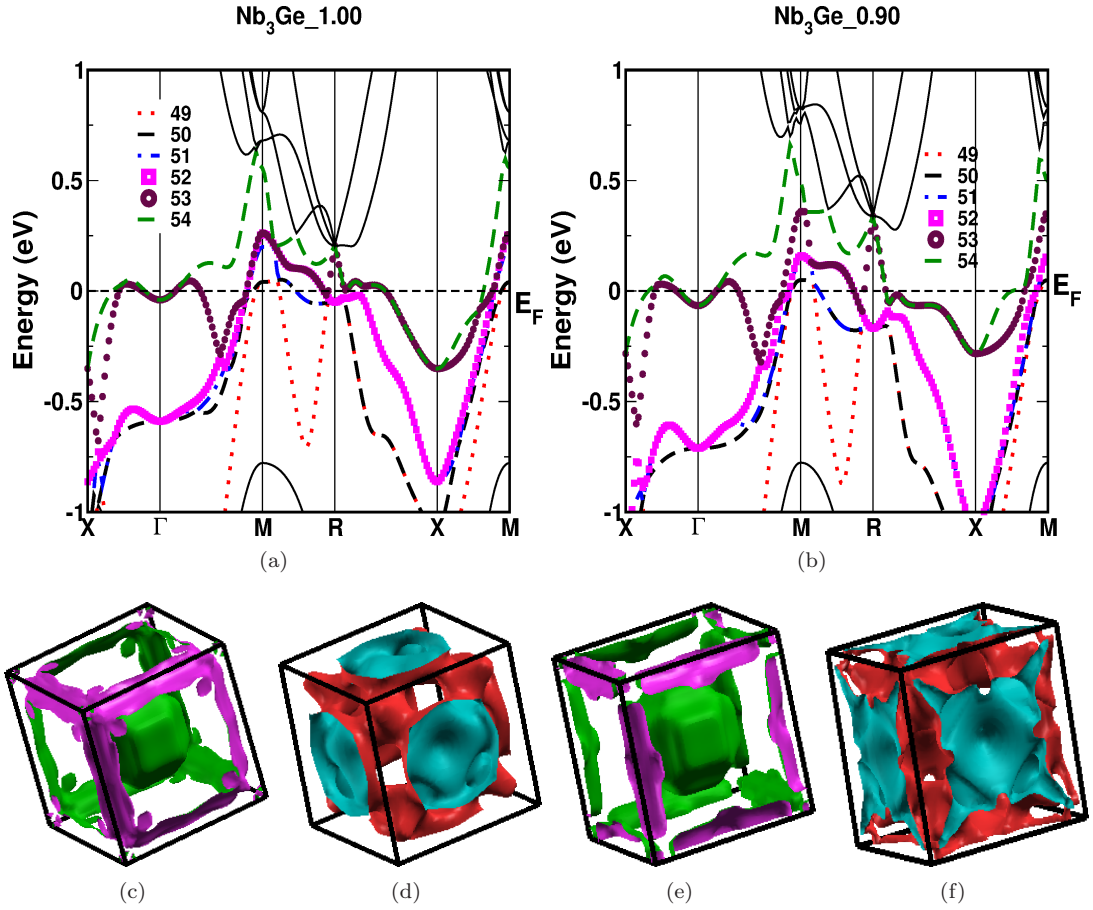

Figure 4.16: Band structure of Nb_3Ge at (a) $V/V_0 = 1.00$, (b) $V/V_0 = 0.90$ (pressure of 22.4 GPa). (c), (d) FS for band no. 53 and 54 at $V/V_0 = 1.00$ and (e), (f) FS for same bands at $V/V_0 = 0.90$ where change in FS topology is observed.

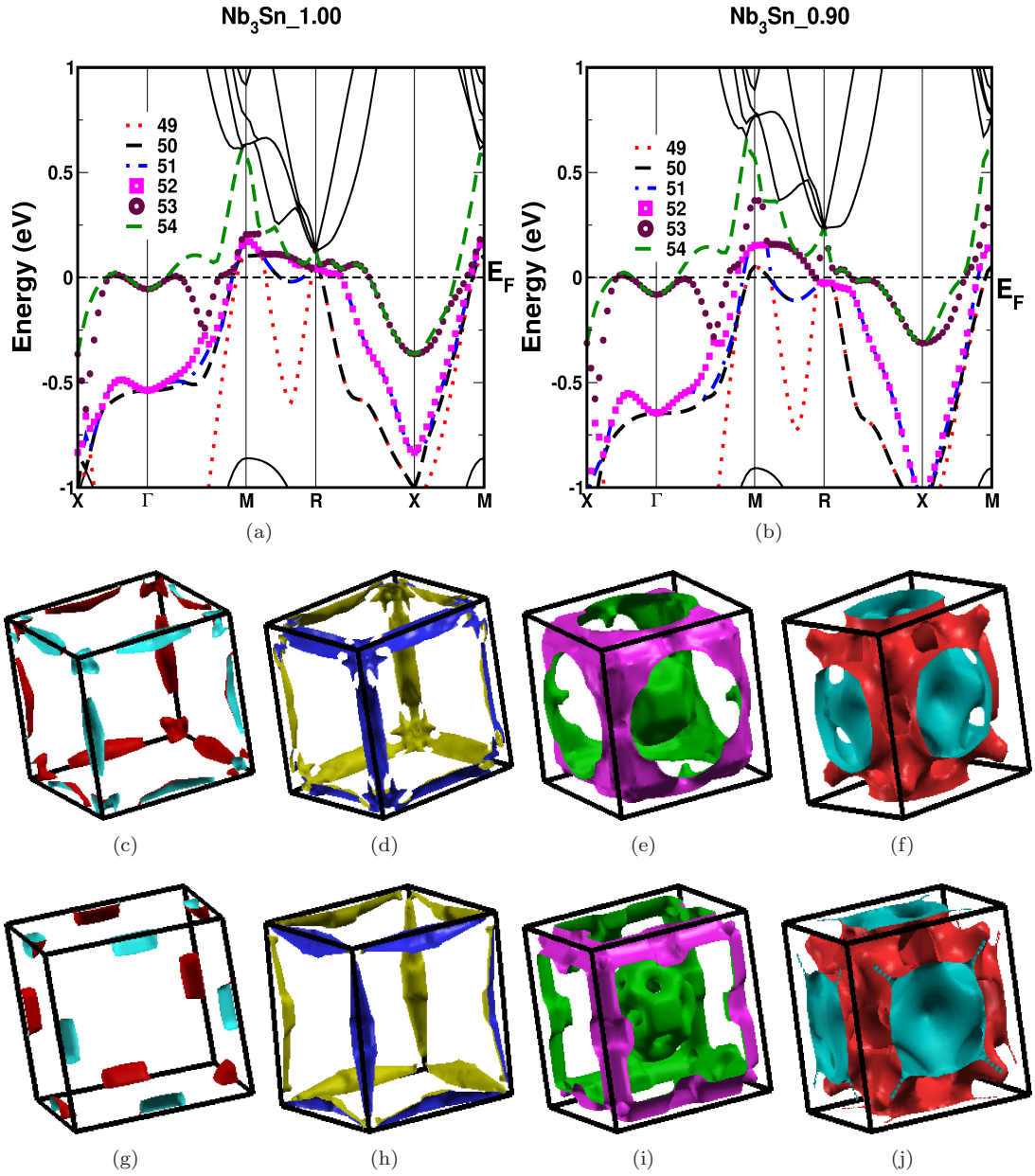

Figure 4.17: Band structure of Nb_3Sn at (a) $V/V_0 = 1.00$, (b) $V/V_0 = 0.90$ (pressure of 25 GPa). (c), (d), (e), (f) FS for band no. 51, 52, 53 and 54 at $V/V_0 = 1.00$ and (g), (h), (i), (j) FS for same bands at $V/V_0 = 0.90$ where change in FS topology is observed.

The ribbon like single Fermi sheets corresponding to band 50 and 51 parallel to M-R direction of BZ, now splitted into two due to destruction of its part under compression. The calculated susceptibility plots at this compression for Nb_3Ga show the similar behaviour as Nb_3Al except, for the point that at M point the FS nesting decreased and at q=(0,0.13,0)$2\pi/a$ it is found to increase. In the same way, pressure effect on the band structure of Nb_3In is also found to have more effect at M and along M-R. Upto V/V_0=0.90, pressure effect is more on the bands 50 and 51. Above this pressures remaining bands are also affected, especially at M point, where we find the first two bands to shift down completely leading to the absence of the FS sheets at M point. In Fig. 4.14 we have given the band structure of Nb_3In at V/V_0=0.92, where we observe the change in band structure along M-R. As in Nb_3Ga the ribbon like single FS parallel to M-R corresponding to band 50 is splitted in to two. The calculated imaginary part of susceptibility is found to increase a little at M point and more at q=(0,0.33,0)$2\pi/a$ indicating the increase of nesting feature.

In Nb_3Ge, effect of pressure on the band structure is found to be more along R-X where last two bands is found to shift continuously below the E_F. Due to these two bands (53 and 54), a continuous change in the FS topology is observed under pressure. To compare with ambient we have given the change in FS topology at $V/V_0 = 0.90$ in Fig. 4.16. At higher compression the FS nesting decreases in this compound as is evident from the imaginary part of susceptibility plot. In the FS corresponding to the band 53, we have observed changes in FS topology near R point at this compression which is due to the increase in the electron concentration at that point, which is evident from the band structure given in Fig. 4.16(b). In the case of Nb_3Sn, band structure topology is found to change continuously along M-R and R-X due to the bands 51, 52, 53 and 54 under pressure. Due to this a continuous change in the FS topology is found under pressure upto $V/V_0 = 0.90$. Above this pressures the number of bands crossing E_F is found to decrease from six to four. Band structure and FS of this compound at $V/V_0 = 0.90$ is given in Fig. 4.17. Bands 51 and 52 give rise to ETT near R point of the BZ around this compression as they descend through Fermi level leading to the destruction of Fermi sheets around R. Here also like Nb_3Ge, the decrease of nesting property of the Fermi surfaces is evident from the imaginary part of the susceptibility plot.

In Nb_3Os it is observed that E_F moves towards the valence region under compression. In this compound topology of band is not changed much but the change in the FS topology is observed in the first two FS starting from V/V_0=0.94 and for further compressions (see Fig. 4.18). In the case of Nb_3Ir we observed the absence of last FS and change in the topology of second and third FS at V/V_0=0.96 compared to ambient (see Fig. 4.19, here band structure is given at V/V_0=0.90 to observe the change) due to reduction in the number bands crossing E_F. Similarly, in Nb_3Pt (see Fig. 4.20) we have observed addition of one more FS which is having hole nature compared to ambient one and also the widening of the last FS is observed at the compression V/V_0=0.96.

Under compression, real part of susceptibility is found to decrease in all the compounds. In the case of Nb_3Sn, at R point, the peak observed at ambient conditions is found to be absent under compression. From the susceptibility plots, in Nb_3Os and Nb_3Pt both real and imaginary values are found to decrease, whereas in Nb_3Ir imaginary part is found to increase. In Nb_3Os, peak in imaginary part still sustain indicating the nesting feature at the same 'q' vector. Due to this FS topology change, we have observed the non-monotonic variation in the DOS under compression in all the compounds as shown in Fig. 4.21. In the case of Nb_3Os and Nb_3Pt we have observed a non-monotonic decrease in the total density of states under compression, but in the case of Nb_3Ir it

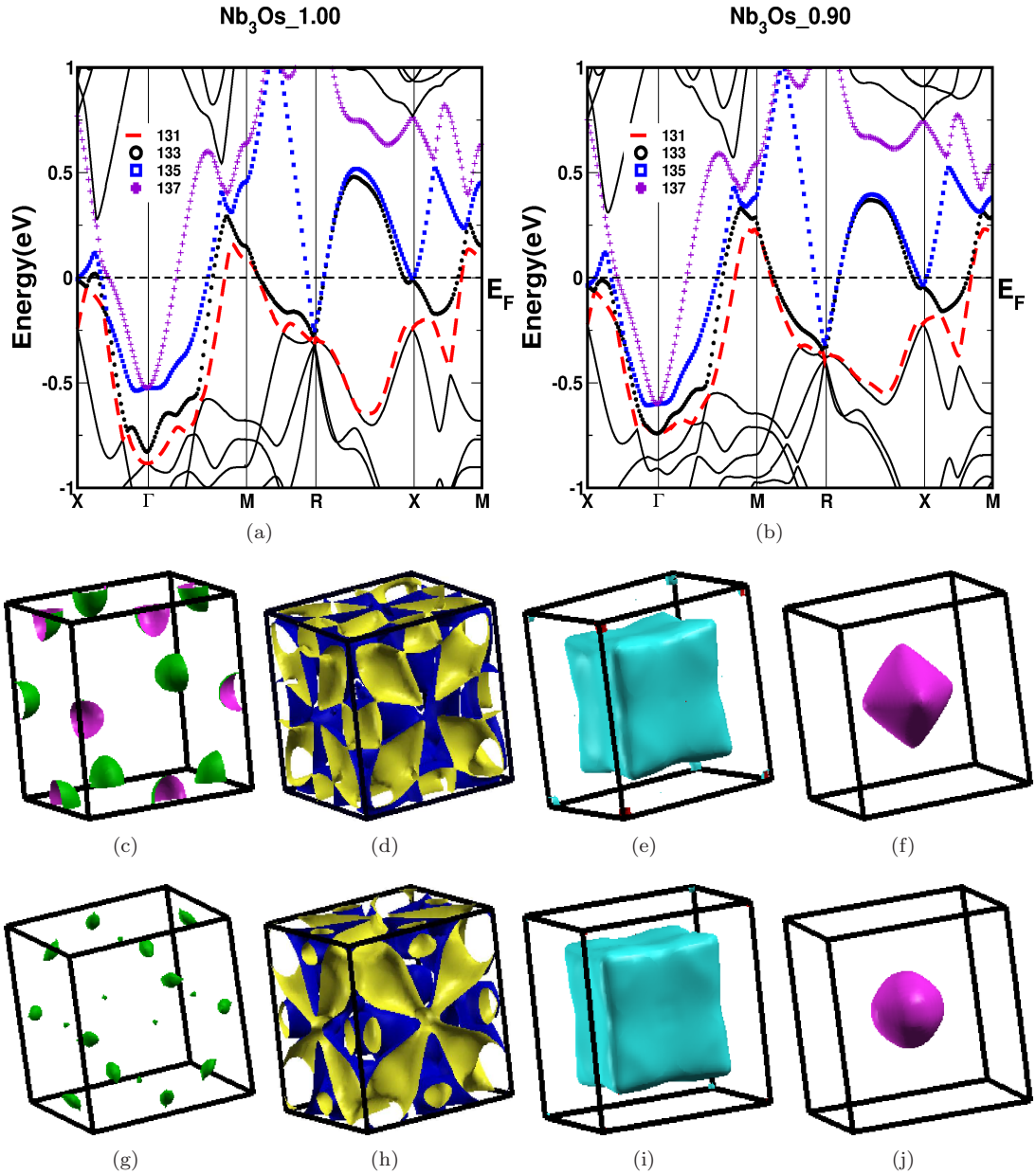

Figure 4.18: Band structure of Nb_3Os at (a) $V/V_0 = 1.00$, (b) $V/V_0 = 0.90$ (pressure of 25 GPa). (c), (d), (e), (f) FS for band no. 131, 133, 135 and 137 at $V/V_0 = 1.00$ and (g), (h), (i), (j) FS for same bands at $V/V_0 = 0.90$ where change in FS topology is observed.

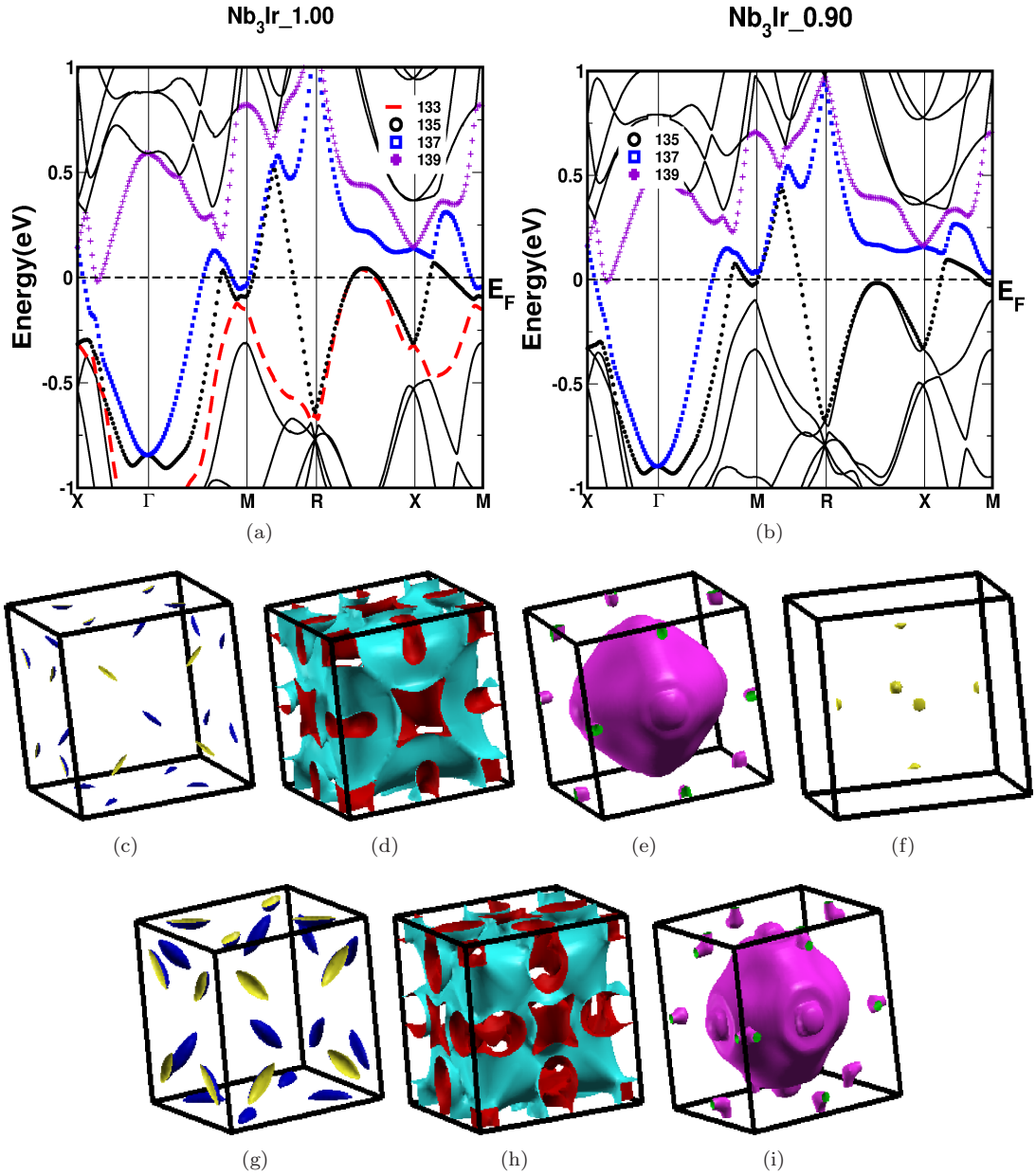

Figure 4.19: Band structure of Nb_3Ir at (a) $V/V_0 = 1.00$, (b) $V/V_0 = 0.90$ (pressure of 25 GPa). (c), (d), (e), (f) FS for band no. 133, 135, 137 and 139 at $V/V_0 = 1.00$ and (g), (h), (i) FS for same bands at $V/V_0 = 0.90$ where change in FS topology is observed.

is found to increase upto certain pressure and decrease at higher pressures.

Now to study the effect of ETT on equation of state(EOS) and elastic properties, we have calculated the EOS for Nb_3Al and Nb_3Ga, for which the experimental anomalies are observed, and pressure effect on the elastic constants for all the compounds is also computed. The study of P-V relation for Nb_3Al and Nb_3Ga is particularly important because earlier experiments [239, 228] observed an anomaly near 19.2 and 15 GPa respectively. Figure 4.22 shows the calculated P-V relation for these two compounds along with earlier experimental data. It is clear from the figure that the calculated P-V curve varies smoothly and there is no anomaly for both of these compounds. Since ETT is an subtle electronic transition, its effect on EOS is expected to be very weak and may be washed out during fitting [240]. However its effect may be pronounced in the pressure variation of elastic constants. Hence we have calculated elastic constants for these compounds at different pressures and are shown in Fig. 4.23. The calculated elastic shear modulus ($C_s = (C_{11}\text{-}C_{12})/2$) is also given under pressure. From the plots it is observed that values of elastic constants increase with pressure. The effect of pressure is observed to be more in C_{11} than in C_{44} in all the compounds. Under pressure non-linear variation in C_{11} and C_s is observed in all the compounds. Calculated C_{44} and C_s is found to have a non-linear variation and can be correlated with the observed ETT's under pressure and are shown along with the FS topology change. Recently [241], in Nb_3Sn a structural modification is found around 6 GPa but no structural phase transition is observed which is driven by phonon behaviour. In our study a small softening is observed in the C_{11}, C_{44} and C_s elastic constants around the same pressure indicating a ETT around this pressure in Nb_3Sn.

4.5 Conclusions

Electronic structure of Nb_3Y (Y = Al, Ga, In, Ge, Sn, Os, Ir and Pt) compounds was studied both at ambient conditions and under compression by using density functional theory calculations. In all the compounds it is observed that '*d*' states of Nb atoms has dominant nature at E_F with admixture of '*p*' or '*d*' sates of Y atom. All the compounds are found to possess both hole and electron FS. Parallel sheets are observed along X-Γ in the last two FS, which indicate the nesting property in these compounds which is also confirmed from the calculated Lindhard susceptibility plots, where sharp peaks are observed along X-Γ and at M point in the imaginary part of susceptibility plots in all the compounds at ambient conditions. Under compression continuous change in the FS topology is observed in all the compounds. For the given ETT's corresponding changes are observed under compression in the imaginary part of susceptibility and huge peaks are found along X-Γ and at M point in Nb_3Al. In Nb_3Ga and Nb_3In it is observed only along X-Γ. In Nb_3Ge, we have observed peaks at M, R and along X-Γ under compression. But in Nb_3Sn the peak is observed to decrease along X-Γ. The change in the band structure under compression lead to the non-monotonic variation in density of states. Mechanical stability of these compounds is also confirmed both at ambient conditions as well as under compression and non-linear nature in C_{44} and C_s is observed in all the compounds under pressure. Further experiments are needed to realise the continuous FS topology changes observed in these compounds.

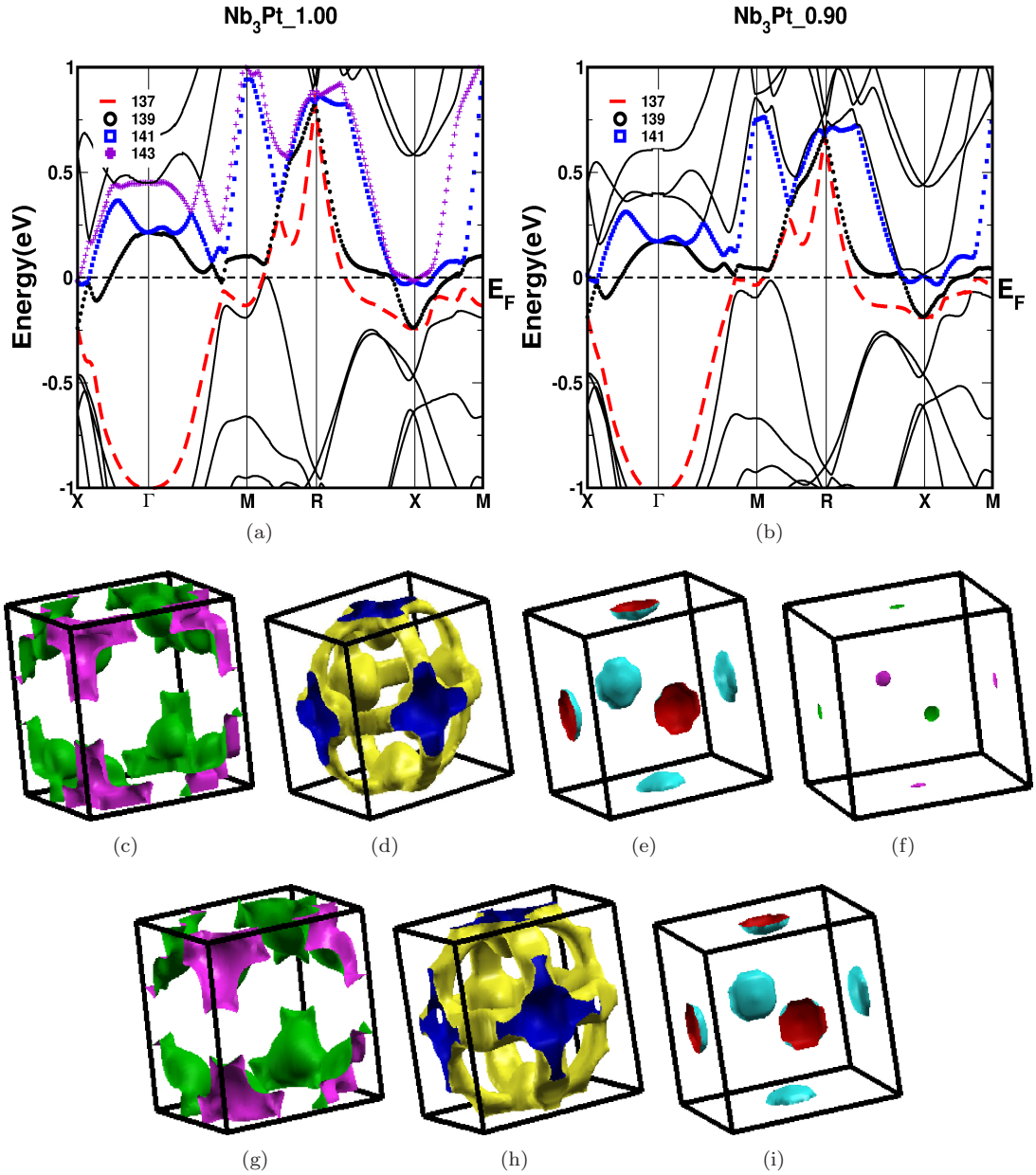

Figure 4.20: Band structure of Nb_3Pt at (a) $V/V_0 = 1.00$, (b) $V/V_0 = 0.90$ (pressure of 25 GPa). (c), (d), (e), (f) FS for band no. 137, 139, 141 and 143 at $V/V_0 = 1.00$ and (g), (h), (i) FS for same bands at $V/V_0 = 0.90$ where change in FS topology is observed.

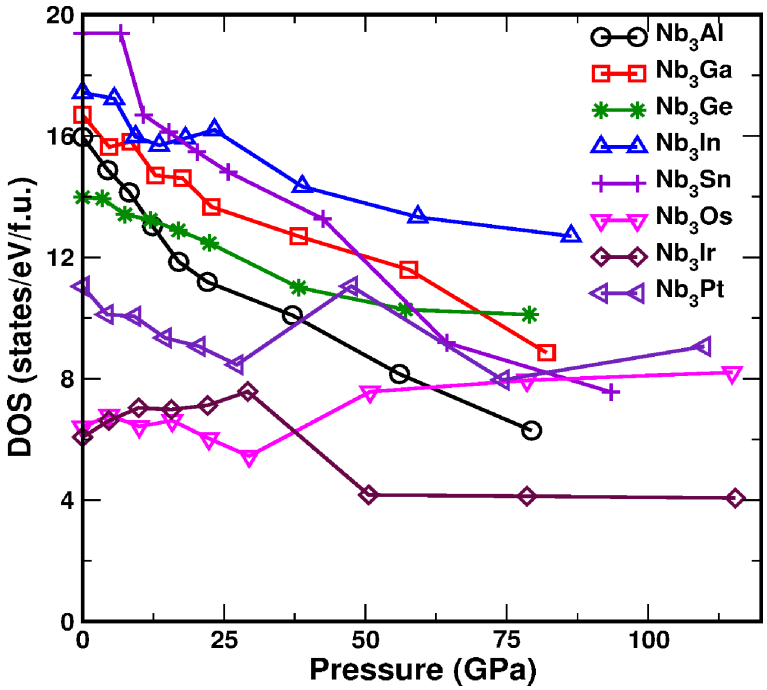

Figure 4.21: Total electronic density of states at E_F under compression.

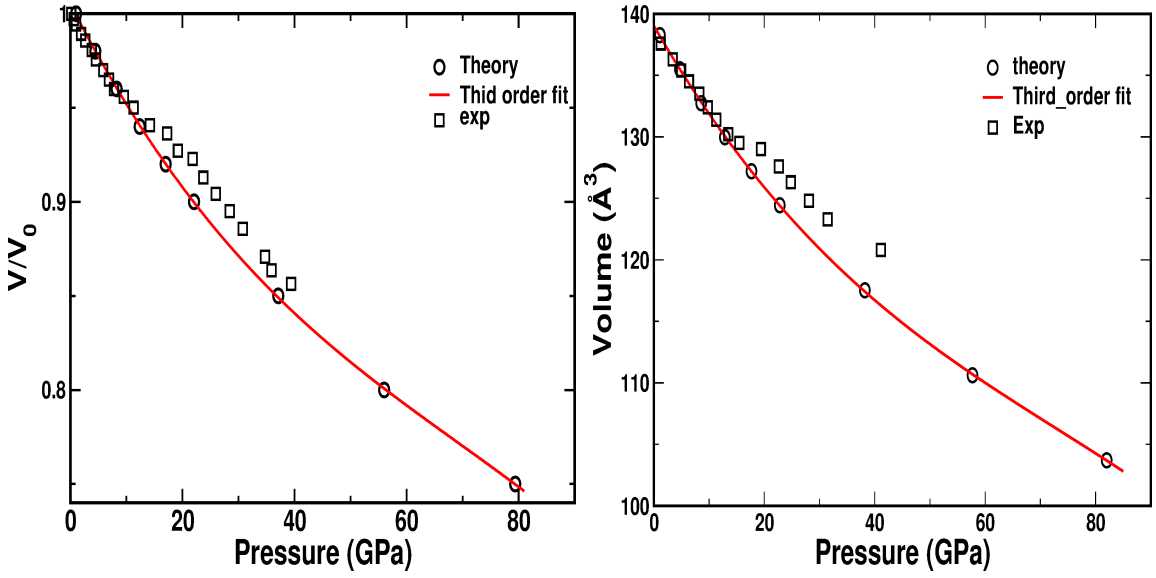

(a) (b)

Figure 4.22: (a) Variation of V/V_0 with respect to pressure in Nb_3Al and (b) variation of volume under pressure in Nb_3Ga. Here circles indicate theory values in this work, squares indicate the experimental values and solid line is a third order fit for the theoretical values.

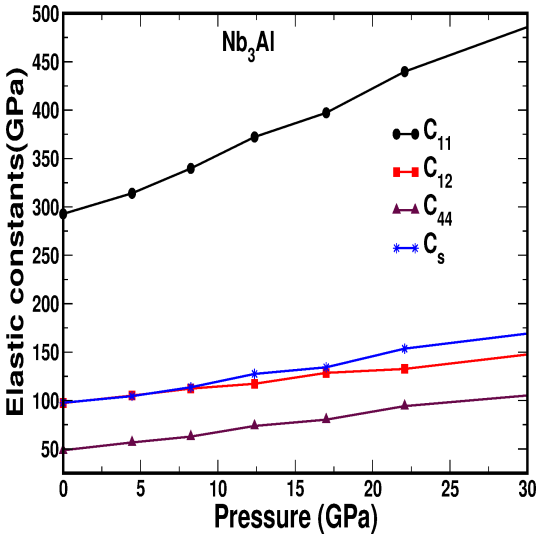
Nb3Al
Elastic constants(GPa)
Pressure (GPa)
C11
C12
C44
Cs

(a)

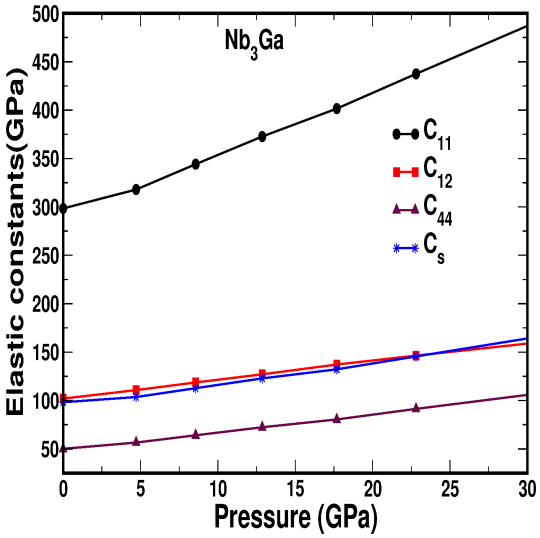
Nb3Ga
Elastic constants(GPa)
Pressure (GPa)
C11
C12
C44
Cs

(b)

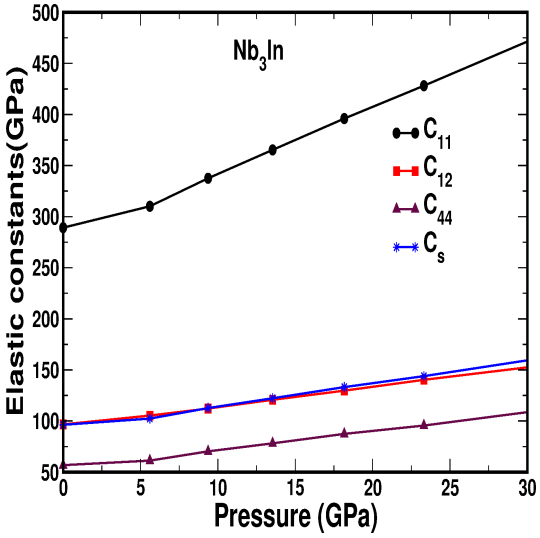
Nb3In
Elastic constants(GPa)
Pressure (GPa)
C11
C12
C44
Cs

(c)

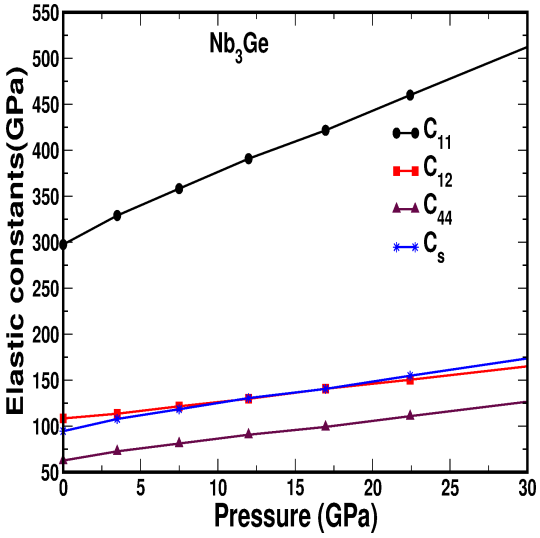
Nb3Ge
Elastic constants(GPa)
Pressure (GPa)
C11
C12
C44
Cs

(d)

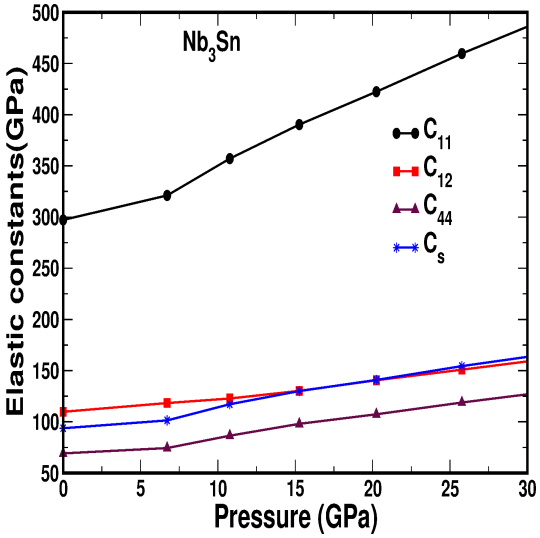
Nb3Sn
Elastic constants(GPa)
Pressure (GPa)
C11
C12
C44
Cs

(e)

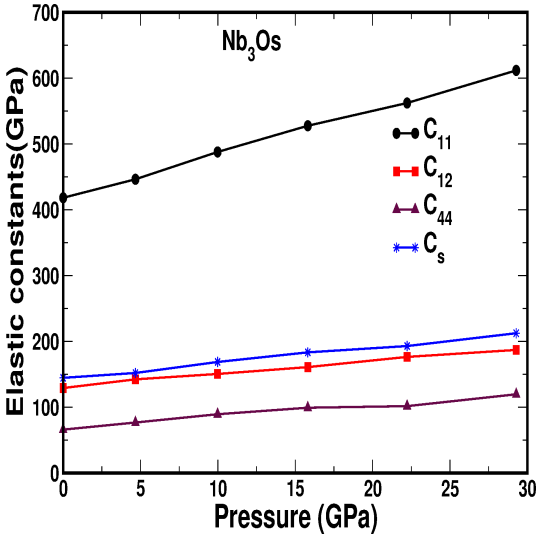
Nb3Os
Elastic constants(GPa)
Pressure (GPa)
C11
C12
C44
Cs

(f)

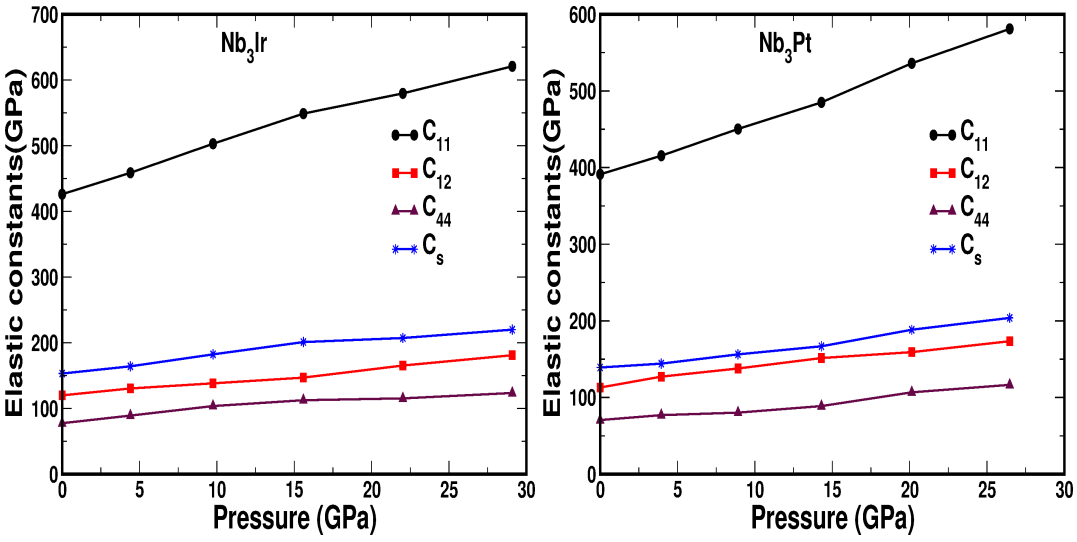

(g) (h)

Figure 4.23: Elastic constants under pressure for (a) Nb_3Al, (b) Nb_3Ga, (c) Nb_3In, (d) Nb_3Ge, (e) Nb_3Sn, (f) Nb_3Os, (g) Nb_3Ir and (h) Nb_3Pt respectively.

Table 4.1: Calculated lattice parameter a in Å, bulk modulus B in GPa, γ_{exp} and γ_{th} are experimental and theoretical Sommerfeld coefficient in the units of mJ/mol K^2, $N(E_F)$ is density of states at E_F in the units of states/eV/f.u. for Nb_3X (X= Al, Ga, In, Ge, Sn, Os, Ir and Pt) compounds.

Parameters	Nb_3Al	Nb_3Ga	Nb_3In	Nb_3Ge	Nb_3Sn	Nb_3Os	Nb_3Ir	Nb_3Pt
a_{exp}	5.187[a],	5.171[a],	5.303	5.166[a],	5.289	5.1348[m]	5.1333[m]	5.1524[m]
	5.185[b]	5.1674[c]		5.161[f]				
a_{the}	5.198,	5.183,	5.328	5.165,	5.322	5.160,	5.160,	5.180,
	5.210[d],	5.200[d],		5.185[d],		5.176[n]	5.1585[l]	5.1897[l]
	5.187[g],	5.171[g]		5.160[g]			5.0777[l],	5.1059[l],
	5.164[f]						5.177[n]	5.199[n]
B_{exp}	177[h]	198[c]	-	115[f]	-	-	-	-
B_{the}	158,	162,	152	172,	160,	227,	224,	207,
	156.33[d],	156.93[d],	152.71[i]	168.04[d]	160.51[i]	218.78[n]	227.433[l]	207[l]
	166.815[j],	169.97[i]					255.1[l],	236.9[l],
	165.49[i]						216.40[n]	201.76[n]
γ_{exp}	31.81[a],	-	-	-	-	-	-	-
	30[b]							
γ_{th}	37.63,	39.34	41.08	32.95	45.68	15.09,	14.32,	26.03,
	31.231[j]					12.2[n]	13.6[n]	31.44[n]
$N(E_F)$	15.96,	16.70,	17.44	13.98,	19.39	6.40,	6.07,	11.04,
	16.60[d],	18.23[d],		14.40[d],		7.05[n]	7.65[n]	13.48[n]
	14.64[g]	14.10[g],		7.84[g],				
		15.36[k]		14.39[k]				

a : Ref. [229]; b : Ref. [230]; c : Ref. [228]; d : Ref. [220]; f : Ref. [231]; g : Ref. [102]; h : Ref. [239]; i : Ref. [221];j : Ref. [219]; k : Ref. [235]; l : Ref. [233]; m : Ref. [232]; n : Ref. [234]

Table 4.2: Calculated single crystalline and poly crystalline elastic constants (in GPa) at ambient conditions for Nb_3X (X = Al, Ga, Ge, In, Sn, Os, Ir and Pt). Where E is Young's modulus (in GPa), G_H is Voigt-Reuss-Hill modulus, σ is Poisson's ratio, A is Anisotropy factor, CP = Cauchy's pressure (C_{11}-C_{44}) and PR = Pugh's ratio.

Parameters	Nb_3Al	Nb_3Ga	Nb_3In	Nb_3Ge	Nb_3Sn	Nb_3Os	Nb_3Ir	Nb_3Pt
C_{11}	273,	298,	289	297	297	418	426,	391,
	310.530[a],	305.41[b]					433.7[c],	377.7[c],
	310.53[b]						477.7[c]	424.2[c]
C_{12}	97,	102,	97	108	110	129	120,	113,
	92.976[a],	104.09[b]					123.7[c],	120[c],
	92.98[b]						144.9[c]	142.1[c]
C_{44}	49,	50,	57	63	69	66	77,	70,
	49.119[a],	48.78[b]					84.5[c],	60[c],
	57.12[b]						86.9[c]	62.4[c]
E	171,	175,	184	194	203	240	266,	242,
	179.486[a],	174.11[b]					279.7[c],	217[c],
	193.54[b]						295.7[c]	232.7[c]
A	0.49,	0.51,	0.59	0.51	0.74	0.456	0.506	0.507
	0.451[a],	0.485						
	0.525[b]							
CP	48.81,	51.84,	39.86	45.74	40.68	63.21	42.43,	42.44,
	43.857[a],	55.314[b]					39.2[c],	60[c],
	35.857[b]						58[c]	79.7[c]
PR	0.39	0.39	0.44	0.43	0.45	0.40	0.46	0.45
σ	0.36,	0.33,	0.31	0.66	0.30	0.322	0.300,	0.304,
	0.286[a],	0.30[b]					0.295[c],	0.324[c],
	0.27[b]						0.307[c]	0.336[c]

a : Ref. [219]; *b* : Ref. [221]; *c* : Ref. [233]

Chapter 5

Enhanced superconductivity in CsCl-type binary SnX(X=As and Sb) compounds

In the present chapter, first principles electronic structure calculations are performed using density functional theory for SnAs and SnSb. Total energy calculations show the first order phase transition from NaCl structure to CsCl one at around 37 GPa and 13 GPa for SnAs and SnSb respectively, which is also confirmed from enthalpy calculations and agrees well with experimental work. Calculations of the phonon structure and hence the electron-phonon coupling, $\lambda_{\rm ep}$, and superconducting transition temperature, T_c, across the phase transition are performed for both the compounds. These calculations give an ambient pressure T_c, in the NaCl structure, of 3.08 K and 3.08 K for both SnAs and SnSb and in good agreement with experiment whilst at the transition pressure, in the CsCl structure, a drastically increased value of T_c=12.2 K, 9.18 K is found for SnAs and SnSb respectively. Calculations also show a dramatic increase in the electronic density of states at this pressure. The lowest energy acoustic phonon branch in each structure also demonstrates some softening effects. Electronic structure calculations of the Fermi surface in both the phases are presented for the first time, together with further calculations of the generalised susceptibility.

5.1 Introduction

The effect that pressure has on materials can be classified into two categories: changes to the lattice and changes to the electronic structure. One way to interpret the link between the change of the lattice and the electronic structure is that the decrease in the inter-atomic distance leads to overlapping of outer electronic orbitals which will further lead to increase in the energy band widths. These subtle changes in electronic structure can lead to changes in material properties [242, 243] such as closing of gaps in the electronic energy spectrum leading to metal-insulator transitions [244], shifting of the electronic bands towards or away from the Fermi level leading to interband electron transitions [245, 246] and changes in the Fermi surface topology leading to Lifshitz transitions [247, 248] etc. In addition, physical properties such as electronic specific heat, superconducting transition temperature and magnetic nature may also change under pressure, enabling the ability to tune the physical properties and hence understand material properties under the application of pressure.

In many 11-type compounds, pressure leads to a phase change from NaCl-type to CsCl-type structure. For instance, in lanthanide monophosphides LnP (Ln=La, Ce, Pr, Nd, Sm, Gd, Tb, Tm and Yb), the phase change occurs at pressures around 25-50 GPa [104]. In the case of calcium chalcogenides, CaS, CaSe and CaTe, it is observed at 40 GPa, 38 GPa and 33 GPa, respectively [105]. A similar transition is also observed in IIIB-nitrides (ScN, YN) and IIIA-nitrides (GaN, InN) [106]. In the case of AgBr, an intermediate KOH-type structure is also observed from 8 to 35 GPa [107] between the NaCl-type and CsCl-type structures. The semiconducting family of tin based monochalcogenides, SnCh (Ch=O, S, Se, Te), have band gaps ranging between 1.1 and 2.9 eV and lone pair effects in these compounds have been studied by Lefebvre et al [108]. In 1984, Losev et al [110, 111] used x-ray diffraction to observe the same NaCl to CsCl structure transformation in SnAs at a pressure of around 32 GPa with an associated volume discontinuity of around 5%. Recently, superconductivity was reported in NaCl-type SnAs by Wang et al [112] with a superconducting critical temperature, T_c, of 3.58 K and electron-phonon coupling constant, λ_{ep}, to be around 0.62. Calculations, using density functional theory (DFT) and density functional perturbation theory (DFPT), have also been performed by Tütüncü et al [113] on NaCl-type SnAs to investigate the electronic structure and hence the electron-phonon coupling, finding good agreement with experimental work. Further DFT calculations by Shrivastava et al [114] showed the effect of pressure on the electronic structure of SnAs, further demonstrating the structural change that occurs. Recently Hase et al [115] reported that the moderate charge fluctuation and electron phonon interaction is the cause for superconductivity at ambient pressure. SnSb is useful in energy storage applications [116] and also posses NaCl type structure as ground state and it is observed to undergo a phase change at high pressures from NaCl to CsCl type structure. DFT calculations by Shrivastava et al [117] has shed light on the effect of pressure on the electronic structure of SnSb, further demonstrating the structural change that occurs. Crystal structure for the present investigated compounds is presented in Fig. 5.1 for both NaCl and CsCl phases.

Pressure has long been known to have a profound effect on the superconducting properties of elements and compounds [55, 56]. Recent studies achieved a world record in high superconducting transition temperature with a value of 203 K at the pressure of 200 GPa by Drozdov et al [62] in H_2S highlighting the importance of pressure in the investigation of superconductors. In SnO, Forthaus et al [60] observed the appearance of a superconducting phase under pressure which is

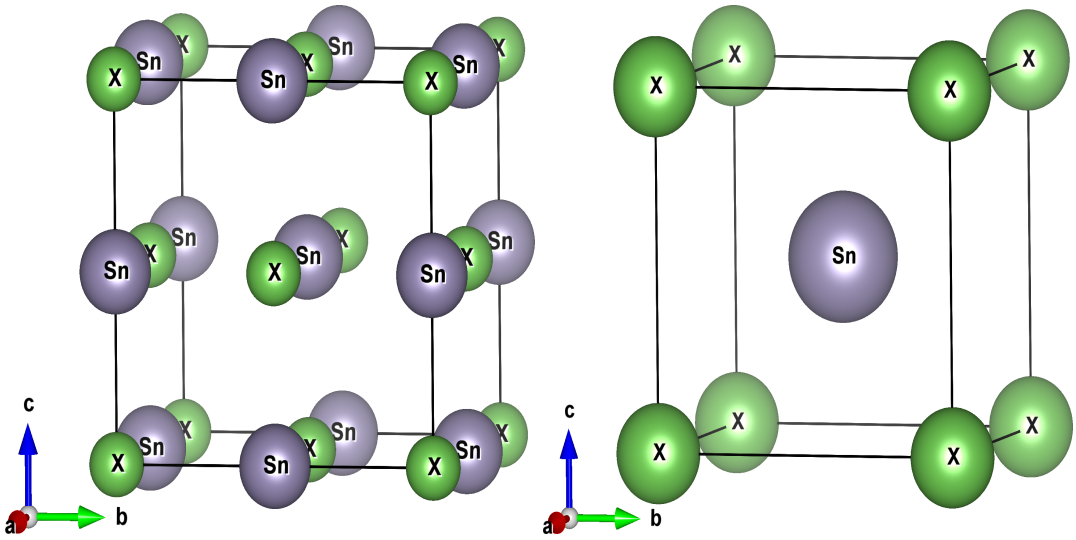

(a) (b)

Figure 5.1: Crystal structure of SnX (X= As and Sb) in (a) NaCl type structure and (b) CsCl type structure.

having dome shape phase diagram with a maximum T_c value of 1.43 K at around 9.3 GPa and also found the disappearance of superconductivity above the pressure of 16 GPa. In addition to inducing superconductivity, pressure can have the effect of enhancing T_c, motivating the investigation of the effect that pressure has on the superconducting properties of SnAs and SnSb, a structurally similar system to SnO, but one that are already superconducting at ambient pressure.

In this work, DFPT has been employed to investigate the important changes in phonon structure and superconducting properties that occur when simulating the effect of pressure in SnAs across the phase change between the NaCl and CsCl-type structures. Furthermore, using DFT, calculations of the generalised susceptibility of SnAs are performed to ascertain the role of the electronic structure in the softening of certain phonon modes. In section 5.2, the details of the computational methods are discussed. In section 5.3, the results of these calculations are presented, including the vibrational spectra of SnAs and SnSb in both the structures as well as the superconducting properties across the phase change. The Fermi surface of SnAs and SnSb is also presented for the first time together with the numerical analysis of its role in the phonon softening. Conclusions are given in section 5.5.

5.2 Computational details

The planewave pseudopotential formalism of DFT implemented within the QUANTUM ESPRESSO [154] code has been used for structural and volume optimization of the present compounds. This same code was used to compute the phonon dispersions and electron-phonon interactions using DFPT. The local density approximation (LDA) to the exchange correlation functional was used for all calculations and the electron-ion interaction is described using norm-conserving pseudopotentials. The maximum planewave cut-off energy is 120 Ry and the electronic charge density is expanded up to 480 Ry. A $16 \times 16 \times 16$ k-point grid within the Brillouin zone (BZ) is used for the phonon

calculations. Gaussian broadening of 0.005 Ry and a $8 \times 8 \times 8$ uniform grid of 'q'-points is used for the calculation of the phonons.

Density functional calculations have been performed in the present work to calculate the band structure, density of states and Fermi surface. The Full-Potential Linearized Augmented Plane Wave (FP-LAPW) method as implemented in WIEN2k [153] code is used. We have used local density approximation (LDA) [249] for the exchange correlation potential. Throughout the calculations, the R_{MT} (radius of muffin tin spheres) value for each atom was fixed as 2.2 a.u, 2.4 a.u and 2.5 a.u for As, Sn and Sb atoms respectively. For the energy convergence, the criterion R_{MT}*K_{max}=7 was used, where K_{max} is the plane wave cut-off. The potential and charge density were Fourier expanded up to G_{max}=12 a.u^{-1}. All electronic structure calculations are performed with 44×44×44 grid of k points in the Monkhorst-Pack [187] scheme which gives 2168 and 2300 k-points for NaCl and CsCl-types respectively in the irreducible part of the Brillouin Zone (BZ). Tetrahedron method [188] was used to integrate the Brillouin zone. Energy convergence up to 10^{-5} Ry is used to get proper convergence of the self consistent calculation. Birch-Murnaghan [189] equation of state was used to fit the total energies as a function of primitive cell volume to obtain the bulk modulus. We have checked the effect of spin-orbit coupling (SOC) and have not found any significant changes at the Fermi level with the inclusion of SOC. Further calculations are performed without including SOC.

We have also calculated the real and imaginary part of Lindhard function $Re[\chi(q)]$ for $\omega = 0.001$ to check the possibility of nesting by using

$$Re[\chi(q)] = \sum_{kjj'} \frac{f_{kj} - f_{k+qj'}}{\in_{kj} - \in_{qj'}} \tag{5.1}$$

and

$$Im[\chi(q)] = \sum_{kjj'} \delta(\in_F - \in_{kj})\delta(\in_F - \in_{k+qj'}) \tag{5.2}$$

where f is Fermi-Dirac distribution function, $\in_{kj}$ and $\in_{qj'}$ are the energy eigenvalues for band indices j and j', and $\in_F$ is the Fermi energy. We have evaluated these functions with constant matrix element approximation together with a grid of 60×60×60 and considered only those bands which cross the Fermi level.

5.3 Results and discussions

5.3.1 Ground state properties and structural phase transition

To begin with, calculations to reproduce the structural transition that has been reported experimentally [110, 111] and presented in other works [114, 117] are performed for both the compounds. The total energy has been calculated as a function of relative volume for both NaCl and CsCl forms of SnAs and SnSb to find the stable ground state as plotted in Fig. 5.2(a,b). From this it is evident that at ambient pressure, both the compounds stabilizes in the NaCl-type cubic structure (space group $Fm\bar{3}m$ (No. 225)) with atomic positions As/Sb (0.00, 0.00, 0.00) and Sn (0.50, 0.50, 0.50) in agreement with the recent DFT study by Shrivastava et al [114, 117]. From the same figure it is also observed from the crossover of the two energy parabola that both compounds undergo a phase

transition from NaCl-type to CsCl-type (space group $Pm\bar{3}m$ (No. 221)) at a compression around V/V_0=0.76 and 0.86 for SnAs and SnSb respectively. At this pressure, a volume collapse of around 4.34% and 6.31% is seen for SnAs and SnSb respectively, in good agreement with available data [111, 117]. The calculated lattice parameter and bulk modulus values are given in Table 5.1 for the NaCl-type structure. It is already known that LDA might underestimate the lattice parameter and the same will be overestimated with Generalized Gradient Approximation (GGA). In our case LDA lattice parameter is close to experimental value as given in Table 5.1 and we further proceeded with rest of the calculations using LDA. The calculated lattice parameter is close to the experimental value, the discrepancy being due to the inherent underbinding that the LDA provides. For the NaCl structure, the calculated bulk modulus value of 75.38 GPa for SnAs is in good agreement with the results of Tütüncü et al [113]. In the case of SnSb the calculated value is 63 GPa which is more than that observed by Shrivastava et al [117] and Dabhi et al [250]. This difference might be due to the usage of different approximations (GGA) for the exchange correlation potential for SnSb. The change in enthalpy as a function of pressure has also been calculated to compute the exact transition pressure, as given in Fig. 5.2(c,d), and it is observed that the phase transition occurs at around 37 GPa for SnAs and 13 GPa for SnSb indicating a first order phase transition in these compounds.

5.3.2 Electronic structure

Now we move ahead to analyse the electronic structure properties of stable NaCl-type SnAs and SnSb at ambient conditions. All the electronic structure calculations are performed at the equilibrium lattice parameter. The calculated band structure along different high symmetry directions is given in Fig. 5.3 at ambient conditions. From the band structure, we have observed only one band to cross the Fermi level (E_F) in SnAs from conduction band to valence band at Γ, X and K high symmetry points. This implies that the Fermi surface corresponding to the band might have multiple sheets. Recent experiments done by Bezotosnyi et al [251] on ARPES measurements of SnAs electronic band structure is in agreement with our calculated band structure for SnAs. As we move from SnAs to SnSb, Fermi level is found to shift towards lower energy region resulting in addition of an extra band crossing the E_F in SnSb (see Fig. 5.3(b)) compared to SnAs, which is having hole nature due to the band crossing from valence band to conduction band. In both the compounds, the band at Γ point is found to posses As/Sb-'*p*' character and at L point around 1 eV has Sn-'*p*' character.

To probe more at E_F, we have calculated the total and atom projected density of states (DOS) for SnAs and SnSb at ambient conditions and are plotted in Fig. 5.5. From the plots, it is clear that low lying peak at -11 eV is due to the As/Sb-'*s*' states as discussed in the band structure. Another peak at -8 eV is due to the '*s*' states of Sn atom in both the compounds. The total DOS at Fermi level ($N(E_F)$) is found to be 0.63, 0.891 states/eV/f.u. for SnAs and SnSb respectively which is also in agreement with other theoretical [113, 117, 250] results. We find the '*p*'-sates of both the atoms to contribute more at E_F, with As/Sb-'*p*' states dominating more than Sn-'*p*' states. We have also observed the covalent nature between the As/Sb and Sn atoms in these compounds.

Purely on an electronic basis, we can try to get an idea of the extent of the possible electron-phonon coupling within the system in the NaCl structure by calculating the electronic linear specific heat coefficient or Sommerfeld coefficient, γ_{calc}, and comparing it to the experimental value, γ_{exp}. This is given in Table 5.1. The experimental value is higher than the calculated one as the calculation explicitly neglects many-body effects and our value agree well with the theoretical work of Hase et

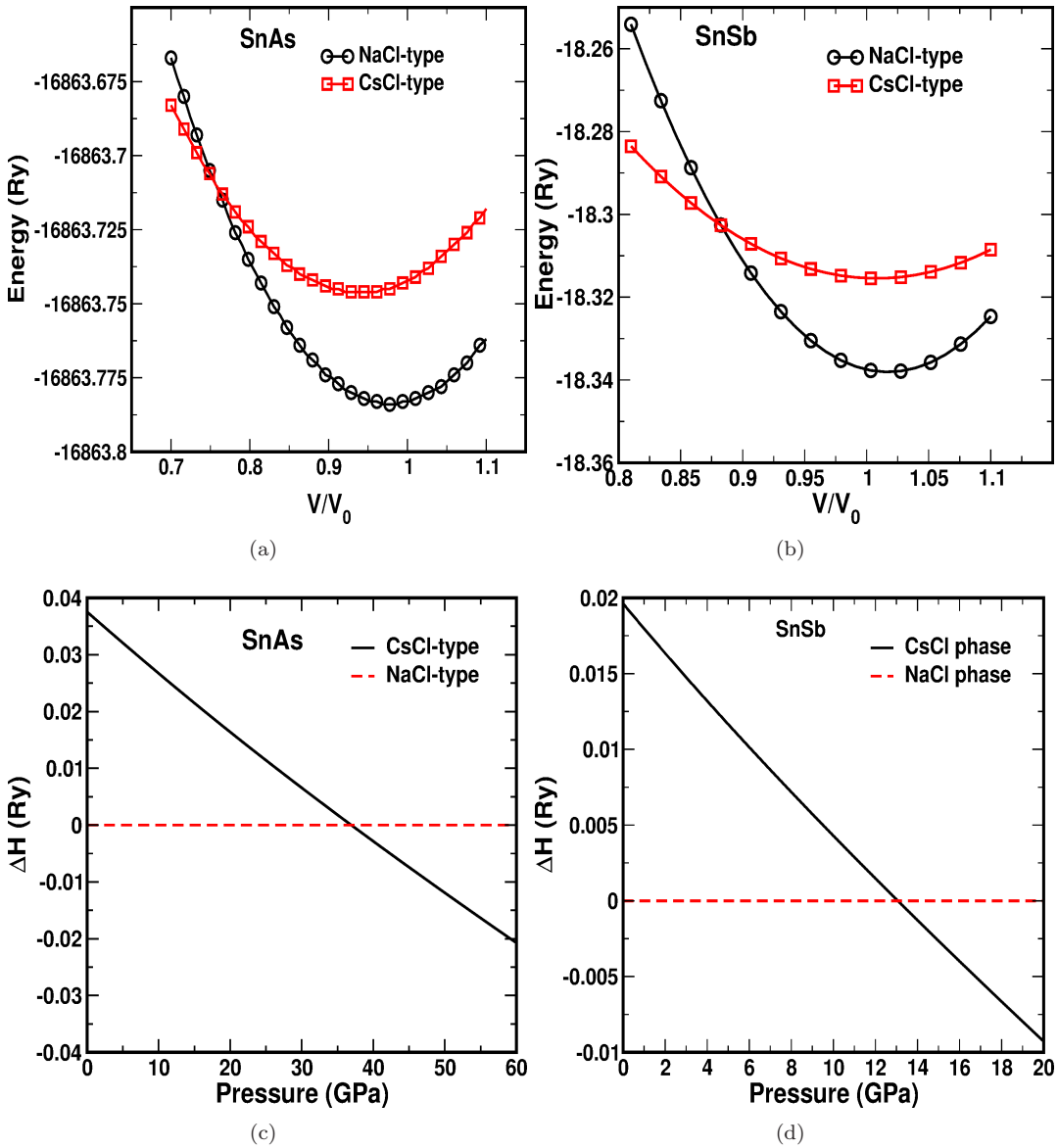

Figure 5.2: Total energy as a function of relative volume for (a) SnAs and (b) SnSb where circle and square symbols represent the NaCl and CsCl phases respectively. Change in enthalpy as a function of pressure to demonstrate the phase change between NaCl and CsCl type at a pressure of (c) 37 GPa in SnAs and (c) 13 GPa in SnSb respectively.

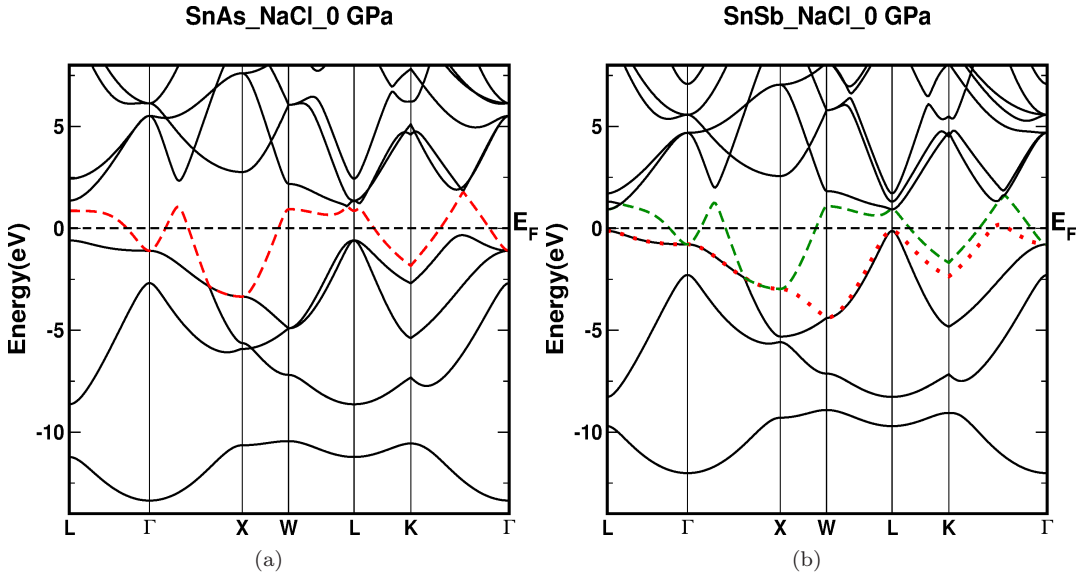

Figure 5.3: Band structure of (a) SnAs and (b) SnSb at ambient conditions.

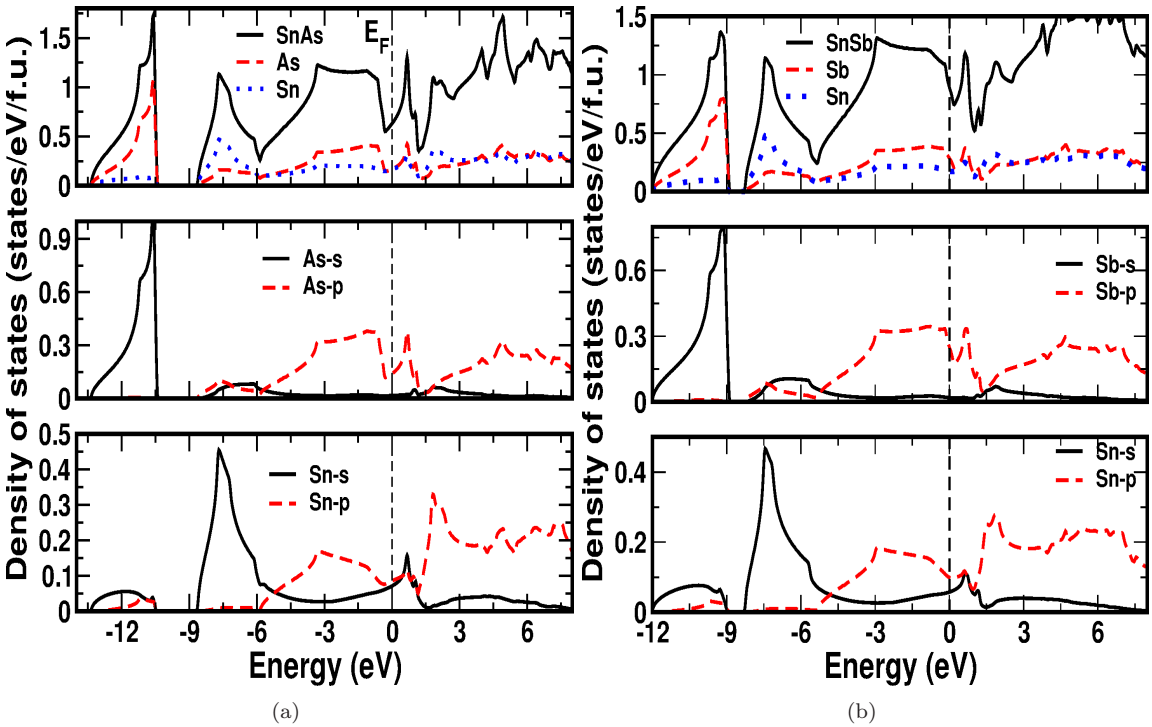

Figure 5.4: Total and atom projected density of states at ambient conditions NaCl-type for (a) SnAs and (b) SnSb.

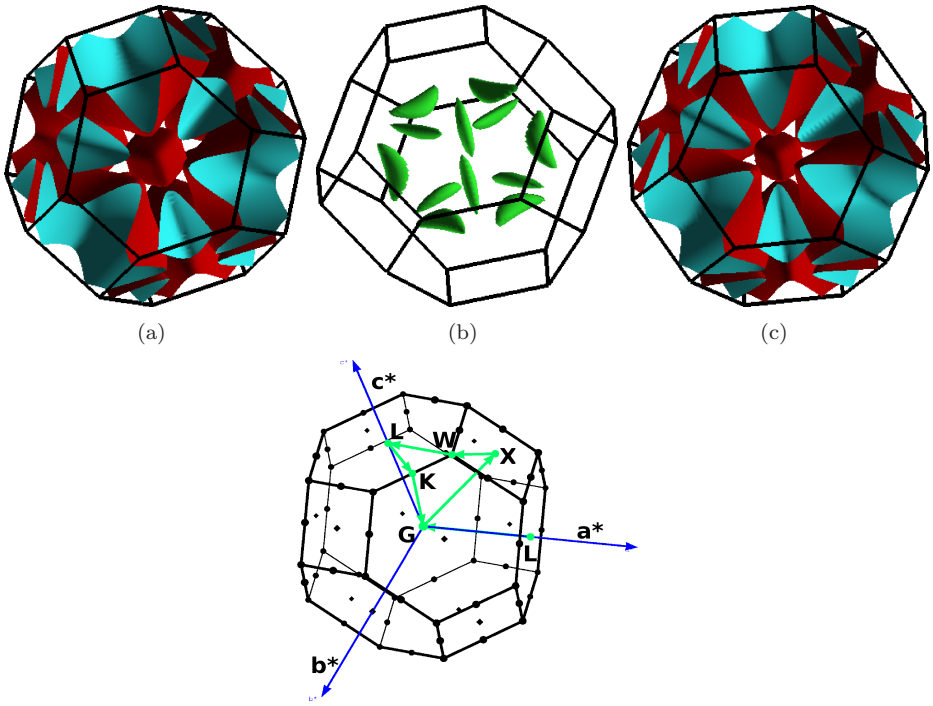

Figure 5.5: Fermi surface at ambient conditions NaCl-type structure for (a) SnAs, (b, c) SnSb and (d) BZ of NaCl-type structure.

al [115] in the case of SnAs. The ratio of γ_{exp} to γ_{calc}, gives an estimate of the mass renormalisation, λ, through

$$\frac{\gamma_{\text{exp}}}{\gamma_{\text{calc}}} = 1 + \lambda. \tag{5.3}$$

Using the experimental value of 2.18 mJ/mol K^2 reported by Wang et al [112], along with the calculated value from this work of 1.49 mJ/mol K^2, the value of λ is found to be 0.46. If we assume that the dominant renormalisation comes from the coupling between the electrons and the lattice, such that we can say $\lambda = \lambda_{\text{ep}}$, then this value can be directly compared to the value of λ_{ep} of 0.62 inferred from experiment [112]. Whilst there is reasonable agreement, it should be noted that experimental measurements of the Sommerfeld coefficient are incredibly challenging but the higher experimental value for λ_{ep} may point to the electrons coupling more strongly to special modes as has been seen previously [252, 253]. In the case of SnSb, no other reports are available to compare our calculated γ values.

It is very interesting to know about the Fermi surfaces which has specific importance on the physical properties of a metal through its impact on electron screening. The calculated Fermi surfaces (FS) at ambient conditions is given in Fig. 5.5(a) for SnAs and in Fig. 5.5(b, c) for SnSb, where we find multiple sheets due to a band crossing E_F at different high symmetry points in both the compounds. An electron pocket at Γ point and sheets near X and K points are observed in both the compounds. From the keen observation of FS, parallel sheets along X-Γ direction are observed in both the compounds resulting in nesting feature along this direction in the present compounds.

Such a visual inspection of the nesting features of a Fermi surface, however, is not sufficient, as

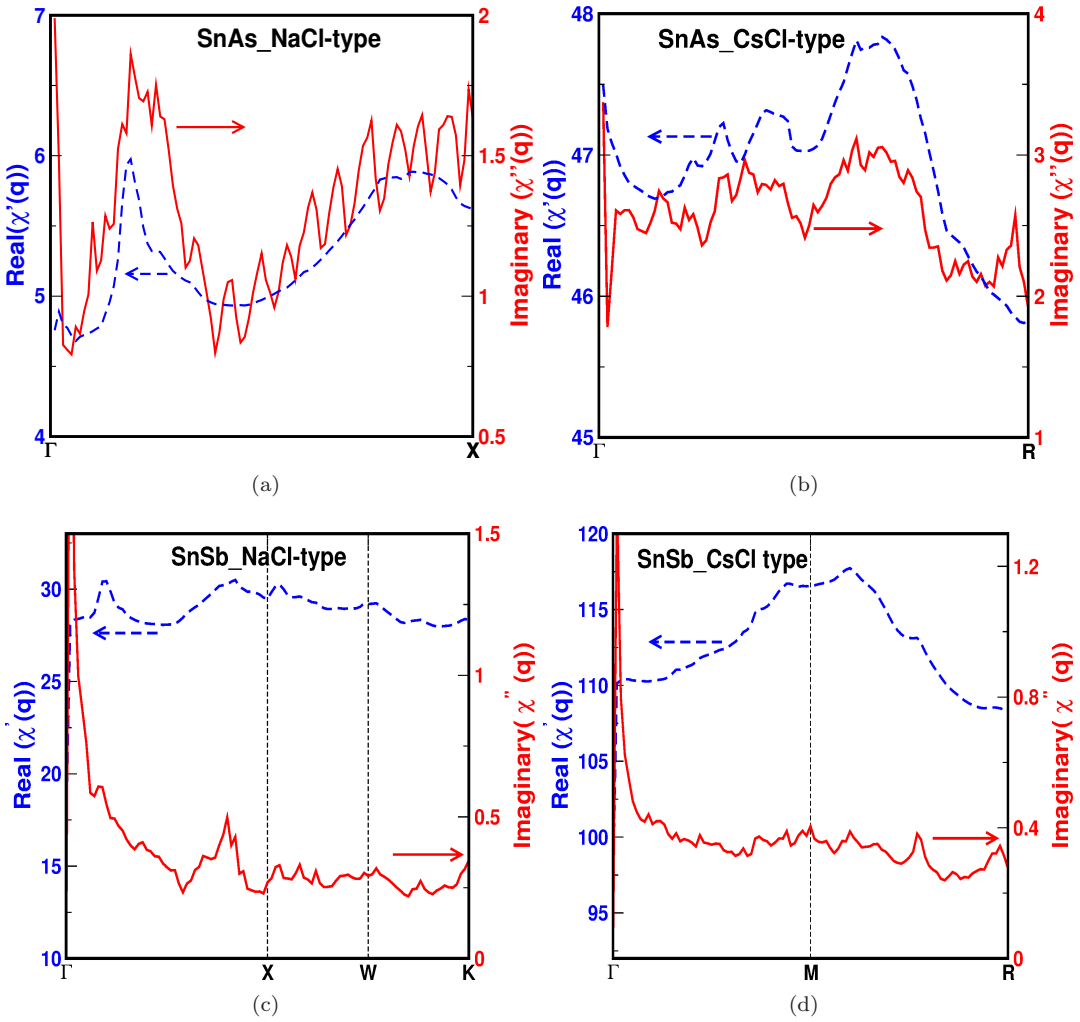

Figure 5.6: Real and imaginary part of susceptibility for (a) NaCl-phase of SnAs at ambient conditions, (b) CsCl-phase of SnAs at transition pressure (37 GPa), (c) NaCl-phase of SnSb at ambient conditions and (d) CsCl-phase of SnSb at transition pressure (13 GPa). Arrow's direction indicates the axis direction to be referred in the figure.

was shown by Johannes et al [34]. Through calculating both the real and imaginary parts of the generalised susceptibility, $\chi(\mathbf{q})$, where $\mathbf{q}$ is the wavevector of the perturbation, an assessment can be made as to the geometrical nesting properties of the Fermi surface (in the imaginary part($\chi''(\mathbf{q})$)) as well as the response that the electrons will have (through the real part($\chi'(\mathbf{q})$)). A true nesting effect will be seen through singularities in both the real and imaginary parts at the same wavevector, showing the electronic response at a particular '$\mathbf{q}$' is a consequence of the geometry of the Fermi surface. $\chi(\mathbf{q})$ has been calculated for both the compounds at ambient conditions NaCl structures as shown in Fig. 5.6(a) and 5.6(c). In the NaCl structure, a peak is seen in both the real and imaginary parts at a wavevector of $[0.0, 0.0, 0.1] \times 2\pi/a$ in both the compounds along Γ-X. indicating a strong electronic response that is driven by the shape of the Fermi surface.

5.3.3 Elastic constants

To understand the mechanical stability of present compounds at ambient conditions, we have calculated the elastic constants and the calculated single and poly crystalline constants are given in Table 5.2. The calculated single crystalline elastic constants are satisfying the Born's stability criteria, C_{11} >0, C_{44} >0, C_{11} >C_{12}, and C_{11} + 2C_{12}>0 indicating the mechanically stable nature of the present compounds at ambient conditions. The polycrystalline elastic constants can be calculated from the single crystalline elastic constants using the empirical relations which can be found elsewhere [194, 195, 196, 197]. The calculated Young's modulus (E) is 56.32 and 51.94 GPa for SnAs and SnSb respectively. The presence of elastic anisotropy [194] in the present compounds is also confirmed by calculating the anisotropy factor(A). Calculated positive value of Cauchy's pressure (C_{12}-C_{44}) indicate the ductile nature of the present compounds, and the same is also confirmed from the calculated Pugh's ratio ($\frac{G_H}{B}$) [198]. The value of Pugh's ratio is less than 0.57 which is known as critical number to separate brittle and ductile nature. The Poisson's [199] ratio (σ) indicate the stability of the crystal against shear and takes value in between -1 to 0.5, where -1 and 0.5 serve as lower and upper bounds respectively. From our calculations, Poisson's ratio value for the present compounds is closer to the upper limit indicating the stiffness of the present compounds. Debye temperature (Θ_D) is one of the important parameter and it determines the thermal characteristics of the materials. The Debye temperature can be obtained from the mean sound velocity, which gives the explicit information about lattice vibration and can be computed directly from $\Theta_D = \frac{h}{k}\left[\frac{3n}{4\pi}\left(\frac{\rho N_A}{M}\right)\right]^{1/3} v_m$. The calculated Debye temperature value for both the compounds is in agreement with the earlier theoretical [112, 250] work as given in the same table.

5.3.4 Vibrational and superconducting properties

Now we proceed further with the computation of vibrational properties, which can be used to check the dynamical stability of the present compounds at ambient conditions NaCl structure. We have calculated the phonon dispersion curves along different high symmetry directions and the same is given in Fig. 5.7(a,b) along with the phonon density of states (PDOS). The primitive cell of the present compounds have one formula unit with two atoms which gives six phonon branches including three acoustic and three optical branches. The absence of imaginary phonon frequencies indicate the dynamical stability of the present compounds at ambient conditions. In both the compounds, we observe an interaction of higher frequency acoustic mode with the optical modes along Γ-X, K-Γ

and at L points at different frequencies. We also observe degenerate LA2 mode along L-Γ-X and this degeneracy is lifted out in other directions. An anomaly (dip) in the degenerate LA2 mode is observed along Γ-X direction which may have significant effect in the physical properties of the present compounds. The same anomaly is observed in some of the Heusler compounds such as Ni_2MnGa [200], Ni_2MnIn [203], Ni_2MnX (X= Sn, Sb) [204], Ni_2VAl and Ni_2NbX (X=Al, Ga, Sn) [254], which are having same FCC structure. The softening in the acoustic mode leads to Kohn anomaly [31], which is due to the interaction of electronic states with phonon at the E_F together with parallel sheets in the FS topology. The mechanism behind a Kohn anomaly is one of electronic screening [31] due to the perturbation. Under the action of a perturbation (in this case, a phonon), the electrons at the Fermi surface (which have access to unoccupied states) will attempt to screen it [255]. The ions of the lattice will then interact via this screened potential which modifies the phonon frequencies. The extent of this softening can therefore be dictated by how responsive the electrons are to the initial perturbation. Kohn summarised that the shape of the Fermi surface would play a vital role in this mechanism [31]. In the present compounds also this interaction might be a reason for the anomaly. This is confirmed from the susceptibility calculations as discussed above at 'q'-vector around [0.0 0.0 0.1]×2π/a along Γ-X direction, where we observe the FS nesting and phonon softening.

By first looking at the total PDOS in the NaCl structure, the major peak is found near a frequency of 150 cm^{-1} and from the atom-projected phonon DOS in Fig. 5.7(c), it can be seen that this is derived from As. It is also observed that the higher frequency optical modes above the frequency 125 cm^{-1} are due to As and the remaining modes below 125 cm^{-1} are due to Sn. In the case of SnSb, from Fig. 5.7(b), major peak in the total PDOS observed around 120 cm^{-1} is due to both Sn and Sb atoms, which are having almost equal contribution (which is due to the nearly same atomic mass) around this frequency range (see Fig. 5.7(d)).

Having determined the phonon structure as discussed above, the electron-phonon coupling can be calculated to explore the superconducting properties. As discussed in section 5.1, present compounds are found to have superconducting nature in NaCl structure which is the ground state. The electron phonon coupling constant (λ_{ep}) is extracted from the Eliashberg function ($\alpha^2F(\omega)$) which can be used to determine the superconducting transition temperature (T_c) of a conventional phonon mediated superconductor. The T_c of the present compound is calculated by using Allen-Dynes [205] formula,

$$T_c = \frac{\omega_{ln}}{1.2} exp(-\frac{1.04(1+\lambda_{ep})}{\lambda_{ep} - \mu^*(1+0.62\lambda_{ep})}) \tag{5.4}$$

where ω_{ln} is logarithmically averaged phonon frequency, λ_{ep} is electron phonon coupling constant and μ^* is Coulomb pseudopotential. The representation of $\alpha^2F(\omega)$ is

$$\alpha^2F(\omega) = \frac{1}{2\pi N(\epsilon_f)} \sum_{qj} \frac{\nu_{qj}}{\hbar\omega_{qj}} \delta(\omega - \omega_{qj}) \tag{5.5}$$

This function is often very similar to the phonon DOS ($F(\omega) = \sum_{qj} \delta(\omega - \omega_{qj})$) and differs from the phonon DOS by having a weight factor $1/2\pi N(\epsilon_f)$ inside the summation. In the above formula $N(\epsilon_f)$ is the electronic density of states at the E_F and ν_{qj} is the phonon line width, which can be

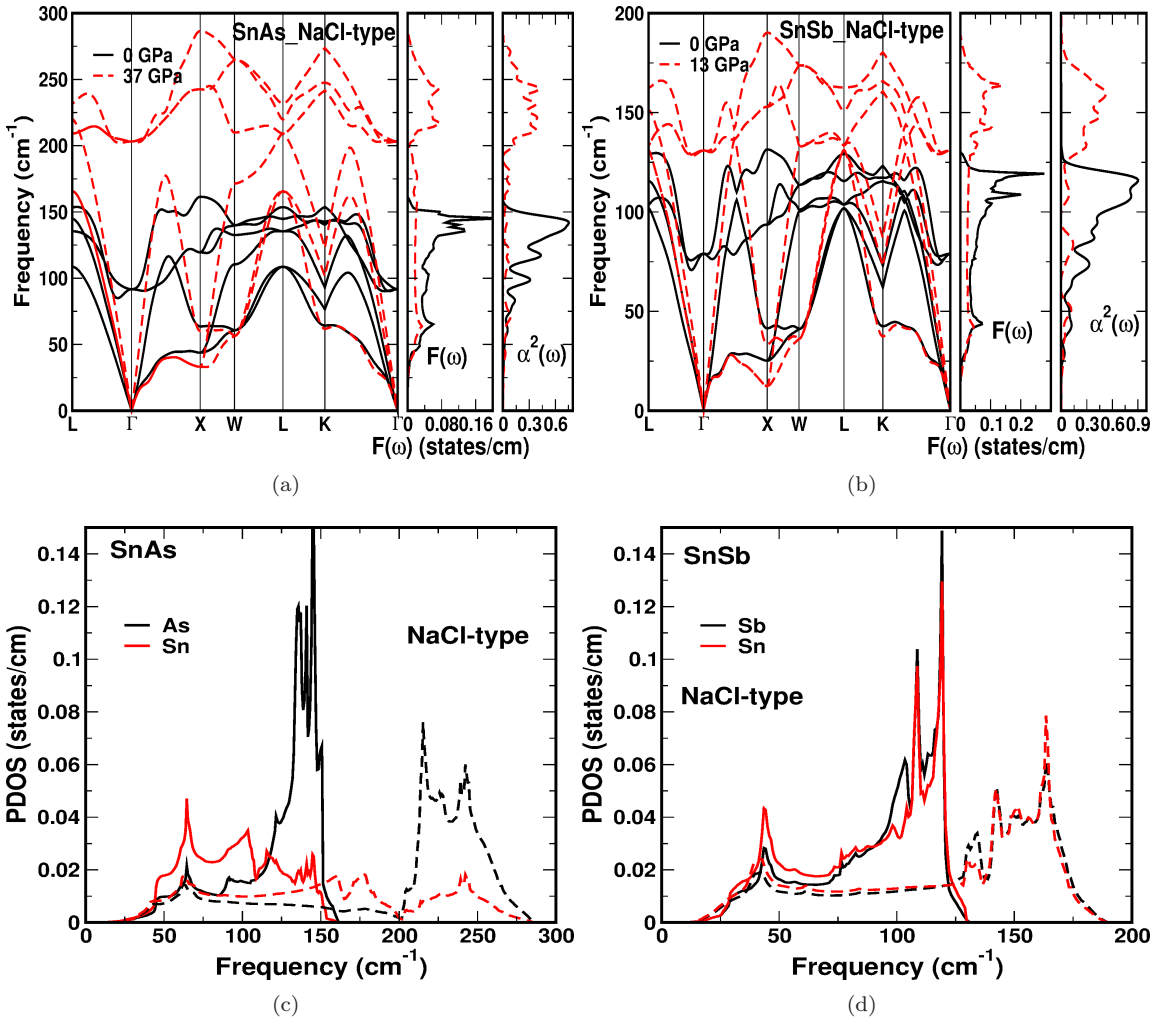

Figure 5.7: Phonon dispersion along with total phonon density of states and Eliashberg function for (a) NaCl phase of SnAs at ambient conditions and 37 GPa, (b) NaCl phase of SnSb at ambient conditions and 13 GPa. (c) Atom projected phonon density of states for SnAs in NaCl phase at ambient conditions (solid lines) and 37 GPa (dotted lines). (d) Atom projected phonon density of states for SnSb in NaCl phase at ambient conditions (solid lines) and 13 GPa (dotted lines).

represented as

$$\nu_{qj} = 2\pi\omega_{qj} \sum_{knm} |g^{qj}_{(k+q)m,kn}|^2 \delta(\varepsilon_{kn} - \varepsilon_F)\delta(\varepsilon_{(k+q)m} - \varepsilon_F) \tag{5.6}$$

where Dirac delta function express the energy conservation conditions and 'g' is the electron phonon matrix element. λ_{ep} can be expressed in terms of $\alpha^2F(\omega)$ as

$$\lambda_{ep} = 2\int \frac{d\omega}{\omega}\alpha^2F(\omega) = \int \lambda(\omega)d\omega \tag{5.7}$$

where

$$\lambda(\omega) = \frac{2\alpha^2F(\omega)}{\omega} \tag{5.8}$$

The calculated Eliashberg function is plotted in Fig. 5.7(a) and 5.7(b) for SnAs and SnSb respectively, where we find peaks at frequency around 140, 120, 100 cm^{-1} in SnAs and around 120, 70 cm^{-1} in SnSb. The height of the peak indicate the higher phonon line width and higher electron phonon coupling constant at that frequency region and is found to decrease gradually to lower frequencies. The calculated T_c values of the investigated compounds are 3.08 and 3.08 K with a value of λ_{ep} around 0.62 and 0.68 for SnAs and SnSb respectively by considering the μ^* value to be 0.13. These calculated values are in good agreement with the other reported values [112, 113, 250] and are given in Table 5.3. Calculated λ_{ep} and T_c of the present compounds are almost same.

From the above discussions superconducting nature is confirmed in both the compounds at ambient conditions NaCl structure. From the calculated total energy and enthalpy calculations (as discussed from Fig. 5.2) phase transition is observed in both the compounds from NaCl to CsCl-type structure. So, it is quite reasonable to study the pressure effect on the above mentioned properties of SnSb which are presented in next section.

5.4 Pressure effect on the electronic structure, phase transition, vibrational and superconducting properties

As we already discussed above, from the enthalpy calculations, SnAs and SnSb compounds undergo a phase transition from NaCl to CsCl structure at pressure around 37 and 13 GPa respectively. The calculated lattice parameter in CsCl phase for both the compounds is given Table 5.1. We have calculated the band structure of NaCl-type and CsCl-type structures at transition pressure and are given in Fig. 5.8. As pressure increases widening of valence band region is observed in NaCl-type structure together with the band shifting at Γ point. As pressure increases, the band at Γ point is shifted towards E_F, resulting in decrease of As/Sb-'p' character with pressure. Due to this, the occupied area of the band which cross the E_F at Γ point is decreased which might have an effect on the size of electron pocket at the Γ point in the FS.

The band structure scenario of CsCl-type structure is completely different in comparison with NaCl-type structure. In CsCl-type structure, six bands are found to cross at E_F, whereas in NaCl-type structure it is only one in SnAs and two in SnSb which implies the significant change on the FS topology in CsCl-type compared to NaCl-type structure. Upto a maximum studied pressure of 60 GPa for SnAs and 20 GPa for SnSb we have not found any change in the band structure topology in CsCl-type, and hence no change in FS is observed.

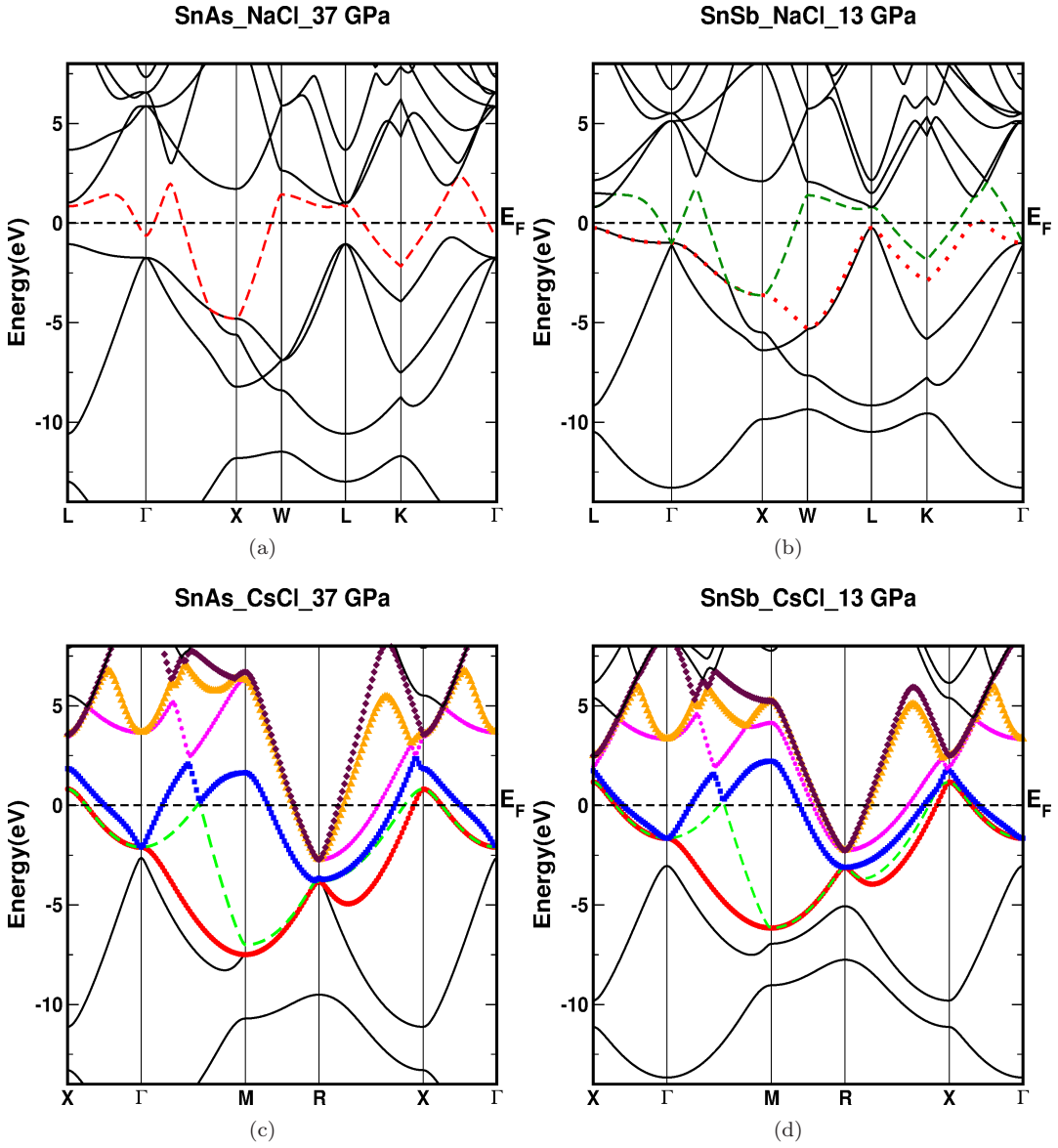

Figure 5.8: Band structure for (a) SnAs in NaCl-type structure at transition pressure around 37 GPa, (b) SnSb in NaCl-type structure at transition pressure around 13 GPa, (c) SnAs in CsCl-type structure at transition pressure around 37 GPa and (d) SnAs in CsCl-type structure at transition pressure around 13 GPa. The bands which are crossing the Fermi level are indicated with colours.

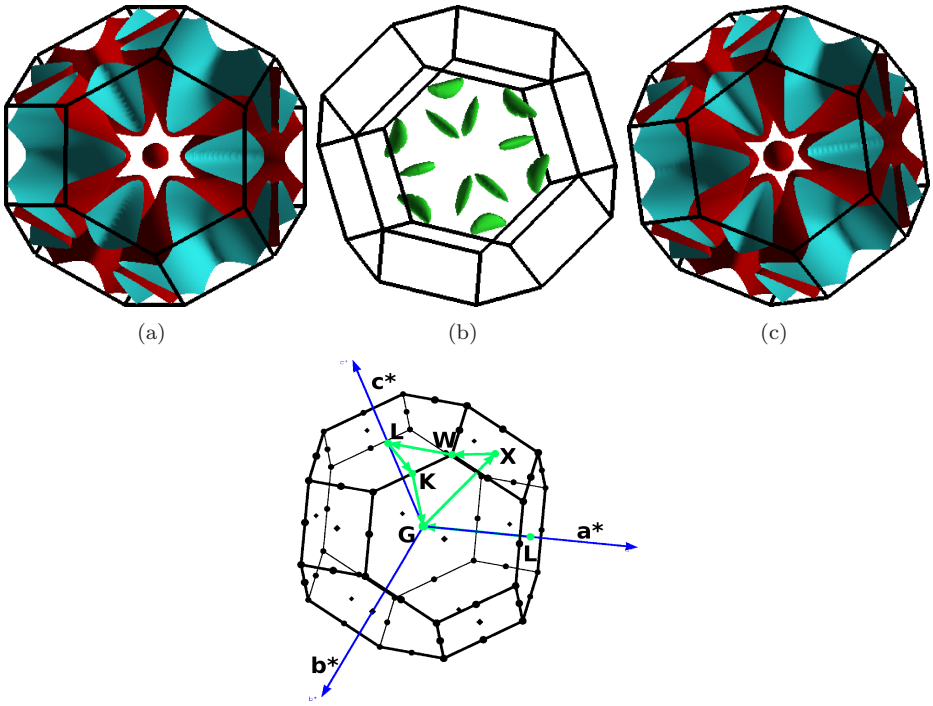

Figure 5.9: Fermi surface at the transition pressure for NaCl-type structure (a) SnAs at 37 GPa, (b, c) SnSb at 13 GPa and (d) BZ for NaCl-type structure.

Calculated FS for NaCl-type structure at transition pressure is given in Fig. 5.9(a,b,c), where we can see the decrease in the size of the electron pocket at Γ point (Fig. 5.9(a,c)) which is due to the band shifting at this pressure. At the same pressure, FS topology of CsCl-type is given in Fig. 5.10 for SnAs and Fig. 5.11 for SnSb along with the corresponding Brillouin zone. From this figures, we have observed six FS corresponding to six bands crossing the E_F, which is evident from band structure plots in Fig. 5.8(c,d) and might lead to drastic changes in T_c. Among these six FS's, third one (Fig. 5.10(c) and Fig. 5.11(c)) has parallel sheets around M point, along R-M, X-M and Γ-M. Beyond this pressure no FS topology change is observed in CsCl-type upto the final pressures studied.

We have calculated the susceptibility at the transition pressure in CsCl-type for both the compounds and the same is plotted in Fig. 5.6(b,d). Along the [111] direction, in Fig. 5.6(b) there is a broad peak in both the real and imaginary parts of $\chi(\mathbf{q})$ around $[0.33, 0.33, 0.33] \times 2\pi/a$ in SnAs. In the case of SnSb, form Fig. 5.6(d), a peak in both real and imaginary parts is observed along M-R at a 'q'-vector around [0.5 0.5 0.3]×2π/a.

Calculated density of states for CsCl-type structure is given in Fig. 5.12(a,b) for both SnAs and SnSb compounds. From this we can see an increase in the total DOS at E_F in both the compounds compared to NaCl-type. In CsCl phase also As/Sb contribution is more towards total DOS compared to Sn. Calculated total electronic density of states as a function of pressure is given in Fig. 5.12(c,d), As pressure increases, the total DOS in both the structures is found to decrease monotonically. At the transition pressure total density of states is found to be increased by two fold in SnAs and around

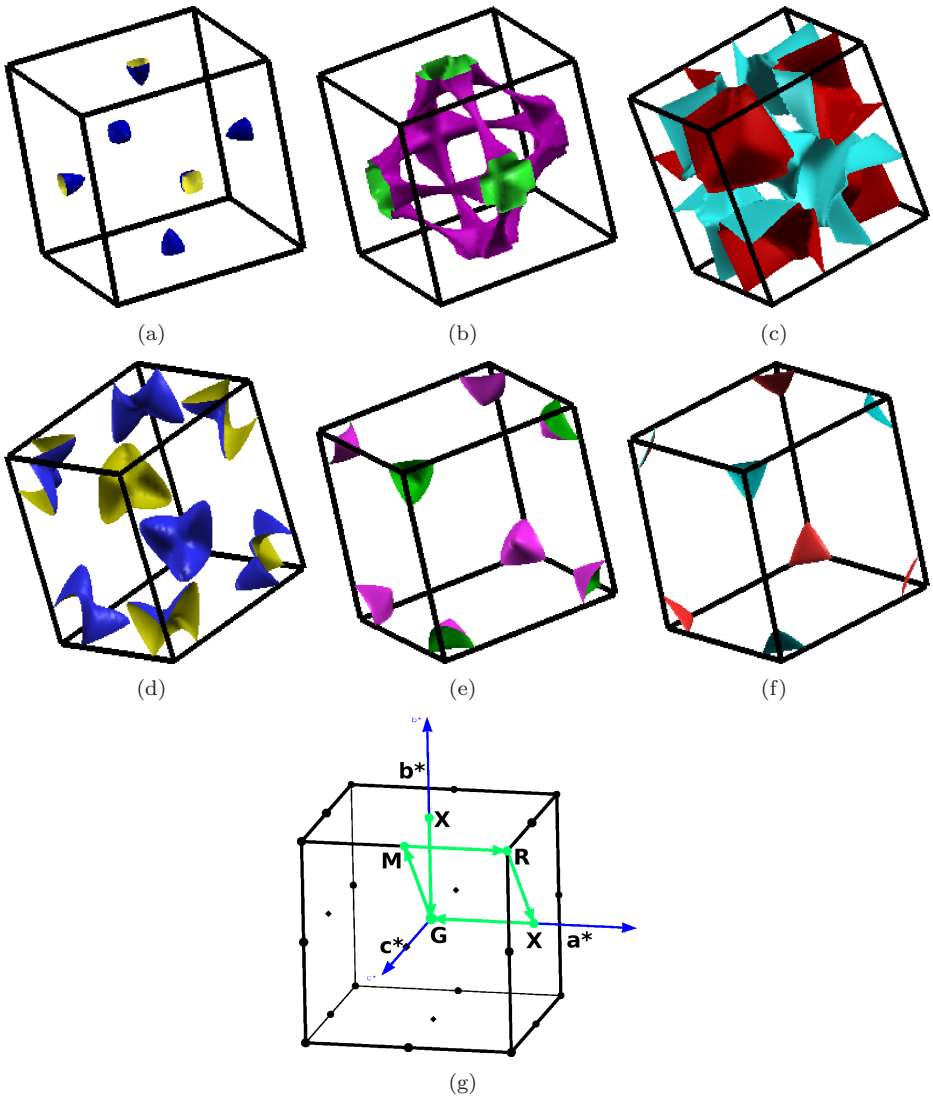

Figure 5.10: Fermi surface for SnAs in the CsCl structure at the transition pressure of 37 GPa for (a) band no. 13, (b) band no. 14, (c) band no. 15, (d) band no. 16, (e) band no. 17, (f) band no. 18 and (g) the Brillouin zone for the CsCl structure.

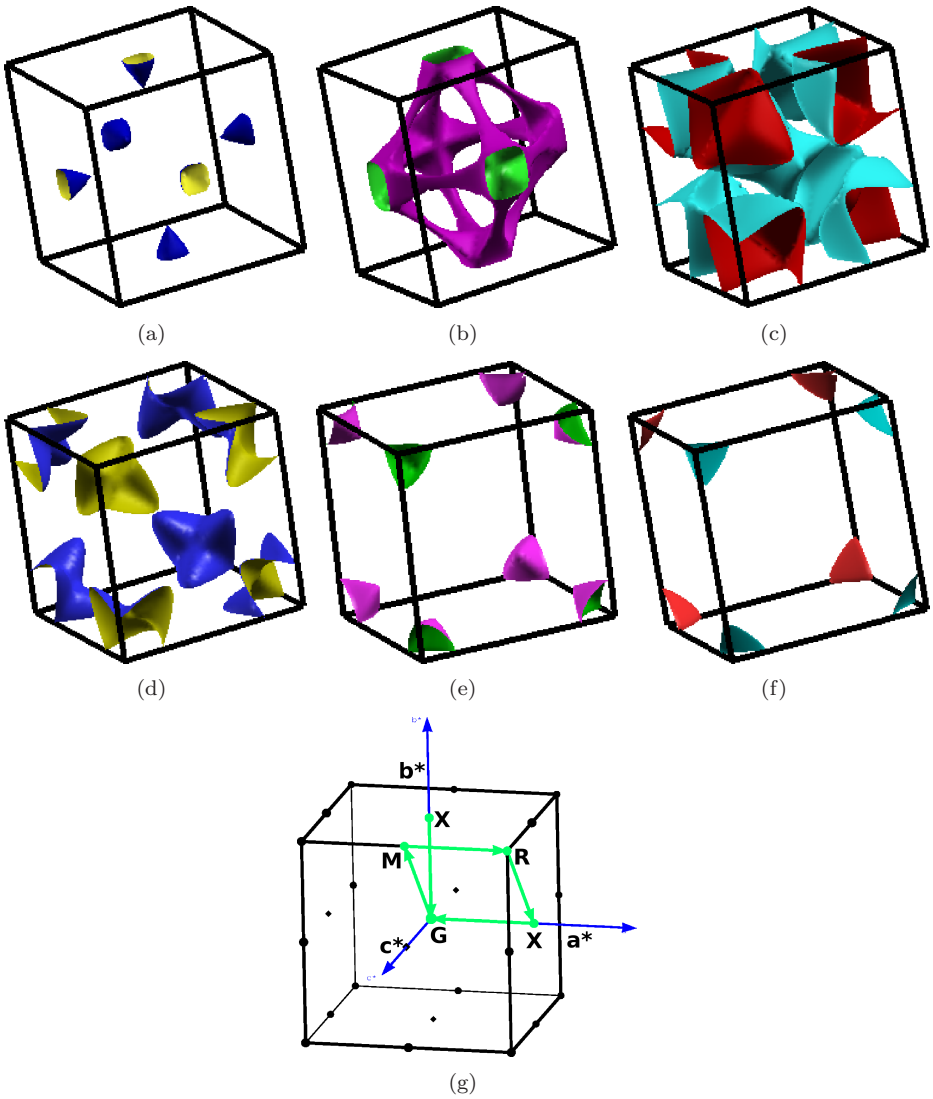

Figure 5.11: Fermi surface for SnSb in the CsCl structure at the transition pressure of 13 GPa for (a) band no. 13, (b) band no. 14, (c) band no. 15, (d) band no. 16, (e) band no. 17, (f) band no. 18 and (g) the Brillouin zone for the CsCl structure.

12% in SnSb compared to ambient structure, which certainly might alter the T_c in CsCl structure in both the compounds.

To check the mechanical stability of CsCl-type SnAs and SnSb at transition pressure we have calculated the single and poly crystalline elastic constants at transition pressure and are given in Table 5.2. These values are satisfying the mechanical stability criteria at this pressure indicating the stable nature of CsCl-type structure at this pressure. The calculated bulk modulus, as given in Table 5.1, is found to be 207 and 113 GPa for SnAs and SnSb compounds respectively which is large compared to the ambient NaCl-type structure. The calculated single crystalline elastic constants as a function of pressure is plotted in Fig. 5.13(a,b) for both NaCl and CsCl-type SnAs and SnSb, where we can observe C_{11} and C_{12} to be more sensitive to pressure compared to C_{44}. We have also observed the decrease in the value of C_{11} and increase in C_{12} and C_{44} in CsCl-type structure when compared to NaCl-type structure at transition pressure in SnSb but in SnAs C_{12} is almost same in CsCl and NaCl type at transition pressure. From the same figure, non-monotonic variation in C_{11}, C_{12} and C_{44} is observed in CsCl-type structure with increase in pressure upto the maximum pressure studied in both the compounds. This non-monotonic behaviour may further lead to changes in the other physical properties in the CsCl-type SnSb under pressure.

Pressure effect on the vibrational properties is always an interesting phenomenon which can be used to understand the dynamical behaviour of the system under the application of pressure. We have calculated phonon dispersion curves at transition pressure for both the phases of SnAs and SnSb. For NaCl-type at the transition pressure (red colour dotted line) softening in the lower acoustic mode is observed near Γ, X and K high symmetry points as shown in Fig. 5.7(a,b). There are some interesting features in the dispersions that alter both between the two structures and with the application of pressure. In the NaCl structure, in both the compounds, there is a degeneracy in the LA2 mode along L-Γ-X which is lifted out in other directions but the same degeneracy still remain throughout the application of pressure. The calculated phonon dispersion for CsCl-type SnAs and SnSb at the transition pressure is given in Fig. 5.14(a,b), where we have observed a similar degeneracy in the CsCl structure along the Γ-X direction that still remains under pressure. An interaction of the higher frequency acoustic modes with the optical modes is seen at various points in the BZ for both the structures. In the NaCl structure, pressure acts to lift this interaction quite considerably, pulling apart the acoustic and optical modes whilst in the CsCl structure the application of further pressure has little effect on the interplay between the acoustic and optical branches. The height of the calculated Eliashberg function is found to decrease at transition pressure (37 GPa in SnAs and 13 GPa in SnSb) compared to ambient NaCl-type structure indicating the decrease in the electron-phonon coupling constant at this pressure, which may further lead to decrease in the T_c for the NaCl-type structure at this pressure. In CsCl phase, from Fig. 5.14(a,b), we have observed overlapping of acoustic and optical modes at different high symmetry directions. Phonon softening around 'M' high symmetry point is observed in CsCl-type for both the compounds. From the susceptibility calculations (from Fig. 5.6(b,d)) these phonon softening may due to Fermi surface nesting in this phase at q-vector around $[0.33, 0.33, 0.33] \times 2\pi/a$ in SnAs and around [0.5 0.5 0.3]×2π/a in SnSb. At the same frequency region, we have observed a peak in the Eliashberg function indicating the T_c in CsCl-type SnSb to be high. This may be a reason for the high T_c in CsCl-type structure compared with NaCl-type structure. Above this pressure and up to the pressure studied, frequency hardening in the same mode is observed with pressure.

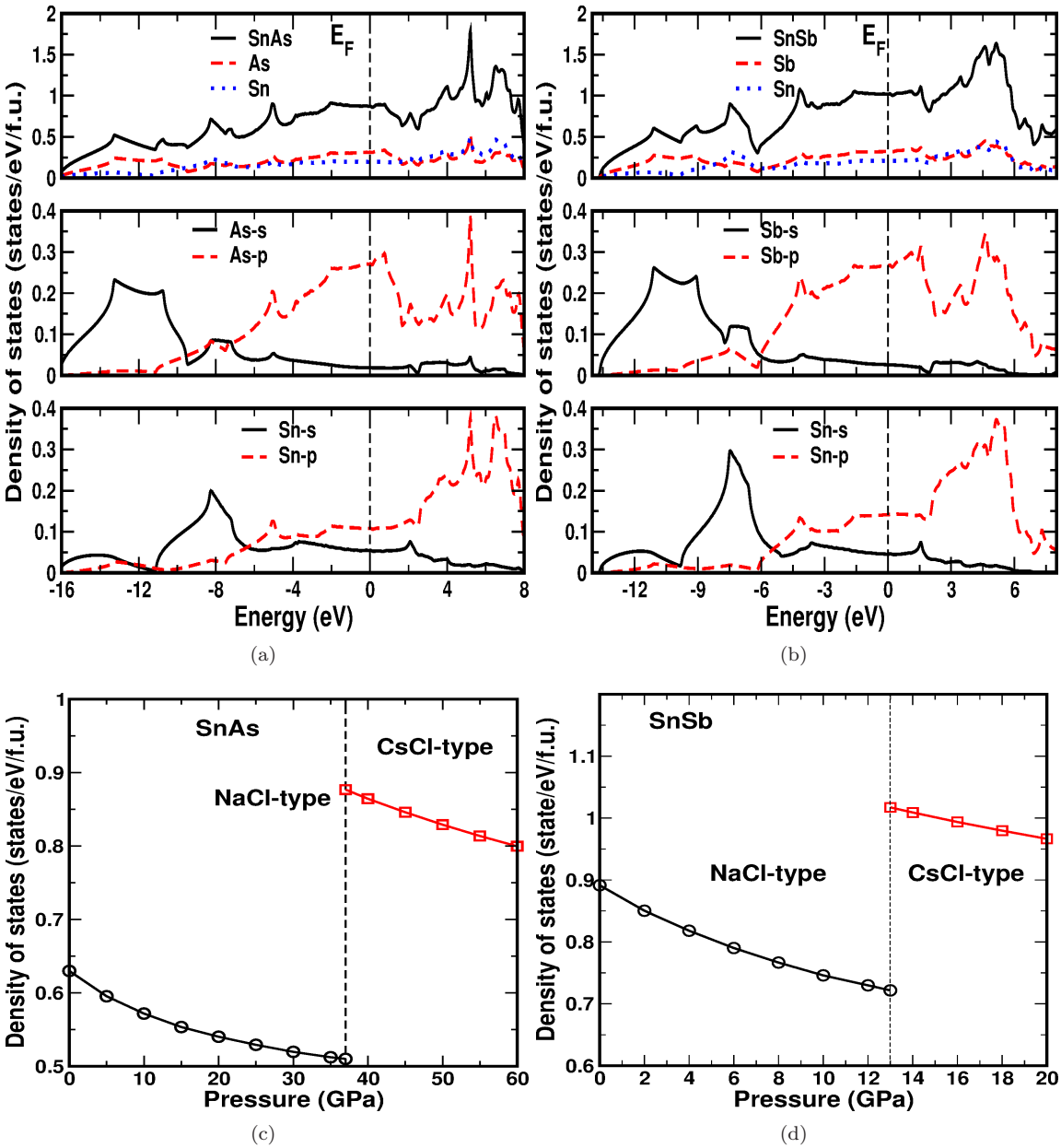

Figure 5.12: Total and atom projected density of states at transition pressure in CsCl-type structure for (a) SnAs at 37 GPa and (b) SnSb at 13 GPa. Variation of total density of states with pressure in (c) SnAs and (d) SnSb.

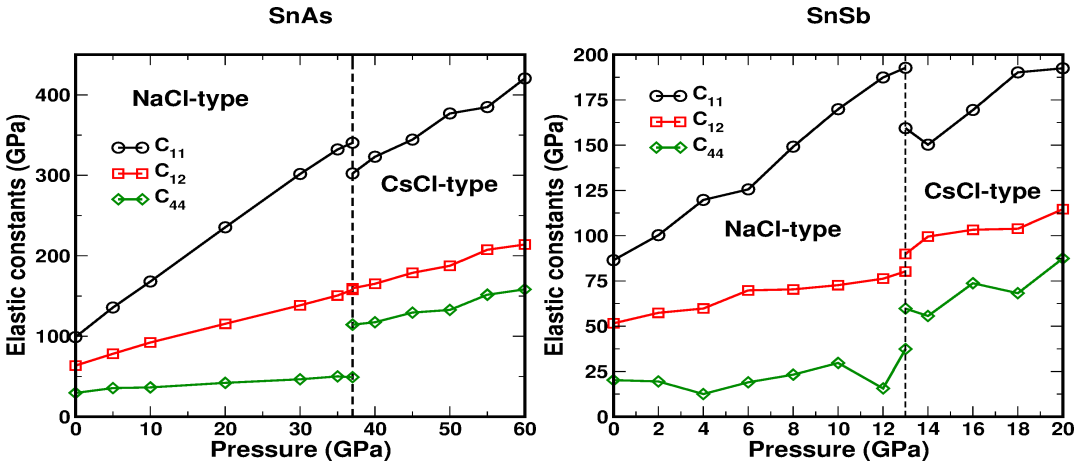

Figure 5.13: Elastic constants as a function of pressure for (a) SnAs and (b) SnSb.

At the transition pressure, when we compare the phonon dispersion plots for both NaCl and CsCl structures, frequency of higher optical modes decreased in CsCl-type structure compared to NaCl-type structure. In addition, a softening nature is observed in CsCl-type near Γ point along Γ-M. In the same way maximum peak in the total PDOS is observed at high frequency optical region in NaCl-type and the same peak is found to be broadened in CsCl-type. In NaCl-type, total PDOS corresponding to acoustic modes is found to be flat but the same in CsCl-type is found to have multiple peaks. As pressure increases up to maximum pressure studied, we have observed hardening in the frequencies of all modes in CsCl-type.

To check the superconducting nature in CsCl phase, we have calculated the superconducting properties of CsCl-type for both the compounds at transition pressure. Surprisingly we have observed high T_c value in the CsCl-type structure around 12.2 and 9.18 K with higher λ_{ep} of 1.08 and 1.55 for SnAs and SnSb respectively. These values are also given in Table 5.3. The reason may be due to the increase in the total electronic DOS in CsCl-type when compared to NaCl-type which will lead to increase the probability of electron-phonon interaction which again may be a reason for the increase in the λ_{ep} and T_c in CsCl-type compared to NaCl-type. Nesting feature in CsCl-type may be another reason for the higher T_c in CsCl-type, where we find a peak in the Eliashberg function ($\alpha^2(\omega)$) in the lower frequency region. But there is no other evidence to confirm our T_c values for CsCl-type in SnAs and SnSb. We have also calculated the variation of T_c, λ_{ep} and ω_{ln} with pressure for both NaCl and CsCl-type structures and are plotted in Fig. 5.15. As pressure increases T_c and λ_{ep} decreases monotonically in NaCl-type but in CsCl-type it is found to have non-monotonic variation with pressure. Eventhough we have not observed any non-monotonic variation in total electronic DOS and change in FS topology with increasing pressure in CsCl-type, but observed non-monotonic variation in λ_{ep} and T_c. This behaviour may be mainly phonon driven and may not be electron driven in the CsCl-type structure in both the compounds [258]. It is also found that T_c follows ω_{ln} behaviour in CsCl-type structure but the same is not observed in NaCl structure. From the present work, CsCl phase is found to have higher T_c and λ_{ep} values compared to NaCl-type indicating the strong coupling nature in CsCl phase for both the investigated compounds.

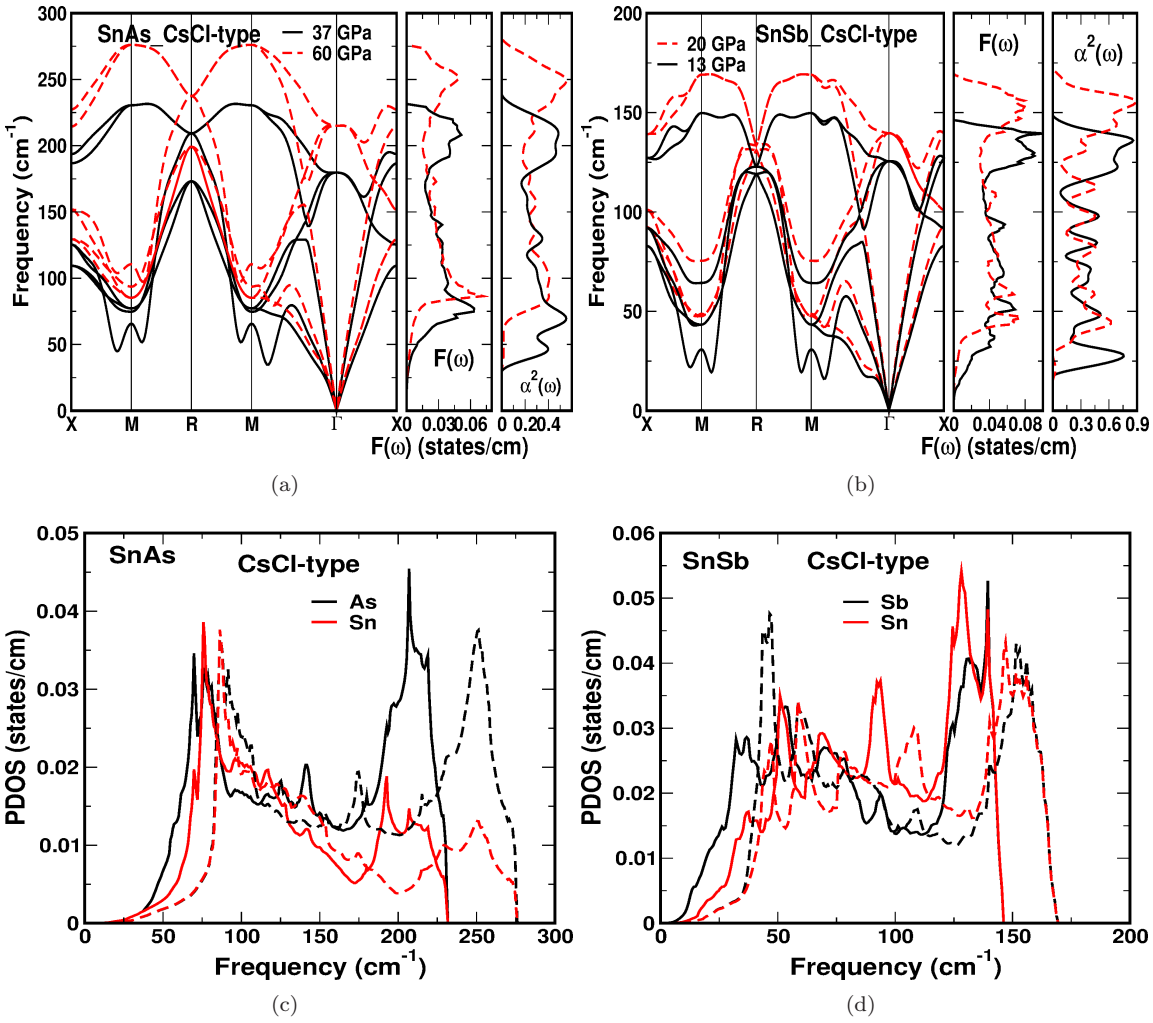

Figure 5.14: Phonon dispersion along with total phonon density of states and Eliashberg function for (a) CsCl phase of SnAs at 37 GPa and 60 GPa, (b) CsCl phase of SnSb at 13 GPa and 20 GPa. (c) Atom projected phonon density of states for SnAs in CsCl phase at 37 (solid lines) and 60 GPa (dotted lines). (d) Atom projected phonon density of states for SnSb in CsCl phase at 13 (solid lines) and 20 GPa (dotted lines).

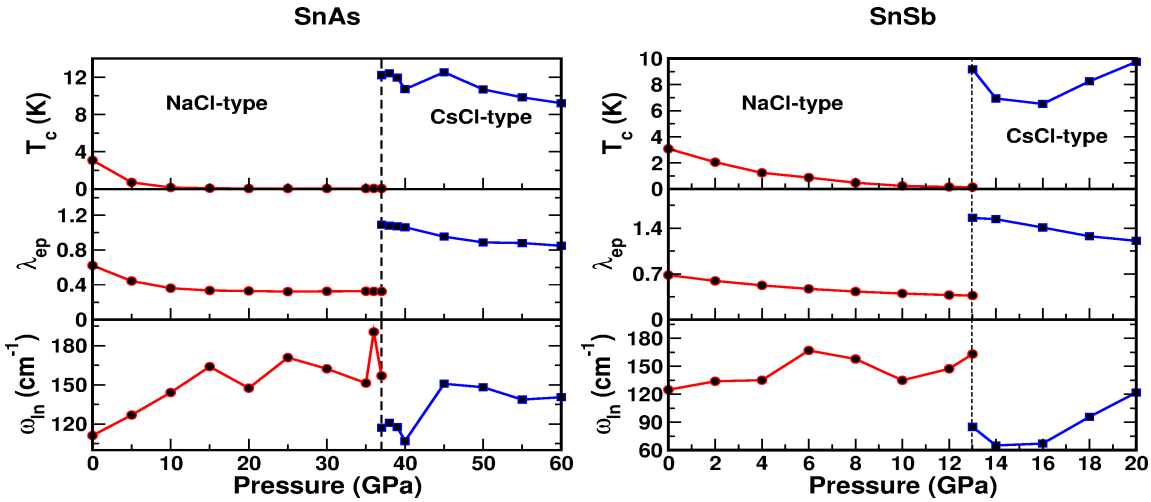

(a) (b)

Figure 5.15: Pressure dependence of T_c, λ_{ep} and ω_{ln} (a) for NaCl-type SnAs up to 37 GPa and CsCl-type above 37 Gpa, (b) for NaCl-type SnSb up to 13 GPa and CsCl-type above 13 Gpa.

5.5 Conclusions

Density functional calculations are performed for both SnAs and SnSb compounds which confirm the stable NaCl ground state in both the compounds. Fermi surface nesting feature is observed and confirmed from the susceptibility calculations in both the compounds at ambient conditions. Phase transition from NaCl to CsCl-type structure is observed at around 37 GPa (V/V_0=0.76) in SnAs and 13 GPa (V/V_0=0.86) in SnSb. At the transition pressure, change in the band structure and FS topology is observed in NaCl-phase together with a softening in the acoustic mode in NaCl type SnAs and SnSb and the same softening nature in the CsCl-type SnAs and SnSb is also observed in the acoustic mode at the same transition pressure. Sudden drop in the T_c and λ_{ep} is observed in NaCl-type with increasing pressure. At the transition pressure around two fold and four fold increase in the T_c is observed in CsCl phase with high λ_{ep} of 1.08 and 1.55 for SnAs and SnSb respectively indicating strongly coupled superconducting nature in CsCl phase which needs to be verified experimentally.

Table 5.1: Calculated lattice parameter (a) in $\AA$, bulk modulus (B) in GPa, total density of states ($N(E_F)$) in states/eV/f.u. and Sommerfeld coefficient (γ) in the units of mJ/mol K^2 for present investigated compounds at ambient conditions in NaCl-type structure and for CsCl-type structure at phase transition compared with available studies.

Parameters	SnAs		SnSb	
	NaCl	CsCl	NaCl	CsCl
a_{exp}	5.72513[a], 5.72[b]	3.300[e]	6.092[f]	-
a_{the}	5.684, 5.812[c]	3.213	6.050, 6.1807[g], 6.173[h]	3.548, 3.7937[g]
B_{exp}	-	-	-	-
B_{the}	75.38, 62.1[c]	207	63, 52.7[g], 53.1[h]	113, 53.8[g]
γ_{exp}	2.18[a]	-	-	-
γ_{th}	1.49, 1.49[d]	2.07	2.10	2.40
$N(E_F)$	0.63, 0.68[c], 0.63[d]	0.88	0.891, 0.95[g], 1.04[h]	1.017

a : Ref. [112]; b : Ref. [256]; c : Ref. [113]; d : Ref. [115]; e : Ref. [110]; f : Ref. [257]; g : Ref. [117]; h : Ref. [250]

Table 5.2: Calculated single crystalline elastic constants C_{11}, C_{12}, C_{44} (in GPa) and mechanical properties of SnAs and SnSb at ambient conditions NaCl-type structure and in CsCl-type structure at transition pressure, where E is Young's modulus (in GPa), A is Anisotropy factor, CP is Cauchy's pressure (in GPa), σ is Poisson's ratio, v_l, v_t, v_m (in km/s) are the longitudinal, transverse and mean sound velocities respectively and Θ_D is Debye temperature (in K). Other values are given in brackets.

Parameters	SnAs		SnSb	
	NaCl	CsCl	NaCl	CsCl
C_{11}	95.85	302.32	86.44	159.36
C_{12}	69.02	159.62	51.60	89.88
C_{44}	27.04	114.44	20.23	59.73
E	56.32	246.51	51.94	126.28
A	2.01	1.60	1.16	1.72
CP (C_{12}-C_{44})	41.98	45.18	31.37	30.15
Pugh's ratio	0.26	0.46	0.30	0.42
σ	0.38	0.30	0.36	0.31
v_l	7.72	5.86	7.01	11.56
v_t	3.40	3.12	3.25	6.02
v_m	3.84	3.49	3.66	6.74
Θ_D	201.71(235[a])	323.67	227(213[b])	377

a : Ref. [112]; b : Ref. [250]

Table 5.3: Superconducting properties (T_c in the units of K) of SnAs and SnSb both at ambient conditions NaCl-type structure and at the transition pressure in CsCl-type structure along with other reported values.

Parameters	SnAs		SnSb	
	NaCl	CsCl	NaCl	CsCl
T_c	3.08 (3.58[a], 3.24[b])	12.2	3.08 (3.1[c])	9.18
λ_{ep}	0.62 (0.62[a], 0.64[b])	1.08	0.68(0.70[c])	1.55

a : Ref. [112]; b : Ref. [113]; c : Ref. [250]

Chapter 6

Magnetic to Non-magnetic transition in Zr_2TiAl and quasi two dimensionality in Cu_2Sb type Mn-based magnetic compounds

In the present chapter, a detailed study on the new ternary Zr_2TiAl and some of Mn-based compounds has been carried out using first principles electronic structure calculations. From the total energy calculations, in Zr_2TiAl, we find an antiferromagnetic $L1_1$-like (AFM) phase with alternating (111) majority spin and minority spin layers to be a stable phase among some others with magnetic moment on Ti being $1.22\mu_B$. The phonon dispersion relations further confirm the stability of the magnetic phase in Zr_2TiAl while the non-magnetic phase is found to have imaginary phonon modes and the same is also found from the calculated elastic constants. In Zr_2TiAl, the magnetic moment of Ti is found to decrease under pressure eventually driving the system to the non-magnetic phase at around 46 GPa, where the phonon modes are found to be positive indicating the stability of the non-magnetic phase. A continuous change in the band structure under compression leads to the corresponding change of the Fermi surface topology resulting in Electronic Topological Transitions (ETT) in both majority and minority spin cases of Zr_2TiAl, which are also evident from the calculated elastic constants and density of states calculations for the material under compression.

In the case of Mn-based compounds, MnAlGe, MnGaGe and MnZnSb, quasi two dimensional nature is observed from the Fermi surface calculations. Under compression decrease in the magnetic moment of Mn atom and change in the band and FS topology is observed in all the Mn-based compounds. Non-linear nature in the elastic constants is observed under compression in all the compounds. Particularly in MnZnSb, a sudden drop in magnetic moment is observed at around $V/V_0 = 0.94$ and also a spin flipping in the total density of states at the same compression is observed. Negative values in the elastic constants are observed in MnZnSb at the same compression around $V/V_0 = 0.94$, where we find a change in band and FS topology correspondingly, and the pressure values corresponding to the compression around $V/V_0 = 0.94$ are in good agreement with experimentally observed anomalies in the calculations of lattice parameters under pressure, which

might imply a possible structural phase transition or an ETT in MnZnSb around this compression.

6.1 Introduction

Zirconium and titanium alloys are of great interest due to a variety of structural and electronic transitions in these materials. They are widely used in aerospace industry due to their light weight, static strength, stiffness and oxidation resistance [259, 260, 261, 262, 263, 264, 265]. This especially concerns their aluminides, Zr_3Al and Ti_3Al, which are important in high temperature applications [266, 267, 268, 269, 270].

Titanium rich and zirconium ternary aluminides can be obtained by mixing Zr_3Al and Ti_3Al. Banerjee [271] and Yang et al [272] confirmed that the Zr atom indeed gets substituted at Ti sites in Ti_3Al. Ravi et al [273, 274] have reported the site preference of Zr atoms in Ti_3Al and the phase stability of Ti_2ZrAl compound. Recently, Zr-rich ternary intermetallic compound Zr_2TiAl has been synthesized by Sornadurai et al. using the arc-melting, vacuum annealing technique [275]. However, no further experimental or theoretical studies have been conducted for Zr_2TiAl. These points are the main motivation of this investigation. Zr_2TiAl has X_2YZ type Heusler structure [275], which is quite different from binary aluminides, and thus interesting physical properties can exists in this case. In particular, as is known, X_2YZ type Heusler compounds can exhibit unusual magnetic properties [276]. For instance, Cu_2MnAl and Cu_2MnSn have a high value of the saturation magnetization and Curie temperature [81, 80].

Some Zr based compounds like $ZrMn_2$ and $ZrFe_2$ have a large magnetic moment as found for Zr, which are coupled anti-parallel to the magnetic moments of Fe and Mn [277]. The electronic structure and physical properties of the solids change under pressure leading to semi-metal to metal transition, magnetic to non-magnetic nature and brittle to ductile nature etc. The magnetic moment, which is one of the physical property of the solid will vanish under pressure. In the case of 3d transition metals like Fe, Co and Ni, the magnetic moment becomes zero at 18 GPa, 150 GPa and 250 GPa respectively [278]. It is also observed that as pressure increases phase change [279] from an antiferromagnetic (AFM) phase to nonmagnetic in $CaFe_2As_2$ and AFM2 to AFM1 in $BaFe_2As_2$. In the case of CsCl-type FeSe a transition from AFM phase to NM phase is observed with intermediate FM phase [280]. In recent studies, [223] hcp Co is observed to become non-magnetic at a pressure of 180 GPa with a series of Electronic Topological Transitions (ETT) at different pressures. Non-monotonic variation of the density of states and superconducting transition temperature (T_C) [281, 282, 215, 283] is observed under pressure. Recently change in the FS topology and non-monotonic variation in the density of states and single crystalline elastic constants is found to lead to the ETT's in Nb based superconducting compounds [284] under compression.

The study of 2D (two dimensional) materials got enormous attention after the invention of graphene, and these materials are explored for wide range of applications, whereas the lack of ferromagnetic order in graphene restricts the application of graphene in magnetic or magnetoelectric field in its pure form. Here comes the importance of inherent 2D ferromagnetic materials. The investigation of low dimensional ferromagnetic materials are of current interest, and the scientific world is now fascinated by the result of the experimental realization of 2D magnet [285]. Van der waals crystals are the main platform to identify the 2D magnetism, and in recent past few of the layered materials are identified as quasi two dimensional magnetic materials [286, 287]. From this point of view, understanding the electronic structure of layered magnetic materials, can open up the possibility of two dimensional magnetism which is very crucial. Here we would like to investigate few of the Mn based compounds, which has been claimed as quasi two dimensional material and

need to be give more attention.

The intermetallic compounds MnAlGe, MnGaGe and MnZnSb crystallize in tetragonal Cu_2Sb-type structure. These compounds are derived from Mn_2Sb which is ferrimagnet with a Neel temperature of 550 K, where Mn atoms have inequivalent sites, MnI and MnII. By doping MnII atoms with non-magnetic elements like Al, Ga and Zn, we can get the ternary MnAlGe, MnGaGe and MnZnSb compounds. These compounds are reported to be ferromagnet with Curie temperature around 503 K, 453 K and 320 K respectively for MnAlGe, MnGaGe and MnZnSb. From the crystal structure point of view, the magnetic Mn layers are separated by two non-magnetic layers containing elements Al-Ge or Ga-Ge or Zn-Sb which projects these layered compounds to possess nearly two dimensional magnetic nature. The distance between Mn-Mn along a or b-axis(inplane) is equivalent with lattice parameter 'a or b' and along c-axis(out of plane) is equivalent to lattice parameter 'c'. In these compounds, as length of 'c' axis increases Curie temperature is also found to increase [124] and indicating the importance of interlayer distance along 'c' axis in raising of the Curie temperature.

These Mn-based magnetic materials of present study are ferromagnetic with a large uniaxial magneto crystalline anisotropy with the easy axis along tetragonal 'c' axis. These type of materials useful applications in spintronic devices [125]. To study the application of MnAlGe in magneto-optic field, Sherwood et al [126] prepared the polycrystalline thin films and found to have promising application for magneto-optic devices. These systems can be used in magneto-optic devices for the storage of large amount of information. Particularly present compounds are suitable for storage applications[127] with a capacity of 10^7 bits/cm^2.

Apart from the above mentioned studies self consistent band structure calculations were performed by Motizuki et al [128] and confirmed that the magnetic moments arise from the itinerant electrons. Later quasi two dimensional magnetism in MnGaGe is observed by Mohn and Schwarz [129]. In 2006, kimura et al [130] confirmed a strong two dimensional nature in these compounds form the calculated Fermi surfaces particularly for minority spin case.

In 1963, Velge and De Vos [131] observed the influence of milling on the magnetic properties of MnAlGe, where the saturation magnetisation and the coercivity decrease appreciably after the mechanical loading which does not involve a reduction in particle size which indicate that structural imperfections, rather than the changes in particle size, may play an important role. After that, a linear decrease in the 'a' and 'c' lattice parameters is observed with increasing pressure upto 4 GPa in both MnAlGe and MnGaGe by Kanomata et al [132]. In the case of MnZnSb Mastuzaki et al [133] studied the effect of pressure on Curie temperature and lattice parameters up to 8 GPa and observed anomalies in the pressure ranges between 4.2 to 6 GPa. In the present compounds increase in the Curie temperature is observed with pressure. The values of dT_c/dP is found to be 32 K/GPa, 30 K/GPa and 28 K/GPa for MnAlGe [134], MnGaGe [135] and MnZnSb [133] respectively. It also confirmed that this large positive pressure effect on Curie temperature is due to superexchange between Mn-Mn atoms along c-axis [133]. No literature is available about the band, Fermi surface and magnetic nature under pressure and this motivated us to perform the present calculations.

The main aim of the present chapter is to study the magnetic behaviour of the present compounds and its pressure dependence. The chapter is organized as follows: Section 6.2 presents computational details. The results and discussions at ambient conditions are presented in section 6.3. The pressure effect on various properties of the investigated compounds discussed in section 6.4. Finally, conclusions are presented in section 6.5.

6.2 Methodology

Several first-principles methods based on density functional theory (DFT) have been used in the present work to calculate the electronic structure, elastic constants and magnetic properties of Zr_2TiAl and Mn-based compounds. Full-Potential Linearized Augmented Plane Wave (FP-LAPW) method as implemented in the WIEN2k [153] code is used to calculate the electronic structure and Fermi surface properties with spin polarization. We have used PBE-GGA [186] (Perdew-Burke-Ernzerhof parametrization of the Generalized Gradient Approximation) approximation for the exchange correlation potential. Throughout the calculations, the R_{MT} (radius of muffin tin spheres) value for each atom was fixed as 2.39 a.u for Zr atom, 2.45 a.u for both Ti and Al atoms for Zr_2TiAl, 2.2 a.u for Mn, 1.9 a.u for Al, 2.0 a.u for Ge, 2.0 a.u for Ga, 2.2 a.u for Zn and 2.3 a.u for Sb atom for Mn-based compounds. For Zr_2TiAl, the plane wave cut-off has been chosen to satisfy R_{MT}*K_{max}=9 and the potential and charge density were Fourier expanded up to G_{max}=9 a.u^{-1}.In the case of Mn-based compounds R_{MT}*K_{max}=9 G_{max}=12 a.u^{-1} was used. For Zr_2TiAl, all the electronic properties like density of states and the Fermi surface have been calculated using $44 \times 44 \times 44$ k-point grid of the Monkhorst-Pack [187] mesh, which yields 2168 k-points in the irreducible part of the Brillouin Zone (BZ). In the case of Mn-based compounds, $35 \times 35 \times 23$ k-mesh in the Monkhorst-Pack [187] scheme which gives 2223 k-points in the irreducible part of the Brillouin Zone was used. This ensures accurate determination of the Fermi level and ground state properties. Energy convergence up to 10^{-5} Ry is used to get the proper convergence of the self consistent calculation. The Brillouin zone integration has been done by the tetrahedron method [188]. The Birch-Murnaghan [189] equation of state has been used to fit the total energies as a function of primitive cell volume to obtain the bulk modulus and the equilibrium lattice parameter for the investigated compound.

For Zr_2TiAl, phonon dispersions and electron-phonon interaction were calculated using the plane wave ultrasoft pseudopotential method (PWSCF) which is implemented in QUANTUM ESPRESSO code [154]. The GGA-PBE exchange correlation functional is used in these calculations for all the compounds. The maximum plane wave cut-off energy (ecutwfc) was 50 Ry and the electronic charge density was expanded up to 500 Ry. Gaussian broadening of 0.01 Ry and a $4 \times 4 \times 4$ uniform grid of q-points are used for phonon calculations.

We have not found any significant change in the electronic structure at the Fermi level with the inclusion of spin-orbit coupling (SOC), so the reported calculations are without SOC.

6.3 Results and discussions at ambient conditions

6.3.1 Zr_2TiAl

Ground state properties

In order to study the ground state properties, the total energy of Zr_2TiAl has been calculated in four different magnetic states: ferromagnetic (FM), two AFM states, AFM1 and AFM2, as well as non-spin-polarized or nonmagnetic (NM) state. The calculated AFM structures are shown in Fig. 6.1. For AFM1, the spin orientation of Ti (111) planes is anti-parallel to each other between the adjacent Ti (111) planes (Fig. 6.1(a)). In case of AFM2, the spin orientation of first two Ti planes is parallel to each other and anti-parallel to next two Ti planes as shown in Fig. 6.1(b).

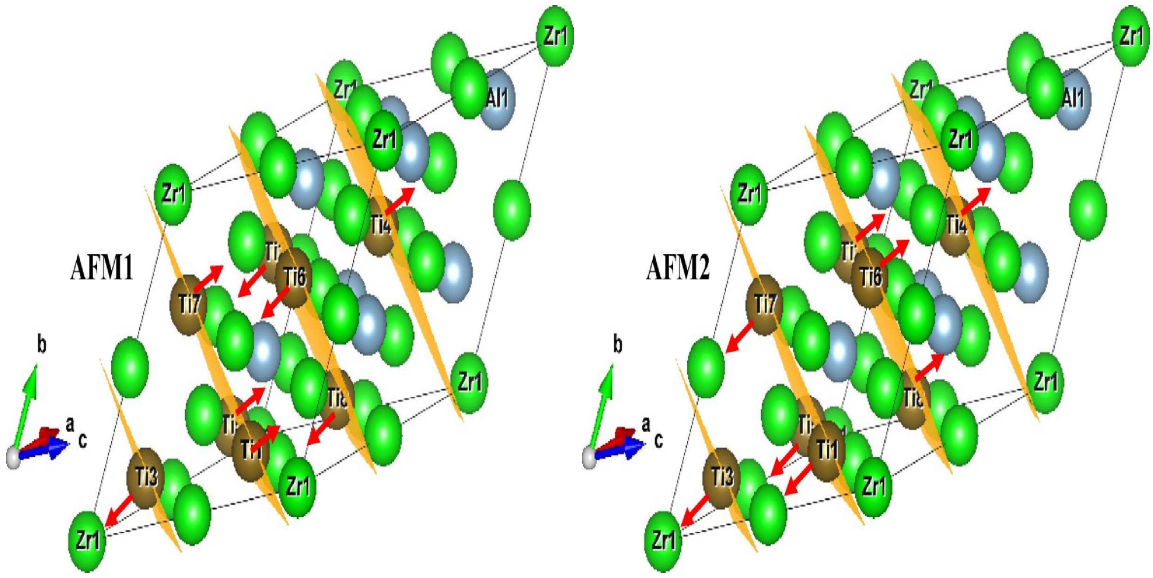

(a) (b)

Figure 6.1: Calculated AFM structures: (a) AFM1: Anti-parallel spin alignment between two Ti (111) planes in the [111] direction; (b) AFM2: Double ferromagnetically aligned (111) Ti planes, which are antiferromagnetically aligned to the next two ferromagnetically aligned Ti(111) planes in the [111] direction.

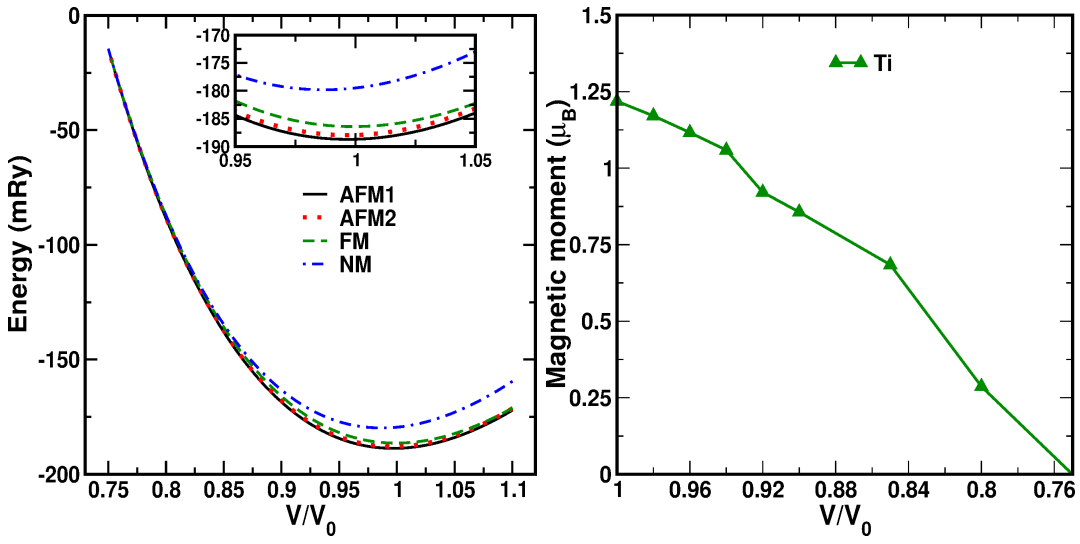

(a) (b)

Figure 6.2: (a) Total energy variation as a function of V/V_0 for Zr_2TiAl in AFM1, AFM2, Ferromagnetic and non-magnetic cases, (b) magnetic moment of Ti under compression for Zr_2TiAl.

The total energies are shown in Fig. 6.2(a). As one can see, the AFM1 state has the lowest energy among the considered structures with a magnetic moment of 1.22 μ_B at Ti site. The total energy increases in the sequence: AFM1 $\rightarrow$ AFM2 $\rightarrow$ FM $\rightarrow$ NM. The energy difference between AFM1 and AFM2 is 0.76 mRy/f.u., while it is 2.22 mRy/f.u. between AFM1 and FM and 9.17 mRy/f.u. between AFM1 and NM states. This result is highly unexpected since none of the alloy components is magnetic.

The calculated lattice parameter (a) and bulk modulus values using the Birch-Murnaghan equation of state are given in Table 6.1. The calculated lattice parameter is in good agreement with the experiment [275]. Sieberer et al [293] concluded that if both LDA and GGA predict a magnetic ground state at equilibrium lattice constant, then the system is magnetic. From Table 6.1 we can observe that both LDA and GGA predict a magnetic moment for Ti atom indicating the magnetic nature of present compound. We further performed the electronic structure calculations using the optimized lattice parameter.

Electronic structure

The calculated band structures are given in Fig.6.3 for AFM1, AFM2 and FM states in the supercell as shown in Fig.6.1. In AFM1 case the majority and minority band structures are degenerate and we have plotted only majority spin bands in Fig.6.3(a). The Fermi level is aligned to 0 eV. From the band structure we have observed five bands to cross Fermi level (E_F) and are given in different colours in AFM1. Similarly, band structure of AFM2 state is given in Fig.6.3(b), which is almost similar to AFM1 with a change in the band structure topology along W-L and X-W-K directions where the bands are compressed near E_F in comparison with AFM1 band structure. For the same supercell FM calculations are done and the calculated majority and minority band structures are given in Fig.6.3(c) and 6.3(d). The number of bands to cross Fermi level (E_F) is different in both majority (five bands) and minority spin (four bands) cases of FM state which are indicating the non-degenerate behaviour in the band structure topology. In FM case we find absence and presence of bands near the E_F around Γ point in majority and minority spin cases respectively. For further calculations we proceed with the initial Heusler structure(with space group $Fm\bar{3}m$) as the energy difference between FM and AFM is very low.

The calculated energy bands corresponding to both majority and minority spin case for the ferro magnetic phase of Zr_2TiAl for normal Heusler structure(with space group $Fm\bar{3}m$) are shown in Fig.6.4(a,b) along the high symmetry directions of the cubic FCC (face centred cubic) Brillouin zone (BZ). We have observed that in both majority and minority spin channels only one band is crossing the Fermi level (E_F) and indicate the metallic nature of the investigated compound. The valence band has a band width of around 7 eV in both majority and minority spin. It may be seen that the low lying band (at -5 eV), which give rise to the low energy tail in the density of states is mainly of Al-'s' states. The higher lying bands in the vicinity of Fermi level are primarily Zr-'d' and Ti-'d' derived states. The band which is crossing the E_F from valence band to conduction band in the case of majority spin is of hole nature and in the case of minority spin it is having same nature with a pocket at the Γ point. From the keen observation of the band structure, we have found almost non-dispersive band just below the E_F in both majority and minority spin cases. In majority spin case it is observed along L-Γ-X and the same is observed in minority spin case along W-L and W-K directions. This feature is particularly called as van Hove singularity which might result in a peak

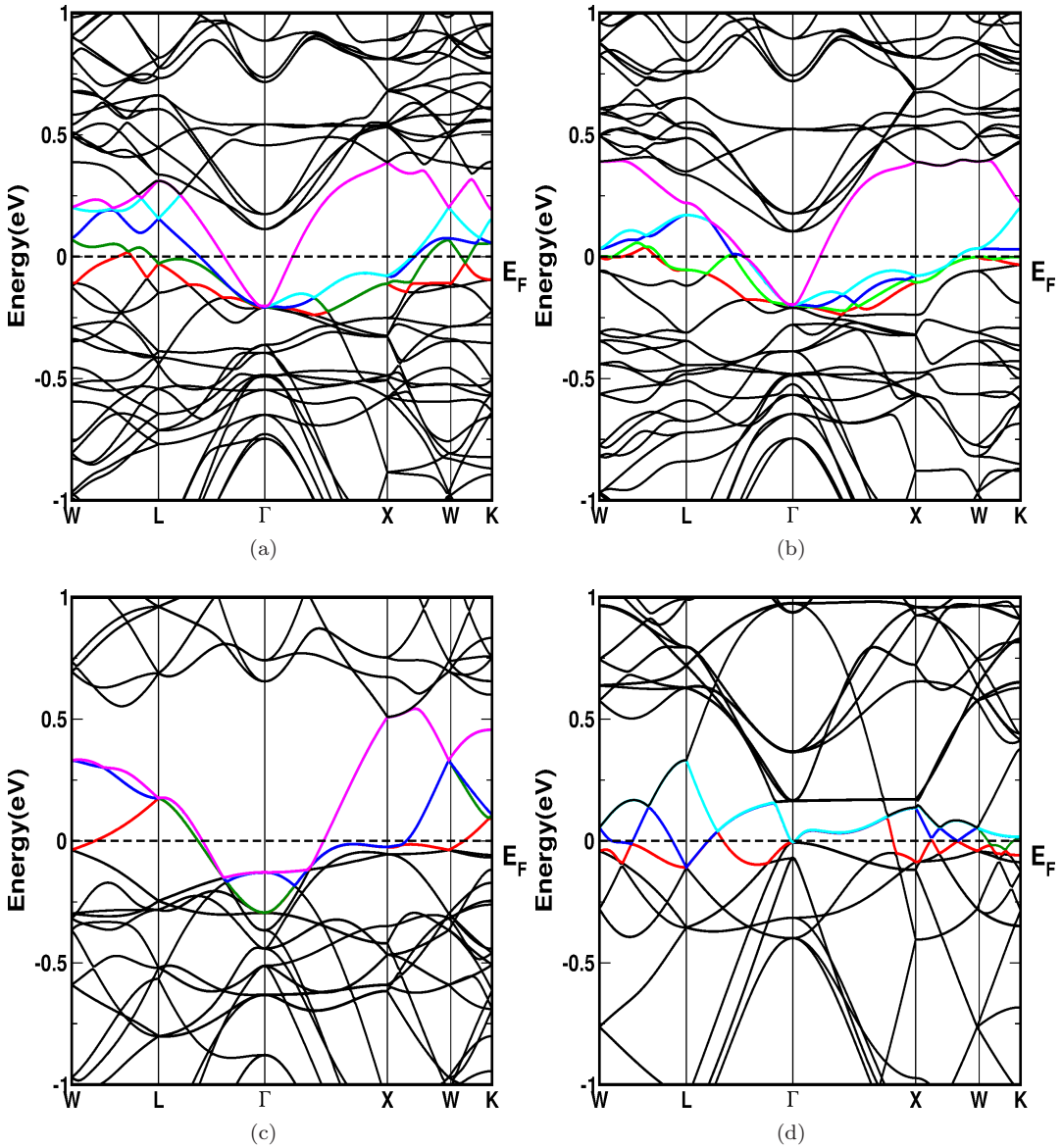

Figure 6.3: Band structure for Zr_2TiAl at ambient conditions (a) AFM1 state, (b) AFM2 state and Ferromagnetic (c) majority spin (d) minority spin in extended cell case.

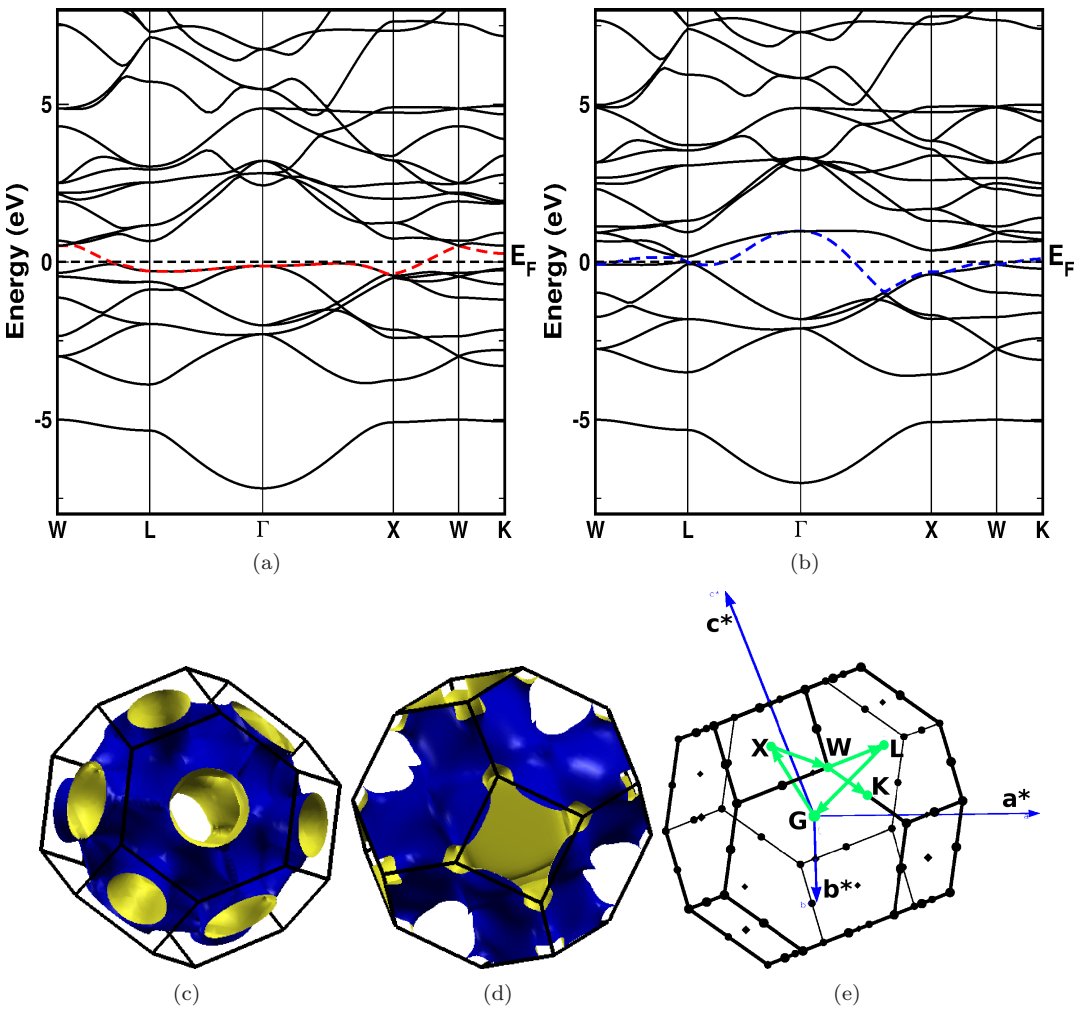

Figure 6.4: Band structure for Zr_2TiAl at in Ferromagnetic state in primitive cell (a) majority band, (b) minority band. Fermi surface for Zr_2TiAl at Ferromagnetic state (c) majority case, (d) minority case and (e) Brillouin zone.

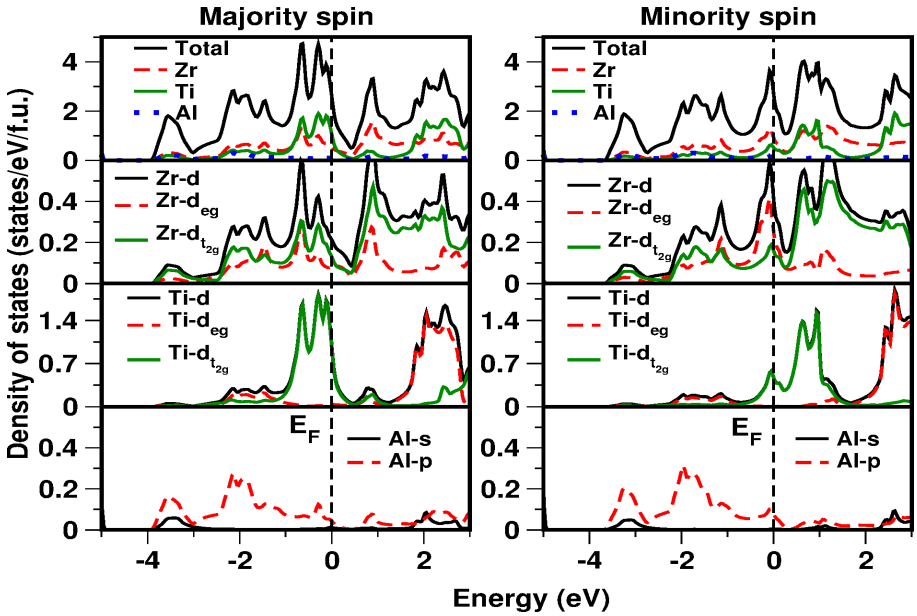

Figure 6.5: Density of states at ambient conditions for Zr_2TiAl for both majority and minority spins.

in the electronic density of states.

Further to understand the electronic density of states (DOS) at the E_F in the present investigated compound, we have calculated the total, atom projected and orbital projected density of states using tetrahedron method [188] and are given in Fig.6.5. For both majority and minority spin there is a separation between bonding and anti bonding regions and the Fermi level lies in the bonding region and lies very close to the pseudo gap. The total DOS ($N(E_F)$) value for the majority spin is 2.677 states/eV/f.u. and for the minority spin, it is 2.630 states/eV/f.u. It is evident that the low lying bands in both majority and minority spin are mainly due to Al-'*s*' orbitals as stated earlier and are well separated from the higher lying '*p*-*d*' band gap indicating a weak hybridization with higher bands in both majority and minority spin. From the calculated atom projected DOS, we can see that at E_F, the major contribution is from the Ti atom in the majority spin, especially Ti '$d_{t_{2g}}$' states. In the minority spin especially 'd_{eg}' states of Zr atom contribute more at the E_F. As previously discussed the peak below the E_F in majority spin case and on the E_F in the minority spin case are due to van Hove singularity in the band structure.

To analyse the Fermi surface topology of the bands which cross the E_F in both spin cases we have calculated Fermi surfaces (FS) for the corresponding bands and are shown in the Fig. 6.4(c,d). As we already discussed, the FS for majority spin has a hole sheet (Fig. 6.4(c)) which is due to the band crossing the E_F from valence band to conduction band along W-L and X-W-K directions as shown with dotted line in Fig. 6.4(a). In this FS we have openings at X and L points in the BZ where the band crossing is absent in the BZ. In the case of minority spin we have single FS (Fig.6.4(d)) which have pocket around Γ point due to the band crossing at the same Γ point from valence band to conduction band. This Γ point pocket is covered with a sheet except at the square face of the BZ which is due to the band crossing E_F along W-L and W-K directions from valence band to conduction band which is shown with dotted line in Fig.6.4(b).

To discuss the bonding in the present compound, we have calculated the difference charge den-

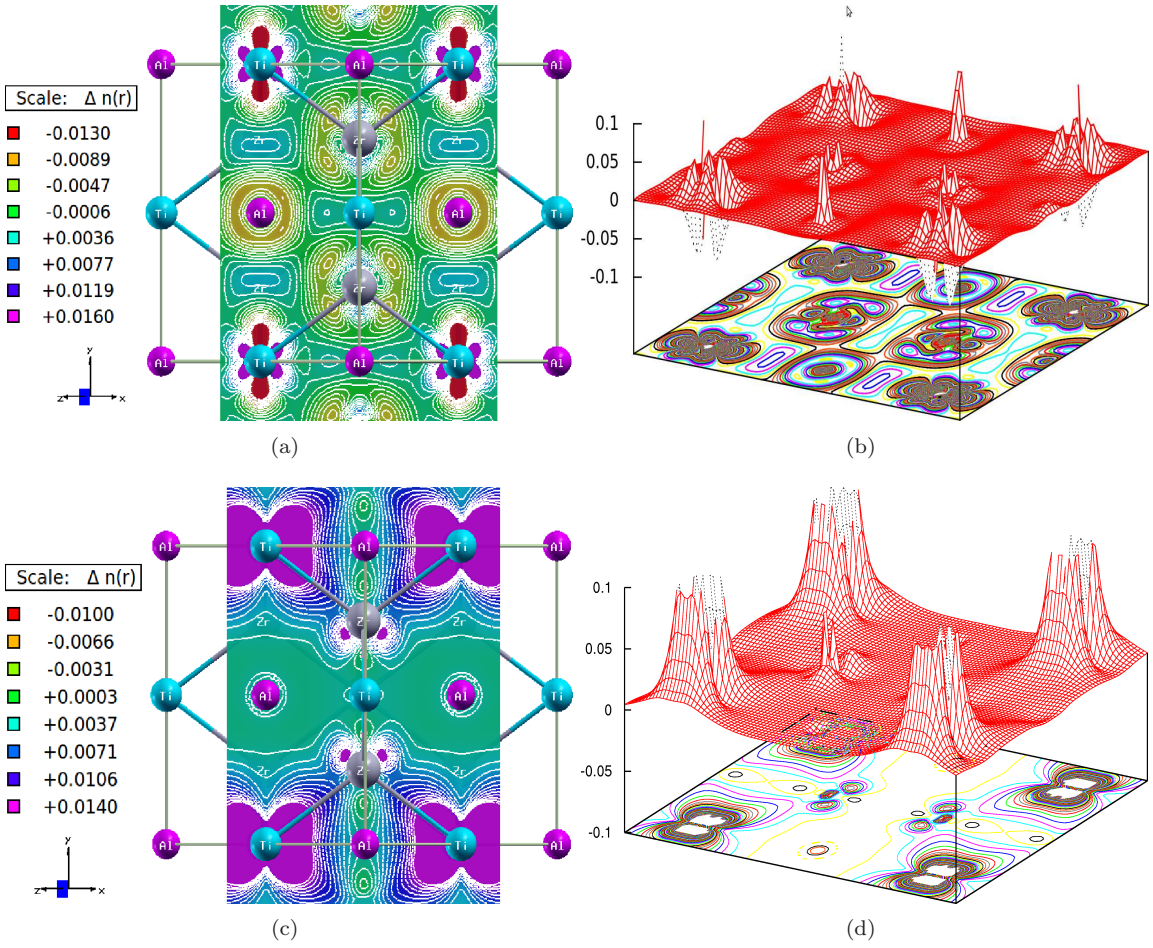

Figure 6.6: Difference charge density plot for Zr_2TiAl (a) in 2D and (b) in 3D, spin charge density plot (c) in 2D and (d) in 3D.

sity(indicates charge gain and loss) and spin charge density and are given in Fig. 6.6. Pauling electro negativity values for the constituent atoms are 1.33, 1.54 and 1.61 for Zr, Ti and Al atoms respectively. There is a possibility of charge transfer from Zr and Ti to Al due to its high electro negativity values. Due to this charge transfer the Ti^{3+} state would be formed, which is due to the loss of three valence electrons and has only one free electron. Due to this free electron a possible spin magnetic moment will arise which could be a reason for the present magnetic moment at Ti site. We have also calculated the Bader charge [294] to identify the charge flow among the constituent elements as given in Table 6.2. The calculated values are 0.47e for each Zr atom, 0.12e for Ti and -1.07e for Al at ambient conditions. This shows the charge flow from Zr and Ti elements to Al. As Al is the most electronegative element in this compound it will pickup 0.47e from each Zr and 0.12e from Titanium. The latter again follows from the electro negativities, as Zr is more electro positive than Ti. From the calculated spin charge density plots we can observe that the magnitude of the spin density is more at the Ti atoms site rather than other atoms. This indicates that the effect of Ti is more compared to other elements contributing to the magnetic nature in the present compound.

Elastic constants

To check the mechanical stability of the present compound we have calculated the elastic constants for both magnetic and non-magnetic cases and are given in the Table 6.3 at ambient conditions. The calculated single crystalline elastic constants C_{11}, C_{12} and C_{44} are found to satisfy the Born mechanical stability criteria [192] i.e. $C_{11} > 0$, $C_{44} > 0$, $C_{11} > C_{12}$, and $C_{11}+2C_{12} > 0$, in magnetic case. But in the case of non-magnetic case these criteria are not fulfilled. This further confirms the mechanically stable nature of the present compound in magnetic case.

Phonon dispersion

In order to comment on the phase stability of the investigated compound, we have calculated the phonon dispersion relations along the high symmetry directions of the Brillouin zone at ambient conditions for both magnetic and non-magnetic phases illustrated in Fig.6.7 along with the partial phonon density of states. In each plot there are 12 phonon branches as the unit cell of Zr_2TiAl contains four atoms. There are three acoustic and nine optical branches. The absence of imaginary modes in the magnetic phase as shown in Fig.6.7(a) indicates the stability in the magnetic phase at ambient conditions, whereas the instability in the non-magnetic phase at ambient conditions is observed with the presence of imaginary mode along Γ- X - W direction as shown in Fig.6.7(b). By comparing these phonon dispersion plots in both the cases at ambient conditions, frequency hardening is observed in magnetic phase rather than in non-magnetic phase. In both phases the higher frequency optical modes at nearly 265 cm^{-1} are separated with a gap of 80 cm^{-1} from other lower frequency modes. From the calculated partial phonon density of states we can say that the vibrational energies are higher in magnetic phase compared to the non-magnetic phase. Again from the partial phonon density of states, the higher frequency optical modes are due to the lighter Al atoms in both magnetic and non magnetic case. In the magnetic case the modes near the frequency 175 cm^{-1} are separated from higher and lower frequency branches and are due to the contribution of the Ti atoms. In lower frequency region the contribution of all atoms is same in both magnetic and non-magnetic case.

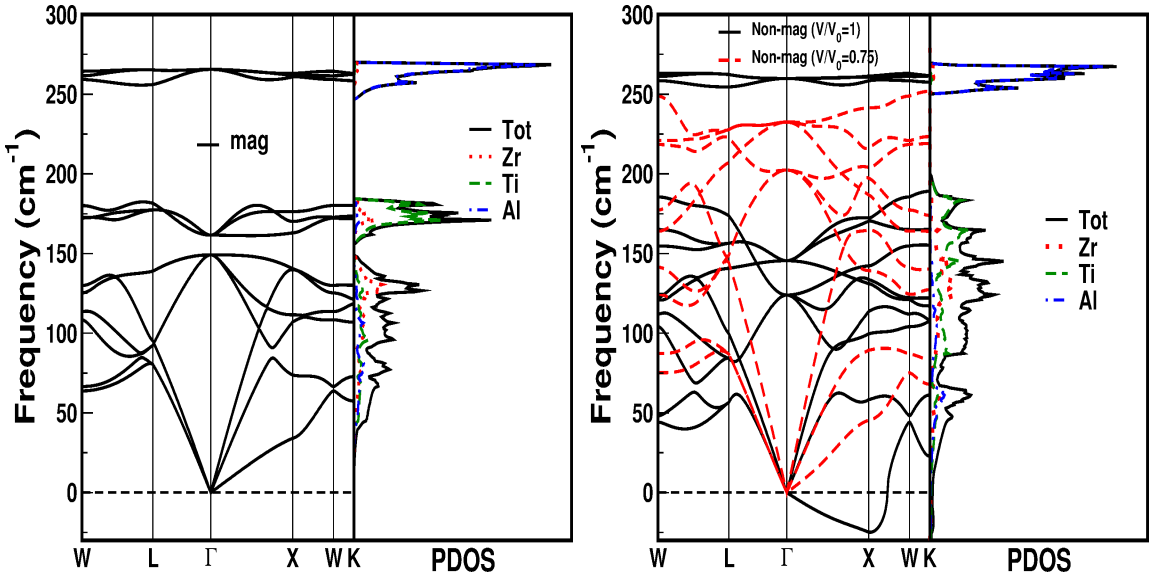

Figure 6.7: Phonon dispersion plots along with partial phonon density of states at ambient conditions (a) magnetic case and (b) non magnetic case (black continuous line for V/V_0=1.0, red dotted line for V/V_0=0.75) for Zr_2TiAl.

As shown and already discussed, the magnetic phase is found to be stable at ambient conditions, but under pressure we find a second order phase transition from magnetic to non-magnetic phase, where we find the magnetic moment of Ti to vanish as shown in Fig.6.2(b) at a pressure of 46 GPa. A detailed discussion of the pressure effect on the above mentioned properties is given in the next section.

6.3.2 Mn-based compounds

Ground state and electronic structure properties

Cu_2Sb type Mn based compounds have tetragonal structure with space group $P4/nmm$ (no. 129). Atomic positions are taken as Mn at 2a (0.00, 0.00, 0.00), Al/Ga/Zn at 2c (0.00, 0.50, z), and Ge/Sb at 2c (0.00, 0.50, z') where z and z' values are taken as 0.273 and 0.720 for all the compounds and the optimized positions are given in Table 6.4. Crystal structure for the present compounds is given in Fig. 6.8(a) for structure with origin choice 1 and in Fig. 6.8(b) for origin choice 2. All the calculations are performed with origin choice 2 structure. By using these optimized positions we have calculated the equilibrium lattice parameters for all the investigated compounds and are given in Table 6.5. The calculated magnetic moment of 'Mn' atom with the equilibrium lattice parameters for these compounds is also given in the same table and the values are in good agreement with the experiments for MnAlGe and MnGaGe, but is over estimated for MnZnSb, yet comparable with the other available results. Crystal structure of these compounds is isostructural with Mn_2Sb, but magnetic structure is very simple as one of the Mn atoms of the molecule is replaced by a nonmagnetic atom Al/Ga/Zn. The planes consisting of Mn atoms are perpendicular to the 'z' axis and the distance between the adjacent planes is very large. It seems to be a strong direct bonding

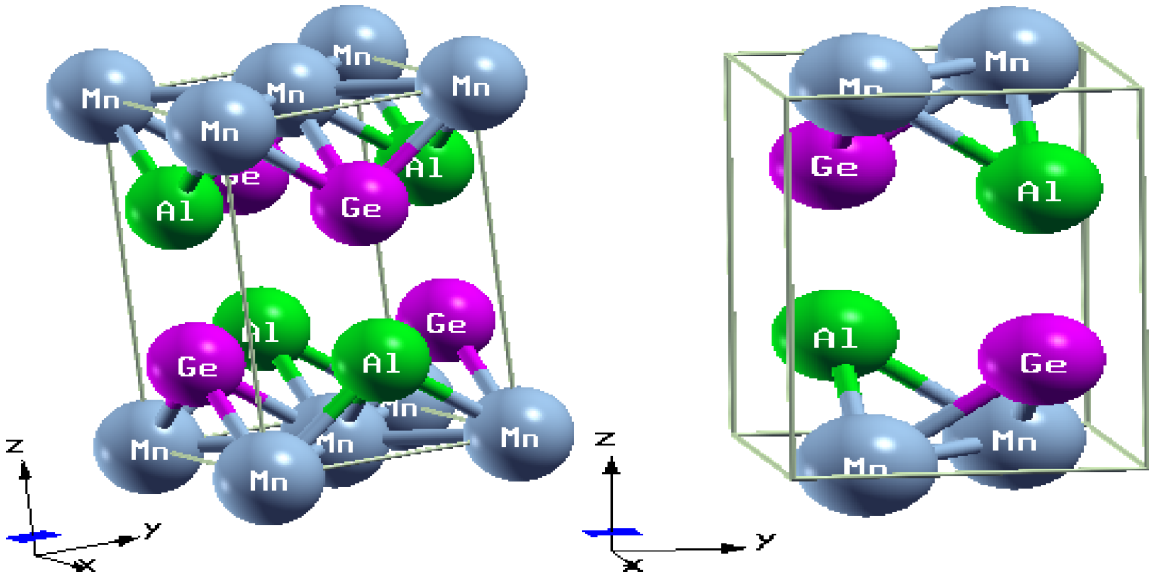

(a) (b)

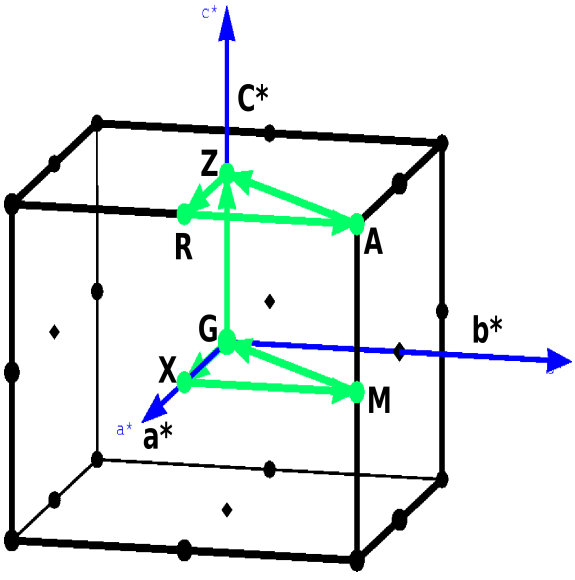

(c)

Figure 6.8: Crystal structure of Mn based compounds (a) origin choice 1 (b) origin choice 2. All the present calculations are performed by using origin choice 2 structure. (c) Brillouin zone for the present compounds

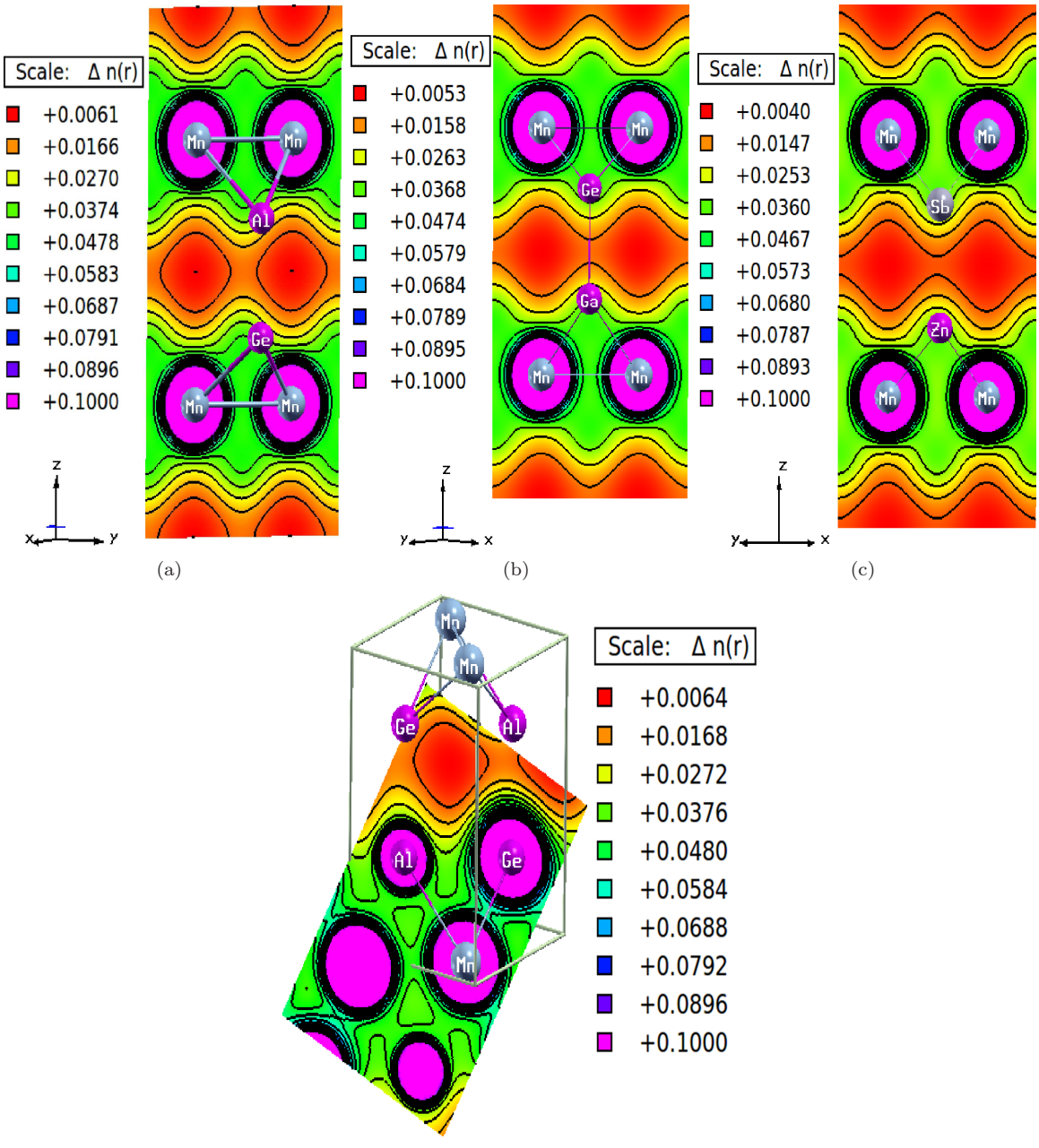

Figure 6.9: Charge density plots among in-plane and out-of plane Mn atoms (a) MnAlGe, (b) MnGaGe, (c) MnZnSb and (d) among all atoms in MnAlGe(this is similar to remaining compounds also).

of magnetic atoms in the net planes and a relatively weak bonding between two planes of magnetic and nonmagnetic atoms which is considered to be a typical two dimensional ferromagnetic system. Though the magnetic moment of Mn atoms is usually large in some of the intermetallic compounds such as 11-type MnAs, MnSb (around 3.5 μ_B) and in some of the Heuslar alloys (around 4 μ_B), the magnetic moment per Mn atom making the two-dimensional net plane in the present compounds is small (see the Table 6.5). Calculated atomic distances are also given in the same table where one can see the Mn-Mn distance along the '*c*'-axis to be almost twice as that of the Mn-Mn distance within the layer which causes the magnetically two dimensional nature in the present compounds. To understand the chemical bonding of the constituent elements in the present compounds, we have given the electronic charge density plots for all the compounds in Fig. 6.9. From the figure it is quite clear that bonding within the '*ab*' plane Mn atoms (shown with green colour) is stronger than the bonding along '*c*'-axis Mn atoms(shown in red colour). To know the charge density among the constituent elements the charge density plot for Mn-Al-Ge is given in Fig. 6.9(d). From this, we have observed that the bonding is more pronounced between Mn-Ge/Sb atoms compared to Mn-Al/Ga/Zn and Al/Ga/Zn-Ge/Sb. The strong in-plane bonding and weak out of plane bonding clearly give an insight towards quasi two dimensional nature of these compounds. This charge flow depends on the electronegativity of the atoms and the difference in electronegativity values between them. The electronegativity values for the constituent elements are 1.55(Mn), 1.61(Al), 2.01(Ge), 1.81(Ga), 1.65(Zn) and 2.05(Sb). If we consider the systems like MnXY(X=Al/Ga/Zn and Y=Ge/Sb), electronegativity value of Y element is more, less for Mn and moderate for X element in all the compounds. So, charge flow will be more between Mn-Y atom compared to Mn-X and X-Y which is concluded from the charge density plots.

The calculated band structure and Fermi surface (FS) for all the compounds is given from Fig. 6.10 to Fig. 6.12 for both majority and minority spins. The overall band profile is looking similar for all the compounds except the number of bands crossing the Fermi level (E_F) and nature (electron/hloe) of these bands at E_F. For all compounds in both majority and minority spin cases, the bands are doubly degenerate along X-R-A-M-X and in remaining directions the degeneracy is lifted out. Highly flat bands are observed along Γ-Z (along *c*-axis) direction, and a dispersive nature is observed along Γ-X (along *a*-axis) direction, which shows the signature of quasi two dimensional nature of these compounds, and the mixture of heavy and light bands might contribute for better thermoelectric properties in these compounds. It is to be noted that the first FS in all the investigated compounds for majority spin case, is similar and have a hole pocket at R point. From the overall FS topology, we can see the two dimensionality in FS particularly in minority spin case for all the compounds.

In MnAlGe, two bands are found to cross E_F in both the spin cases and are indicated with colour(red and green) as shown in Fig. 6.10. In the case of majority spin the red colour band crosses the E_F only at R point from valence band to conduction band which may have hole pockets at R point in the Fermi surface. The remaining band which is shown in green is crossing the E_F twice and may have a mixed sheet in the Fermi surface. These two bands have Mn-'d_{xz}+d_{yz}' character near E_F. In the case of minority spin band, red color band cross E_F at different high symmetry points and have mixed character of Mn-'d_{z^2}' and 'd_{xy}' but the remaining band cross E_F along X-R and have Mn-'d_{xy}' character. As we move from MnAlGe to MnGaGe, where 'Al' is replaced with 'Ga', which is same group element(band structure and FS are given in Fig. 6.11), E_F is found to

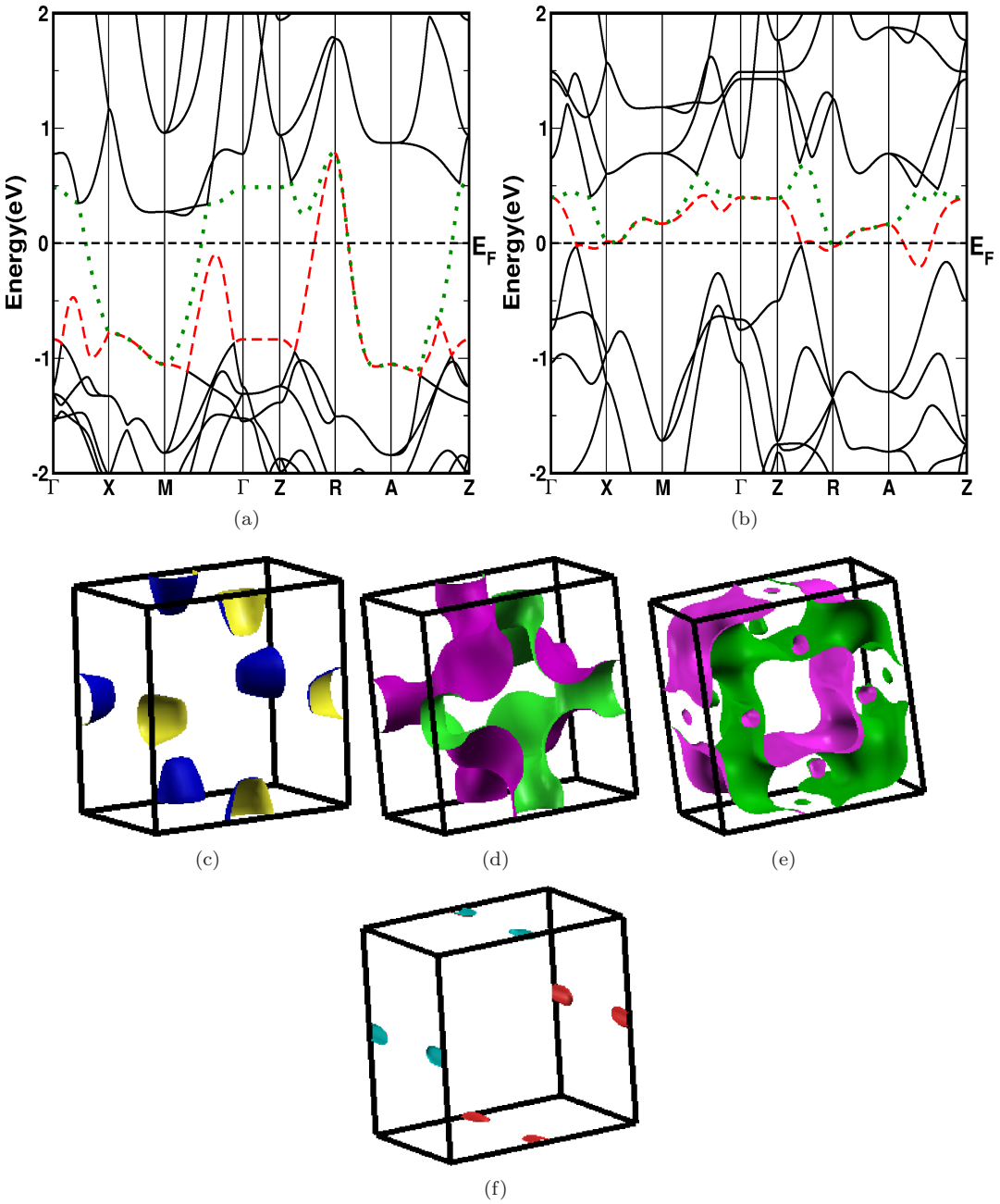

Figure 6.10: Band structure for MnAlGe (a) majority spin (b) minority spin. Fermi surfaces of MnAlGe in both majority spin and minority spin cases. First two (c, d) FS belongs to majority spin case and the remaining two (e, f) belong to minority spin case.

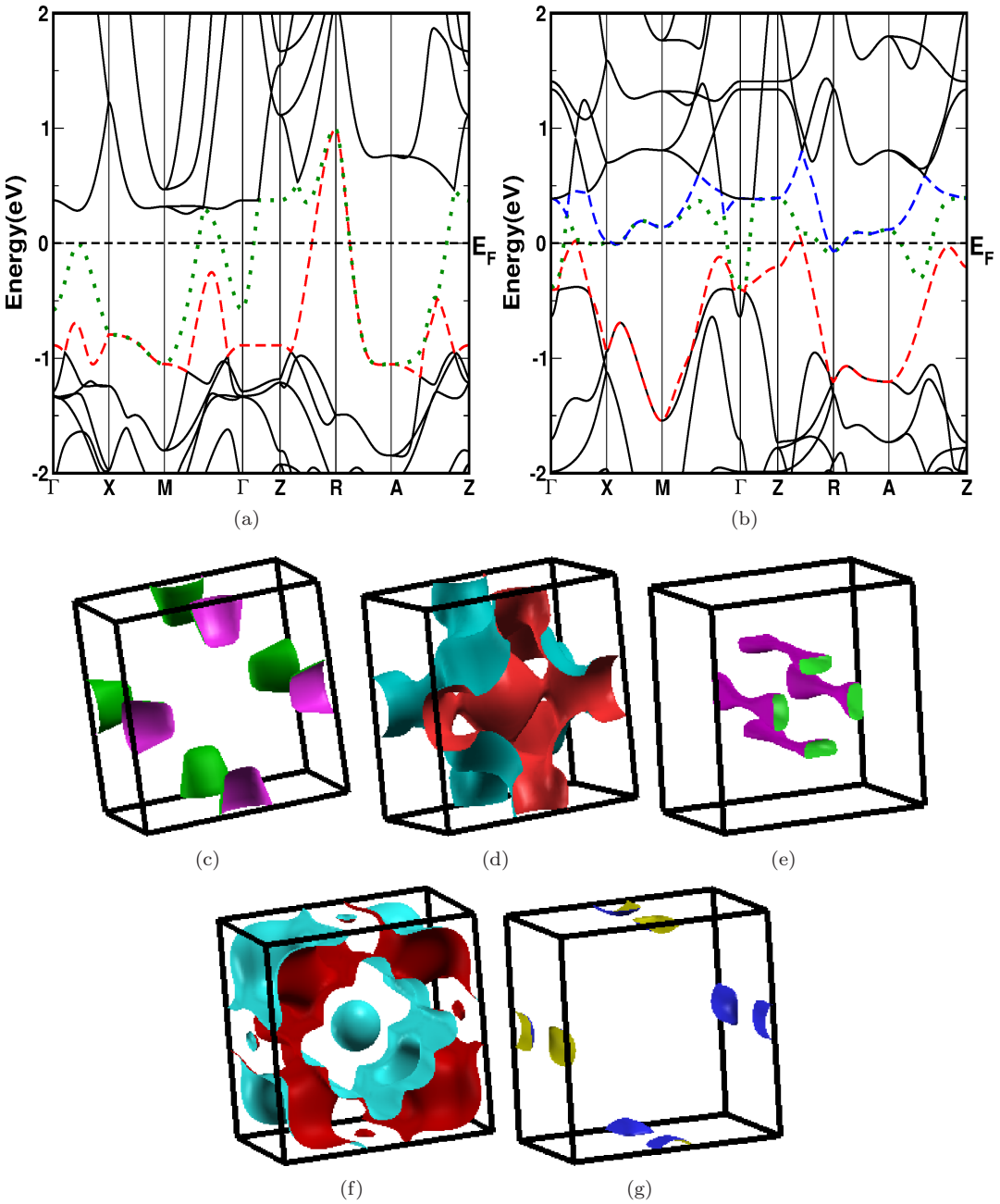

Figure 6.11: Band structure for MnGaGe (a) majority spin (b) minority spin. Fermi surfaces of MnGaGe in both majority spin and minority spin cases. First two (c, d) FS belongs to majority spin case and the remaining three (e, f, g) belong to minority spin case.

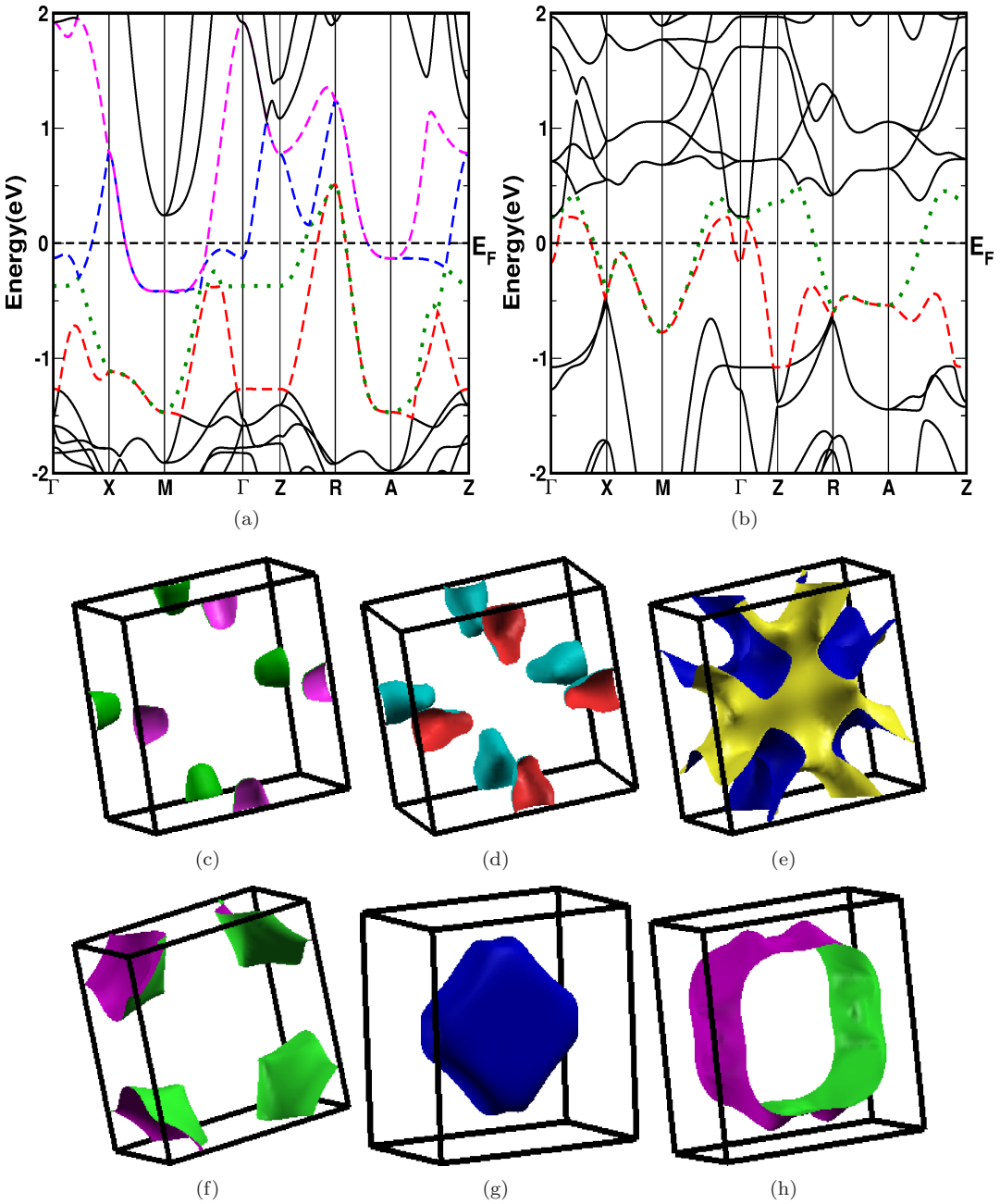

Figure 6.12: Band structure for MnZnSb (a) majority spin (b)minority spin. Fermi surfaces of MnZnSb in both majority spin and minority spin cases. First four (c, d, e, f) FS belongs to majority spin case and the remaining two (g, h) belong to minority spin case.

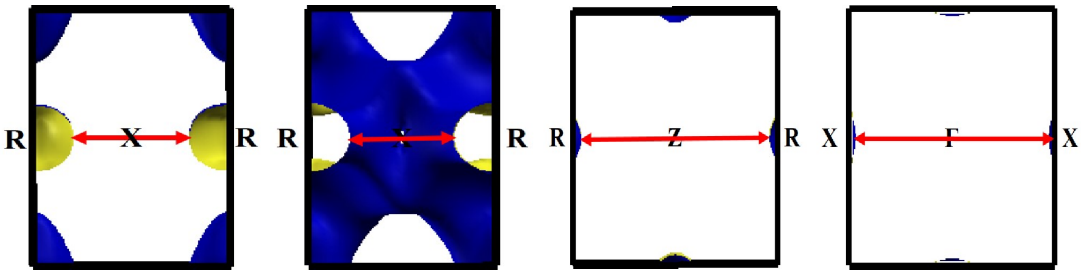

Figure 6.13: Schematic representation of nesting vector directions for different Fermi surfaces (a) 2D representation of first FS in majority spin of the all the compounds, (b) 2D representation of second FS of in majority spin of MnAlGe and MnGaGe, (c) 2D representation of last FS in minority spin case MnAlGe and MnGaGe, (d) 2D representation of last FS in minority spin case MnZnSb.

shift towards valence region. Due to this shift, one more band in addition is found to cross E_F in minority spin case along Γ-X and Z-R. In the minority spin case first band has Mn-'d_{xz}+d_{yz}' character, second band has mixed nature of Mn-'d_{z^2}' and 'd_{xz}+d_{yz}' and the final band possess Mn-'d_{xy}' character. In majority spin case, the band structure scenario is same as MnAlGe except at Γ point, where we find a band to cross E_F from conduction band to valence band. Due to this one can expect a pocket/sheet around Γ point in the Fermi surface topology but the orbital character is same as MnAlGe majority spin. In the case of MnZnSb, we have observed four bands and two bands to cross the E_F in majority spin and minority spin case respectively as shown in Fig. 6.12. The first two bands in the majority spin case are crossing E_F only at R point from valence to conduction region. The next blue coloured dotted band cross E_F at A, M and around Γ from conduction to valence region. The remaining band in the majority spin case cross E_F at A and M points only form conduction to valence region. Among these first band has Mn-'d_{xz}+d_{yz}' character, second one has a mixed nature of Mn-'$d_{x^2-y^2}$' and 'd_{xz}+d_{yz}', third one has Mn-'$d_{x^2-y^2}$' character and last one has same character as second one. In the case of minority spin of MnZnSb red colour band cross around Γ and has Mn-'d_{z^2}' character and the remaining green dotted band continuously stay in conduction region around Z and Γ, where one we expect sheet like Fermi surface and has a mixed nature of Mn-'d_{z^2}' and 'd_{xz}+d_{yz}'.

To understand more about the scenario at the Fermi level, we have calculated Fermi surfaces (FS) for all the compounds in both the spin cases and are given along with band structure plots. First to note is that the first FS in all the investigated compounds for majority spin case, is similar and have a hole pocket at R point. The second FS in majority spin case in MnAlGe and MnGaGe is similar except for a sheet around Γ point in MnGaGe. Now let us analyse the FS of MnAlGe in detail. For both majority and minority spin cases, FS possess flat sheet like shape, which is expected for a quasi two dimensional system. If we look at the first FS of majority spin and second FS of minority spin, there is a possibility of Fermi surface nesting along Γ to R and X to R, and the remaining FS are found to be little complicated. For MnGaGe minority spin case, we have three FS due to crossing of three bands at E_F, which are also having quasi two dimensional character. First FS have dumbbell like FS along Γ-X and Z-R due to band crossing along these directions. Next FS is similar as first minority FS except having a pocket at Γ point. The last FS has sheet along X-R direction. Fermi surface nesting possibility similar to MnAlGe is observed in this compound. In

the case of MnZnSb, second FS in majority spin has similar character as first one. Remaining two FS in majority spin case are found to have electron nature. In minority spin case, we have two FS and are having hole nature with quasi two dimensional character in these two FS. Unlike the other two compounds possibility of Fermi surface nesting is found to be more in this compound, such as all the FS for both majority and minority spin case may have nesting feature. Overall, the FS analysis also confirmed the quasi two dimensional nature in the investigated compounds. To discuss the nesting feature in these compounds at ambient conditions, schematic representation of nesting vector direction is given in Fig. 6.13 for some of the Fermi surfaces. Fig. 6.13(a) represents the first FS in majority spin case for all the compounds having a nesting vector along X-R direction around $\sim 0.30\times 2\pi/a$. Nesting vector in the second FS of majority spin case of MnAlGe and MnGaGe is represented in Fig. 6.13(b) having a nesting vector along X-R around $\sim 0.28\times 2\pi/a$. Fig. 6.13(c) represents the nesting vector in the last FS of minority spin in both MnAlGe and MnGaGe along Z-R direction around $\sim 0.47\times 2\pi/a$. Fig. 6.13(d) indicates the nesting vector direction of the last FS in the minority spin of MnZnSb along Γ-X around $\sim 0.345\times 2\pi/a$.

We have calculated total and atom projected density of states(DOS) for all the compounds and are given in Fig. 6.14. From this we have observed exchange splitting in all the compounds. The compounds MnAlGe and MnGaGe have high electronic DOS at E_F in minority spin case with a value of 4.25 and 4.32 states/eV/f.u. compared to majority spin (0.60 and 0.78 states/eV/f.u. for MnAlGe and MnGaGe respectively for majority spin case). But in the case of MnZnSb it is found that DOS in majority spin case is higher with a value of 1.80 states/eV/f.u. compared to minority spin(1.56 states/eV/f.u.) at E_F. This indicates strong ferro magnetic nature in MnAlGe and MnGaGe(because of more directionality in majority spin case) compared to MnZnSb. In all the compounds major contribution to the DOS at E_F is from Mn-'d' atoms in both majority and minority spin cases. Particularly in the case of MnAlGe and MnGaGe compounds Mn-'$d_{xy} + d_{yz}$' states and in the case of remaining MnZnSb, Mn-'$d_{x^2y^2}$' states are contributing more in majority spin case at E_F. In the similar way, for minority spin case Mn-'d_{xy}' states are contributing more in MnAlGe and Mn-'d_{z^2}' states are contributing more in the case of remaining compounds at E_F. Ge/Sb atoms have secondary contribution in majority spin case and Al/Ga/Zn atoms are found to have secondary contribution in minority spin case. In all the compounds, states around the energy -9 eV are due to the 's' states of Ge/Sb. We have also calculated Sommerfield coefficient values for the investigated compounds and are given in Table. 6.5 along with the available results. The calculated values are in good agreement for MnGaGe and MnZnSb compounds and slightly overestimated for MnAlGe.

Elastic constants

To check the mechanical stability, in the present compounds we have calculated the single and poly crystalline elastic constants for all the compounds and are given in Table 6.6. Calculated single crystal elastic constants are following the stability criteria [192] for a tetragonal system as given below indicating the mechanically stable nature of the investigated compounds at ambient conditions. $C_{11} > 0$, $C_{33} > 0$, $C_{44} > 0$, $C_{66} > 0$, $(C_{11}-C_{12}) > 0$, $(C_{11}+C_{33}-2C_{13}) > 0$, $2(C_{11}+C_{12})+C_{33}+4C_{13} > 0$ From the tabulated data, it is found that in all the compounds C_{11} ($C_{22}=C_{11}$) is smaller than C_{33} indicating that 'a' or 'b' axis is more compressible than the 'c' axis. In the same way, C_{44} ($C_{55}=C_{44}$) for all the compounds is larger than C_{66} indicating that deforming by a shear in (1 0 0) or (0 1 0)

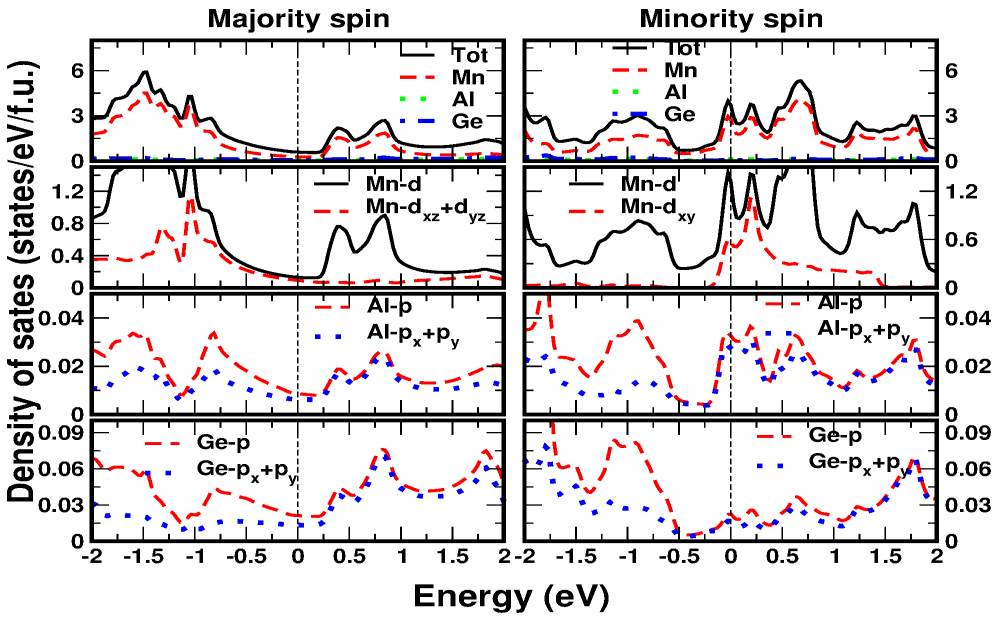
Majority spin
Minority spin
Density of sates (states/eV/f.u.)
Energy (eV)
Tot
Mn
Al
Ge
Mn-d
Mn-d$_{xz}$+d$_{yz}$
Mn-d$_{xy}$
Al-p
Al-p$_x$+p$_y$
Ge-p
Ge-p$_x$+p$_y$

(a)

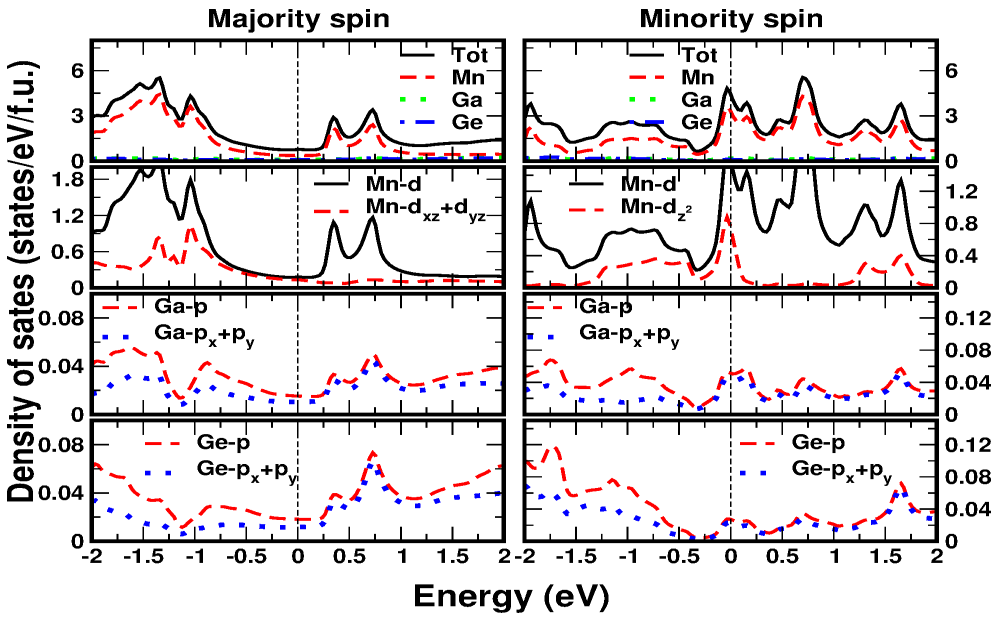
Majority spin
Minority spin
Density of sates (states/eV/f.u.)
Energy (eV)
Tot
Mn
Ga
Ge
Mn-d
Mn-d$_{xz}$+d$_{yz}$
Mn-d$_{z^2}$
Ga-p
Ga-p$_x$+p$_y$
Ge-p
Ge-p$_x$+p$_y$

(b)

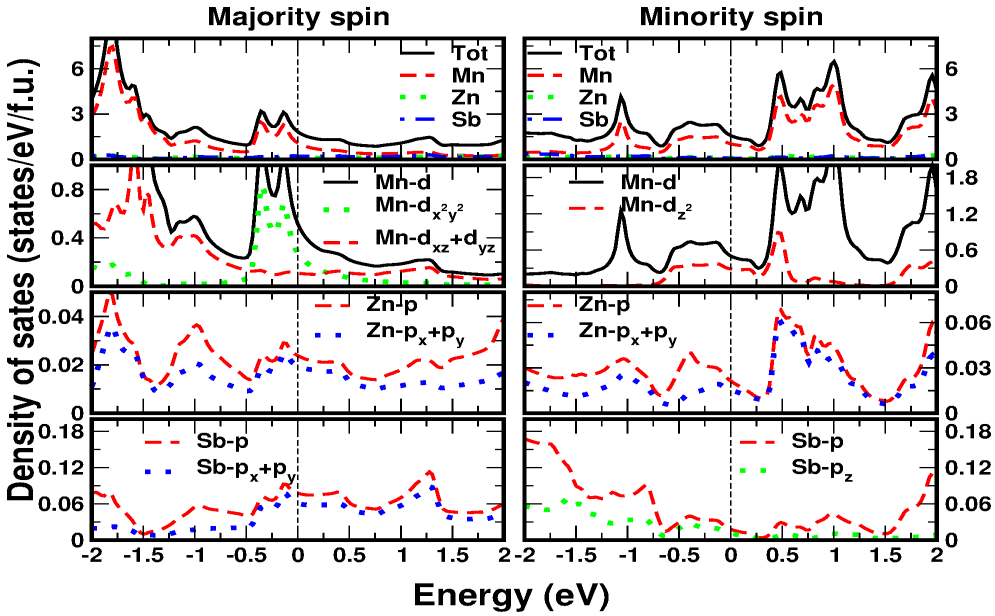

(c)

Figure 6.14: Density of states for (a) MnAlGe, (b) MnGaGe and (c) MnZnSb.

plane is more difficult than in (0 0 1) plane. The calculated bulk modulus is found to be higher for MnGaGe with a value of 120 GPa and lower for MnZnSb with a value of 75 GPa. Calculated anisotropy values indicate MnGaGe to have more anisotropy compared to other two compounds. Calculated Young's modulus is found to be higher for MnAlGe with a value of 181 GPa and lower for MnZnSb with a value of 98 GPa. No other data is available to compare the calculated poly crystalline elastic constants for the present compounds.

As we discussed above, anomalies are observed in all the compounds with the application of pressure in the lattice parameters and Curie temperatures. It is quite reasonable to study the properties of these materials under pressure which is discussed in the next subsection.

6.4 Results and discussions for systems under pressure

6.4.1 Zr_2TiAl

The calculated effects of applied pressure on the band structure of Zr_2TiAl are illustrated in Fig. 6.15 for both majority and minority spins. Here we have applied uniform compression in all the crystallographic directions. With increasing pressure the number of bands crossing E_F is increased from one to three in both spin cases upto the final compression. This indicates the Electronic topological transitions (ETT) in the present compound at different compressions. The corresponding change in the FS topology at each compression is given in the Fig. 6.16 and 6.17. As pressure increases, E_F shift towards either higher or lower energy region. This shift in the E_F can cause changes in the band structure which again leads to a change in the FS topology. In our case we find E_F to shift towards the valence region in majority spin case and towards the conduction region in the minority spin case which is evident from Fig. 6.15. Due to this, the number of bands to cross

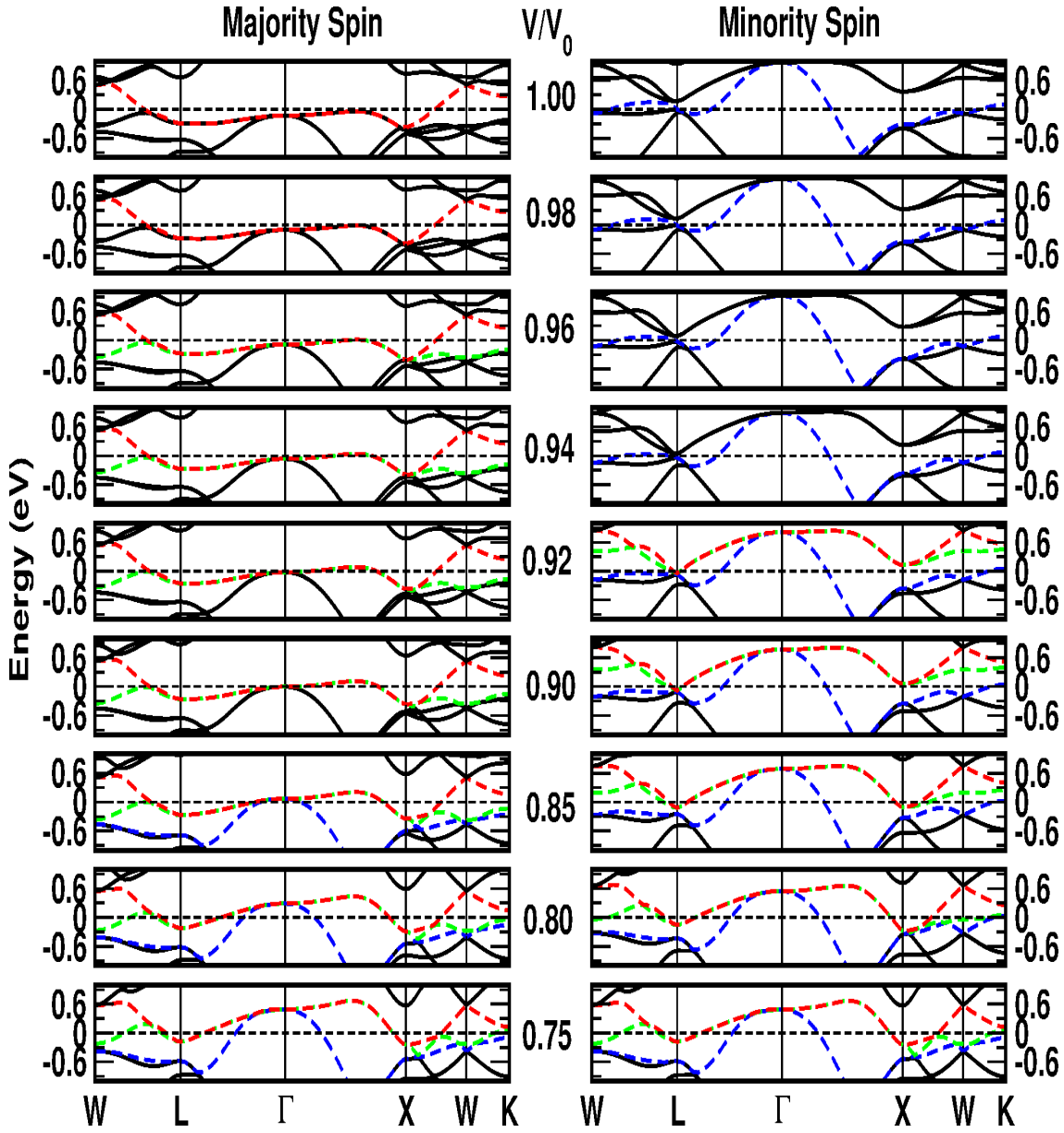

Figure 6.15: Band structure for Zr_2TiAl under compression, given near the vicinity of the Fermi level (0 eV). The bands which cross the E_F are indicated with colour.

V/V_0=1.00 and 0.98

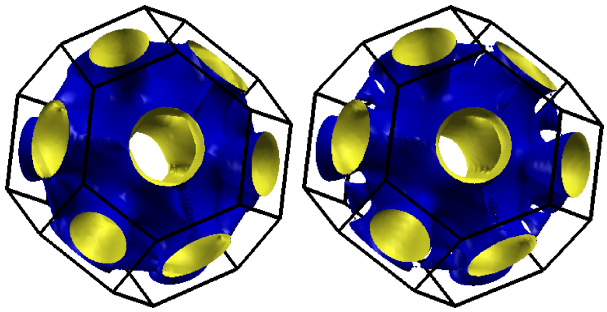

V/V_0=0.96

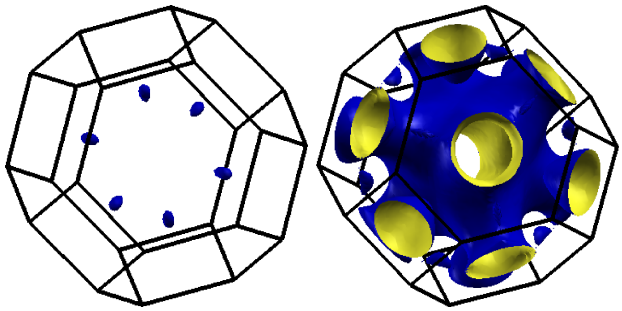

V/V_0=0.94

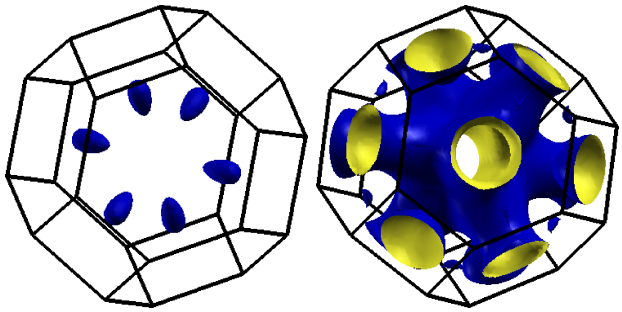

V/V_0=0.92

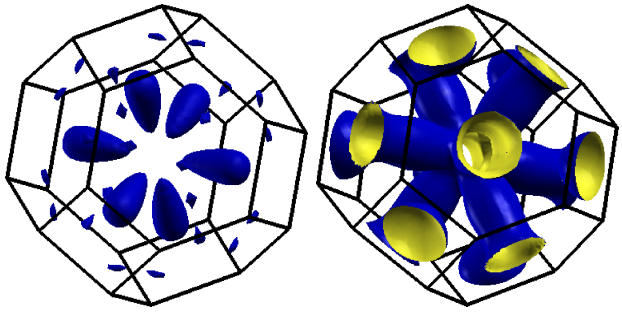

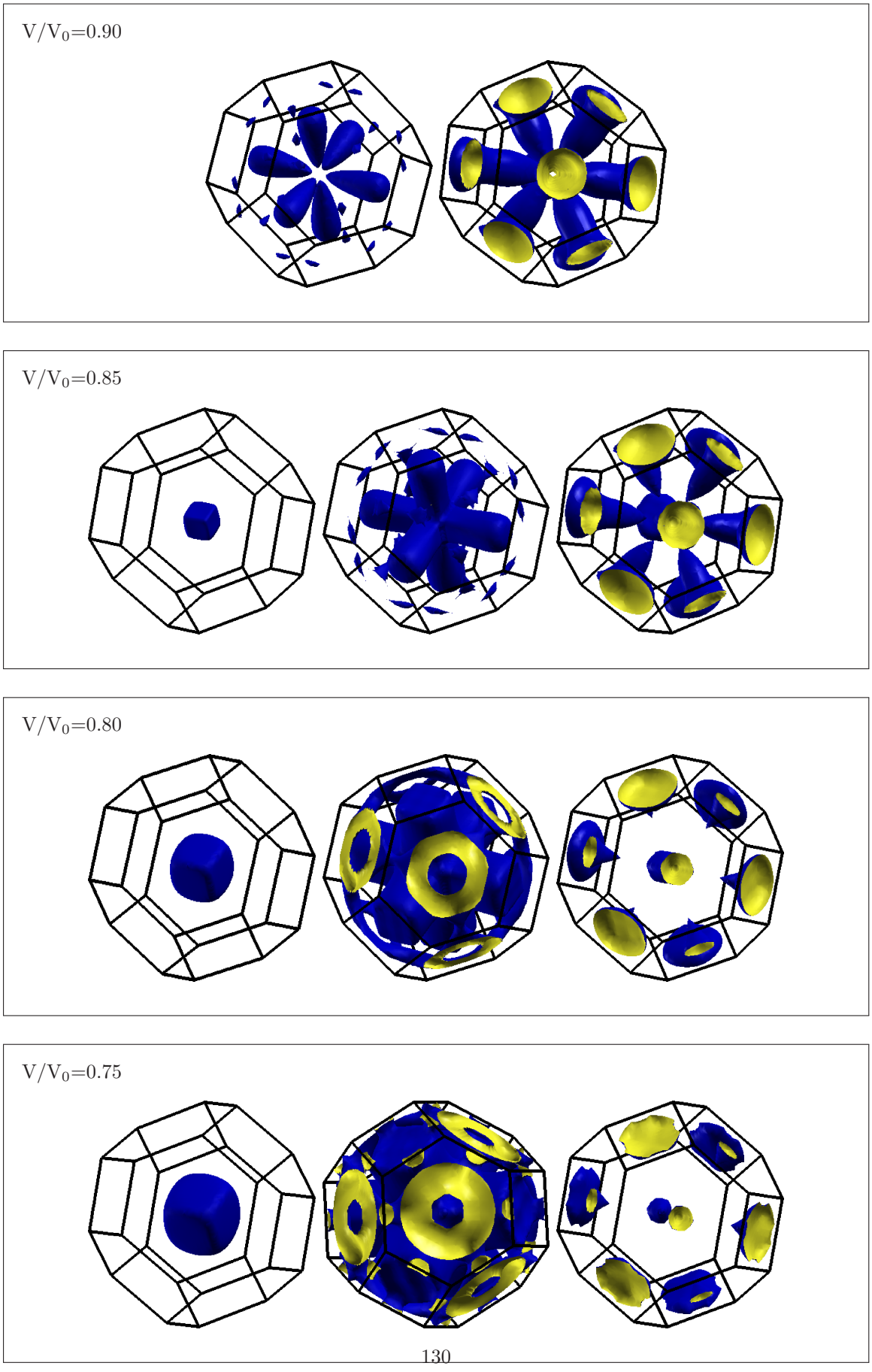

Figure 6.16: Majority spin Fermi surface of Zr_2TiAl under compression.

V/V_0=1.00 and 0.98

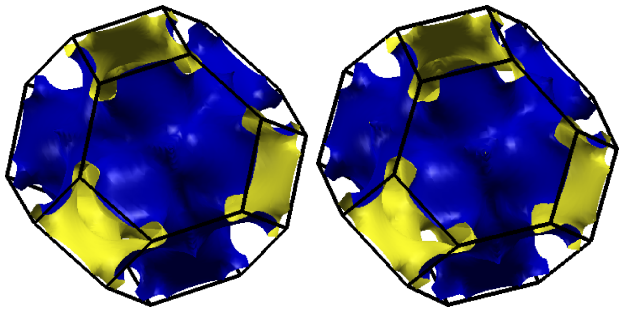

V/V_0= 0.96 and 0.94

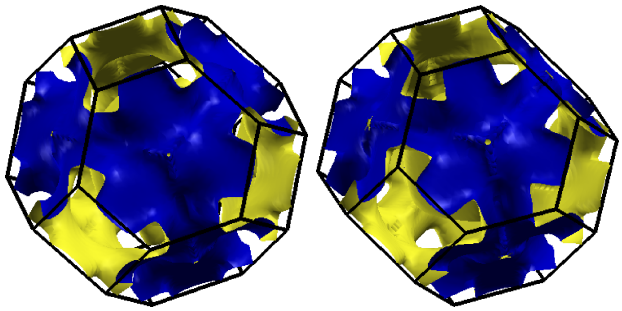

V/V_0=0.92

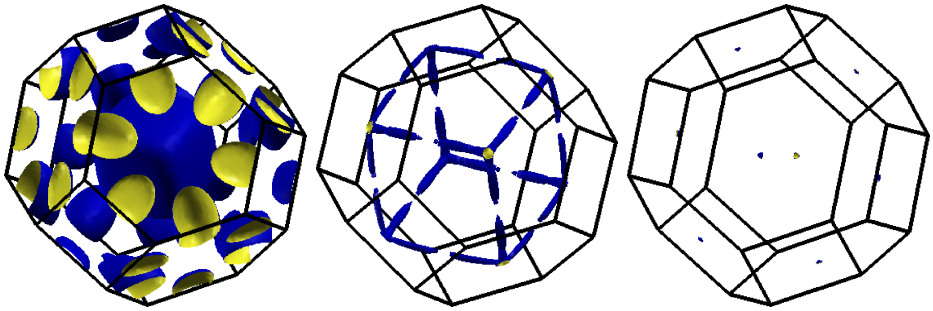

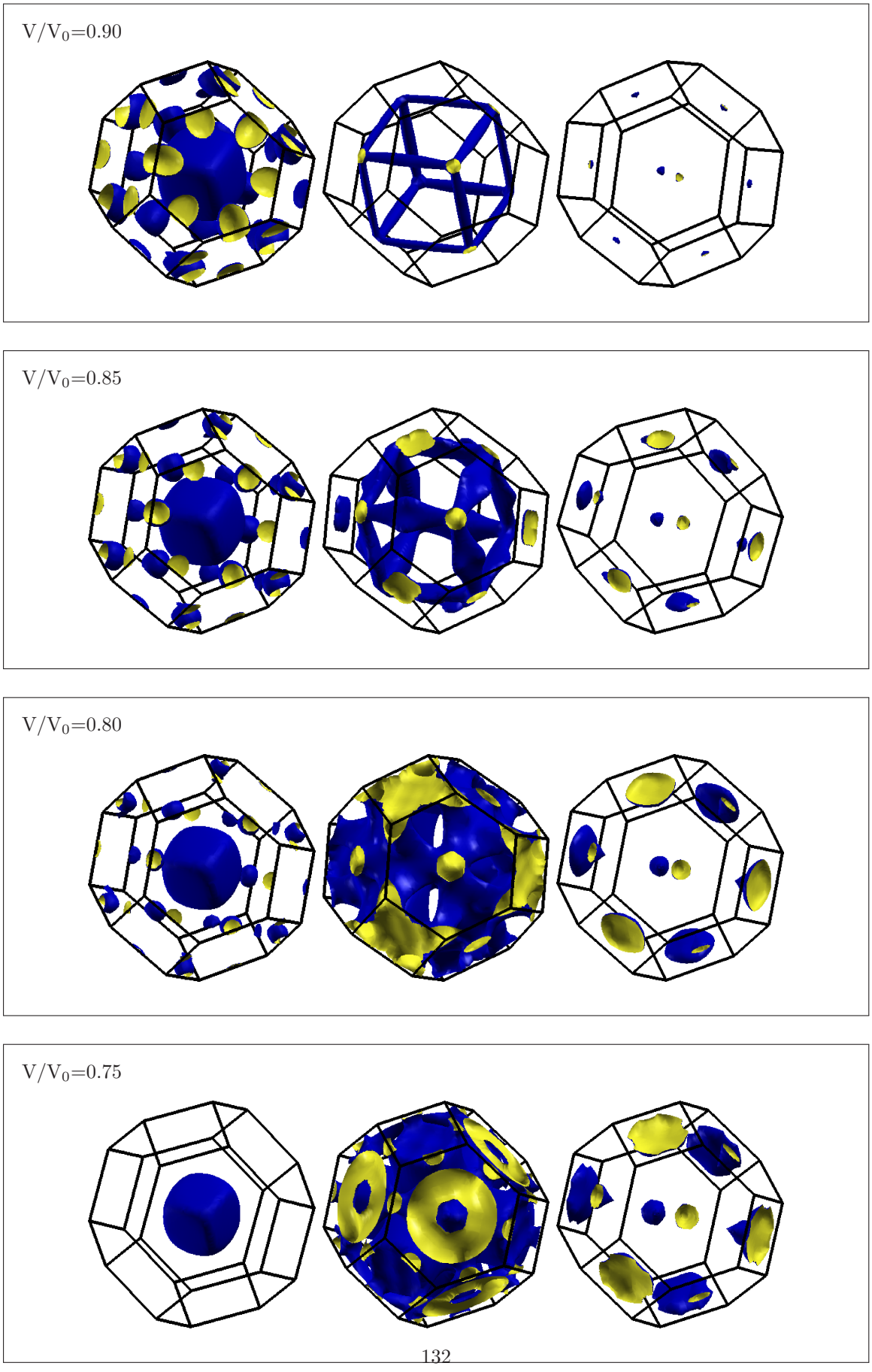

Figure 6.17: Minority spin Fermi surface of Zr_2TiAl under compression.

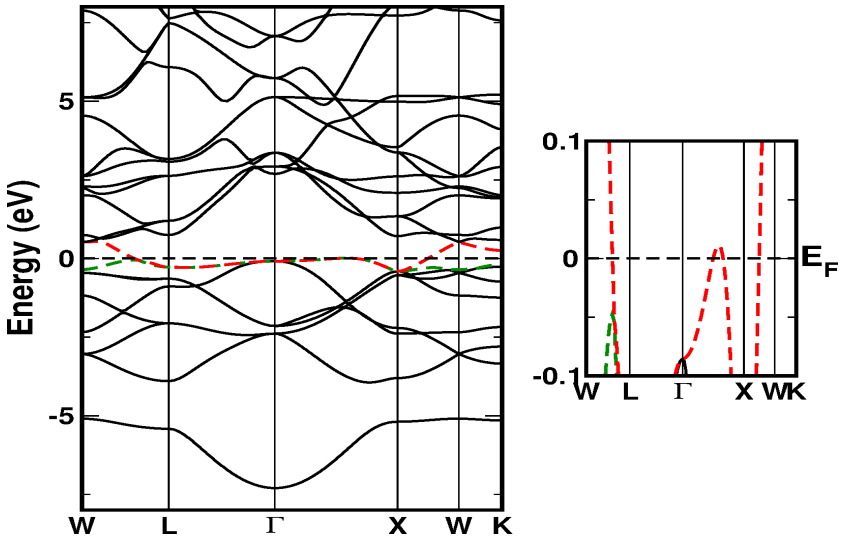

Figure 6.18: Majority spin band structure for Zr_2TiAl at V/V_0=0.96 (zoomed at the E_F).

E_F is increasing at particular pressures in both the spin cases. The topology of the FS depends on the area occupied by the band near E_F. As pressure increases, there is a change in the occupied area of the band at E_F which leads to a change in the FS topology. From Fig. 6.16 and 6.17, it is observed that a continuous change in the topology of FS at all the compression along with the addition of new FS sheets at certain compressions lead to ETT's. From Fig. 6.15, it is observed that the additional band to cross the E_F in majority spin case occurs at V/V_0=0.96 (pressure of 4.22 GPa) along Γ-X direction. Due to this, we find an additional FS which is evident from the Fig. 6.15 at the same compression. The complete band structure at this compression is given in Fig. 6.18 and the corresponding FS topology can be found in Fig. 6.16. From this, we found small pockets along Γ-X in the first FS which is evident from Fig. 6.18 at this compression compared to ambient. At the same point the second band is also found to cross the E_F which is evident from the zoomed figure from Fig. 6.18 and the corresponding FS is shown in Fig. 6.16. For higher compressions, the FS topology change still continues, and at V/V_0=0.92 (pressure 9.45 GPa) for minority spins two additional bands are found to cross the E_F and due to this two additional FS sheets are found (see Fig. 6.15). From Fig. 6.19, where the complete band structure is given and corresponding FS topology presented in Fig. 6.17., the changes in the band structure and FS topology are observed at L point where the new bands are added as shown from the zoomed band structure in Fig. 6.19. The FS for these new bands are given in Fig. 6.17. Above this compression at V/V_0=0.85 (pressure of 21 GPa) in majority spin case another band is found to cross the E_F at Γ point. Due to this an extra FS sheet is found at the Γ point which is evident from Fig. 6.16. At the final compression V/V_0=0.75 (pressure of 46 GPa) it is found that the band structure and FS for both majority and minority spin cases is found to be same indicating the non-magnetic nature of the present compound at this compression. The complete band structure is given for this compression in Fig. 6.20 (corresponding FS can be see in Fig. 6.16 and 6.17). This non-magnetic nature is again confirmed from the calculated magnetic moment of the Ti, which is found to be 0 μ_B at this compression as shown in Fig. 6.2(b).

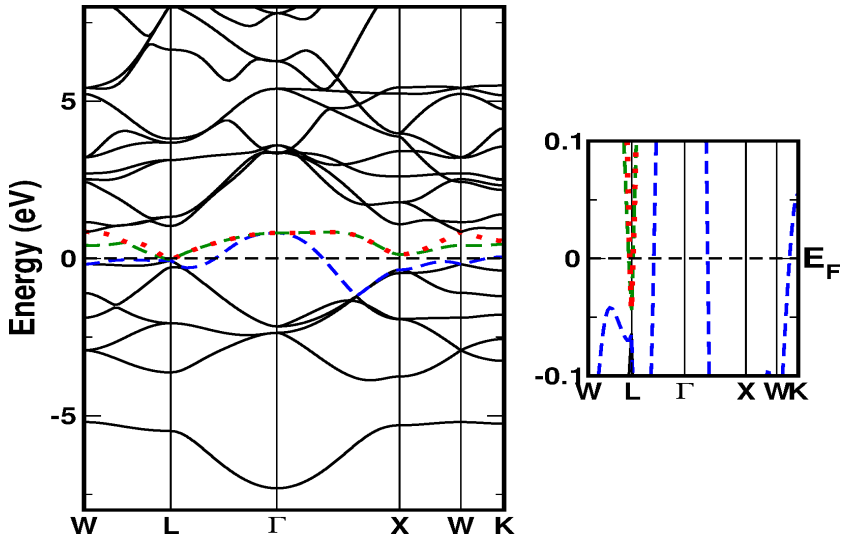

Figure 6.19: Minority band structure for Zr_2TiAl at V/V_0=0.92 (zoomed at the E_F).

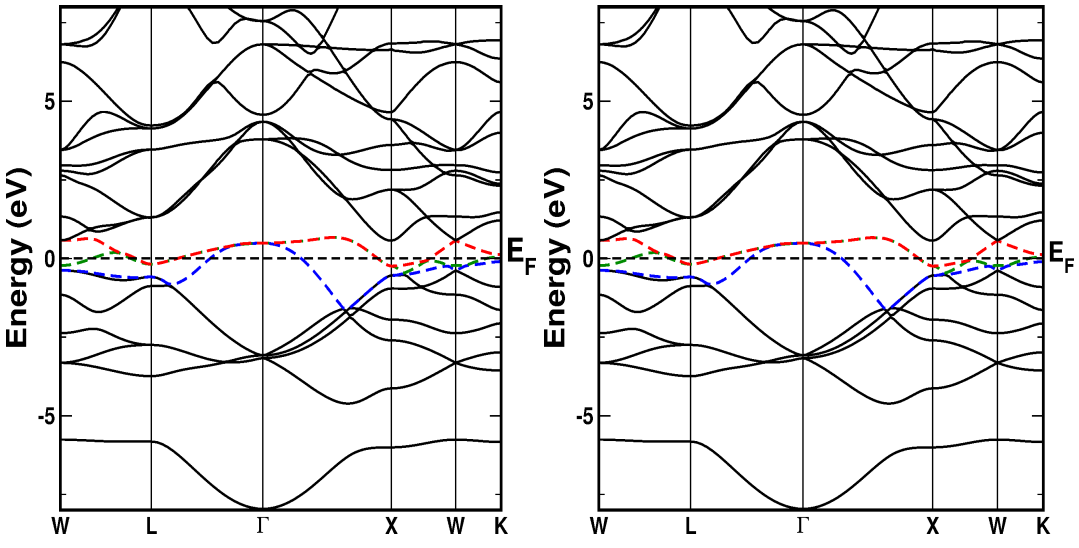

Figure 6.20: Band structure for Zr_2TiAl at V/V_0=0.75 (a) majority spin band and (b) minority spin band.

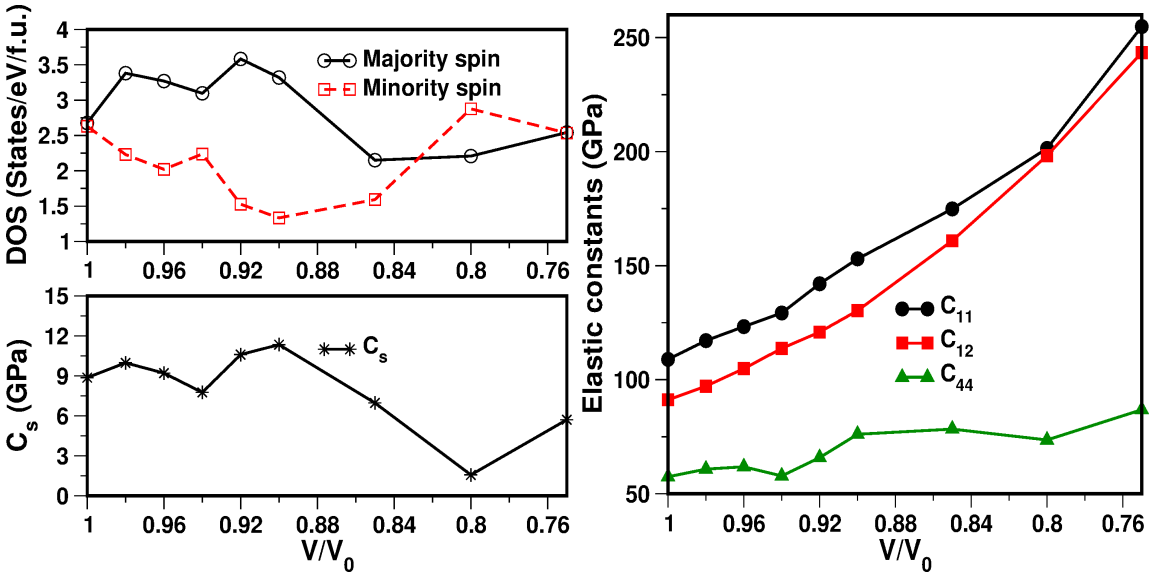

(a) (b)

Figure 6.21: (a) Total electronic density of states for Zr_2TiAl under compression for both majority and minority spin case along with the shear modulus (C_s) elastic constant under compression. (b) Single crystalline elastic constants under pressure.

These changes in the FS topology are again an indication of some anomalies in the system. For further investigations we have also calculated the DOS under compression and the results are given in Fig. 6.21(a). Non-monotonic variations in the DOS under compression in both majority spin and minority spin are found. Recently it was shown that the Fermi surface topology change and non monotonic variation in the DOS can be used to predict the ETT's in the Nb based superconducting compounds [284]. In the present compound this could be a reason for second order magnetic to non-magnetic phase transition.

To confirm the signatures of ETT's we have also calculated the single crystalline elastic constants and shear modulus (C_s=(C_{11}-C_{12})/2) for all the compressions and the values are plotted in Fig. 6.21. From the above discussion, we have observed ETT's at V/V_0=0.96(for majority spin), V/V_0=0.92(for minority spin) and V/V_0=0.85(majority spin) and in remaining compressions a continuous change in the band structure and FS topology is also observed. The ETT's due to the majority spin (V/V_0=0.96, 0.85) can be directly observed from the softening of C_s elastic constant at that compression from Fig. 6.21(a). The remaining ETT due to the minority spin (V/V_0=0.92) is not observed directly form the C_s but it can be observed form the calculated total DOS in minority spin case at that compression where we can see the decrease in the total DOS value from Fig. 6.21(a). A sudden drop in the total magnetic moment is observed at V/V_0=0.92 and 0.85 due to complete occupancy of minority spin at V/V_0=0.92 and majority spin case at V/V_0=0.85. The resulting decrease in the magnetic moment is the primary reason for the destabilization of magnetic phase in Zr_2TiAl at high compressions. Again to confirm the non-magnetic phase at V/V_0=0.75 we have calculated the phonon dispersion relations at the same compression and they are given in Fig. 6.7(b) (red coloured dotted line), where we observed the phonon hardening and the disappearance of imaginary mode.

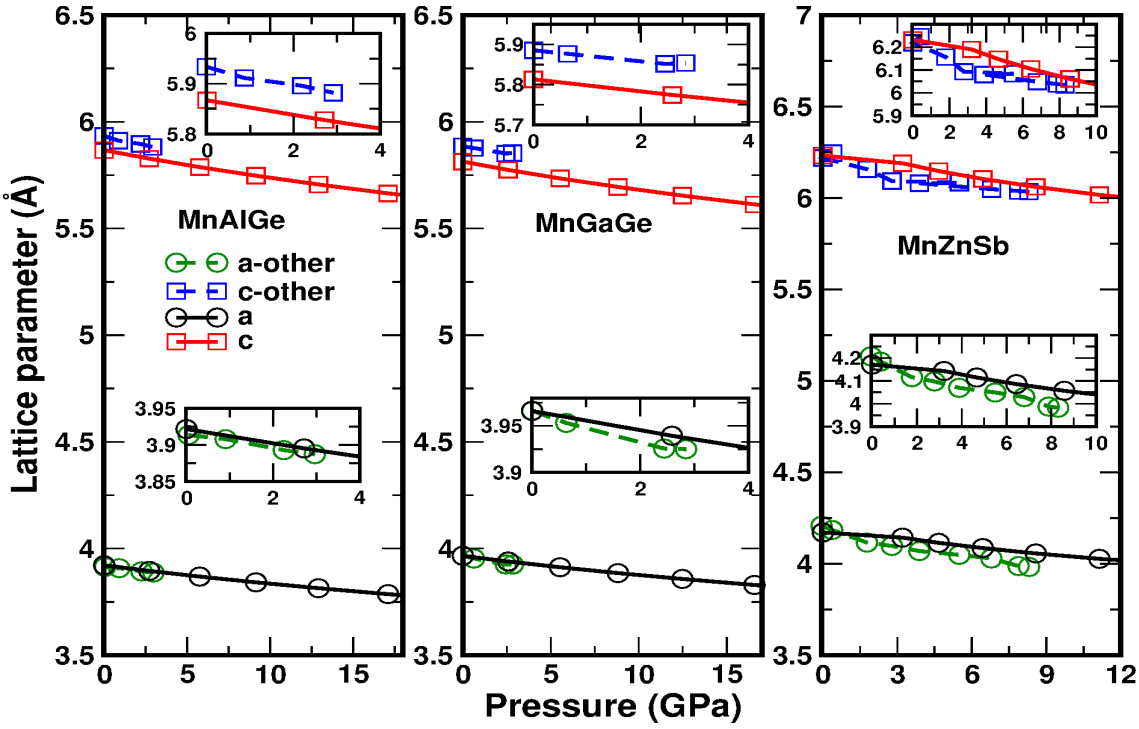

Figure 6.22: Effect of pressure on the lattice parameters for all the Mn-based compounds along with available experimental results.

6.4.2 Mn-based compounds

As these compounds are found to have quasi two dimensional nature, it is interesting to check the pressure effect on the quasi two dimensionality and also the effect of pressure on the electronic structure properties. Here we have applied hydrostatic pressure for all the compounds with V/V_0 ranging from 1.00 to 0.90. Effect of pressure on the lattice parameters for all the compounds are given in Fig. 6.22 along with the available experimental results. Linear decrease in the 'a' and 'c' lattice parameters is observed under pressure in all the compounds. The values are comparable with available experimental results, shown as an inset in the same figure. We have also calculated the total DOS and magnetic moment of Mn atom under compression and are given in the Fig. 6.23. Decrease in the magnetic moment of Mn atom is observed to be more in MnZnSb when compared to other compounds. Total DOS of minority spin is found to decrease in MnAlGe and MnGaGe compounds with small increase in the minority spin case. In the case of MnZnSb it is quite different from other two compounds, upto the compression around V/V_0=0.96, majority spin total DOS is found to increase and minority total DOS is found to decrease. After this compression the scenario in inverting.

As pressure increases a continuous change in the band and FS topology is observed in all the compounds. In MnAlGe and MnGaGe at compression around V/V_0=0.92 a sudden change in the FS and band topology is observed. The band and FS for MnAlGe and MnGaGe at this V/V_0=0.92 compression are given in Fig. 6.24 and 6.25. In the case of MnAlGe we have observed that the first band in majority spin case is found to cut the E_F along M-Γ direction, leading to a hole pockets in

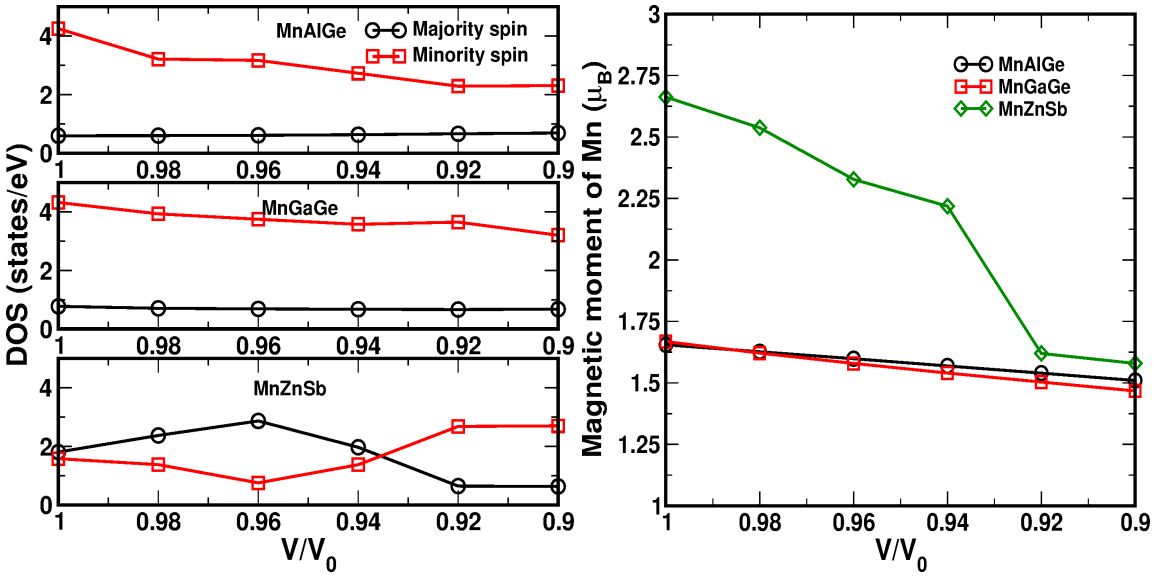

(a) (b)

Figure 6.23: (a) Density of states under compression for all the Mn-based compounds and (b) magnetic moment of Mn under compression for all the Mn-based compounds.

the FS topology as shown in Fig. 6.24. In the same way, we found the absence of pockets at X point in minority spin case compared to ambient one. Similarly, absence of pockets at Γ point in MnGaGe for both majority and minority spin cases is observed as shown in Fig. 6.25 compared to ambient. At the same compression we have found the sudden drop in the total DOS of minority spin in MnAlGe and a sudden increase in the minority spin case in MnGaGe is observed. The pressure corresponding to these compression in MnAlGe and MnGaGe is around 12.9 and 12.5 GPa respectively. In the case of MnZnSb, absence of one FS in minority spin case is observed at V/V_0=0.96 (pressure of 4.2 GPa) and a drastic change in the complete band and FS topology is observed at V/V_0=0.92 (pressure of 8.5 GPa). Band and FS topology of these two compressions is given in Fig. 6.26 and Fig. 6.27. Experimentally Matsuzaki et al [133] observed small anomalies in the lattice parameters '*a*' and '*c*' in the pressure range between 4.2 and 6 GPa. In our study, we have observed changes in the band structure, FS topology in MnZnSb around the experimentally mentioned pressures. A drastic decrease in the magnetic moment of Mn atom in MnZnSb is also confirmed at V/V_0=0.92 as shown in Fig. 6.23(b).

As pressure increase further, a continuous change in both band and FS are observed. The band structure and FS topology is given for the final compression V/V_0=0.90 for all the compounds to observe the effect of pressure in Fig. 6.28-6.30. In majority spin case, additional band is found to cross E_F in MnAlGe around Γ point and the corresponding FS is shown in Fig. 6.28. As pressure increases, E_F is found to shift towards lower energy regions which will effect the size and shape of the FS topology as compared to ambient. Similar to MnAlGe, we have also observed changes in the FS topology in MnGaGe and MnZnSb and the plots are given in Fig. 6.29 and Fig. 6.30 respectively. At the final compression the band and FS topology are found to be same in all the investigated compounds. The pressure values corresponding to the final compression for MnAlGe,

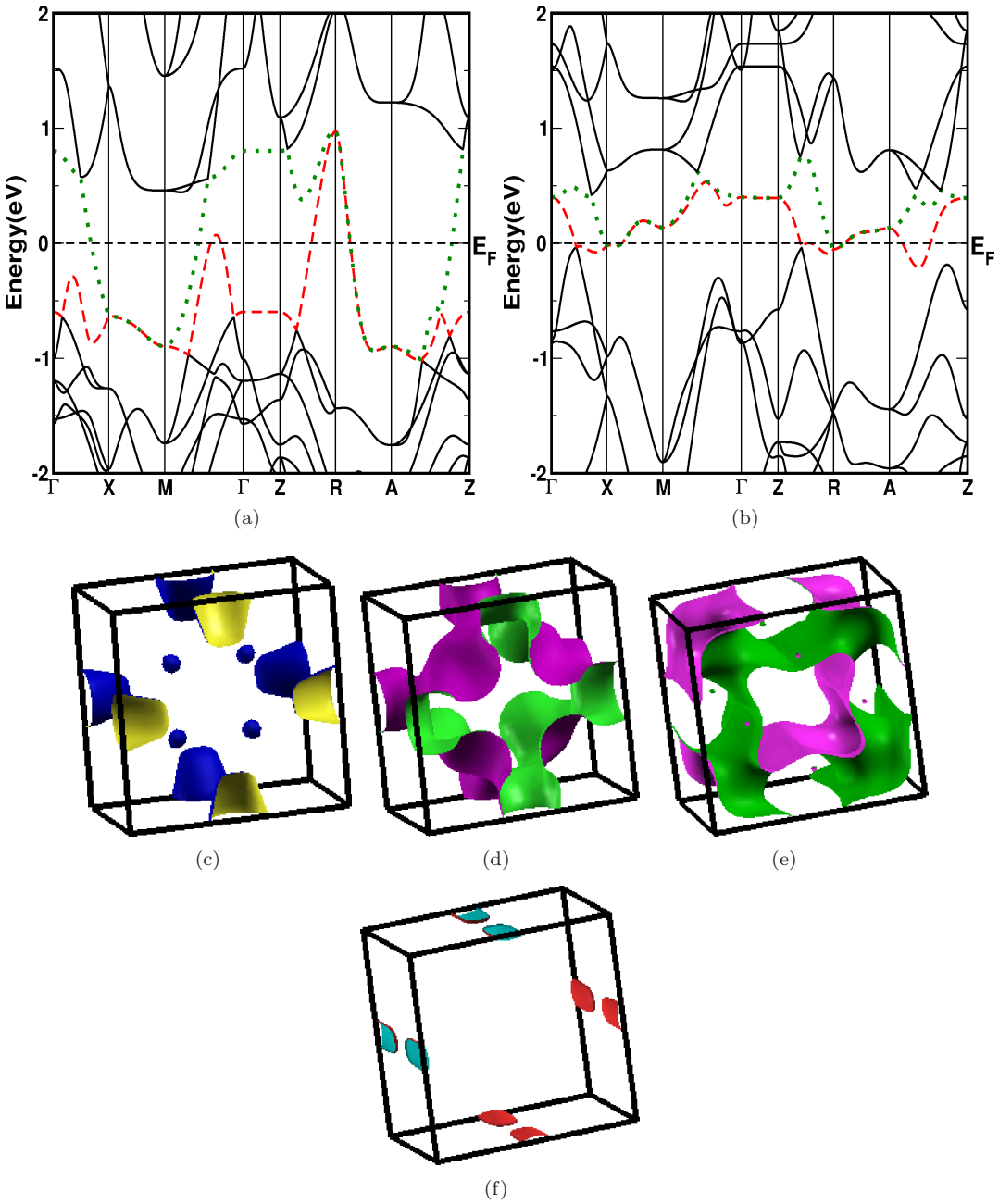

Figure 6.24: Band structure for MnAlGe at V/V_0=0.92 (a) majority spin (b) minority spin case. FS of (c, d) majority spin and (e, f) minority spin case.

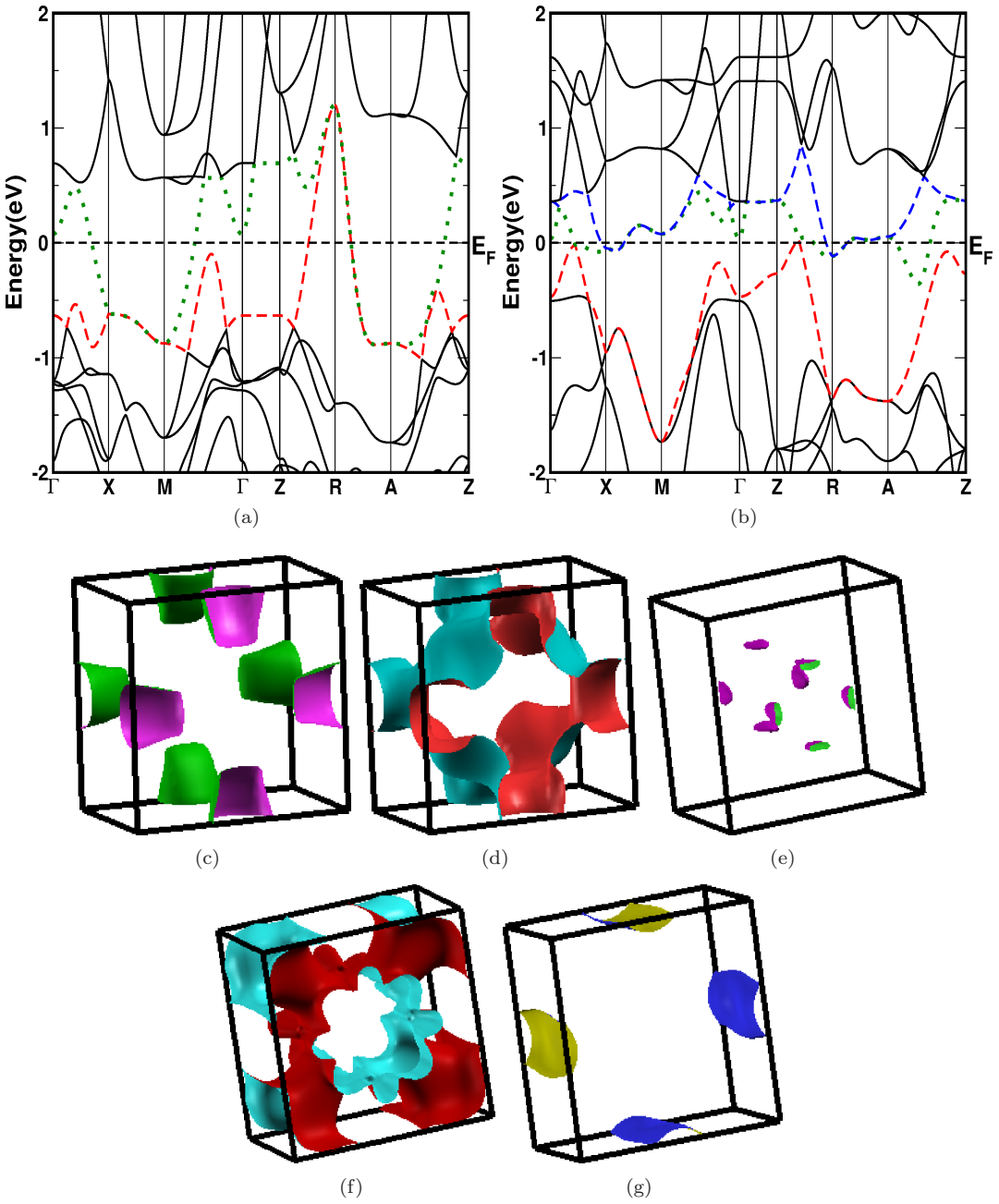

Figure 6.25: Band structure for MnGaGe at V/V_0=0.92 (a) majority spin (b) minority spin case. FS of (c, d, e) majority spin and (f, g) minority spin case.

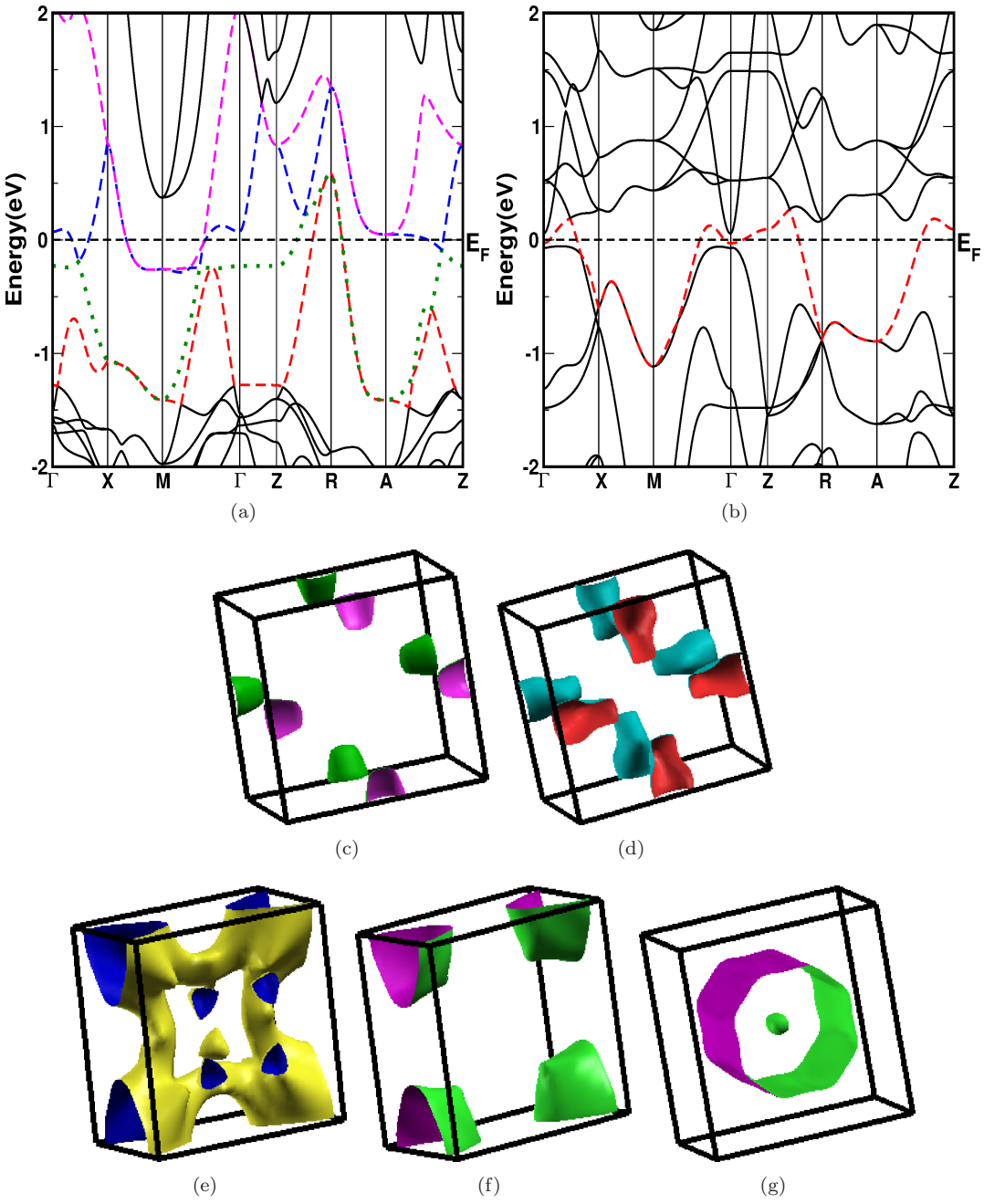

Figure 6.26: Band structure for MnZnSb at V/V_0=0.96 (a) majority spin (b) minority spin case. FS of MnZnSb at V/V_0=0.96 (c, d, e, f) majority spin and (g) minority spin case.

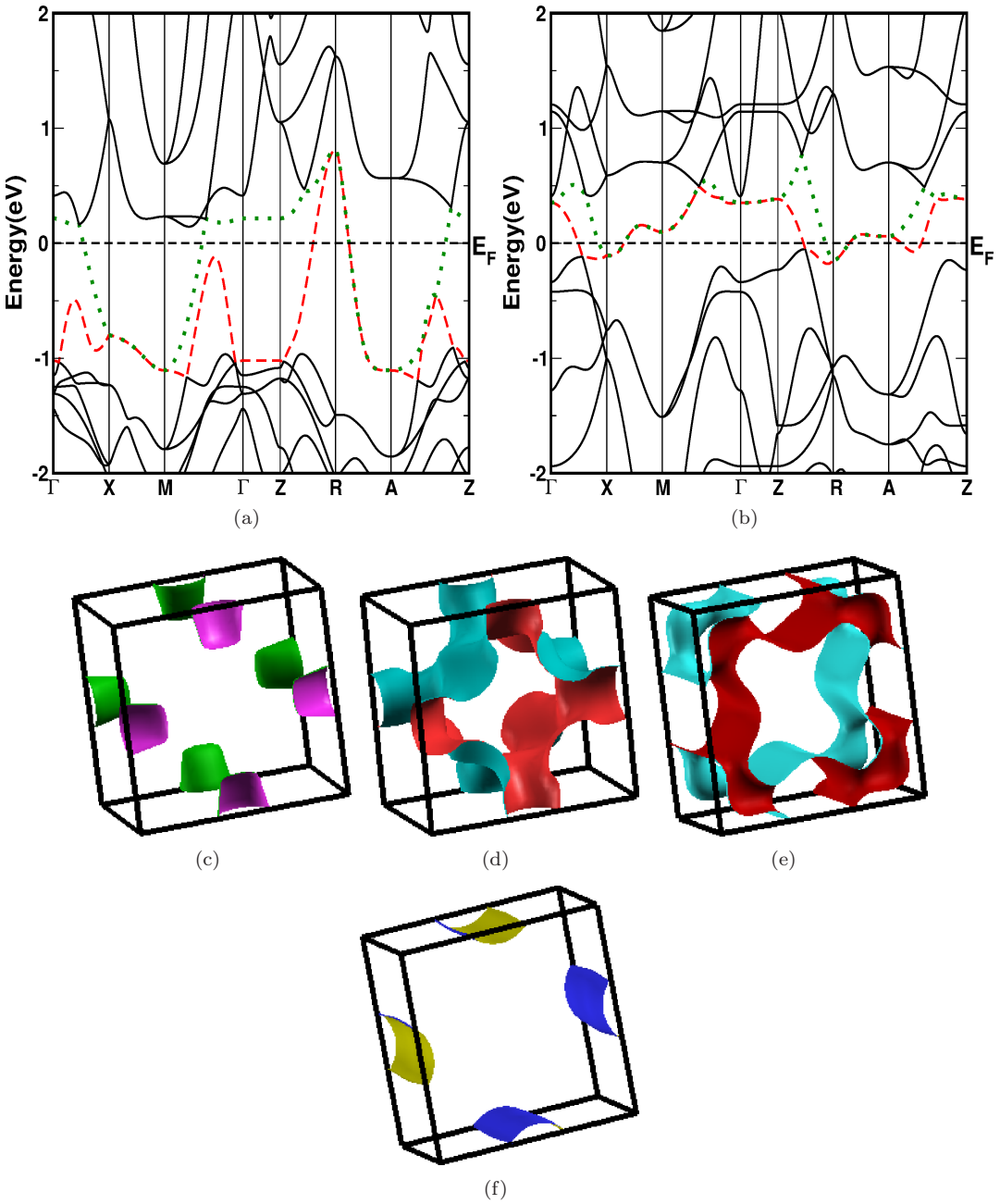

Figure 6.27: Band structure for MnZnSb at V/V_0=0.92 (a) majority spin (b) minority spin case and FS of MnZnSb at V/V_0=0.92 (c, d) majority spin and (e, f) minority spin case.

MnGaGe and MnZnSb are around 17.10 GPa, 16.6 GPa and 11.15 GPa respectively. Now let us analyse the enhancement of quasi two dimensional nature under pressure. If we look at MnAlGe, at ambient conditions state itself the system is quasi two dimensional which we have already shown, and in the compressed state, the two dimensional character is found to increase which is evident from the FS shape. The last FS in minority spin case clearly indicate the enhanced two dimensionality. The possibility of Fermi surface nesting is also found to be increased, each FS might show nesting nature in this compressed state. Similar behaviour is observed for other compounds also. For the last FS of minority spin, schematic representation of nesting vector is given in Fig. 6.31 along Γ-X direction and the nesting vector is around $\sim 0.48\times 2\pi/a$ for all the compounds.

The calculated single crystalline elastic constants under compression for all the compounds is given in Fig. 6.32, where we observed a non-monotonic variation in all the compounds. In MnZnSb, under compression, negative values are observed in C_{12} (at V/V_0=0.96 (pressure of 4.66 GPa)), C_{13} and C_{33} (both at V/V_0=0.94 (pressure of 6.44 GPa)) elastic constants. The pressure values for these compressions are the same where the experimental [133] anomalies are observed in the lattice parameters under pressure. This further confirms either the structural instability or an ETT in MnZnSb. To check the possible structural transition in MnZnSb, we have calculated total energies under compression for different possible phases (cubic-α, β, γ and Orthorhombic, Hexagonal phases) and are plotted in Fig. 6.33. From this figure we are not able to find any phase transition among the given structures. It may lead to the phase transition to another new structure which needs further studies on MnZnSb and will serve as the future scope of this work. It might be possible that the ETT observed at V/V_0 around 0.96 might have lead to the mechanical instability and this can be observed from the FS topology.

From the above discussions it is found the quasi two dimensional nature is found to increase in all the compounds with pressure and is evident from the calculated FS topology. With pressure decrease in the magnetic moment of the Mn atom is observed.

6.5 Conclusion

We have investigated the electronic, magnetic, elastic, and vibrational properties of the Zr_2TiAl at ambient pressure as well as under compression. The obtained structural parameters are in good agreement with the existing experimental data. We have determined that Zr_2TiAl has antiferromagnetic ground state with ordering majority spin and minority spin Ti (111) layers with the magnetic moment of Ti atoms around $\sim$1.22 μ_B. The stability of the magnetic phase is also confirmed from the calculated elastic constants and phonon dispersion relations. We have also observed the magnetic to non-magnetic phase transition under compression due to the disappearance of the Ti magnetic moment, which tends to zero at V/V_0=0.75 ($\approx$ 46 GPa). Three ETT's are observed at V/V_0=0.96, 0.92 and 0.85, due to which a sudden drop in the magnetic moment of Ti atom is observed under compression.

Quasi two dimensional nature is confirmed in Mn-based compounds from the Fermi surface calculations. Under compression decrease in the magnetic moment of Mn atom and change in the band and FS topology is observed in all the compounds. In MnZnSb, negative values in the elastic constants are observed under compression where we find change in band and FS topology correspondingly. These pressure values are in good agreement with experiment, which might further indicate

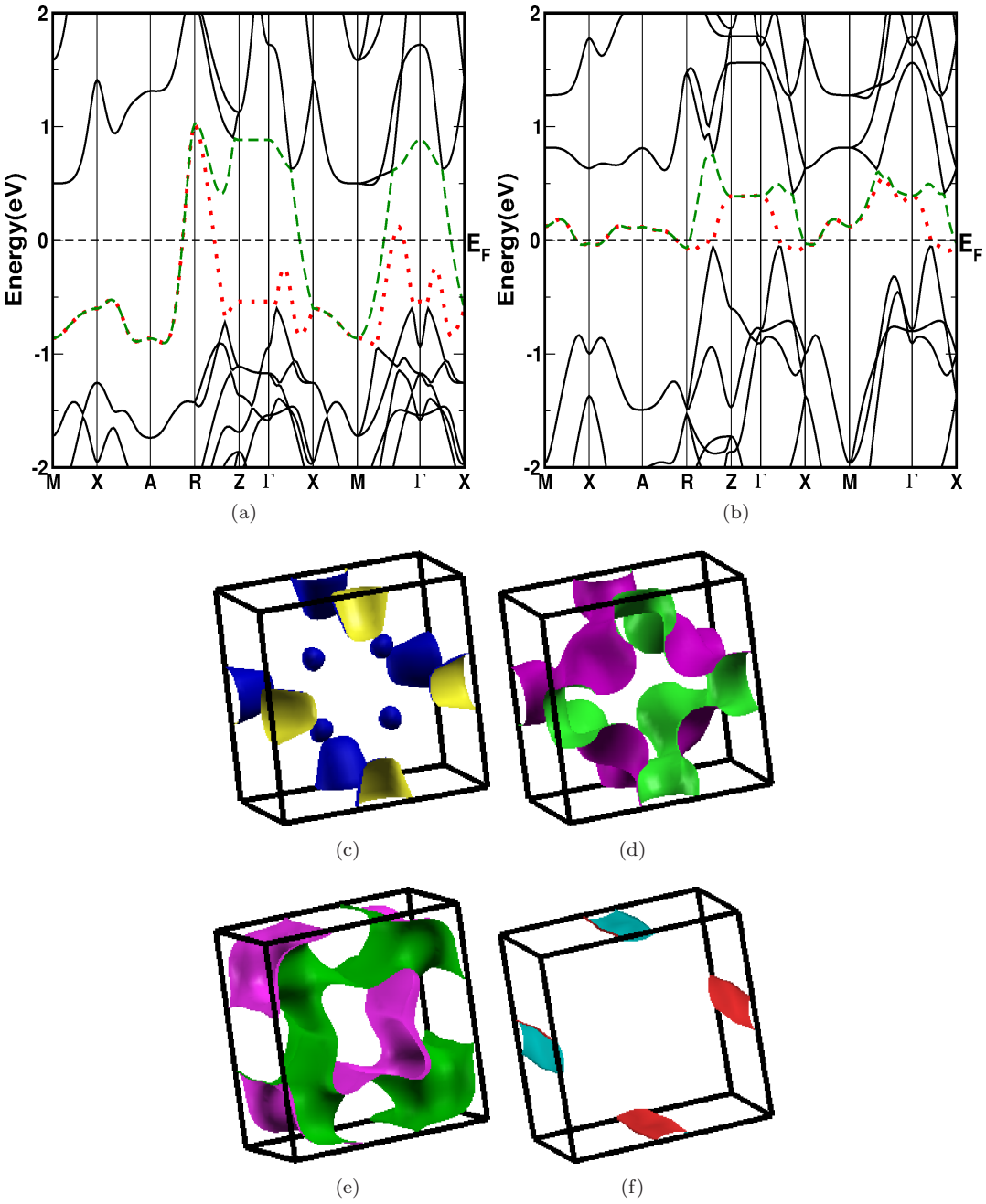

Figure 6.28: Band structure for MnAlGe at V/V_0=0.90 (a) majority spin (b) minority spin case . FS of (c, d) majority spin and (e, f) minority spin case.

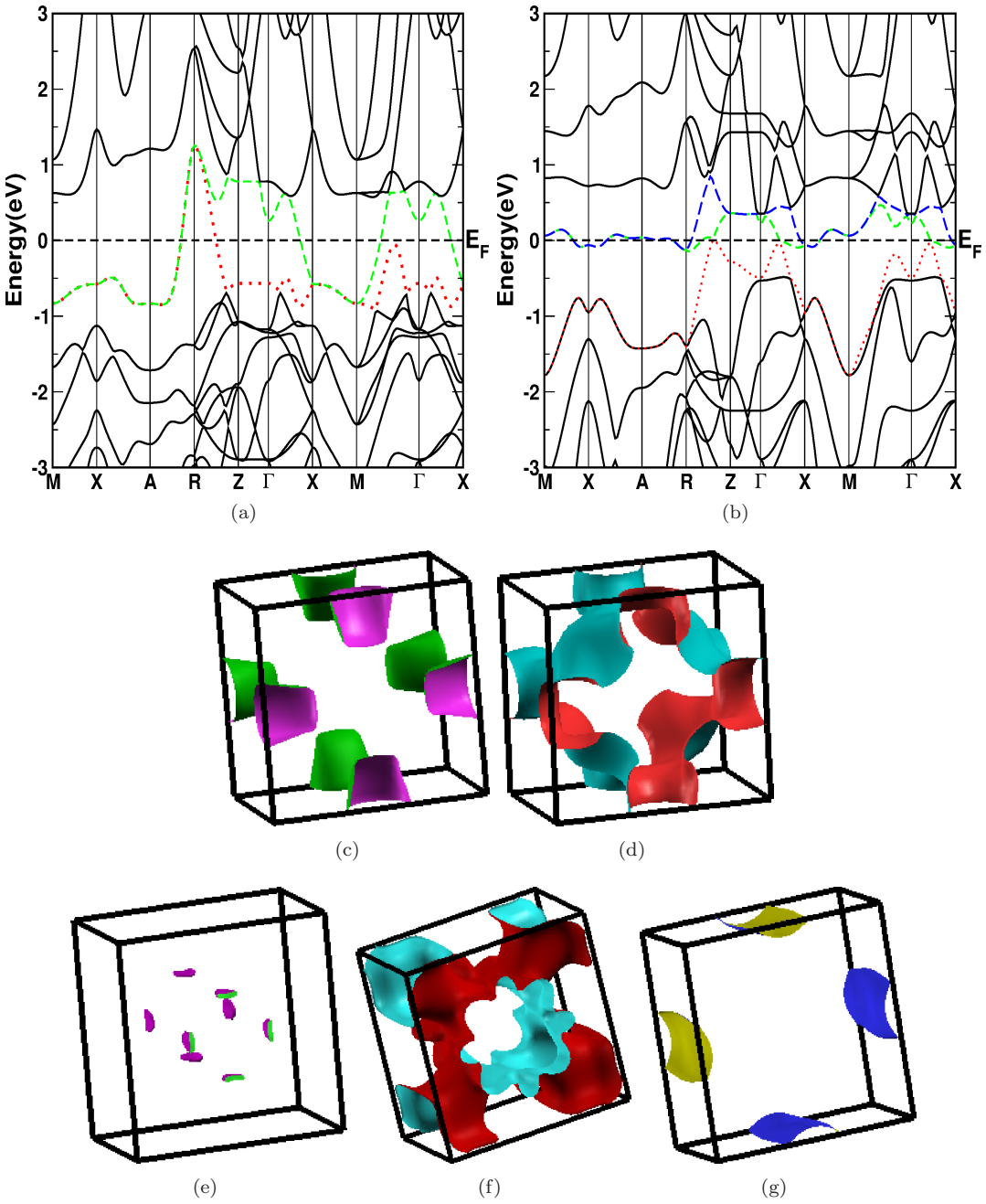

Figure 6.29: Band structure for MnGaGe at V/V_0=0.90 (a)majority spin (b)minority spin case. FS of (c, d) majority spin and (e, f, g) minority spin case.

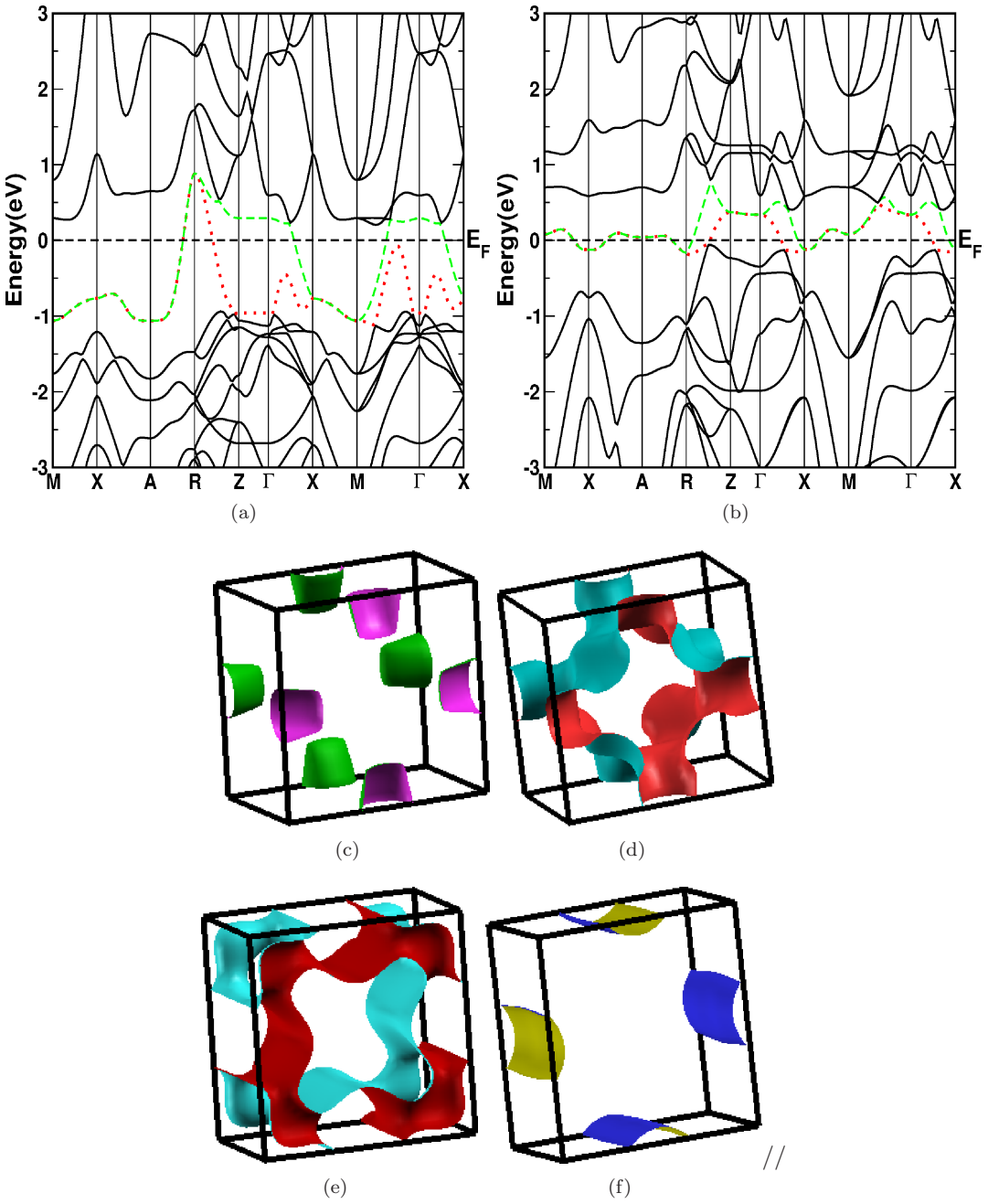

Figure 6.30: Band structure for MnZnSb at V/V_0=0.90 (a) majority spin (b) minority spin case. FS of (c, d) majority spin and (e, f) minority spin case.

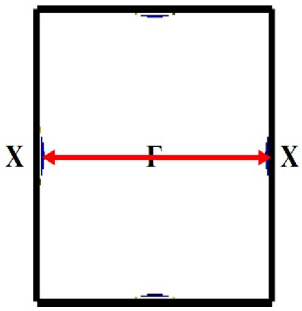

Figure 6.31: Nesting vector direction of the last FS in minority spin case in 2D representation.

the structural instability around this compression in MnZnSb, which needs further investigation.

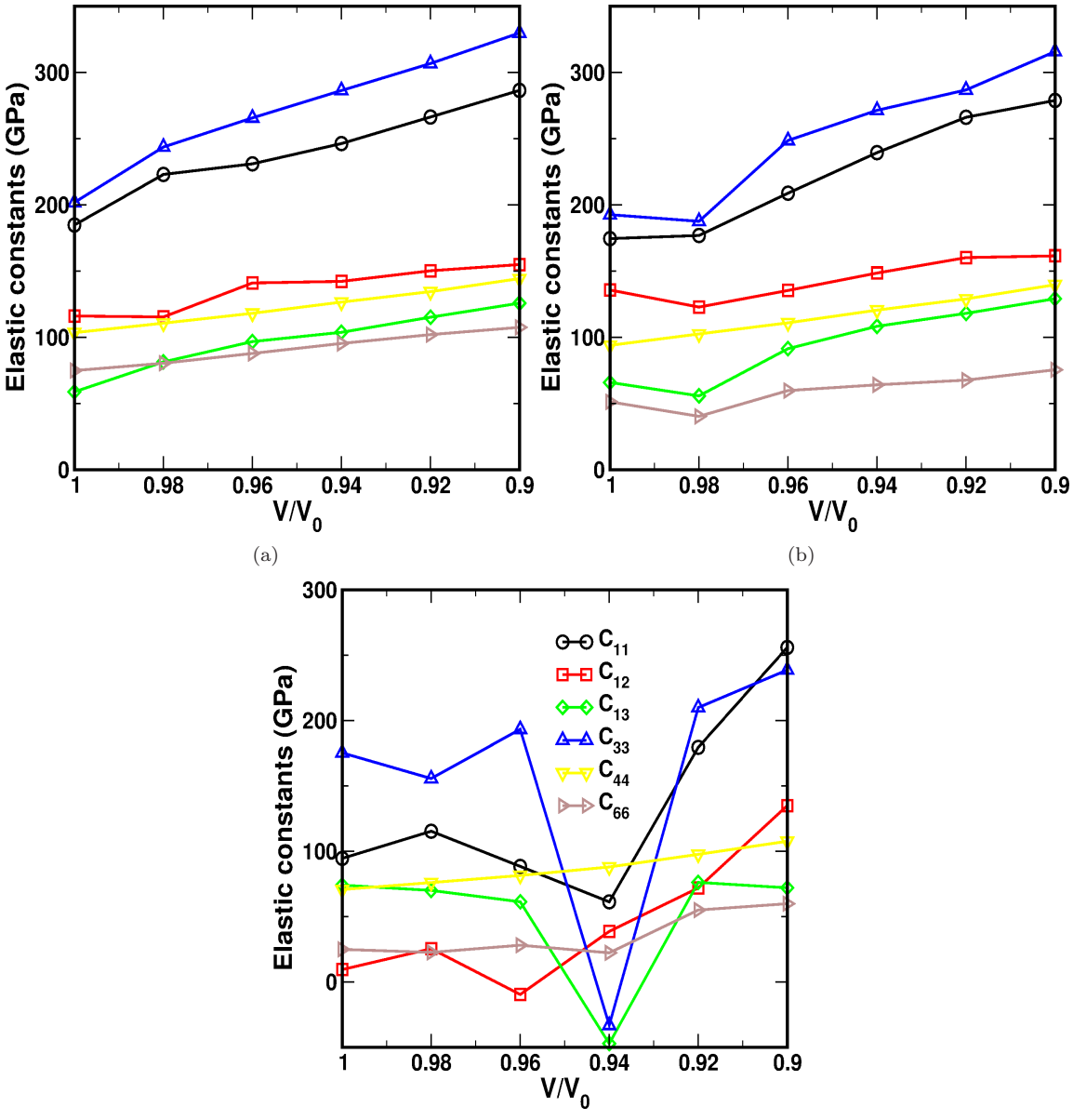

Figure 6.32: Elastic constants under compression (a) MnAlGe, (b) MnGaGe and (c) MnZnSb.

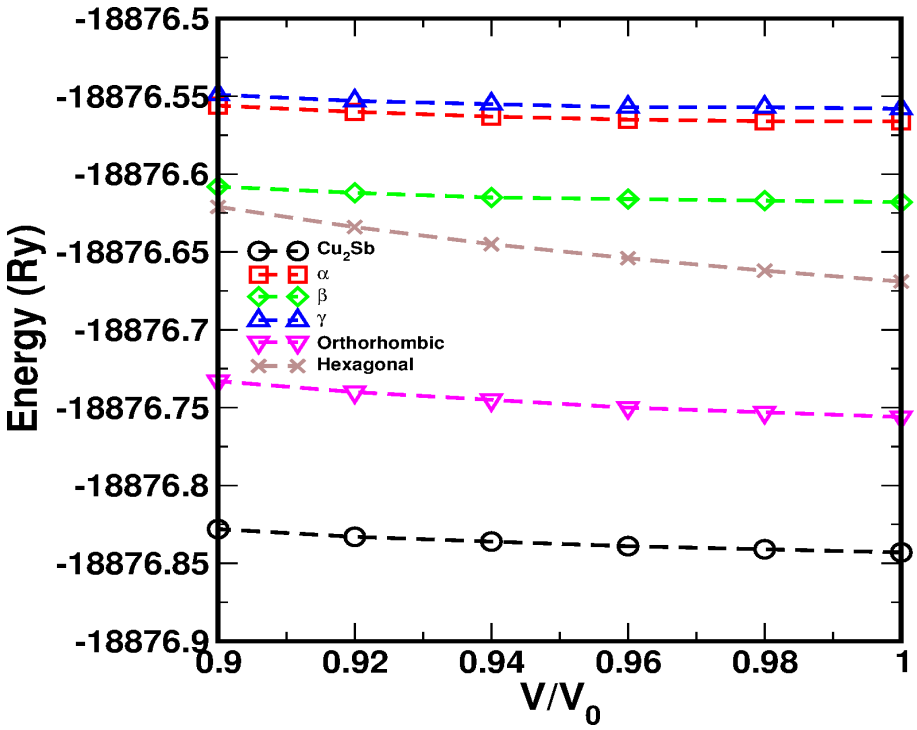

Figure 6.33: Energy versus compression for different possible structures of MnZnSb.

Table 6.1: Ground state properties of Zr_2TiAl at ambient pressure combined with experimental reports. Lattice parameter a in Å, Bulk modulus B in GPa and Magnetic moment in μ_B.

Parameters	LDA	LDA-mag	GGA	GGA-mag	Experimental[a]
Lattice parameter a	6.668	6.712	6.813	6.841	6.8400
Bulk modulus B	115	110	102	97	–
Magnetic moment of Ti	–	0.8	–	1.22	–

a : Ref. [275]

Table 6.2: Calculated Bader charge in the unit of electron charge (e) for all the compressions of Zr_2TiAl.

V/V_0	Zr1	Zr2	Ti	Al
1.00	0.47	0.47	0.12	-1.07
0.98	0.46	0.46	0.13	-1.06
0.96	0.45	0.45	0.14	-1.05
0.94	0.44	0.44	0.15	-1.04
0.92	0.42	0.42	0.17	-1.01
0.90	0.41	0.41	0.18	-0.99
0.85	0.36	0.36	0.21	-0.93
0.80	0.30	0.30	0.24	-0.83
0.75	-0.01	-0.01	0.48	-0.46

Table 6.3: Calculated elastic constants (in the unit of GPa) at ambient conditions for both magnetic and non-magnetic phases of Zr_2TiAl.

Parameters	Magnetic case	Non-magnetic case	Experiment
C_{11}	109	94	-
C_{12}	90	100	-
C_{44}	58	53	-

Table 6.4: Optimized z and z' values for Mn-based compounds.

MnXY	z_X	z'_Y
MnAlGe	$z_{Al} = 0.284$	$z'_{Ge} = 0.735$
MnGaGe	$z_{Ga} = 0.288$	$z'_{Ge} = 0.737$
MnZnSb	$z_{Zn} = 0.261$	$z'_{Sb} = 0.733$

Table 6.5: Optimized lattice parameters a, c in $\mathring{A}$ and calculated magnetic moment of total system (in units of μ_B/cell), individual elements (in units of μ_B), Sommerfield coefficient (γ) in the units of mJ/mol K^2 for all the Mn-based compounds. Calculated distances between the atoms are also given (in the units of $\mathring{A}$).

Parameters	MnAlGe		MnGaGe		MnZnSb	
	exp	This work	exp	This work	exp	This work
a	3.914[a]	3.92	3.966[c]	3.97	4.173[d]	4.171
c	5.933[a]	5.87	5.885[c]	5.81	6.233[d]	6.232
Total magnetic moment	-	3.25	-	3.20	-	5.25
$\mu_{B_{Mn}}$	1.40[a],1.7[b]	1.66	1.66[c]	1.67	1.50[e], 1.2[d]	2.66
$\mu_{B_{Al/Ga/Zn}}$	-0.02[b]	-0.013	-0.02[b]	-0.018	-	-0.021
$\mu_{B_{Ge/Sb}}$	-0.06[b]	-0.043	-0.07[b]	-0.045	-	-0.072
γ	8.9[f]	14.605	8.7[f]	9.105	11.3[f]	14.42
Mn-Mn (in plane)	-	2.773	2.8[g]	2.804	-	2.949
Mn-Al/Ga/Zn (in plane)	-	2.573	-	2.595	-	.644
Mn-Ge/Sb (in plane)	-	2.501	-	2.504	-	2.668
Mn-Mn (along c-axis)	-	5.87	5.89[g]	5.81	-	6.232

a : Ref. [288]; b : Ref. [128]; c : Ref. [289]; d : Ref. [290]; e : Ref. [291]; f : Ref. [292]; g : Ref. [135]

Table 6.6: Elastic constants (in the units of GPa), bulk modulus (B) (in the units of GPa), A is Anisotropy factor, σ is Poisson's ratio and E is Young's modulus (in the units of GPa) for Mn-based compounds.

	MnAlGe	MnGaGe	MnZnSb
C_{11}	185	174	94
C_{12}	116	136	9
C_{13}	59	66	74
C_{33}	202	193	175
C_{44}	103	94	71
C_{66}	75	51	25
B	115	120	75
A	3	5	2
σ	0.24	0.29	0.23
E	181	146	98

Chapter 7

Conclusions

In condensed matter physics, researchers have paid considerable attention towards the study of electronic structure properties to understand different material properties through Density Functional Theory (DFT), which is used to solve quantum many body problem. In the present thesis, DFT is used to calculate the electronic structure properties of different types of materials both at ambient conditions and at high pressures.

The importance of the Fermi surface topology in explaining different properties of metals, effect of pressure and it's importance is discussed in the introduction chapter along with a brief introduction about the compounds studied in the present thesis work. We have given an overview of DFT in the second chapter together with a short discussion about the linearized augmented plane wave method, pseudopotential method which are two different electronic structure calculation methods implemented in the WIEN2k [153] and Quantum Espresso codes [154], respectively. In our present thesis we have used WIEN2k code to calculate the electronic structure properties, FS topology, mechanical properties. To analyse the superconducting properties in some of the studied compounds, we have used Quantum Espresso package.

We have reported a theoretical description of the ground state, electronic structure, mechanical, vibrational properties of Ni-based Heuslar compounds, Ni_2XAl (X=Ti, Zr, Hf, V, Nb, and Ta), Ni_2NbGa and Ni_2NbSn, both at ambient conditions and under compression in chapter 3. Our calculated ground state properties agree well with experimental and other theoretical results. From these calculations, it is evident that at E_F, the contribution to total electronic density of states (DOS) is mainly from Ni-'d_{eg}' states with the admixture of Nb/X-'$d_{t_{2g}}$' states in all the compounds. Nesting features in FS are evident in all the compounds, and are found to be mechanically stable at ambient conditions and under compression. The absence of imaginary frequencies in phonon dispersion indicate the dynamical stability of the present compounds. Kohn anomaly is observed in TA2 mode in Ni_2NbX (X = Al, Ga and Sn) and Ni_2VAl compounds which might be due to the nesting in the FS. The computed T_c using Allen-Dynes formula agree well with the experimental results for Ni_2NbX (X = Al, Ga and Sn). Importantly, Ni_2VAl is predicted to be a superconductor which has a T_c value comparable to other Heusler compounds. From the calculated Eliashberg function ($\alpha^2F(\omega)$) we have observed that Ni atom contribution is more towards T_c in all the compounds. Under compression we have observed changes in the band structure of Ni_2NbAl, where we find an extra band to cross the E_F. In addition we also observed a pronounced softening in the Kohn anomalies existing in TA2

mode under compression. This phonon softening again lead to softening in the phonon density of states. A non-monotonic variation in the T_c under compression is noticed which is due to softening of the lower frequency acoustic mode and phonon DOS. Among the compounds studied, we observe that the variation in T_c under pressure is minimal in Ni_2VAl. It will be of interest to experimentally search for superconductivity in Ni_2VAl and study its pressure dependence.

In continuation to chapter 3, we extended our interest towards Nb-based A-15 compounds Nb_3Y (Y = Al, Ga, In, Ge, Sn, Os, Ir and Pt). In chapter 4 we have discussed the electronic structure of Nb_3Y (Y = Al, Ga, In, Ge, Sn, Os, Ir and Pt) compounds both at ambient conditions and under compression. In all the compounds it is observed that '*d*' states of Nb atoms has dominant nature at E_F with admixture of '*p*' or '*d*' sates of Y atom. All the compounds are found to possess both hole and electron FS. Parallel sheets are observed along X-Γ in the last two FS, which indicate the nesting property in these compounds which is also confirmed from the calculated Lindhard susceptibility plots, where sharp peaks are observed along X-Γ and at M point in the imaginary part of susceptibility plots in all the compounds at ambient conditions. Under compression continuous change in the FS topology is observed in all the compounds. For the given ETT's corresponding changes are observed under compression in the imaginary part of susceptibility and huge peaks are found along X-Γ and at M point in Nb_3Al. In Nb_3Ga and Nb_3In it is observed only along X-Γ. In Nb_3Ge, we have observed peaks at M, R and along X-Γ under compression. But in Nb_3Sn the peak is observed to decrease along X-Γ. The change in the band structure under compression lead to the non-monotonic variation in density of states. Mechanical stability of these compounds is also confirmed both at ambient conditions as well as under compression and non linear nature in C_{44} and C_s is observed in all the compounds under pressure. Further experiments are needed to realise the continuous FS topology changes observed in these compounds.

In chapter 5, a theoretical description of phase transition of SnAs and SnSb compounds is presented. The calculated structural properties are in good agreement with available experiments and other theoretical reports. From this study, we have concluded that both SnAs and SnSb have NaCl ground state and transforms to CsCl phase at high pressures. Total energy calculations confirms a first order phase transition in both the compounds with a volume collapse of 4.34% and 6.31% in SnAs and SnSb respectively. The pressure values corresponding to the phase transition are 37 GPa, 13 GPa for SnAs and SnSb compounds respectively. Fermi surface nesting feature is observed and confirmed from the susceptibility calculations in both the compounds at ambient conditions. Calculated T_c and λ_{ep} values are in good agreement with experiments. At the transition pressure, change in the band structure and FS topology is observed in NaCl-phase together with a softening of the acoustic mode in NaCl type SnAs and SnSb and the same softening nature is also observed in the CsCl-type SnAs and SnSb at the same transition pressure. Sudden drop in the T_c and λ_{ep} is observed in NaCl-type with increasing pressure. At the transition pressure around two fold and four fold increase in the T_c is observed in CsCl phase with high λ_{ep} of 1.08 and 1.55 for SnAs and SnSb respectively indicating strongly coupled superconducting nature in CsCl phase which needs to be verified experimentally.

In addition to the above mentioned non-magnetic compounds, a study on the new magnetic Zr_2TiAl Heusler compound and Cu_2Sb type Mn-based MnAlGe, MnGaGe and MnZnSb compounds are presented in chapter 6. We have investigated the electronic, magnetic, elastic, and vibrational properties of the Zr_2TiAl compound at ambient pressure as well as under compression. The obtained

structural parameters are in good agreement with the existing experimental data. We have determined that Zr_2TiAl has antiferromagnetic ground state with ordering of spin-up and spin-down Ti (111) layers with the magnetic moment on Ti atoms around $\sim$1.22 μ_B. The stability of the magnetic phase is also confirmed from the calculated elastic constants and phonon dispersion relations. We have also observed the magnetic to non-magnetic phase transition under compression due to the disappearance of the Ti magnetic moment, which tends to zero at V/V_0=0.75 ($\approx$ 46 GPa). Three ETT's are observed at V/V_0=0.96, 0.92 and 0.85, due to which a sudden drop in the magnetic moment of Ti atom is observed under compression.

In the case of Mn-based compounds, a quasi two dimensional nature is confirmed in Mn-based compounds from the Fermi surface calculations. Under compression decrease in the magnetic moment of Mn atom and change in the band and FS topology is observed in all the compounds. In MnZnSb, negative values in the elastic constants are observed under compression, where we find changes in band and FS topology correspondingly. These pressure values are in good agreement with experiment and might indicate an ETT or a structural phase transition, which needs to be verified elaborately. To confirm the phase stability, phonon calculations at ambient conditions and at high pressures may be very much helpful as in the case of Zr_2TiAl which need huse more computational sources and can be taken as future work. In addition, similar calculations are needed for computing the electron-phonon coupling of A-15 compounds, which also can form a part of the future work.

References

[1] A. R. Mackintosh. The Fermi surface of metals. *Scientific American* 209, (1963) 110-121.

[2] M. I. Kaganov and I. M. Lifshits. Electron theory of metals and geometry. *Soviet Physics Uspekhi* 22, (1979) 904.

[3] L. Onsager. Interpretation of the de Haas-van Alphen effect. *Phil. Mag.* 43, (1952) 1006-1008.

[4] I. M. Lifshitz and A. M. Kosevich. Theory of magnetic susceptibility in metals at low temperatures. *Sov. Phys. JETP* 2, (1956) 636-645.

[5] J. M. Ziman. Electrons in metals: A short guide to the Fermi surface. *Contemporary Physics* 4, (1962) 81-99.

[6] L. Van Hove. The occurrence of singularities in the elastic frequency distribution of a crystal. *Phys. Rev.* 89, (1953) 1189.

[7] I. M. Lifshitz. Anomalies of electron characteristics of a metal in the high pressure region. *Sov. Phys. JETP* 11, (1960) 1130-1135.

[8] Y. M. Blanter, M. I. Kaganov, A. V. Pantsulaya and A. A. Varlamov. The theory of electronic topological transitions. *Physics Reports* 245, (1994) 159-257.

[9] V. S. Egorov and A. N. Fedorov. Thermopower of lithium-magnesium alloys at the 24-order transition. *Zh. Eksp. Teor. Fiz* 85, (1983) 1647-1657.

[10] G. Bruno, B. Ginatempo, E. S. Giuliano and A. Stancanelli. Electronic properties of nonhomovalent alloys: A study of the bcc Li-Mg solid solution. *Il Nuovo Cimento D* 9, (1987) 1495-1513.

[11] S. V. Varyukhin and V. S. Egorov. Anomalies in the thermo-emf and resistance of cadmium-magnesium alloys at low temperature. *JETP Lett* 39, (1984). [Pis'ma Zh. Eksp. Teor. Fiz. 39, No. 11, (1984) 510-513]

[12] S. V. Varyukhin. Low-temperature anomalies in the resistance of metallic glasses. *JETP LETTERS* 48, (1988) 663-666.

[13] S. V. Varyukhin, V. S. Egorov and M. N. Khlopkin. Experimental and theoretical investigation of anomalies in the low-temperature specific heat on electron topological transitions in alloys. *Zhurnal Ehksperimental'noj i Teoreticheskoj Fiziki* 94, (1988) 254-262.

[14] S. V. Varyukhin, V. S. Egorov, M. N. Khlopkin, V. P. Antropov, V. G. Vaks, M. I. Katsnel'son, V. G. Koreshkov, A. I. Likhtenshtein and A. V. Trefilov. Experimental and Theoretical Investigations of Low-Temperature Specific-Heat Anomalies at Electronic Topological Transitions in Cd–Mg Alloys. *Sov. Phys. JETP* 67, (1988) 2318-2323.

[15] R. Daou, C. Bergemann and S. R. Julian. Continuous evolution of the Fermi surface of $CeRu_2Si_2$ across the metamagnetic transition. *Phys. Rev. Lett.* 96, (2006) 026401.

[16] M. Bercx and F. F. Assaad. Metamagnetism and Lifshitz transitions in models for heavy fermions. *Phys. Rev. B* 86, (2012) 075108.

[17] D. Aoki, Andrew Huxley, Eric Ressouche, Daniel Braithwaite, Jacques Flouquet, Jean-Pascal Brison, Elsa Lhotel and Carley Paulsen. Coexistence of superconductivity and ferromagnetism in URhGe. *Nature* 413, (2001) 613-616.

[18] F. Lévy, I. Sheikin, B. Grenier and Andrew D. Huxley. Magnetic field-induced superconductivity in the ferromagnet URhGe. *Science* 309, (2005) 1343-1346.

[19] E. A. Yelland, J. M. Barraclough, Weiwei Wang, K. V. Kamenev and A. D. Huxley. High-field superconductivity at an electronic topological transition in URhGe. *Nat. Phys.* 7, (2011) 890-894.

[20] Dai Aoki, Georg Knebel and Jacques Flouquet. Fermi Surface Instabilities in Ferromagnetic Superconductor URhGe. *J. Phys. Soc. Japan* 83, (2014) 094719.

[21] S. A. Grigera, R. S. Perry, A. J. Schofield, M. Chiao, S. R. Julian, G. G. Lonzarich, S. I. Ikeda, Y. Maeno, A. J. Millis and A. P. Mackenzie. Magnetic field-tuned quantum criticality in the metallic ruthenate $Sr_3Ru_2O_7$. *Science* 294, (2001) 329-332.

[22] C. Lester, Silvia Ramos, R. S. Perry, T. P. Croft, R. I. Bewley, T. Guidi, P. Manuel, D. D. Khalyavin, E. M. Forgan and S. M. Hayden. Field-tunable spin-density-wave phases in $Sr_3Ru_2O_7$. *Nat. Mater.* 14, (2015) 373-378.

[23] J. Paglione and Richard L. Greene. High-temperature superconductivity in iron-based materials. *Nat. Phys.* 6, (2010) 645-658.

[24] N. Ni, S. L. Budko, A. Kreyssig, S. Nandi, G. E. Rustan, A. I. Goldman, S. Gupta, J. D. Corbett, A. Kracher and P. C. Canfield. Anisotropic thermodynamic and transport properties of single-crystalline $Ba_{1-x}K_xFe_2As_2$ (x= 0 and 0.45). *Phys. Rev. B* 78, (2008) 014507.

[25] F. Ronning, T. Klimczuk, Eric D. Bauer, H. Volz and Joe D. Thompson. Synthesis and properties of $CaFe_2As_2$ single crystals. *J. Phys.: Condens. Matter.* 20, (2008) 322201.

[26] P. C. Canfield, S. L. Budko, N. Ni, A. Kreyssig, A. I. Goldman, R. J. McQueeney, M. S. Torikachvili, D. N. Argyriou, G. Luke and W. Yu. Structural, magnetic and superconducting phase transitions in $CaFe_2As_2$ under ambient and applied pressure. *Physica C: Superconductivity* 469, (2009) 404-412.

[27] J. H. Soh, Ggregory S. Tucker, Daniel K. Pratt, D. L. Abernathy, M. B. Stone, Sheng Ran, Sergey L. Budko, P. C. Canfield, A. Kreyssig, R. J. McQueeney and A. I. Goldman. Inelastic Neutron Scattering Study of a Nonmagnetic Collapsed Tetragonal Phase in Nonsuperconducting $CaFe_2As_2$: Evidence of the Impact of Spin Fluctuations on Superconductivity in the Iron-Arsenide Compounds. *Phys. Rev. Lett.* 111, (2013) 227002.

[28] T. Yildirim. Strong coupling of the Fe-spin state and the As-As hybridization in iron-pnictide superconductors from first-principle calculations. *Phys. Rev. Lett.* 102, (2009) 037003.

[29] K. Gofryk, B. Saparov, T. Durakiewicz, A. Chikina, S. Danzenbächer, D. V. Vyalikh, M. J. Graf and A. S. Sefat. Fermi-surface reconstruction and complex phase equilibria in $CaFe_2As_2$. *Phys. Rev. Lett.* 112, (2014) 186401.

[30] E. Bruno, B. Ginatempo, E. S. Guiliano, A. V. Ruban and Yu Kh Vekilov. Fermi surfaces and electronic topological transitions in metallic solid solutions. *Phys. Rep.* 249, (1994) 353-419.

[31] W. Kohn. Image of the Fermi Surface in the Vibration Spectrum of a Metal. *Phys. Rev. Lett.* 2, (1959) 393.

[32] P. L. Taylor. Theory of Kohn anomalies in the phonon spectra of metals. *Phys. Rev.* 131, (1963) 1995.

[33] A. Afanas'ev and Y. Kagan. Singularities Caused by Electron-phonon Interaction in the Phonon Dispersion Law. *Sov. Phy. -JETP* 16, (1963) 1030-1034.

[34] M. D. Johannes and I. I. Mazin. Fermi surface nesting and the origin of charge density waves in metals. *Phys. Rev. B* 77, (2008) 165135.

[35] X. Zhu, Y. Cao, J. Zhang, E. W. Plummer and J. Guo. Classification of charge density waves based on their nature. *Proc. Natl Acad. Sci.* 112, (2015) 2367-2371.

[36] J. M. Jani, Martin Leary, Aleksandar Subic and Mark A. Gibson. A review of shape memory alloy research, applications and opportunities. *Materials and Design* 56, (2014) 1078-1113.

[37] S. M. Shapiro, J. Z. Larese, Y. Noda, S. C. Moss and L. E. Tanner. Neutron scattering study of premartensitic behavior in Ni-Al alloys. *Phys. Rev. Lett.* 57, (1986) 3199.

[38] G. L. Zhao and B. N. Harmon. Phonon anomalies in β-phase Ni_xAl_{1x} alloys. *Phys. Rev. B* 45, (1992) 2818.

[39] S. B. Dugdale, R. J. Watts, J. Laverock, Zs Major, M. A. Alam, M. Samsel-Czekaa, G. Kontrym-Sznajd, Y. Sakurai, M. Itou and D. Fort. Observation of a Strongly Nested Fermi Surface in the Shape-Memory Alloy $Ni_0.62Al_0.38$. *Phys. Rev. Lett.* 96, (2006) 046406.

[40] Shiotani Nobuhiro, Isao Matsumoto, Hiroshi Kawata, Jinya Katsuyama, Masataka Mizuno, Hideki Araki and Yasuharu Shirai. Fermi surface of a shape memory alloy of TiNi. *J. Phys. Soc. Japan* 73, (2004) 1627-1630.

[41] P. A. Goddard, John Singleton, R. D. McDonald, Neil Harrison, J. C. Lashley, Hisatomo Harima and M-T. Suzuki. Catastrophic Fermi surface reconstruction in the shape-memory alloy AuZn. *Phys. Rev. Lett.* 94, (2005) 116401.

[42] P. J. Webster, K. R. A. Ziebeck, S. L. Town and M. S. Peak. Magnetic order and phase transformation in Ni_2MnGa. *Phil. Mag. B* 49, (1984) 295-310.

[43] O. I. Velikokhatnyi and I. I. Naumov. Electronic structure and instability of Ni_2MnGa. *Physics of the Solid State* 41, (1999) 617-623.

[44] Y. Lee, Joo Yull Rhee and B. N. Harmon. Generalized susceptibility of the magnetic shape-memory alloy Ni_2MnGa. *Phys. Rev. B* 66, (2002) 054424.

[45] A. Zheludev, S. M. Shapiro, P. Wochner, A. Schwartz, M. Wall and L. E. Tanner. Phonon anomaly, central peak, and microstructures in Ni_2MnGa. *Phys. Rev. B* 51, (1995) 11310.

[46] T. D. Haynes, R. J. Watts, J. Laverock, Zs Major, M. A. Alam, J. W. Taylor, J. A. Duffy and S. B. Dugdale. Positron annihilation study of the Fermi surface of Ni_2MnGa. *New J. Phys.* 14, (2012) 035020.

[47] A. Jayaraman. The diamond anvil cell and high pressure research. *Le Journal de Physique Colloques* 45, (1984) C8-355.

[48] Zhao Zhao, Haijun Zhang, Hongtao Yuan, Shibing Wang, Yu Lin, Qiaoshi Zeng, Gang Xu, Zhenxian Liu, G.K. Solanki, K.D. Patel, Yi Cui, Harold Y. Hwang and Wendy L. Mao. Pressure induced metallization with absence of structural transition in layered molybdenumdiselenide. *Nat. Commun.* 6, (2015) 7312.

[49] Dawei Zhou, Yonghui Zhou, Chunying Pu, Xuliang Chen, Pengchao Lu, Xuefei Wang, Chao An, Ying Zhou, Feng Miao, Ching-Hwa Ho, Jian Sun, Zhaorong Yang and Dingyu Xing. Pressure-induced metallization and superconducting phase in ReS_2. *npj Quantum Materials* 2, (2017) 19.

[50] L Petit, A Svane, M Lüders, Z Szotek, G Vaitheeswaran, V Kanchana and W M Temmerman. Phase transitions in rare earth tellurides under pressure. *J. Phys.: Condens. Matter.* 26, (2014) 274213.

[51] A. Chatterjee, A. K. Singh and A. Jayaraman, Pressure-Induced Electronic Collapse and Structural Changes in Rare-Earth Monochalcogenides. *Phy. Rev. B* 6, (1972) 2285.

[52] L. Petit, Z. Szotek, M. Lüders, W. M. Temmerman and A. Svane. First-principles study of valence and structural transitions in EuO under pressure. *Phy. Rev. B* 90, (2014) 035110.

[53] Chunju Hou, Jorge Botana, Xu Zhang, Xianlong Wang and Maosheng Miao. Pressure-induced structural and valence transition in AgO. *Phys.Chem.Chem.Phys.* 18, (2016) 15322.

[54] A.K. Mcmahan. Pressure-induced changes in the electronic structure of solids. *Physica B+C* 139-140, (1986) 31-41.

[55] A. V. Narlikar. Superconductors. Oxford University Press, ISBN:9780199584116, (2014) page no. 98 .

[56] J. E. Hirsch and J. J. Hamlin. Why non-superconducting metallic elements become superconducting under high pressure. *Physica C* 470, (2010) S937-S939.

[57] J. G. Bednorz and K. A. Müller. Possible high T_c superconductivity in the Ba-La-Cu-O system. *Z. Phys. B -Condensed Matter* 64, (1986) 189-193.

[58] C. W. Chu, P. H. Hor, R. L. Meng, L. Gao, Z. J. Huang and Y. Q. Wang. Evidence for superconductivity above 40 K in the La-Ba-Cu-O compound system. *Phys. Rev. Lett.* 58, (1987) 405-407.

[59] M. K. Wu, J. R. Ashburn, C. J. Torng, P. H. Hor, R. L. Meng, L. Gao, Z. J. Huang, Y. Q. Wang and C. W. Chu. Superconductivity at 93 K in a new mixed-phase Y-Ba-Cu-O compound system at ambient pressure. *Phys. Rev. Lett.* 58, (1987) 908.

[60] M. K. Forthaus, K. Sengupta, O. Heyer, N. E. Christensen, A. Svane, K. Syassen, D. I. Khomskii, T. Lorenz and M. M. Abd-Elmeguid. Superconductivity in SnO: A nonmagnetic analog to Fe-based superconductors?. *Phys. Rev. Lett.* 105, (2010) 157001.

[61] S. V. Vonsovsky, Yu. A. Izyumov and E. Z. Kurmaev. Superconductivity of transition metals. Germany: Springer, 1982.

[62] A. P. Drozdov, M. I. Eremets, I. A. Troyan, V. Ksenofontov and S. I. Shylin. Conventional superconductivity at 203 kelvin at high pressures in the sulfur hydride system. *Nature* 525, (2015) 73-76.

[63] J. Kübler, A. R. Williams and C. B. Sommers. Formation and coupling of magnetic moments in Heusler alloys. *Phys. Rev. B* 28, (1983) 1745-1755.

[64] C. Felser, G. H. Fecher. and B. Balke. Spintronics: A challenge for materials science and solid-state chemistry. *Angew. Chem. Int. Ed.* 46, (2007) 668-699.

[65] S. Wurmehl, H. C. Kandpal, G. H. Fecher and C. Felser. Valence electron rules for prediction of half-metallic compensated-ferrimagnetic behaviour of Heusler compounds with complete spin polarization. *J. Phys.: Condens. Matter* 18, (2006) 6171-6181.

[66] D. Jung, H.-J. Koo and M.-H. Whangbo. Study of the 18-electron band gap and ferromagnetism in semi-Heusler compounds by non-spin-polarized electronic band structure calculations. *J. Mol. Struct. (Theochem)* 527, (2000) 113-119.

[67] J. Pierre, R. V. Skolozdra, J. Tobola, S. Kaprzyk, C. Hordequin, M. A. Kouacou, I. Karla, R. Currat and E. Lelievre-Berna. Properties on request in semi-Heusler phases. *J. Alloys Comp.*262-263, (1997) 101107.

[68] R. A. De Groot, F. M. Mueller, P. G. Van Engen and K. H. J. Buschow. New class of materials: half-metallic ferromagnets. *Phys. Rev.Lett.* 50, (1983) 2024.

[69] C. Felser, B. Heitkamp, F. Kronast, D. Schmitz, St Cramm, H. A. Dürr, H. J. Elmers, G. H. Fecher, S. Wurmehl, T. Block, D. Valdaitsev, S. A. Nepijko, A. Gloskovskii, G. Jakob, G. Schönhense and W. Eberhardt. Investigation of a novel material for magnetoelectronics: $Co_2Cr_{0.6}Fe_{0.4}Al$. *J. Phys.: Condens.Matter* 15, (2003) 7019-7027.

[70] C. Felser, Gerhard H. Fecher and Benjamin Balke. Spintronics: a challenge for materials science and solidstate chemistry. *Angew. Chem. Int. Ed.* 46, (2007) 668-699.

[71] David Kieven, Reiner Klenk, Shahab Naghavi, Claudia Felser and Thomas Gruhn. I-II-V half-Heusler compounds for optoelectronics: Ab initio calculations. *Phys. Rev. B* 81, (2010) 075208.

[72] Christian G. F. Blum, Siham Ouardi, Gerhard H. Fecher, Benjamin Balke, Xeniya Kozina, Gregory Stryganyuk, Shigenori Ueda, Keisuke Kobayashi, Claudia Felser, Sabine Wurmehl and Bernd Büchner. Exploring the details of the martensite-austenite phase transition of the shape memory Heusler compound Mn_2NiGa by hard x-ray photoelectron spectroscopy, magnetic and transport measurements. *Appl. Phys. Lett.* 98, (2011) 252501.

[73] J. H. Wernick, G. W. Hull, T. H. Geballe, J. E. Bernadini and J. V. Waszczak. Superconductivity in ternary Heusler intermetallic compounds. *Mater. Lett.* 2, (1983) 90-92.

[74] J. Winterlik, G. H. Fecher, A. Thomas and C. Felser. Superconductivity in ternary Heusler intermetallic compounds. *Phys. Rev. B* 79 (2009) 064 508-064 517.

[75] S. Sakurada and N. Shutoh. Effect of Ti substitution on the thermoelectric properties of (Zr, Hf) NiSn half-Heusler compounds. *Appl. Phys. Lett.* 86, (2005) 082105.

[76] C. Uher, J. Yang, S. Hu, D. T. Morelli and G. P. Meisner. Transport properties of pure and doped MNiSn(M=Zr, Hf). *Phys. Rev. B* 59, (1999) 8615-8621.

[77] D. Kieven, R. Klenk, S. Naghavi, C. Felser and T. Gruhn. I-II-V half-Heusler compounds for optoelectronics: Ab initio calculations. *Phys. Rev. B* 81, (2010) 075 208-075 214,.

[78] S. Chadov, X. Qi, J. Kübler, G. H. Fecher, C. Felser and S. C. Zhang. Tunable multifunctional topological insulators in ternary Heusler compounds. *Nat. Mat.* 9, (2010) 541-545.

[79] H. Lin, A. Wray, Y. Xia, S. Xu, S. Jia, R. J. Cava, A. Bansil and M. Z. Hasan. Half-Heusler ternary compounds as new multifunctional experimental platforms for topological quantum phenomena. *Nat. Mat.* 9, (2010) 546549.

[80] F. Heusler, W. Starck and E. Haupt. Uber die Synthese ferromagnetis cher Manganlegierungen. *Verh. d. DPG*5, (1903) 220-223.

[81] F. Heusler. Uber magnetische Maganlegierungen. *Verh. d. DPG* 5, (1903) 219.

[82] F. G. Aliev, N. B. Brandt, V. V. Moshchalkov, V. V. Kozyrkov, R. V. Skolozdra and A. I. Belogorokhov. Gap at the Fermi level in the intermetallic vacancy system RBiSn (R= Ti, Zr, Hf). *Z. Phys. B-Condens. Matter* 75, (1989) 167-171.

[83] P. Webster. Magnetic and chemical order in Heusler alloys containing cobalt and manganese. *J. Phys. Chem. Solids* 32, (1971) 1221-31.

[84] S. Ishida, S. Akazawa, Y. Kubo and J. Ishida. Band theory of Co_2MnSn, Co_2TiSn and Co_2TiAl. *J. Phys. F Met. Phys.* 12, (1982) 1111.

[85] W. Lin and A. J. Freeman. Cohesive properties and electronic structure of Heusler $L2_1$-phase compounds Ni_2XAl (X= Ti, V, Zr, Nb, Hf, and Ta). *Phys. Rev. B* 45, (1992) 61.

[86] P. R. Strutt, R. S. Polvani and J. C. Ingram. Creep behavior of the Heusler type structure alloy Ni_2AlTi. *Metallurgical and Materials Transactions* A 7, (1976) 23-31.

[87] A. Taylor and R. W. Floyd. The constitution of nickel-rich alloys of the nickel-titanium-aluminium system. *J. Inst. Metals* 81, (1952) 25.

[88] Y. Umakoshi, M. Yamaguchi and T. Yamane. Effects of non-stoichiometry on the high-temperature deformation of Ni_2AlTi. *Phil. Mag. A* 52, (1985) 357-367.

[89] A. Raman and K. Schubert. UBER DEN AUFBAU EINIGEN ZU TIAL3 VERWANDTER LEGIERUNGSREIHEN. 3. UNTERSUCHUNGEN IN EINIGEN T-NI-AL- UND T-CU-AL-SYSTEMEN. *Zeitschrift fur Metallkunde* 56, (1965) 99.

[90] F. S. Da Rocha, G. L. F. Fraga, D. E. Brandao, C. M. Da Silva and A. A. Gomes. Specific Heat and Electronic Structure of Heusler Compounds Ni_2TAl (T= Ti, Zr, Hf, V, Nb, Ta). *Physica B* 269, (1999) 154-162.

[91] Shinya Waki, Yuji Yamaguchi and Kazuyoshi Mitsugi. Superconductivity of Ni_2NbX (X= Al, Ga and Sn). *J. Phys. Soc. Jpn.* 54, (1985) 1673-1676.

[92] B. Boren. X-ray investigation of alloys of silicon with chromium, manganese, cobalt and nickel. *Arkiv för Kemi, Mineralogi och Geologi* 11, (1933) 2-10.

[93] George F. Hardy and John K. Hulm. Superconducting Silicides and Germanides. *Phys. Rev.* 89, (1953) 884.

[94] B. T. Matthias, T. H. Geballe, S. Geller and E. Corenzwit. Superconductivity of Nb_3Sn. *Phys. Rev.* 95, (1954) 1435.

[95] B. W. Batterman and C. S. Barrett. Low-temperature structural transformation in V_3Si. *Phys. Rev.* 145, (1966) 296.

[96] L. R. Testardi. Structural instability and superconductivity in A-15 compounds. *Rev. Mod. Phys.* 47, (1975) 637.

[97] B. N. Kodess. and V. Sh Shekhtman. SUPERCONDUCTIVITY AND STRUCTURE OF COMPOUNDS BASED ON NIOBIUM AND VANADIUM. Inst. of Solid State Physics, Moscow, 1971; B. N. Kodess and V. Sh Shekhtman. *"Pis ma Zh. Eksp. Teor. Fiz.* 14, (1971) 338. [JETP Lett. 14, 225 (1971)]; B. N Kodess, V. B. Kurithzin and B. N. Kodess. *Solid State Commun* 16 (1975) 269.

[98] Eckhard Nembach, Kyöji Tachikawa and Shigeo Takano. Martensitic transformation in V_3Ga foils at low temperatures. *Philos. Mag.* 21, (1970) 869-872.

[99] R. Viswanathan, C. T. Wu, H. L. Luo and G. W. Webb. Low temperature heat-capacity measurements of V_3Ga and Nb_3Al. *Solid State Commun.* 14, (1974) 1051-1054.

[100] P.H. Schmidt, E.Q. Spencer, D.C. Joy and J.M. arid Rowell. Superconductivity in d-and f-band Metals. Edited by D. H. Douglass (Plenum, New York, 1976), p. 431.

[101] G. Shirane and J. D. Axe. Neutron scattering study of the lattice-dynamical phase transition in Nb_3Sn. *Phys. Rev. B* 4, (1971) 2957.; R. Viswanathan, C. T. Wu, H. L. Luo and G. W. Webb. Low temperature heat-capacity measurements of V_3Ga and Nb_3Al. *Solid State Communications* 14, (1974) 1051-1054.; B.N. Kodess. *Fiz. Tverd. Tela.* 15, (1978) 1252. [Sov. Phys. Solid State. **15**, 844 (1978)]; B.N. Kodess. *Solid State Commun.* 16, (1975) 269.

[102] B. M. Klein, L. L. Boyer, D. A. Papaconstantopoulos and L. F. Mattheiss. Self-consistent augmented-plane-wave electronic-structure calculations for the A 15 compounds V_3X and Nb_3X, X= Al, Ga, Si, Ge, and Sn. *Phy. Rev. B* 18, (1978) 6411.

[103] D. Dew-Hughes. Superconducting A-15 compounds: A review. *Cryogenics* 15(8), (1975) 435-454.

[104] Takafumi Adachi, Ichimin Shirotani, Junichi Hayashi and Osamu Shimomura. Phase transitions of lanthenide monophospides with NaCl-type structure at high pressures. *Physics Letters A* 250, (1998) 389-393.

[105] Huan Luo, Raymond G. Greene, kouros Ghandehari, Ting Li and Arthur L. Ruoff. Structural phase transformations and the equations of state of calcium chalcogenides at high pressure. *Phy. Rev. B* 50, (1994) 16232-16237.

[106] Luis Mancera, Jairo A. Rodrguez and Noboru Takeuchi. Theoretical study of the stability of wurtzite, zincblende, NaCl and CsCl phases in group IIIB and IIIA nitrides. *physica status solidi (b)* 241, (2004) 2424-2428.

[107] P. T. Jochym and K. Parlinski. Elastic properties and phase stability of AgBr under pressure. *Phys. Rev. B* 65 (2001) 024106.

[108] I. Lefebvre, M. A. Szymanski, J. Olivier-Fourcade and J. C. Jumas. Electronic structure of tin monochalcogenides from SnO to SnTe. *Phys. Rev. B* 58, (1998) 1896-1906.

[109] T. Soma. The electronic theory of III-V and II-VI tetrahedral compounds. II. Covalent-metallic or covalent-ionic phase transition under pressure. *J. Phys. C: Solid State Phys.* 11, (1978) 2681.

[110] V. G. Losev, G. B. Demishev, T. I. Dyuzheva, T. N. Kolobyanina and S. S. Kabalkina. SnAs polymorphism at high-pressure to 43-GPa. *Fiz. Tverd. Tela.* 26, (1984) 3452-3454.

[111] G. B. Demishev, S. S. Kabalkina, T. N. Kolobyanina, T. I. Dyuzheva and V. G. Losev. X-ray studies of the semiconductors SnAs, InTe, TlS and TiSe up to 43 GPa. *High Pressure Research* 1, (1989) 325-327.

[112] Yue Wang, Hikaru Sato, Yoshitake Toda, Shigenori Ueda, Hidenori Hiramatsu and Hideo Hosono. SnAs with the NaCl-type structure: type-I superconductivity and single valence state of Sn. *Chem. Mater.* 26, (2014) 7209-7213.

[113] H. M. Tütüncü and G. P. Srivastava. Electron-phonon interaction and super conductivity in SnAs with the sodium chloride crystal structure. *Solid State Commun.* 221, (2015) 24-27.

[114] Deepika Shrivastava, Shweta D. Dabhi, Prafulla K. Jha and Sankar P. Sanyal. Structural phase transition, electronic and elastic properties of rocksalt structure SnAs and SnSb. *Solid State Commun.* 243, (2016) 16-22.

[115] Izumi Hase, kouki Yasutomi, Takashi Yanagisawa, Kousuke Odagiri and Taichiro Nishio. Electronic structure of InTe, SnAs and PbSb: Valence-skip compound or not?. *Physica C: Superconductivity and its applications* 527, (2016) 85-90.

[116] Zhufeng Hou, Aiyu Li, Zizhong Zhu, Meichun Hung and Yong Yang. Ab initio calculations of the formation energies of lithium intercalations in SnSb. *J. Mater. Sci. Technol.* 20, (2004) 743-745.

[117] Deepika Shrivastava, Shweta D. Dabhi, Prafulla K. Jha and Sankar P. Sanyal. Structural phase transition, electronic and elastic properties of rocksalt structure SnAs and SnSb. *Solid State Communications* 243, (2016) 16-22.

[118] W. B. Pearson. *Z. Kristallogr.* 171 (1985) 23.

[119] Motoyoshi Yuzuri. On the Magnetic Properties of Cr_2As and Cu_2Sb. *J. Phys. Soc. Jpn.* 15, (1960) 2007-2012.

[120] L. C. Gupta, Satish K. Malik and R. Vijayaraghavan. NMR evidence to the absence of antiferromagnetism in Cu_2Sb. *Phys. Lett. A* 28, (1968) 255-256.

[121] K. Andres, E. Bucher, J. P. Maita and A. S. Cooper. Superconductivity of Cu_2Sb phases and absence of antiferromagnetism in Cu_2Sb. *Phys. Lett. A* 28, (1968) 67-68.

[122] M. K. Wilkinson, N. S. Gingrich and C. G. Shull. The magnetic structure of Mn_2Sb. *J. Phys. Chem. Solids* 2, (1957) 289-300.

[123] A. Kimura, S. Suga, T. Matsushita, T. Kaneko and T. Kanomata. Unoccupied electronic states and exchange splitting of M_2As (M= Cr, Fe, Mn) and MnAlGe. *Solid State Commun.* 85, (1993) 901-905.

[124] Rie Y. Umetsu, Yoshifuru Mitsui, Isamu Yuito, Teruaki Takeuchi and Hiroshi Kawarada. Substitution Effects of Cr or Fe on the Curie Temperature for Mn-Based Layered Compounds MnAlGe and MnGaGe With Cu_2Sb-Type Structure. *IEEE Transactions on Magnetics* 50, (2014) 1-4.

[125] S. Mizukami, A. Sakuma, T. Kubota, A. Sigihara and T. Miyazaki. Fast magnetization precession for perpendicularly magnetized MnAlGe epitaxial filmswith atomic layered structures. *Appl. Phys. Lett.* 103, (2013) 142405.

[126] R. C. Sherwood, E. A. Nesbitt, J. H. Wernick, D. D. Bacon, A. J. Kurtzig and R. Wolfe. MnAlGe Films for MagnetoOptic Applications. *J. Appl. phys.* 42, (1971) 1704-1705.

[127] B. R. Brown. Optical data storage potential of six materials. *Applied optics* 13, (1974) 761-766.

[128] K. Motizuki, T. Korenari and M. Shirai. Electronic band structures and magnetism of intermetallic Cu_2Sb-type manganese compounds MnAlGe and MnGaGe. *Journal of Magnetism and Magnetic Materials* 104, (1992) 1923-1924.

[129] Peter Mohn and Karlheinz Schwarz. Quasi two-dimensional magnetism in MnGaGe. *Journal of magnetism and magnetic materials* 157, (1996) 721-722.

[130] A. Kimura, S. Suga, T. Kanomata and K. Motizuki. Electronic structure of ternary ferromagnetic compounds MnAlGe and MnGaGe. *Phys. Stat. Sol. (c)* 3, (2006) 2791-2795.

[131] W. A. J. J. Velge and K. J. De Vos. Influence of milling upon the magnetic properties of the intermetallic compound MnAlGe. *Journal of Applied Physics* 34, (1963) 3568-3571.

[132] Takeshi Kanomata, Takashi Kawashima, Takejiro Kaneko, Hiroki Takahashi and Nobuo Mōri. Pressure effect of the lattice parameters for Mn_2Sb and MnMGe (M= Al, Ga). *Jpn. J. Appl. Phys.* 30, (1991) 541.

[133] Hiroyasu Matsuzaki, Shoichi Endo, Yukio Notsu, Fumihisa Ono, Takeshi Kanomata and Takejiro Kaneko. Pressure Effect on Curie Temperature in MnZnSb. *Jpn. J. Appl. Phys.* 32, (1993) 271.

[134] T. Kanomata, T. Suzuki, H. Yoshida and T. Kaneko. Pressure effect on the Curie temperature and thermal expansion of MnAlGe. *J. Mag. Mag. Mat.* 104, (1992) 1957-1958.

[135] S. Endo, H. Matsuzaki, F. Ono, T. Kanomata and T. Kaneko. Pressure dependence of the Curie temperature in MnGaGe. *J. Mag. Mag. Mat.* 140, (1995) 139-140.

[136] M. Born and R. Oppenheimer. Quantum theory of the molecules. *Ann. der Physik* 84, (1927) 457.

[137] P. Hohenberg and W. Kohn. Inhomogeneous electron gas. *Phys. Rev.* 136, (1964) B864.

[138] W. Kohn and L. J. Sham. Self-consistent equations including exchange and correlation effects. *Phys. Rev.* 140(4A), (1965) A1133-A1138.

[139] R. G. Parr and W. Yang. Density functional theory of atoms and molecules. Oxford University, Oxford, 1989.

[140] W. Kohn. Nobel Lecture: Electronic structure of matterwave functions and density functionals. *Rev. Mod. Phys.* 71, (1998) 1253-1266.

[141] R. O. Jones and O. Gunnarsson. The density functional formalism, its applications and prospects. *Rev. Mod. Phys.* 61, (1989) 689-746.

[142] W. Koch and M. C. Holthausen. A Chemists guide to density functional theory. WILEY-VCH 2001.

[143] M. R. Dreizler and E. K. U. Gross. Density functional theory : An approach to the quantum many-body problem. Springer, Berlin, 1990.

[144] N. M. Harrison. An introduction to density functional theory. 2002 (*http* : *//www.ch.ic.ac.uk/harrison/Teaching/DFT$_N$ATO.pdf*.).

[145] Richard M. Martin. Electronic structure: basic theory and practical methods. Cambridge University Press, Cambridge, UK; New York, 2004. ISBN 0521782856.

[146] Klaus Capelle. A bird's-eye view of density-functional theory, November 2006 (*http* : *//arxiv.org/abs/cond − mat/*0211443*v*5).

[147] L. H. Thomas. The calculation of atomic fields. *Math. Proc. Cambridge* 23, (1927) 542.

[148] E. Fermi. Un Metodo Statistico per la Determinazione di alcune Prioprietá dell'Atomo. *Rend. Accard. Naz. Lincei* 6, (1927) 602.

[149] I. N. Levine. Quantum Chemistry, Prentice-Hall of India Private Limited, 2006.

[150] P. Haas, F. Tran and P. Blaha. Calculation of the lattice constant of solids with semilocal functionals. *Phys. Rev. B* 79, (2009) 085104.

[151] J. Harl, L. Schimka and G. Kresse. Assessing the quality of the random phase approximation for lattice constants and atomization energies of solids. *Phys. Rev. B* 81, (2010) 115126.

[152] J. Sun, M. Marsman, G. I. Csonka, A. Ruzsinszky, P. Hao, Y.-S. Kim, G. Kresse and J. P. Perdew. Self-consistent meta-generalized gradient approximation within the projector-augmented-wave method. *Phys. Rev. B* 84, (2011) 035117.

[153] P. Blaha, K. Schwarz, G. K. H. Madsen, D. Kvasnicka and J. Luitz. WIEN2k, An augmented plane wave + local orbitals program for calculating crystal properties (Karlheinz Schwarz, Techn. Universit t Wien, Austria), 2001 < *http* : *//www.wien*2*k.at/* >. P. Blaha, K. Schwarz, P. I. Sorantin and S. B. Tricky. Full-potential linearinsed augmented plane wave programs for crystalline systems. *Computer. Phys. Commun.* 59, (1990) 399-415.

[154] P. Giannozzi, S. Baroni, N. Bonini, M. Calandra, R. Car, C. Cavazzoni, D. Ceresoli, G. L. Chiarotti, M. Cococcioni, I. Dabo, A. D. Corso, S. de Gironcoli, S. Fabris, G. Fratesi, R. Gebauer, U. Gerstmann, C. Gougoussis, A. Kokalj, M. Lazzeri, L. Martin-Samos, N. Marzari, F. Mauri, R. Mazzarello, S. Paolini, A. Pasquarello, L. Paulatto, C. Sbraccia, S. Scandolo, G. Sclauzero, A. P. Seitsonen, A. Smogunov, P. Umari and R. M. Wentzcovitch. QUANTUM ESPRESSO: a modular and open-source software project for quantum simulations of materials. *J. Phys.: Condens. Matter* 21, (2009) 395502-1-395502-19 (< *http* : *//www.pwscf.org* >).

[155] H. C. Kandpal,G. H. Fecher and C. Felser. Calculated electronic and magnetic properties of the half-metallic, transition metal based Heusler compounds. *J. Phys. D: Appl. Phys.* 40, (2007) 1507-1523

[156] S. Galehgirian and F. Ahmadian. First principles study on half-metallic properties of Heusler compounds Ti_2VZ (Z=Al, Ga, and In). *Solid State Commun.* 202, (2015) 52-57.

[157] F. Lei, C. Tang, S. Wang and W. He. Half-metallic full-Heusler compound Ti_2NiAl: A first-principles study, *J. Alloy. Comp.* 509, (2011) 5187-5189.

[158] K. Gofryk, D. Kaczorowski, T. Plackowski, A. Leithe-Jasper and Yu. Grin. Magnetic and transport properties of the rare-earth-based Heusler phases RPdZ and RPd_2Z (Z= Sb,Bi). *Phys. Rev. B* 72, (2005) 094409.

[159] D. Kaczorowski, K. Gofryk, T. Plackowski, A. Leithe-Jasper and Yu. Grin. Unusual features of erbium-based Heusler phases. *J. Magn. Magn. Mater.* 290-291, (2005) 573-579.

[160] K. Gofryk, D. Kaczorowski and A. Czopnik. Magnetic and transport properties of UPd_2Sb. *Solid State Commun.* 133, (2005) 625-628.

[161] H. Nakamura, Y. Kitaoka, K. Asayama, Y. Õnuki and T. Komatsubara. Observation of two phase transitions in the Heuslaer heavy fermion system $CeInCu_2$. *J. Magn. Magn. Mater.* 76-77, (1988) 467-468.

[162] S. Takayanagi, S. B. Woods, N. Wada, T. Watanabe, Y. Õnuki, A. Kobori, T. Komatsubara, M. Imai and H. Asano. Magnetic and transport properties of in the cubic heavy fermion system $CeInCu_2$, *J. Magn. Magn. Mater.* 76-77, (1988) 281-282.

[163] M. Wuttig, J. Li and C. Craciunescu. A new ferromagnetic shape memory alloy system. *Scripta Mater.* 44, (2001) 2393-2397.

[164] Y. Sutou, Y. Imano, N. Koeda, T. Omori, R. Kainuma, K. Ishida and K. Oikawa. Magnetic and martensitic transformations of NiMnX(X=In,Sn,Sb) ferromagnetic shape memory alloys. *Appl. Phys. Lett.* 85, (2004) 4358-4360.

[165] J. Tobola and J. Pierre. Electronic phase diagram of the XTZ (X=Fe, Co, Ni; T=Ti, V, Zr, Nb, Mn; Z=Sn, Sb) semi-Heusler compounds. *J. Alloy. Comp.* 296, (2000) 243-252.

[166] S. Bhattacharya, A. L. Pope, R. T. Littleton IV, Terry M. Tritt, V. Ponnambalam, Y. Xia and S. J. Poon. Effect of Sb doping on the thermoelectric properties of Ti-based half-Heusler compounds, $TiNiSn_{1-x}Sb_x$. *Appl. Phys. Lett.* 77, (2000) 2476-2478.

[167] Tanja Graf, Claudia Felser and Stuart SP Parkin. Simple rules for the understanding of Heusler compounds. *Progress in solid state chemistry* 39, (2011) 1-50.

[168] Jagrati Sahariya and B. L. Ahuja. Electronic structure of Ni_2TiAl: Theoretical aspects and Compton scattering measurement. *Physica B* 407, (2012) 4182-4185.

[169] E. Shreder, S. V. Streltsov, A. Svyazhin, A. Makhnev, V. V. Marchenkov, A. Lukoyanov and H. W. Weber. Evolution of the electronic structure and physical properties of Fe_2MeAl (Me= Ti, V, Cr) Heusler alloys. *J. Phys.: Condens. Matter.* 20, (2008) 045212.

[170] Yoshio Miura, Masafumi Shirai and Kazutaka Nagao. Ab initio study on stability of half-metallic Co-based full-Heusler alloys. *J. App. Phy.* 99, (2006) 08J112.

[171] M. Ishikawa, J. -L. Jorda and A. Junod. Superconductivity in d- and f- band Metals. edited by W. Buckel and W. Weber (Kernforschungszentrum, Karlsruhe, 1982), p. 141.

[172] M. A. S. Boff, G. L. F. Fraga, D. E. Brandao and A. A. Gomes. Specific heat of $Ni_2(Nb_{1-x}T_x)Sn$, T= Ti, Ta, superconducting Heusler compounds. *J. Magn. Magn. Mater.* 153, (1996) 135-140.

[173] Christopher Benndorf, Oliver Niehaus, Hellmut Eckert and Oliver Janka. ^{27}Al and ^{45}Sc NMR Spectroscopy on ScT_2Al and $Sc(T_{0.5}T'_{0.5})_2Al$ (T= T'= Ni, Pd, Pt, Cu, Ag, Au) Heusler Phases and Superconductivity in $Sc(Pd_{0.5}Au_{0.5})_2Al$. *Z. Anorg. Allg. Chem.* 641, (2015) 168-175.

[174] B. T. Matthias. Transition temperatures of superconductors. *Phys. Rev.* 92, (1953) 874.

[175] B. T. Matthias. Empirical relation between superconductivity and the number of valence electrons per atom. *Phys. Rev.* 97, (1955) 74.

[176] M. Ishizuka, M. Iketani and S. Endo. Pressure effect on superconductivity of vanadium at megabar pressures. *Phys. Rev. B* 61, (2000) R3823.

[177] G. Vaitheeswaran, IB Shameen Banu and M. Rajagopalan. Theoretical calculation of superconducting transition temperature in vanadium under pressure. *Solid State Commun.* 116, (2000) 401-404.

[178] Naoshi Suzuki and Minoru Otani. Theoretical study on the lattice dynamics and electron-phonon interaction of vanadium under high pressures. *J. Phys.: Condens. Matter* 14, (2002) 10869-10872.

[179] N. Suzuki and M. Otani. The role of the phonon anomaly in the superconductivity of vanadium and selenium under high pressures. *J. Phys.: Condens. Matter* 19, (2007) 125206.

[180] N. F. Berk and J. R. Schrieffer. Effect of ferromagnetic spin correlations on superconductivity. *Phys. Rev. Lett.* 17, (1966) 433.

[181] T. Klimczuk, C. H. Wang, K. Gofryk, F. Ronning, J. Winterlik, G. H. Fecher, J-C. Griveau, E. Colineau, C. Felser, J. D. Thompson, D. J. Safarik and R. J. Cava. Superconductivity in the Heusler family of intermetallics. *Phys. Rev. B* 85, (2012) 174505.

[182] P. P. Singh. From E_{2g} to Other Modes: Effects of Pressure on Electron-Phonon Interaction in MgB_2. *Phys. Rev. Lett.* 97, (2006) 247002.

[183] D. J. Singh. Multiband Semimetallic Electronic Structure of Superconducting Ta_2PdSe_5. *PloS one* 10, (2015) e0123667.

[184] K. Ramesh Kumar, Venkatrao Chunchu and A. Thamizhavel. Van Hove scenario and superconductivity in full Heusler alloy Pd_2ZrGa. *J. Appl. Phys.* 113, (2013) 17E155.

[185] Wenmei Ming, Yi Liu, Wei Zhang, Jianzhi Zhao and Yugui Yao. First-principles study of the electronic, vibrational, electronphonon interaction and thermodynamics properties of $ZrNi_2Ga$. *J. Phys.: Condens. Matter.* 21, (2009) 075501.

[186] John P. Perdew, Kieron Burke and Matthias Ernzerhof. Generalized gradient approximation made simple. *Physical review letters* 77, (1996) 3865.

[187] Hendrik J. Monkhorst and James D. Pack. Special points for brillouin-zone integrations. *Phys. Rev. B* 13, (1976) 5188.

[188] P. Blöchl, O. Jepsen and O. K. Andersen. Improved tetrahedron method for brillouin-zone integrations. *Phys. Rev. B* 49, (1994) 16223.

[189] Francis Birch. Finite elastic strain of cubic crystals. *Phys. Rev.* 71, (1947) 809.

[190] P. Villars and L. D. Calvert. Pearson's Hand book of Crystallographic Data for Intermetallic Phases. (American Society for Metals, Metals Park, OH, 1986).

[191] E. Şaşioğlu, I. Galanakis, C. Friedrich and S. Blügel. Ab initio calculation of the effective on-site Coulomb interaction parameters for half-metallic magnets. *Phy. Rev. B* 88, (2013) 134402.

[192] M. Born. Thermodynamics of crystals and melting. *J. Chem. Phys.* 7, (1939) 591-603.

[193] R. Hill. The elastic behaviour of a crystalline aggregate. *Proc. Phys. Soc.* A 65, (1952) 349.

[194] V. Kanchana. Mechanical properties of Ti_3AlX (X= C, N): Ab initio study. *Euro. Phys. Lett.* 87, (2009) 26006.

[195] V. Kanchana Ganapathy Vaitheeswaran, Yanming Ma, Yu Xie, Axel Svane and O. Eriksson. Density functional study of elastic and vibrational properties of the Heusler-type alloys Fe_2VAl and Fe_2VGa. *Phys. Rev. B* 80, (2009) 125108.

[196] V. Kanchana, G. Vaitheeswaran, Axel Svane and Anna Delin. First-principles study of elastic properties of CeO_2, ThO_2 and PoO_2. *J. Phys.: Condens. Matter* 18, (2006) 9615.

[197] V. Kanchana, G. Vaitheeswaran and Axel Svane. Calculated structural, elastic and electronic properties of $SrCl_2$. *J. Alloy. Comp.* 455, (2008) 480-484.

[198] S. F. Pugh. XCII. Relations between the elastic moduli and the plastic properties of polycrystalline pure metals. *Philos. Mag.* 45, (1954) 823-843.

[199] J. J. Wortman and R. A. Evans. Young's modulus, shear modulus, and Poisson's ratio in silicon and germanium. *J. App. Phys.* 36, (1965) 153-156.

[200] C. Bungaro, K. M. Rabe and A. Dal Corso. First-principles study of lattice instabilities in ferromagnetic Ni_2MnGa. *Phys. Rev. B* 68, (2003) 134104.

[201] A. T. Zayak, P. Entel, J. Enkovaara, A. Ayuela and Risto M. Nieminen. First-principles investigation of phonon softenings and lattice instabilities in the shape-memory system Ni_2MnGa. *Phys. Rev. B* 68, (2003) 132402.

[202] A. Ayuela, J. Enkovaara, K. Ullakko and R. M. Nieminen. Structural properties of magnetic Heusler alloys. *J. Phys.: Condens. Matter* 11, (1999) 2017.

[203] S. Ağduk and G. Gökoğlu. First-principles study of elastic and vibrational properties of Ni_2MnIn magnetic shape memory alloys. *Euro. Phys. J. B* 79, (2011) 509-514.

[204] S. Ağduk and G. Gökoğlu. Ab initio lattice dynamics of Ni_2MnX (X= Sn, Sb) magnetic shape memory alloys. *J. Alloy. Comp.* 511, (2012) 9-13.

[205] P. B. Allen and R. C. Dynes. Superconductivity at very strong coupling. *J. Phys. C: Solid State Phys.* 8, (1975) L158.

[206] B. Wiendlocha, M. J. Winiarski, M. Muras, C. Zvoriste-Walters, J-C. Griveau, S. Heathman, M. Gazda and T. Klimczuk. Pressure effects on the superconductivity of the $HfPd_2Al$ Heusler compound: Experimental and theoretical study. *Phys. Rev. B* 91, (2015) 024509.

[207] H. M. Tütüncü and G. P. Srivastava. Phonon anomalies and superconductivity in the Heusler compound YPd_2Sn. *J. Appl. Phys.* 116, (2014) 013907.

[208] E. I. Isaev, Rajeev Ahuja, S. I. Simak, A. I. Lichtenstein, Yu Kh Vekilov, Börje Johansson and I. A. Abrikosov. Anomalously enhanced superconductivity and ab initio lattice dynamics in transition metal carbides and nitrides. *Phys. Rev. B* 72, (2005) 064515.

[209] E. I. Isaev, Si I. Simak, I. A. Abrikosov, Rajeev Ahuja, Yu Kh Vekilov, M. I. Katsnelson, A. I. Lichtenstein and Börje Johansson. Phonon related properties of transition metals, their carbides, and nitrides: A first-principles study. *J. Appl. Phys.* 101, (2007) 123519.

[210] S. Bağci, S. Duman, H. M. Tütüncü and G. P. Srivastava. Ground state, phonon spectrum, and superconducting properties of the nonoxide perovskite $CdCNi_3$. *Phys. Rev. B* 78, (2008) 174504.

[211] S. Bağci, H. M. Tütüncü, S. Duman and G. P. Srivastava. Phonons and superconductivity in fcc and dhcp lanthanum. *Phys. Rev. B* 81, (2010) 144507.

[212] H. M. Tütüncü, S. Bağci, G. P. Srivastava and A. Akbulut. Electrons, phonons and superconductivity in rocksalt and tungsten-carbide phases of CrC. *Journal of Physics: Condensed Matter* 24, (2012) 455704.

[213] P. B. Allen and Marvin L. Cohen. Superconductivity and phonon softening. *Phys. Rev. Lett.* 29, (1972) 1593.

[214] H. Wühl, A. Eichler and J. Wittig. Phonon softening in lanthanum under pressure. *Phys. Rev. Lett.* 31, (1973) 1393.

[215] P. V. Sreenivasa Reddy and V. Kanchana. Ab initio study of Fermi surface and dynamical properties of Ni_2XAl (X= Ti, V, Zr, Nb, Hf and Ta). *J. Alloy. Comp.* 616, (2014) 527-534.

[216] E. Z. Kurmaev, F. Werfel, O. Brümmer and R. Flükiger. X-ray photoemission spectra of valence electrons in V_3X and Nb_3X compounds. *Solid. State. Commun.* 21, (1977) 239-243; E. Z. Kurmaev, V. P. Belash, S. A. Nemnonov and A. S. Shulakov. XRay KSpectra of Chromium in Cr_3X-Compounds. *Phys. Status Solidi. (b)* 61, (1974) 365-371; E. Z. Kurmaev, V. P. Belash, R. Flukiger and A. Junod. Influence of the crystal structure and the degree of ordering on the vanadium K-emission spectrum from V_3Au-alloy. *Solid. State.*

Commun. 16, (1975) 1139-1142; R. A. Pollak, C. C. Tsuei and R. W. Johnson. Hybridization and bonding in transition metal compound superconductors: X-ray photoemission from crystalline and amorphous Nb_3Ge. *Solid. State. Commun.* 23, (1977) 879-881; A. Junod, T. Jarlborg and J. Muller. Heat-capacity analysis of a large number of A 15-type compounds. *Phys. Rev. B.* 27, (1983) 1568.

[217] S. Tanaka, Handoko, A. Miyake, T. Kagayama, K. Shimizu, A.E. Böhmer, P. Burger, F. Hardy, C. Meingast, H. Tsuisumi and Y. Ōnuki. Superconducting and Martensitic Transitions of V_3Si and Nb_3Sn under High Pressure. *Journal of the Physical Society of Japan* 81, (2012) SB026.

[218] W. E. Pickett, K. M. Ho and Marvin L. Cohen. Electronic properties of Nb_3Ge and Nb_3Al from self-consistent pseudopotentials. I. Band structure and density of states. *Phys. Rev. B* 19, (1979) 1734.

[219] M. Rajagopalan. Electronic topological transition in Nb_3Al under compression: An ab initio study. *Physica B* 413, (2013) 1-5.

[220] C. Paduani. Electronic Structure of the A_3B Compounds: A= Nb; B= Al, Ga, Ge, Sn and In. *Brazilian Journal of Physics* 37, (2007) 1073-1076.

[221] M. Sundareswari, Swaminathan Ramasubramanian and Mathrubutham Rajagopalan. Elastic and thermodynamical properties of A15 Nb_3X (X= Al, Ga, In, Sn and Sb) compounds-First principles DFT study. *Solid State Communications* 150, (2010) 2057-2060.

[222] V. Srinivasan, B. K. Godwal, Jeffrey C. Grossman and Raymond Jeanloz. Electronic topological transitions in Cd at high pressures. *arXiv preprint arXiv:1511* 01989 (2015).

[223] Y. O. Kvashnin, W. Sun, Igor Di Marco and Olle Eriksson. Electronic topological transition and noncollinear magnetism in compressed hcp Co. *Physical Review B* 92, (2015) 134422.

[224] A.P. Kracknell and K.C. Wang. The Fermi Surface: Its Concept, Determination and Use in the Physics of Metals. Oxford University Press (1973).

[225] G. Bilbro and W. L. McMillan. Theoretical model of superconductivity and the martensitic transformation in A15 compounds. *Physical Review B* 14, (1976) 1887.

[226] R. Escudero and F. Morales. Point contact spectroscopy of crystals: Evidence of a CDW gap related to the martensitic transition. *Solid State Communications* 150, (2010) 715-719.

[227] G. Gruner. Density Waves in Solids. (Addison-Wesley, Reading, MA) (1994).

[228] V. Mkrtcheyan, Ravhi Kumar, Jason Baker, Anthony Connolly, Daniel Antonio, Andrew Cornelius and Yusheng Zhao. High pressure transport and structural studies on Nb_3Ga superconductor. *Physica B: Condensed Matter* 459, (2015) 21-23.

[229] M. Neuberger, D. L. Gribsby and Jr. W. H. Veazie. Hand book of Electronic Materials, Vol.4, Niobium Alloys and Compounds. (IFI-Plenum, New Yark, 1972).

[230] R. Viswanathan. Martensitic transformations in V_3Ga and Nb_3Al. *Mat. Res. Bull.* 9, (1974) 277-281.

[231] Haruki Kawamura, Kyoji Tachikawa, Kenichi Takemura and Shigeru Minomura. Bulk Modulus of A-15 Nb_3Ge. *J. Phys. Soc. Japan* 47, (1979) 1365-1366.

[232] E. C. van Reuth and R. M. Waterstrat. Atomic Ordering in Binary A15-Type Phases. *Acta Cryst.* B24, (1968) 186.

[233] Xianfeng Li, dong Chen, yi wu, Mingliang Wang, Naiheng Ma and Haowei Wang. Assesment on the structural, elastic and electronic properties of Nb_3Ir and Nb_3Pt: A first-principles study. *AIP Advances* 7, (2017) 065012.

[234] C. Paduani. Electronic properties of the A-15 Nb based intermetallics Nb_3(Os, Ir, Pt, Au). *Solid State Commun.*, 144, (2007) 352-356.

[235] C. Paduani. Electronic structure and Fermi surfaces of the superconductive A_3B compounds: A= V, Nb; B= Ga, Ge and Sn. *Solid State Commun.* 149, (2009) 1269-1273.

[236] P. V. Sreenivasa Reddy, V. Kanchana, G. Vaitheeswaran, P. Modak and Ashok K. Verma. Electronic topological transitions in Nb_3X (X = Al, Ga, In, Ge, and Sn) under compression investigated by first principles calculations. *J. Appl. Phys.* 119, (2016) 075901

[237] D. Bimberg, M. S. Skolnick and Leonard M. Sander. Camel's back induced stabilization of electron-hole liquids: GaP. *Solid State Commun.* 27, (1978) 949-953.

[238] Jin Li, Chaoyu He, Lijun Meng, Huaping Xiao, Chao Tang, Xiaolin Wei, Jinwoong Kim, Nicholas Kioussis, G. Malcolm Stocks and Jianxin Zhong. Li, Jin, Chaoyu He, Lijun Meng, Huaping Xiao, Chao Tang, Xiaolin Wei, Jinwoong Kim, Nicholas Kioussis, G. Malcolm Stocks, and Jianxin Zhong. Two-dimensional topological insulators with tunable band gaps: Single-layer HgTe and HgSe. *Scientific Reports* 5, (2015) 14115.

[239] Z. H. Yu, C. Y. Li and H. Z. Liu. Compressibility anomaly in the superconducting material Nb_3Al under high pressure. *Physica B: Condensed Matter* 407, (2012) 3635-3638.

[240] B. K. Godwal, P. Modak and R. S. Rao. On the high pressure electronic topological transitions in zinc. *Solid State Commun.* 125, (2003) 401-405.

[241] Rita Loria, Gianluca De Marzi, Simone Anzellini, Luigi Muzzi, Nicola Pompeo, Fabrizio Gala, Enrico Silva, and Carlo Meneghini, The Effect of Hydrostatic Pressure on the Superconducting and Structural Properties of Nb_3Sn: Ab-initio Modeling and SR-XRD Investigation, *IEEE TRANSACTIONS ON APPLIED SUPERCONDUCTIVITY* 27, (2017) 8400305.

[242] J. M. Fournier and L. Manes, "Actinides-Chemistry and Physical Properties-Structure and Bonding", edited by L. Manes and Heidelberg, Springer Verlag, (1985), p. 1.

[243] P. Ch. Sahu, N. V. Chandra Shekar, N. Subramanian, Mohammad Yousuf and K. Govindarajan. Advances in High Pressure Research in Condensed Matter. Edited by S. K. Sikka, S. C. Gupta and B. K. Godwal, NISCOM, New Delhi (1997) p. 187.

[244] A. K. Mcmahan. Pressure-induced changes in the electronic structure of solids. *Physica B+C* 139/140, (1986) 31-41.

[245] H. Tups, K. Takemura and K. Syassen. Interband optical absorption and electronic $s-d$ transition in Rb and Cs at high pressures. *Phys. Rev. Lett.* 49, (1982) 1776-1779.

[246] A. Jayaraman. Handbook on the Physics and Chemistry of Rare Earths. Edited by K. A. Gschneidner Jr and L. Eyring. North Holland, Amsterdam, (1979) Vol 2, p. 575.

[247] Alka B. Garg, B. K. Godwal, S. Meenakshi, P. Modak, R. S. Rao, S. K. Sikka, V. Vijay Kumar, A. Lausi and E. Bussetto. Electronic topological transition in AuX_2 (X = In, Ga and Al) compounds at high pressures. *J. Phys.: Condens. Matter* 14, (2002) 10605-10608.

[248] N. V. Chandrashekar, M. Rajagopalan, J. F. Meng, D. A. Polvani and J. V. Badding. Electronic structure and thermoelectric power of cerium compounds at high pressure. *J. Alloys Compd.* 388, (2005) 215.

[249] D. M. Ceperley and B. J. Alder. Ground state of the electron gas by a stochastic method. *Phys. Rev. Lett.* 45, (1980) 566.

[250] Dabhi D. Shweta, Deepika Shrivastava, Prafulla K. Jha and Sankar P. Sanyal. On possibility of superconductivity in SnSb: A first principle study. *Physica C* 528, (2016) 56-59.

[251] P. I. Bezotosnyi, K. A. Dmitrieva, S. Yu Gavrilkin, K. S. Pervakov, A. Yu Tsvetkov, V. P. Martovitski, A. G. Rybkin, O. Yu Vilkov and V. M. Pudalov. ARPES measurements of SnAs electronic band structure. *Jetp Lett.* (2017) 1-3. https://doi.org/10.1134/S0021364017200024.

[252] D. Billington, Simon A. C. Nickau, Tom Farley, Jack R. Ward, Rosie F. Sperring, Thomas E. Millichamp, David Ernsting and Stephen B. Dugdale. Electron-phonon coupling and superconducting critical temperature of the YIr_2Si_2 and $LaIr_2Si_2$ high-temperature polymorphs from first-principles. *J. Phys. Soc. Japan* 83, (2014) 044710.

[253] David Billington, David Ernsting, Thomas E. Millichamp and Stephen B. Dugdale. Electron-phonon superconductivity in $BaSn_5$. *Phil. Mag.* 95(15), (2015) 1728-1737.

[254] P. V. Sreenivasa Reddy, V. Kanchana, G. Vaitheeswaran and David J. Singh. Predicted superconductivity of Ni_2VAl and pressure dependence of superconductivity in Ni_2NbX (X= Al, Ga and Sn) and Ni_2VAl. *J. Phys.: Condens. Matter.* 28, (2016) 115703.

[255] S. B. Dugdale. Life on the edge: a beginner's guide to the Fermi surface. *Phys. Scr.* 91, (2016) 053009.

[256] S. Geller and G. W. Hull Jr. Superconductivity of intermetallic compounds with NaCl-type and related structures. *Phys. Rev. Lett.* 13, (1964) 127-129.

[257] W. Morris Jones and E. G. Bowen. The Compound SnSb. *Nature* 126, (1930) 846-847.

[258] P. V. Sreenivasa Reddy, V. Kanchana, T. E. Millichamp, G. Vaitheeswaran and S. B. Dugdale. Enhanced superconductivity in the high pressure phase of SnAs studied from first principles. *Physica B* 505, (2017) 33-40.

[259] J. C. Duthie and D. G. Pettifor. Correlation between d-band occupancy and crystal structure in the rare earths. *Phys. Rev. Lett.* 38, (1977) 564.

[260] Hans L. Skriver. Crystal structure from one-electron theory. *Phys. Rev. B* 31, (1985) 1909.

[261] Jyoti S. Gyanchandani, Satish C. Gupta, S. K. Sikka and R. Chidambaram. Structural stability of hafnium under pressure. *J. Phys.: Condens. Matter* 2, (1990) 6457.

[262] Jyoti S. Gyanchandani, S. C. Gupta, S. K. Sikka and R. Chidambaram. The equation of state and structural stability of titanium obtained using the linear muffin-tin orbital band-structure method. *J. Phys.: Condens. Matter* 2, (1990) 301.

[263] A. L. Kutepov and S. G. Kutepova. Crystal structures of Ti under high pressure: theory. *Phys. Rev. B* 67, (2003) 132102.

[264] Rajeev Ahuja, Leonid Dubrovinsky, Natalia Dubrovinskaia, JM Osorio Guillen, Maurizio Mattesini, Börje Johansson and Tristan Le Bihan. Titanium metal at high pressure: Synchrotron experiments and ab initio calculations. *Phys. Rev. B* 69, (2004) 184102.

[265] Yan-Jun Hao, Lin Zhang, Xiang-Rong Chen, Ying-Hua Li and Hong-Liang He. Phase transition and elastic constants of zirconium from first-principles calculations. *J. Phys.: Condens. Matter* 20, (2008) 235230.

[266] Nihat Arikan. The first-principles study on Zr_3Al and Sc_3Al in $L1_2$ structure. *J. Phys. Chem. Solids* 74, (2013) 794-798.

[267] David Geist, Christian Rentenberger and Hans Peter Karnthaler. High pressure torsion of intermetallic Zr_3Al. *In Materials Science Forum* 584, (2008) 553-558.

[268] P. Ravindran and R. Asokamani. Electronic structure, phase stability, equation of state, and pressure-dependent superconducting properties of Zr_3Al. Phys. Rev. B 50, (1994) 668.

[269] T. Hong, T. J. Watson-Yang, X-Q. Guo, A. J. Freeman, T. Oguchi and Jian-hua Xu. Crystal structure, phase stability, and electronic structure of Ti-Al intermetallics: Ti_3Al. *Phys. Rev. B* 43, (1991) 1940.

[270] N. A. Dubrovinskaia, Marie Vennström, I. A. Abrikosov, R. Ahuja, P. Ravindran, Yvonne Andersson, O. Eriksson, V. Dmitriev and L. S. Dubrovinsky. Absence of a pressure-induced structural phase transition in Ti_3Al up to 25 GPa. *Phys. Rev. B* 63, (2000) 024106.

[271] D. Banerjee. in Intermetallic Compounds-Principles and Practice 2. Edited by J. H. Westbrook and R. L. Fleischer 101 (Wiley, NewYork, 1995), p. 101.

[272] Y. Yang, Y. L. Lao and D. Li. Titanium 99: Science and technology, CRISM (St. Petersburg: Prometey) (2000) 278.

[273] C. Ravi, S. MathiJaya, M. C. Valsakumar and R. Asokamani. Site preference of Zr in Ti_3Al and phase stability of Ti_2 ZrAl. *Phys. Rev. B* 65, (2002) 155118.

[274] C. Ravi, P. Vajeeston, S. Mathijaya and R. Asokamani. Electronic structure, phase stability, and cohesive properties of Ti_2XAl (X= N b, V, Zr). *Phys. Rev. B* 60, (1999) 15683.

[275] D. Sornadurai, V. S. Sastry, V. Thomas Paul, Roberta Flemming, Feby Jose, R. Ramaseshan and S. Dash. Microstructure, crystal structure and mechanical properties of the new ternary intermetallic alloy phase Zr_2TiAl. *Intermetallics* 24, (2012) 89-94.

[276] P. J. Webster and K. R. A. Ziebeck. Magnetic and chemical order in Heusler alloys containing cobalt and titanium. *J. Phys. Chem. Solids.* 34, (1973) 1647-1654.

[277] Suklyun Hong and C. L. Fu. Hydrogen in Laves phase ZrX_2 (X= V, Cr, Mn, Fe, Co, Ni) compounds: Binding energies and electronic and magnetic structure. *Phys. Rev. B* 66, (2002) 094109.

[278] Valentin Iota, Jae-Hyun Park Klepeis, Choong-Shik Yoo, Jonathan Lang, Daniel Haskel and George Srajer. Electronic structure and magnetism in compressed 3*d* transition metals. *Appl. Phys. Lett.* 90, (2007) 042505.

[279] Yanli Wang, Yi Ding and Jun Ni. First-principles study of pressure effects on $CaFe_2As_2$ and $BaFe_2As_2$. *Solid. State. Commn.* 149, (2009) 2125-2129.

[280] Gul Rahman, In Gee Kim and Arthur J. Freeman. First-principles prediction of spin-density-reflection symmetry driven magnetic transition of CsCl-type FeSe. *J. Magn. Magn. Mater* 322, (2010) 3153-3158.

[281] Swetarekha Ram, V. Kanchana, G. Vaitheeswaran, Axel Svane, S. B. Dugdale and Niels Egede Christensen. Electronic topological transition in $LaSn_3$ under pressure. *Phys. Rev. B* 85, (2012) 174531.

[282] Swetarekha Ram, V. Kanchana, Axel Svane, S. B. Dugdale and Niels Egede Christensen. Fermi surface properties of AB_3 (A= Y, La; B= Pb, In, Tl) intermetallic compounds under pressure. *J. Phys.: Condens. Matter* 25, (2013) 155501.

[283] P. V. Sreenivasa Reddy, V. Kanchana, G. Vaitheeswaran and David J. Singh. Predicted superconductivity of Ni_2VAl and pressure dependence of superconductivity in Ni_2NbX (X= Al, Ga and Sn) and Ni_2VAl. *J.Phys.:Condens. Matter* 28, (2016) 115703.

[284] P. V. Sreenivasa Reddy, V. Kanchana, G. Vaitheeswaran, P. Modak and Ashok K. Verma. Electronic topological transitions in Nb_3X (X= Al, Ga, In, Ge, and Sn) under compression investigated by first principles calculations. *J. Appl. Phys.* 119, (2016) 075901.

[285] Nitin Samarth. Condensed-matter physics: Magnetism in flatland. *Nature* 546, (2017): 216-218.

[286] Cheng Gong, Lin Li, Zhenglu Li, Huiwen Ji, Alex Stern, Yang Xia, Ting Cao, Wei Bao, Chenzhe Wang, Yuan Wang, Z. Q. Qiu, R. J. Cava, Steven G. Louie, Jing Xia and Xiang Zhang. Discovery of intrinsic ferromagnetism in two-dimensional van der Waals crystals. *Nature* (2017) doi:10.1038/nature22060.

[287] Bevin Huang, Genevieve Clark, Efrén Navarro-Moratalla, Dahlia R. Klein, Ran Cheng, Kyle L. Seyler, Ding Zhong, Emma Schmidgall, Michael A. McGuire, David H. Cobden, Wang Yao, Di Xiao, Pablo Jarillo-Herrero and Xiaodong Xu. Layer-dependent ferromagnetism in a van der Waals crystal down to the monolayer limit. *Nature* 546, (2017) 270.

[288] N. S. Satya Murthy, R. J. Begum, C. S. Somanathan and M. R. L. N. Murthy. Magnetic structure of MnAlGe. *J. Appl. Phys.* 40, (1969) 1870-1871.

[289] Kenzo Shibata, Takeshi Shinohara and Hiroshi Watanabe. Magnetic Properties of A New Ferromagnetic Compound MnGaGe. *J. Phys. Soc. Japan* 32, (1972) 1431-1431.

[290] V. Johnson and W. Jeitschko. Ferromagnetic anti-PbFCl-type ZnMnSb. *J. Solid State Chem.* 22, (1977) 71-75.

[291] Sin-ichi Mori, Takeshi Kanomata, Hiroshi Yamauchi, Shinichi Sakatsume and Takejiro Kaneko. Magnetic Properties of MnZnSb. *Jpn. J. Appl. Phys.* 32, (1993) 273.

[292] T. Kanomata, H. Endo, S. Mori, H. Okajima, T. Hihara, K. Sumiyama, T. Kaneko and K. Suzuki. Specific heat of MnAlGe, MnGaGe and MnZnSb. *J. Mag. Mag. Mat.* 140, (1995) 133-134.

[293] M. Sieberer, S. Khmelevskyi and Peter Mohn. Magnetic instability within the series $T\mathrm{Cu_3N}$ (T= Pd, Rh, and Ru): A first-principles study. *Phys. Rev. B* 74, (2006) 014416.

[294] R. F. W. Bader. Atoms in Molecules: A Quantum Theory. International Series of Monographs on Chemistry (Oxford University Press, Oxford, 1990), Vol. 22.

List of Publications

Refereed journal papers

1. P. V. Sreenivasa Reddy and V. Kanchana, Ab initio study of Fermi surface and dynamical properties of Ni_2XAl (X= Ti, V, Zr, Nb, Hf and Ta), *J. Alloys and Comp.*, 616, (2014) 527-534.

2. P. V. Sreenivasa Reddy, V. Kanchana, G. Vaitheeswaran and David. J. Singh, Predicted superconductivity of Ni_2VAl and pressure dependence of superconductivity in Ni_2NbX (X = Al, Ga and Sn) and Ni_2VAl, *J. Phys.: Conden. Matter*, 28, (2016) 115703.

3. P. V. Sreenivasa Reddy, V. Kanchana, G. Vaitheeswaran, P. Modak and Ashok K. Verma, Electronic topological transitions in Nb_3X (X = Al, Ga, In, Ge, and Sn) under compression investigated by first principles calculations, *J. Appl. Phys.*, 119, (2016) 075901.

4. P. V. Sreenivasa Reddy, V. Kanchana, T.E. Millichamp, G. Vaitheeswaran and S. B. Dugdale, Enhanced superconductivity in the high pressure phase of SnAs studied from first principles, *Physica B*, 505, (2017) 33-40.

5. P. V. Sreenivasa Reddy and V. Kanchana, Enhanced superconductivity in SnSb under pressure: a first principles study, *J. Phys.: Conden. Matter*, 29, (2017) 405502.

6. P. V. Sreenivasa Reddy, V. Kanchana, G. Vaitheeswaran, Andrei V. Ruban and N. E. Christensen, Evidence for the antiferromagnetic ground state of Zr_2TiAl: a first-principles study, *J. Phys.: Conden. Matter*, 29, (2017) 265801.

7. P. V. Sreenivasa Reddy, P. C. Sreeparvathy, V. Kanchana, G. Vaitheeswaran and L. Petit, Enhanced quasi two dimensional nature of MnXGe(X= Al and Ga) and MnZnSb under pressure, revealed from first principles. Under preparation.

8. P. Anand Kumar, A. T. Satya, P. V. Sreenivasa Reddy, M. Sekar, V. Kanchana, G. Vaitheeswaran, Awadhesh Mani, S. Kalavathi and N. V. Chandra Shekar, Structural and low temperature transport properties of Fe_2B and FeB systems at high pressure, *J. Phys. Chem. Solids.*, 109, (2017) 18-25.

Conference papers

1. P. V. Sreenivasa Reddy and V. Kanchana, Electronic and mechanical properties of Zr_2TiAl: A first principles study, *AIP Conf. Proc.* 1591, (2014) 1121.

2. P. V. Sreenivasa Reddy, G. Vaitheeswaran and V. Kanchana, Fermi surface study of $ScAu_2$(Al, In) and $ScPd_2$(Sn, Pb) compounds, *AIP Conf. Proc.* 1665, (2015) 090035.